École Polytechnique
Laboratoire d'Hydrodynamique

Thèse présentée pour obtenir le grade de

DOCTEUR DE L'ÉCOLE POLYTECHNIQUE

Spécialité : Mécanique

par

Pierre AUGIER

Turbulence en milieu stratifié, étude des mécanismes de la cascade

Soutenue le 21 octobre 2011 devant un jury composé de

Paul BILLANT	directeur de thèse	LadHyX, Palaiseau
Jean-Marc CHOMAZ	directeur de thèse	LadHyX, Palaiseau
Thierry DAUXOIS	examinateur	ENS Lyon, Lyon
Olivier Eiff	examinateur	IMFT, Toulouse
Bach Lien HUA	examinatrice	IFREMER, Plouzané
Erik LINDBORG	rapporteur	KTH, Stockholm, Suède
Frédéric MOISY	rapporteur	FAST, Orsay
Joël SOMMERIA	examinateur	LEGI, Grenoble

LadHyX
Ecole Polytechnique
FRANCE

Edité par : Ecole Polytechnique

Résumé

La turbulence fortement influencée par une stratification stable en densité est étudiée expérimentalement, numériquement et théoriquement. Ce type de turbulence est rencontré dans l'atmosphère et les océans dans une gamme d'échelles intermédiaires où la force de Coriolis est négligeable.

Dans une première partie, la transition à la turbulence d'un écoulement simple : une paire de tourbillons colonnaires contra-rotatifs est étudiée. Des Simulations Numériques Directes (DNS) montrent que lorsque la dissipation est suffisamment faible, deux instabilités secondaires, de cisaillement et gravitationnelle, se développent après l'instabilité zigzag. La taille caractéristique des tourbillons de Kelvin-Helmholtz est de l'ordre de l'échelle de flottabilité. Ces deux instabilités mènent à une transition à la turbulence qui présente des spectres anisotropes similaires à ceux associés à la turbulence stratifiée pleinement développée. Pour la première fois, un retour à l'isotropie est observé pour des échelles inférieures à l'échelle d'Ozmidov.

Dans une deuxième partie, un écoulement pleinement turbulent forcé par plusieurs générateurs de dipoles est étudié. Les expériences aux plus grands nombres de Reynolds de flottabilité ont permis pour la première fois de quasiment atteindre le régime de turbulence fortement stratifié. Les simulations numériques forcées dans l'espace physique avec le même type de forcage ont permis de reproduire les résultats expérimentaux et de les étendre aux grands nombres de Reynolds de flottabilité. Elles révèlent que la plus grande échelle des retournements est de l'ordre de l'échelle de flottabilité. Enfin, une généralisation de la loi des 4/5 de Kolmogorov est proposée pour la turbulence stratifiée.

Abstract

Turbulence strongly influenced by a stable density stratification is studied experimentally, numerically and theoretically. This type of turbulence is encountered in the atmosphere and Oceans in an intermediate range of scales for which the Coriolis force is negligible.

In a first part, the transition to turbulence of a simple flow: a pair of columnar contra-rotating vortices is studied. Direct Numerical Simulations (DNS) show that when the dissipation is sufficiently weak, two secondary instabilities, the shear and gravitational instabilities, develop after the zigzag instability. The characteristic length scale of the Kelvin-Helmholtz billows is of the order of the buoyancy scale. Both instabilities lead to a transition to turbulence which exhibits anisotropic spectra similar to those associated to fully developed strongly stratified turbulence. For the first time, a return to isotropy is observed for scales smaller than the Ozmidov length scale.

In a second part, a fully developed turbulent flow forced with several vortex generators is studied. The experiments at the larger buoyancy Reynolds numbers have enabled for the first time to nearly reach the strongly stratified turbulent regime. These experimental results have been reproduced and extended to larger Reynolds numbers with numerical simulations forced in physical space with the same type of forcing. They reveal that the larger scale of the overturnings is of the order of the buoyancy scale. Finally, a generalisation of the 4/5s Kolmogorov law is proposed for stratified turbulence.

Remerciements

Alors que j'écris ces lignes, ce manuscrit de thèse est bouclé et je suis à Waikiki, Honolulu, Hawaii ! Dans le cadre de mon post-doc au KTH à Stockholm, nous allons commencer une collaboration sur la dynamique de l'atmosphère avec des chercheurs hawaïens et japonais. Cette thèse est bien finie : passons au remerciements !

Cette thèse est le fruit du travail collectif qui a duré trois ans. En première ligne, il y avait bien sûr mes directeurs de thèse et moi. Mais pour le reste tout est affaire d'environnement général.

Les résultats de cette thèse sont pour moi de deux natures. Il y a bien sûr les résultats et des productions scientifiques. Mais ce travail a aussi fait de moi un "docteur", jeune scientifique capable (paraît-il) d'une activité propre de recherche et d'enseignement. Ces remerciements ont donc une connotation personnelle particulière et viennent du fond du coeur. Je suis sincèrement très reconnaissant envers tous ceux qui m'ont permis de bien vivre la période passionnante et éminemment formatrice qu'a été cette thèse.

Merci d'abord à mes deux directeurs de thèse si complémentaires. Merci de m'avoir laissé tant de liberté et d'avoir été en même temps disponibles et toujours intéressés.

Merci Paul ! Merci de m'avoir appris tant de choses, autant en terme de connaissances hydrodynamiques et techniques qu'en terme d'attitude scientifique : rigueur, honnêteté, persévérance, perfectionnisme... Merci aussi d'avoir été toujours prêt à réfléchir et aider à avancer. Merci pour cet extraordinaire travail sur la rédaction des articles. Si un jour j'arrive à écrire indépendamment un article, ce sera beaucoup grâce à toi !

Merci Jean-Marc ! Merci pour ces discussions scientifiques et non-scientifiques toujours si enrichissantes surtout quand on arrive à suivre. Merci de montrer qu'on peut continuer à faire de la recherche activement tout en étant directeur du labo, rameur, artiste scientifique et cavalier malchanceux luttant contre les tracteurs.

Je dois des remerciements spéciaux à Axel Deloncle pour le code ns3d si efficace et si bien commenté ; à Sébastien Galtier pour cette expérience de collaboration avec un chercheur travaillant dans un domaine voisin ; et à Maria Eletta Negretti pour son aide précieuse sur l'expérience et la PIV, mais bien plus généralement pour sa présence qui m'a permis de bien commencer cette thèse.

Merci à mes deux rapporteurs de thèse, Erik Lindborg et Frédéric Moizy d'avoir lu de façon critique et constructive ce long manuscrit. Vos remarques pertinentes m'ont été très précieuses. Merci à mes examinateurs de thèse d'être venu à Paris depuis Brest, Grenoble, Lyon et Toulouse pour participer à ma soutenance et apporter leurs regards sur mon travail.

Cette thèse est aussi le résultat de l'unité de production scientifique du LadHyX, laboratoire de l'Ecole Polytechnique. Alors en plus de remercier ses directeurs (et directeur exécutif) en exercice pendant ma thèse, Patrick Huerre, Jean-Marc Chomaz et Christophe Clanet, je remercie tous ceux qui contribuent à la bonne marche de ce labo et à la bonne ambiance qui y règne.

Un merci tout particulier à Antoine Garcia et Daniel Guy de faire en sorte que les choses expérimentales et numériques fonctionnent et de donner de si bons conseils et si bonnes idées. Merci à Thérèse Lescuyer et aux autres secrétaires sans qui rien ne fonctionnerait ! Merci à mes compagnons de thèse, les autres thésards du labo. Je cède à la facilité de ne citer personne mais merci pour les bons moments, les discussions, le café, le foot et les coups de mains pour le numérique.

Bon, comme une thèse ça vient de loin, merci maman, pour tout mais surtout d'avoir fait en sorte que je ne sois pas complètement largué en cours... Merci pour tout à toute la petite famille à qui je dois tant. Merci à mes instits et professeurs, surtout les sympas ! Merci au collège Fabre d'Eglantine, à l'Université de La Rochelle et à l'ENS Lyon. En fait, ce sera plus cours et plus complet de remercier carrément les services publics de notre République.

Une thèse, c'est aussi une sacret bataille pendant laquelle il vaut mieux ne pas perdre courage au premier coup de vent. Merci aux amis, aux copains et à tous les gentils.

Une thèse c'est une réflexion profonde et de longue haleine. En cela, détours et pauses ont pour moi été indispensables. Salut à la nature si belle et toujours étonnante. Salut à la culture humaine aussi. Merci aux artistes, philosophes et autres penseurs qui nous permettent de réfléchir hors de la doxa dominante et de tenter de vivre en homme libre.

Pendant cette thèse, il y a eu matière à réfléchir sur les instabilités, les non-linéarités et la turbulence aussi ailleurs que dans les livres ! Le temps des crises et des bouleversements est revenu. Je voudrais saluer l'humanité impliquée dans cette grande aventure et tout particulièrement ceux qui en montrant tant de courage pour faire avancer l'intérêt général, m'en ont donné du courage ! Pendant cette thèse, des peuples ont pu faire tomber des tyrans ! Cela me conforte dans l'idée qu'il n'y a pas de raisons que l'on ne puisse pas vivre dignement tous. Je salue tous ceux qui se battent pour faire naître un autre monde où l'humain d'abord primera.

En parlant de naissance, la fin de rédaction d'une thèse a quelque chose à voir avec un accouchement. Je salue Max qui a à peu près le même âge que ce manuscrit de thèse et ses parents qui doivent maintenant pouvoir commencer à dormir toute la nuit. Le long cheminement vers le progrès humain est assurément très tortueux mais j'ai la conviction qu'à ton échelle Max, il se remettra en marche. J'aime penser que cette thèse puisse, très modestement, s'inscrire dans ce mouvement.

Pour finir en beauté, un très grand merci à mon amour, Marianne.

Hawaï, le 4 décembre 2011.

Foreword

This manuscript thesis presents a work performed at the LadHyX, the hydrodynamics laboratory of Ecole Polytechnique. During 3 years, between September 2008 and August 2011, I have worked as a PhD student on the direction of Paul Billant and Jean-Marc Chomaz on the dynamics of the turbulence influenced by a stable density stratification.

The major part of this manuscript is written in English. However, the first chapter presenting our motivations and a general introduction on the dynamics of fluids influenced by a stable density stratification and rotation is written in French. No-French-speaking readers and advanced readers can skip these basic reminders and go directly toward page 37 to begin with the main introduction on stratified turbulence.

Table des matières

Chapitre 1

Introduction générale sur la dynamique des fluides géophysiques

1.1 Contexte et motivations

Ce travail de thèse traite de la dynamique des écoulements turbulents fortement influencés par une stratification stable en densité. Nous abordons cette problématique sous l'angle de la dynamique des structures cohérentes et des instabilités hydrodynamiques. Dans ce chapitre, on commence par introduire les notions de turbulence et de stratification. Puis, on présente quelques éléments sur la dynamique des océans et de l'atmosphère qui est le principal domaine d'application des études de la turbulence en milieu stratifié.

1.1.1 Notions de turbulence et de stratification

Turbulence, cascade et mécanismes. La turbulence désigne dans le sens commun une agitation désordonnée. Dans le cadre de ce travail de recherche en hydrodynamique, le mot turbulence peut désigner différents régimes d'écoulements d'un fluide, modifiés ou non par la présence d'éléments influençant la dynamique (dimension de l'espace, stratification, rotation du référentiel, etc.). Ces écoulements partagent la caractéristique d'être fortement désordonnés, dans le sens qu'ils sont imprévisibles aux temps longs (chaotiques, avec une forte sensibilité aux conditions initiales) et présentent une superposition d'échelles spatiales et temporelles très différentes : de très grands et très petits tourbillons se côtoient. Par exemple, dans l'atmosphère, l'écoulement est forcé à une échelle de plusieurs centaines de kilomètres et la dissipation se produit à des échelles de quelques centimètres. Les grandes structures sont beaucoup trop grandes et trop rapides pour être influencées par la dissipation visqueuse. On quantifie cette influence par un nombre sans dimension, le nombre de Reynolds $Re = UL_h/\nu$, où U et L_h sont respectivement une vitesse et une taille horizontale caractéristiques et ν est la viscosité cinématique. Lorsque le nombre de Reynolds est suffisamment grand, les structures hydrodynamiques forcées évoluent selon leur propre dynamique non-linéaire sur des temps longs et des mécanismes non-linéaires liés à des

instabilités peuvent transférer de l'énergie vers des échelles différentes (plus petites dans le cas de la turbulence homogène et isotrope, dite classique). Ce processus se reproduit d'échelles en échelles avec une certaine invariance, ce qui mène à une répartition en énergie dans le domaine inertiel (aux échelles de la cascade) de type auto-similaire, avec des spectres en loi de puissance (par exemple en $k^{-5/3}$ dans le cas de la turbulence classique, où k est le vecteur d'onde). Cette cascade d'énergie, décrite pour la première fois par Richardson (Frisch, 1995), permet dans certains cas (et en particulier dans le cas de la turbulence classique) le transfert de l'énergie vers les petites échelles dissipatives. Si cette représentation peut paraître relativement simple, elle décrit suffisamment bien la turbulence classique pour être à la base de raisonnements d'une grande puissance prédictive (cf. les lois de Kolmogorov rappelées dans la section 1.3). Précisons que les caractéristiques de la cascade turbulente classique ne dépendent pas (en fait peu) de la forme précise du forçage : cette cascade est dite "universelle". Comment les processus turbulents sont-ils affectés par une stratification stable en densité ? Telle est la problématique traitée dans ce manuscrit de thèse.

Stratification stable en densité. A chaque état d'un fluide caractérisé par des hétérogénéités de masse volumique[1], on associe une énergie potentielle liée à la gravité. L'exemple du verre d'eau dans lequel on verse un peu de sirop est parlant. La dynamique tend vers l'état de moindre énergie potentielle : le sirop plus dense descend. Lorsque toute l'énergie cinétique aura été dissipée, le système se sera réorganisé de telle façon que le fluide le plus dense soit sous le fluide le moins dense avec des surfaces isodensités horizontales. Cet état stationnaire stratifié en densité est dynamiquement stable et donc très courant dans la nature. Dans ce travail de thèse, on étudie la dynamique des fluides autour de cet état de moindre énergie.

Par contre cet état n'est pas stable thermodynamiquement. La diffusion du facteur de variation de la densité (la concentration d'un composant chimique ou la température) mènera à terme à l'homogénéisation de la densité. Mais la diffusion est très inefficace pour mélanger sur des grandes distances. On observe déjà ce phénomène d'inefficacité de la diffusion avec l'exemple du sirop dans un verre et cela est pire dans le cas de milieux beaucoup plus grands comme les fluides géophysiques (atmosphère, océans, mers, lacs). Ainsi la diffusion moléculaire de la stratification globale est négligeable dans les milieux fluides de grandes tailles qui sont très couramment stratifiés en densité. Notons que les hétérogénéités de densité proviennent de forçages thermodynamiques, souvent thermiques et la plupart du temps liés au soleil.

Dans beaucoup de cas, la dynamique du fluide et la stratification en densité sont fortement couplées. La stratification intervient dans les équations sous la forme d'une pulsation, dite fréquence de Brunt-Väisälä N. On peut quantifier le couplage avec la dynamique fluide en comparant cette fréquence à la fréquence caractéristique du mouvement U/L_h. Lorsque la fréquence N est grande devant la fréquence caractéristique de l'écoulement, le ratio $F_h = U/(NL_h)$, nombre sans dimension appelé nombre de Froude horizontal, est petit et la stratification influence fortement l'écoulement.

[1]Comme en anglais, on dira de façon équivalente masse volumique et densité, sans faire de différence entre les deux notions.

L'expression du nombre de Froude montre que la stratification influence plus des écoulements de grande taille et relativement lents.

Ainsi le principal domaine d'application de la turbulence fortement influencée par une stratification en densité est la dynamique des fluides géophysiques et astrophysiques. Pour être complet, mentionnons tout de même quelques autres applications plus technologiques. Les sillages des bateaux et des sous-marins constituent des écoulements influencés par la stratification de l'océan. La dynamique du mélange de fluides dans des grandes cuves industrielles (dans des contextes agroalimentaires, chimiques et pétrochimiques) peut également être turbulente et influencée par la stratification.

1.1.2 Survol de la dynamique des enveloppes fluides terrestres

L'enveloppe fluide terrestre constituée de l'atmosphère, des océans, des mers et des lacs est un système couplé d'une grande complexité dans lequel on observe une très grande diversité de phénomènes (voir par exemple les livres Pedlosky, 1987; Cushman-Roisin, 1994; Vallis, 2006, traitant uniquement des aspects hydrodynamiques). Ses sous-parties aérienne et marines ont des différences fondamentales. Par exemple, les océans sont bornés par des parois latérales alors que l'atmosphère est fortement influencée par des effets liés à la compressibilité, à l'humidité et aux changements de phases, avec les nuages.

L'étude d'un tel système met en jeu différentes approches scientifiques avec bien sûr en premier lieu l'observation, les mesures *in-situ*, base de l'océanographie et de la météorologie. L'interprétation des données et la compréhension du système global progressent grâce à une méthode classique de va-et-vient entre l'analyse et la synthèse. Le système complexe est d'abord décomposé en éléments relativement simples qui sont étudiés séparément (l'analyse). Puis le système est reconstruit de manière plus ou moins globale (la synthèse). Dans ces deux mouvements, la simulation numérique est devenue un outil indispensable qui, à force de progrès tant techniques que dans la compréhension globale, a acquis une capacité prédictive impressionnante. On pense par exemple aux prévisions météorologiques à 10 jours ou encore à la capacité de construire des scénarios sur l'évolution du climat en fonction notamment de l'activité humaine.

Le travail de cette thèse s'inscrit dans l'approche réductionniste d'étude d'un élément fondamental du système, ici la dynamique d'un fluide stratifié en densité. On s'appuie sur une idéalisation extrême en oubliant tout ce qui ne semble pas strictement nécessaire à cet élément (en particulier la rotation de la terre, les hétérogénéités des milieux, les parois, etc.). La section 1.2 présentera en détail notre modèle : le fluide incompressible newtonien stratifié linéairement en densité (avec une fréquence de Brunt-Väisälä N constante). Mais d'abord, donnons quelques éléments clés de la dynamique de l'atmosphère et de l'océan. Bien sûr cette présentation est très partielle et synthétique. On se cantonne à quelques éléments permettant la compréhension de nos motivations, nos méthodes et simplifications.

L'enveloppe fluide terrestre est une machine thermique complexe et hors de l'équilibre. La figure 1.1 montre un exemple de modèle des flux énergétiques

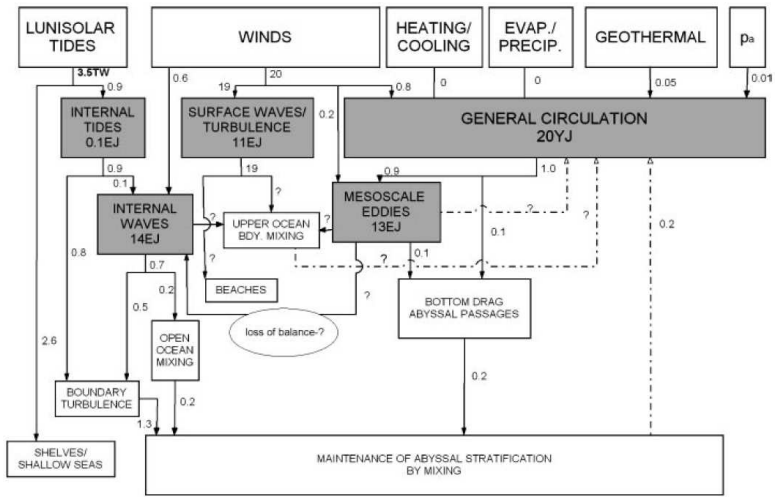

FIGURE 1.1: Bilan énergétique global des différents stocks d'énergie dans l'océan en exajoules (1 EJ = 10^{18} J) et yottajoules (1 YJ = 10^{24} J). Les flèches représentent des flux énergétiques en terrawatts (1 TW = 10^{12} W). Extrait de Wunsch & Ferrari (2004) avec *erratum* "INTERNAL WAVES 1.4 EJ".

associés à la dynamique de l'océan, illustrant bien la complexité de ce milieu. La mise hors équilibre du système par le soleil (dont l'apport énergétique est différent à l'équateur, aux tropiques et aux pôles du fait de la différence d'angle entre les rayons et la surface terrestre entre les différentes latitudes) mène entre autres à une stratification en densité de l'océan et à une circulation globale (voir figure 1.2) avec plongée d'eau dense dans diverses zones de l'océan global (Mer du Labrador, Mer du Groenland au Nord, Mer de Weddell au sud) ou dans des mers régionales comme en Méditerranée (Golfe du Lion, ou Adriatique). Pour boucler la circulation, il est nécessaire que des processus hydrodynamiques mélangent les eaux de densités différentes. Cela représente des quantités d'énergie tout à fait considérables et on ne comprend pas parfaitement les mécanismes à l'œuvre. Par contre, on sait que la turbulence est un processus très efficace en terme de mélange.

Autant dans l'océan que dans l'atmosphère la stratification en densité est la norme. Pour les deux milieux, la variation de la température[2] est cruciale et dans les océans et les mers, les variations de densité sont aussi liées à des différences de salinité. On mesure couramment des fréquences de Brunt-Väisälä N de l'ordre de 1×10^{-2} s^{-1} dans l'atmosphère et 5×10^{-3} s^{-1} dans l'océan (avec des variations importantes selon le lieu, la profondeur et le moment). Dans les milieux naturels, la

[2]Pour être plus précis, il faut considérer une température "potentielle", c'est-à-dire une température compensée des transformations adiabatiques que subit une particule de fluide lorsque sa position verticale est modifiée.

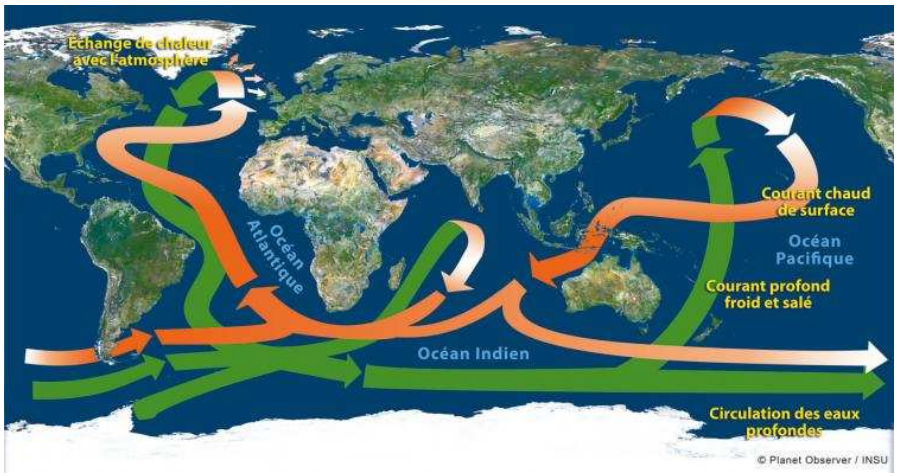

FIGURE 1.2: Schéma de la circulation océanique globale : aux pôles, le refroidissement en hiver et la formation de la glace de mer, qui tend à augmenter la salinité de l'eau libre, entraînent une augmentation de la densité et donc la mise en mouvement vertical des eaux superficielles qui plongent vers le fond. Tiré du site de l'INSU, CNRS.

fréquence de Brunt-Väisälä varie de façon significative selon la verticale et cet effet peut avoir des conséquences importantes. Dans ce travail de thèse, on néglige cet aspect du problème et la pulsation N sera toujours considérée constante.

A quel point les écoulements géophysiques sont-ils influencés par la stratification ? Pour répondre à cette question, quantifions les ordres de grandeur du nombre de Froude $F_h = U/(NL_h)$. On peut prendre pour vitesses et tailles caractéristiques respectivement $U \sim 10$ m/s et $L_h = 1000$ km dans l'atmosphère et $U \sim 1$ m/s et $L_h = 100$ km dans l'océan. Ces estimations mènent à des nombres de Froude de l'ordre de 10^{-3} pour l'atmosphère et de 2×10^{-3} pour l'océan. Ainsi, ces échelles sont fortement influencées par la stratification dans les deux milieux.

Un autre effet structurant la dynamique des fluides géophysiques est la rotation de la terre avec une vitesse angulaire $\Omega_0 \simeq 7.3 \times 10^{-5}$ rad/s. Du fait de la stratification et surtout du fait de la faible épaisseur de l'atmosphère et des océans par rapport au rayon terrestre et aux échelles horizontales, la rotation intervient au final à travers la composante horizontale de la force de Coriolis qui est proportionnelle à une pulsation $f = 2\Omega_0 \sin\lambda$, fonction de la latitude λ. Selon le problème abordé, on peut considérer ou non la variation selon la latitude de f. Dans notre démarche d'idéalisation du problème, nous allons carrément négliger toute rotation d'ensemble. Pourquoi est-ce pertinent dans le contexte géophysique ? Il faut noter que le rapport N/f est généralement grand, de l'ordre de 10 ou 100. Cela signifie que la stratification influence une plus grande gamme d'échelles que la rotation et qu'il existe une gamme d'échelles influencée seulement par la stratification. Ainsi pour étudier la dynamique

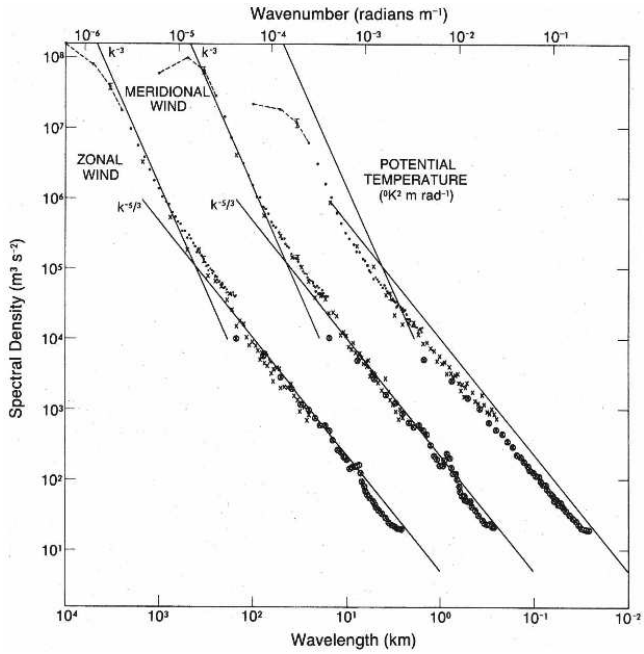

FIGURE 1.3: De la gauche vers la droite, spectres horizontaux de vents zonaux, de vents meridionaux et de température potentielle dans l'atmosphère (tropopause). Les spectres de vents méridionaux et de température ont été décalés de respectivement 1 et 2 décades vers la doite. Tiré de Gage & Nastrom (1986).

de ces échelles, on peut négliger la rotation d'ensemble. Notons enfin qu'à partir de la pulsation f, on construit un nombre sans dimension similaire au nombre de Froude, le nombre de Rossby $Ro = U/(fL_h) = (N/f)F_h$ quantifiant l'influence sur un écoulement de la rotation.

Les ordres de grandeur du nombre de Reynolds dans les écoulements atmosphériques et océaniques sont très importants. Les viscosités cinématiques de l'air et de l'eau sont respectivement $\nu \simeq 10^{-5}$ m^2/s et $\nu \simeq 10^{-6}$ m^2/s. Ces valeurs associées aux valeurs de vitesse et taille caractéristiques mentionnées plus haut donnent des nombres de Reynolds de l'ordre de 10^{12} pour l'atmosphère et 10^{11} pour les océans, c'est-à-dire tout à fait considérables. Cela signifie que les grandes échelles de ces écoulements sont très faiblement influencées par la dissipation et que les phénomènes non-linéaires de transferts entre échelles spatiales, comme par exemple le développement d'instabilité et la turbulence, sont fondamentaux. Précisons que les écoulements géophysiques sont très différents de la turbulence classique, observée par exemple dans le sillage d'une voiture. La turbulence dans les milieux géophysiques est très influencée par les effets structurants que sont la stratification et la rotation plané-

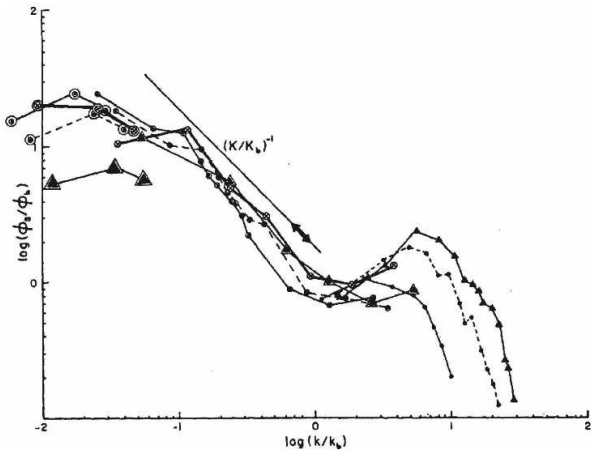

FIGURE 1.4: Spectres verticaux de cisaillement vertical dans l'océan. Les spectres sont normalisés par $\Phi_b = (\varepsilon_K N)^{1/2}$ et le nombre d'onde par $k_b = 1/l_o$, où ε_K est le taux de dissipation d'énergie cinétique et l_o est l'échelle d'Ozmidov (cf. section 1.4). Tiré de Gargett *et al.* (1981).

taire. Les écoulements sont en terme de turbulence très intermittents spatialement et temporellement. Par exemple, des patches de turbulence à petites échelles sont observés dans les océans au sein d'un milieu globalement laminaire à petites échelles (Gregg, 1987). En fait, le terme "turbulent" utilisé pour caractériser l'océan ou l'atmosphère, désigne des caractéristiques globales et statistiques concernant la répartition en énergie entre les différentes échelles de l'écoulement. Nous basons notre discussion sur des résultats concernant la répartition de l'énergie dans l'espace spectral. Puisque l'écoulement est anisotrope, plusieurs types de spectres doivent être utilisés. Par exemple, la figure 1.3 représente des spectres horizontaux (fonction d'un vecteur d'onde horizontal) de vitesse des vents et de température dans l'atmosphère tirés d'un article de Gage & Nastrom (1986). D'un autre côté, la figure 1.4 montre des spectres verticaux (fonction d'un vecteur d'onde vertical) de gradient vertical de vitesse obtenus par Gargett *et al.* (1981) par des lâchés d'appareils de mesures dans l'océan.

Il nous faut mentionner un résultat fondamental pour ce qui nous concerne : il a été observé une importante régularité des spectres océaniques et atmosphériques (Riley & Lindborg, 2008). Des spectres de même type mesurés dans l'océan ou dans l'atmosphère, en différents endroits et moments sont généralement relativement similaires s'ils sont adimensionnés de manière adéquate. Par exemple, un spectre horizontal mesuré dans l'océan dans une certaine gamme d'échelles aura des caractéristiques générales communes avec les spectres de la figure 1.3. Ainsi en décrivant les figures 1.3 et 1.4, on décrit aussi, indirectement, le spectre typique mesuré de manière récurrente dans l'atmosphère et les océans.

Les spectres horizontaux présentés sur la figure 1.3 sont continus avec des pentes constantes correspondant à des lois d'échelle (caractéristiques typiques de la turbu-

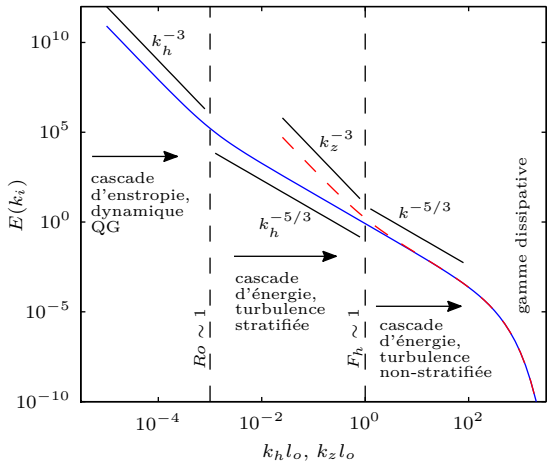

FIGURE 1.5: Schéma simplifié des spectres anisotropes observés dans les fluides géophysiques de l'enveloppe terrestre. Les spectres horizontal (ligne bleu) et vertical (pointillés rouges) sont tracés en fonction des vecteurs d'onde normalisés par $1/l_o$. Les flèches symbolisent les différents types de cascade turbulente.

lence). A très grande échelle (supérieures à $\sim$ 500 km), on a une loi de puissance en k_h^{-3}, c'est-à-dire un spectre très pentu avec beaucoup d'énergie aux grandes échelles par rapport au cas de la turbulence classique. Cette répartition énergétique selon les échelles horizontales s'explique par une dynamique de turbulence quasi-géostrophique, fortement influencée par la stratification et par la rotation terrestre (on reviendra en détail sur ce régime dans la section 1.4). Puis on observe une rupture de pente menant à un spectre en $k_h^{-5/3}$ comme en turbulence classique. En fait, aux échelles relativement grandes supérieures à 100 m, cette pente ne peut pas s'interpréter en terme de turbulence classique : l'écoulement est bien trop influencé par la stratification. Notons que de tels spectres horizontaux sont maintenant reproduits numériquement grâce à des simulations numériques de l'atmosphère basées sur des codes plus ou moins idéalisés (Koshyk & Hamilton, 2001; Skamarock, 2004; Hamilton *et al.*, 2008; Waite & Snyder, 2009; Vallgren *et al.*, 2012). Les spectres verticaux de gradient vertical de vitesse présentés sur la figure 1.4 sont reliés au spectre vertical de vitesse par une division par ${k_z}^2$ et la droite correspond à une loi d'échelle en k_z^{-3}. Nous voyons qu'aux grandes échelles verticales (associées à une pente en $k_h^{-5/3}$ en terme de spectre horizontal), les spectres verticaux sont en $N^2 k_z^{-3}$. Enfin, aux échelles relativement petites, on observe une rupture de pente menant à des spectres en $k_z^{-5/3}$. Ainsi, contrairement au cas de la turbulence classique, les spectres atmosphériques et océaniques sont très fortement anisotropes : le spectre vertical est très différent du spectre horizontal. Le nombre de Froude horizontal associé à l'échelle où la rupture de pente a lieu (appelée échelle d'Ozmidov) est d'ordre 1. Cela explique pourquoi la turbulence redevient relativement isotrope et peu influencée par la stratification.

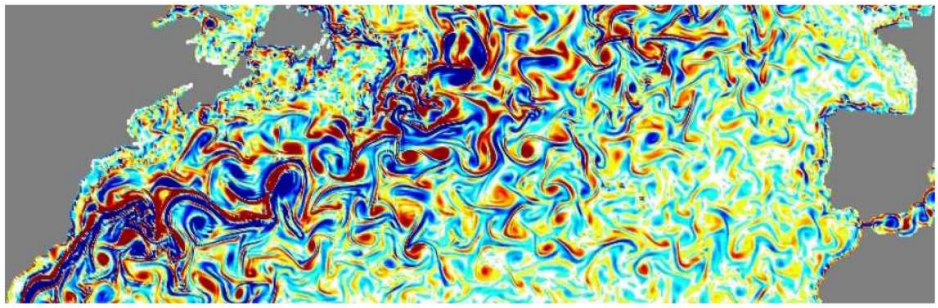

FIGURE 1.6: Champ de vorticité verticale obtenu par simulation numérique (Parallel Ocean Program) de l'Atlantique Nord. Tiré de Lapeyre (2010).

Une représentation schématique des spectres anisotropes observés de façon relativement universelle dans la nature est présentée dans la figure 1.5. Les spectres horizontal et vertical sont superposés pour souligner l'anisotropie à grande échelle et le retour à l'isotropie aux plus petites échelles inférieures à l'échelle d'Ozmidov. Mentionnons enfin un résultat récent obtenu par Lindborg & Cho (2001) par des traitements fins de signaux mesurés lors de vols commerciaux d'avions de ligne (cf. chapitre 2). En reliant des quantités mesurées à la direction de la cascade, les auteurs ont montré que le régime inertiel lié aux spectres en $k_h^{-5/3}$ était associé à une cascade d'énergie vers les petites échelles, comme en turbulence classique non influencée par la stratification.

Structures cohérentes : ondes internes de gravité et tourbillons aplatis. Un fluide stratifié en densité est un milieu supportant la propagation d'ondes internes de gravité. Comme la houle propage de l'énergie à la surface des océans, ces ondes - qui peuvent être linéaires ou fortement non-linéaires - se propagent à l'intérieur de l'océan et de l'atmosphère. Ce mode de mouvement a été largement étudié et de nombreuses observations sont interprétées comme étant la signature d'ondes internes. En particulier, Garrett & Munk (1979) interprètent les spectres anisotropes océaniques par des superpositions d'ondes internes (sans expliquer dynamiquement la répartition en énergie entre ces ondes). D'un autre côté, il existe aussi des structures non-propagatives liées à des écoulements quasi-horizontaux et rotationels. Ces tourbillons intrinsèquement non-linéaires sont aussi largement observés dans la nature, notamment grâce à des bouées dérivantes (Gerin *et al.*, 2009) et aux satellites (P. Y. Le Traon *et al.*, 2008), et se retrouvent dans les simulations numériques d'écoulements géophysiques (cf. figure 1.6)[3]. Une caractéristique fondamentale de ces tourbillons est qu'ils sont fortement anisotropes et très aplatis. Historiquement, les deux types de mouvements ont souvent été considérés séparément, ou en interactions faibles. Dans ce travail de thèse, on s'intéresse en général à la dynamique turbulente des fluides strati-

[3]Notons que dynamique des méso-échelles dans la couche peu profonde des océans (environ les premiers 500m) s'interprète à l'aide du modèle quasi-géostrophique de surface (voir par exemple Lapeyre, 2010; Klein *et al.*, 2008; P. Y. Le Traon *et al.*, 2008)

FIGURE 1.7: Photographie de l'atmosphère. La régularité observée sur les nuages est le signe du dévelopement d'une instabilité de cisaillement de type Kelvin-Helmholtz menant à un évènement de retournement.

fiés à grand nombre de Reynolds sans considérer a priori de séparation stricte entre les modes propagatifs et non-propagatifs. En ce qui concerne la dynamique et la structure tridimensionnelle des moyennes et petites échelles, notons que des tourbillons d'axe horizontal liés à des instabilités de cisaillement (cf. figure 1.7) et des zones localisées de turbulence à très petites échelles sont couramment observés (Gregg, 1987).

Nous avons déjà souligné que la modélisation numérique des systèmes océaniques et atmosphériques (modèles de circulation générale, GCM et modèles régionaux) était un outil très important pour la compréhension et la prédiction dans les sciences des enveloppes fluides des planètes. La nature même des systèmes à simuler qui sont très complexes et à très grands nombres de degrés de liberté implique qu'il est absolument impossible de tout calculer de façon exacte. Chaque simulation numérique est donc basée sur des simplifications et des modélisations des échelles et phénomènes non-résolus. C'est le principe des LES ("Large Eddy Simulation", ou simulation des grands tourbillons) mais avec des écoulements turbulents fortement influencés par des effets structurants, dont en premier lieu la stratification en densité. Pour modéliser au mieux les phénomènes "sous-mailles" (non-résolus), il faut insérer à la main leur dynamique physique. Cette étape de modélisation est critique car les simulations sont fortement sensibles aux modèles sous-mailles (Bryan, 1987; Goosse *et al.*, 1999). Dans le cadre de cette problématique, il est donc fondamental d'avoir une bonne compréhension de la dynamique de la turbulence fortement influencée par une stratification en densité.

Dans les prochaines sections, on introduit les éléments nécessaires à la bonne compréhension de ce travail de thèse. On propose une présentation globale des problématiques liées à la dynamique des fluides stratifiés et tournants à grand nombre de Reynolds. Pour être accessible aux non-spécialistes, cette présentation est conduite à partir de concepts de base de l'hydrodynamique. Notre modèle de travail est présenté dans la prochaine section. On abordera ensuite le sujet de la turbulence classique tridimensionnelle puis bidimensionnelle (section 1.3). Enfin, on proposera un tour d'horizon de la riche dynamique des fluides stratifiés en densité et tournants (section 1.4).

1.2 Modèle : fluide incompressible newtonien stratifié en densité

Pour rentrer dans le vif du sujet de la dynamique des écoulements turbulents dans les fluides stratifiés, nous allons nous appuyer sur les équations fondamentales qui la décrivent. A un certain degré d'approximation, ces équations s'expriment simplement. En revanche, leur résolution pose des problèmes fondamentaux. Nous verrons qu'il faudra soit procéder à des approximations et à des développements en terme de petits paramètres, soit utiliser l'outil numérique pour les simuler. Mais d'abord, présentons notre modèle de travail, les approximations sous-jacentes et les équations associées.

1.2.1 Approximation de Boussinesq

La dynamique d'un fluide newtonien stratifié en densité est, lorsque la vitesse est relativement faible devant la vitesse du son et que les variations de densité sont relativement faibles devant la densité moyenne, régie par les équations de Navier-Stokes dans l'approximation de Boussinesq[4]. Partons des équations classiques des milieux continus : (i) l'équation exprimant la conservation de la masse

$$\frac{d\rho_{tot}}{dt} + \rho_{tot}\boldsymbol{\nabla}\cdot\mathbf{u} = 0, \tag{1.1}$$

où ρ_{tot} est la masse volumique totale du fluide, $\mathbf{u}$ la vitesse et $d/dt = \partial_t + \mathbf{u}\cdot\boldsymbol{\nabla}$ la dérivée particulaire ; (ii) l'équation exprimant la conservation de l'impulsion pour un fluide newtonien, i.e. l'équation de Navier-Stokes

$$\rho_{tot}\frac{d\mathbf{u}}{dt} = -\boldsymbol{\nabla}\tilde{p} - \rho_{tot}g\boldsymbol{e_z} + \rho_{tot}\mathbf{f} + \rho_{tot}\nu\boldsymbol{\nabla}^2\mathbf{u}, \tag{1.2}$$

où $\tilde{p}$ est la pression, $\boldsymbol{e_z}$ le vecteur unitaire vertical orienté vers le haut, $\mathbf{f}$ inclu toutes les forces massiques et ν est la viscosité cinétique (une diffusivité). Nous avons comme variables un champ vectoriel (la vitesse) et deux champs scalaires (la pression et la densité totale). Pour fermer le système il manque donc une équation scalaire. Nous l'introduirons plus tard à partir de la thermodynamique.

L'approximation de Boussinesq est basée sur une décomposition de la densité totale ρ_{tot} en une densité moyenne ρ_0, un profil $\overline{\rho}(z)$ intégrant la stratification de base, et une fonction $\rho'(\mathbf{x})$ correspondant aux perturbations de densité : $\rho_{tot} = \rho_0 + \overline{\rho}(z) + \rho'$. Cette approximation consiste à remplacer partout, sauf dans le terme de flottabilité, la densité totale par la densité de référence ρ_0. Cela peut paraître assez brutal mais cela se justifie si certaines conditions sont remplies (voir par exemple Cushman-Roisin, 1994; Staquet, 1998). En plus de la condition liée à l'incompressibilité (vitesses très inférieures à la célérité du son), une condition supplémentaire de faible variation de

[4]Dans ce travail de thèse, on utilisera toujours cette approximation. Notons qu'elle n'est pas adaptée à la description de la dynamique de l'atmosphère. L'approximation anélastique, qui intègre des effets de compressibilité mais pas les ondes acoustiques, est couramment utilisée et mène à des équations très similaires.

la densité, $\overline{\rho}(z)$ et $\rho' \ll \rho_0$, doit être remplie. L'approximation de Boussinesq est très couramment utilisée notamment pour l'étude des océans où ces conditions sont largement remplies.

Le système d'équation se réduit à l'équation de Navier-Stokes incompressible avec un terme de flottabilité

$$\frac{d\mathbf{u}}{dt} = -\boldsymbol{\nabla}\frac{\tilde{p}}{\rho_0} - \frac{\rho_{tot} g}{\rho_0}\boldsymbol{e_z} + \mathbf{f} + \nu\boldsymbol{\nabla}^2\mathbf{u}, \tag{1.3}$$

et à la condition de divergence nulle $\boldsymbol{\nabla}\cdot\mathbf{u} = 0$. En soustrayant à l'équation (1.3) sa solution d'équilibre au repos $0 = -\partial_z\tilde{p}_{stat}/\rho_0 - g(\rho_0 + \overline{\rho}(z))/\rho_0$, on obtient

$$\frac{d\mathbf{u}}{dt} = -\boldsymbol{\nabla}p - \frac{\rho' g}{\rho_0}\boldsymbol{e_z} + \mathbf{f} + \nu\boldsymbol{\nabla}^2\mathbf{u}, \tag{1.4}$$

où $p \equiv (\tilde{p} - \tilde{p}_{stat})/\rho_0$ est une pression redimensionnée en énergie par unité de masse.

Pour fermer le système, on doit considérer les causes de la variation de masse volumique. Classiquement, les variations de densité sont liées à des variations de température T, de salinité S et dans le cas d'un gaz, de pression. Dans une certaine gamme de variations relativement faibles, une équation d'état linéaire de la forme $\rho_{tot} = \rho_0[1 - \alpha(T - T_0) + \beta(S - S_0)]$ s'applique avec α le coefficient d'expansion thermique et β le coefficient de contraction haline. A ce niveau d'approximation, les dynamiques des variables thermodynamiques T et S sont décrites par une équation d'advection-diffusion (découlant de la conservation de l'énergie pour la température et de la quantité de matière pour la salinité, voir par exemple Rieutord, 1997). Si l'on considère le cas où la stratification est liée à la variation d'une seule variable thermodynamique (par exemple la salinité), on a une simple relation de proportionnalité de type $\rho_{tot} = \rho_0[1+\beta(S-S_0)]$ et l'équation d'advection-diffusion s'applique à la densité totale

$$\frac{d\rho_{tot}}{dt} = \kappa\boldsymbol{\nabla}^2\rho_{tot}, \tag{1.5}$$

où κ est la diffusivité. Dans l'équation (1.4), la quantité flottabilité $b = -\rho' g/\rho_0$ apparaît. On obtient son équation d'évolution en utilisant la décomposition de la densité totale introduite plus haut et l'équation (1.5)

$$\frac{d}{dt}\frac{\rho' g}{\rho_0} + w\frac{g}{\rho_0}\frac{d\overline{\rho}}{dz} = \kappa\boldsymbol{\nabla}^2\frac{\rho' g}{\rho_0}. \tag{1.6}$$

On voit que la quantité $g d_z\overline{\rho}/\rho_0$, proportionnelle au gradient moyen de densité, caractérise le couplage entre le champ de vitesse et les variables thermodynamiques. Ainsi on définit la pulsation caractéristique du milieu stratifié en densité appelée fréquence de Brunt-Väisälä $N = \sqrt{-g d_z\overline{\rho}/\rho_0}$. Notons que la mal-nommée "fréquence"[5] de Brunt-Väisälä est bien une pulsation avec une période associée égale à $2\pi/N$.

Selon le contexte, plusieurs variables thermodynamiques sont utilisées. La fonction perturbations de densité ρ' est adaptée au contexte de l'expérimentation. Dans l'atmosphère, la fonction fluctuations de température potentielle θ, i.e. la température

[5] En anglais, le mot frequency désigne indifféremment une fréquence ou une pulsation.

compensée de l'effet des transformations adiabatiques, est utilisée (voir par exemple Pedlosky, 1987). La flottabilité $b = -g\rho'/\rho_0$ (ou son opposé appelée "densité réduite" et notée σ) qui a un sens physique d'accélération, est couramment considérée. Dans ce manuscrit, on préférera souvent utiliser $\zeta \equiv \rho'/|d_z\overline{\rho}| = g\rho'/(N^2\rho_0)$, le déplacement vertical des particules fluides par rapport à l'état au repos. Le sens physique de longueur verticale permet des comparaisons simples avec toutes les autres longueurs caractéristiques importantes dans le problème. Cette variable ζ est aussi employée dans le code numérique que nous avons utilisé (ns3d, cf. chapitre A). La décomposition de la densité totale en fonction du déplacement vertical ζ s'écrit

$$\rho_{tot} = \rho_0 + \overline{\rho}(z) + |d_z\overline{\rho}|\zeta. \tag{1.7}$$

Finalement, en utilisant pour variable thermodynamique le déplacement vertical ζ, on obtient :

$$\frac{\partial \mathbf{u}}{\partial t} + \mathbf{u}\cdot\boldsymbol{\nabla}\mathbf{u} = -\boldsymbol{\nabla}p - N^2\zeta\boldsymbol{e_z} + \nu\boldsymbol{\nabla}^2\mathbf{u}, \tag{1.8}$$

$$\frac{\partial \zeta}{\partial t} + \mathbf{u}\cdot\boldsymbol{\nabla}\zeta = \qquad +w \qquad + \kappa\boldsymbol{\nabla}^2\zeta. \tag{1.9}$$

Le terme de flottabilité brise l'isotropie des équations. La direction verticale devient une direction privilégiée et on peut anticiper le fait que les structures hydrodynamiques sont anisotropes. Par contre nous pourrons nous appuyer sur l'axisymétrie des équations, i.e. leur invariance par rotation autour de l'axe vertical.

Tous les résultats présentés dans ce manuscrit concernent le cas d'un fluide stratifié sans rotation. Cependant, on va considérer dans ce chapitre introductif l'effet de la rotation en introduisant une rotation d'ensemble du référentiel de travail, de vecteur rotation $\boldsymbol{\Omega} = \Omega\boldsymbol{e_z}$ avec Ω constant (c'est l'approximation dite "plan f"). La rotation fait apparaître des termes supplémentaires dont une partie peut s'intégrer dans le terme de pression. Seule reste la force de Coriolis dont l'expression (en terme d'accélération massique) est $-2\boldsymbol{\Omega}\times\mathbf{u} = -f\boldsymbol{e_z}\times\mathbf{u}$, où $f = 2\Omega$ est la pulsation associée à la rotation.

1.2.2 Formulation dans l'espace spectral

Nous allons couramment utiliser la version du système d'équations (1.8-1.9) dans l'espace spectral. Nous présentons notamment de nombreux résultats tirés de simulations numériques directes effectuées grâce à un code numérique pseudo-spectral basé sur la transformée de Fourier (cf. chapitre A). L'espace de Fourier présente quatre avantages importants : (i) les opérateurs différentiels linéaires s'y expriment très simplement, (ii) la condition de divergence nulle s'interprète de façon géométrique, (iii) elle permet une très bonne précision numérique et (iv) il existe un algorithme très efficace de transformée de Fourier appelé "Fast Fourier Transform", ou FFT, de complexité $n \ln n$, où n est le nombre de points de colocation. Le désavantage majeur de la transformation de Fourier est qu'elle est basée sur une symétrie de translation dans l'espace physique (espace infini ou périodique) incompatible avec des parois de forme non-triviale.

Ainsi, dans la suite, on considérera un espace sans paroi et périodique dans les trois dimensions.

Transformée de Fourier 1D : quelques définitions On doit adopter une convention pour la transformée de Fourier. On choisit la définition correspondant à un espace physique continu et périodique et donc un espace spectral discret et infini. Soit f une fonction réelle d'un espace physique unidimensionel et périodique sur l'intervalle $[0\ \mathcal{L}_x]$, $\hat{f}(k_l) = TF_{1D}[f](k_l)$ la série de Fourier associée, avec $k_l = k_1 l$, $l \in \mathbb{Z}$ et $k_1 = 2\pi/\mathcal{L}_x$. Alors la fonction dans l'espace physique et la série de Fourier sont reliées par les relations

$$\hat{f}(k_l) = \int_0^{\mathcal{L}_x} f(x) e^{-ik_l x} dx/\mathcal{L}_x, \tag{1.10}$$

$$f(x) = \sum_l \hat{f}(k_l) e^{ik_l x}. \tag{1.11}$$

En pratique, numériquement et physiquement avec l'échelle de coupure visqueuse, la résolution spatiale est limitée et l'espace des nombres d'onde est borné. Si l'on a N_x points de co-location dans l'espace physique pour la direction x, l'indice l est limité à l'intervalle $[-N_x/2+1\ \ N_x/2]$ et le nombre d'onde maximal est $k_{max} = k_1 N_x/2$.

L'énergie moyenne associée au champ réel $f(x)$,

$$E_f = \langle f^2/2 \rangle = \frac{1}{2} \int_0^{\mathcal{L}_x} f(x)^2 dx/\mathcal{L}_x, \tag{1.12}$$

où les crochets $\langle \cdot \rangle$ signifient une moyenne, s'exprime dans l'espace spectral en vertu du théorème de Parseval comme une somme : $E_f = \sum_l |\hat{f}(k_l)|^2/2$. On définit le spectre associé au champ f, $E(k_l)$ comme la densité spectrale d'énergie[6], c'est-à-dire que

$$E_f = \sum_{k_l \geqslant 0} E(k_l) k_1. \tag{1.13}$$

Cette somme tend dans la limite $k_1 \to 0$ vers l'intégrale $\int_{k>0} E(k) dk$, ce qui signifie que le spectre discret $E(k_l)$ converge vers le spectre continu $E(k)$. Par identification, on trouve que $E(k_l) = |\hat{f}(k_l)|^2/k_1$.

Rappelons enfin qu'une analyse en échelle peut être faite de manière équivalente dans le domaine physique avec la fonction de corrélation $C_f(r) = \langle f(x) f(x+r) \rangle$. On montre que le spectre de la fonction de correlation

$$\hat{C}_f(k) = \int \frac{dr}{\mathcal{L}_x} \int \frac{dx}{\mathcal{L}_x} f(x) f(x+r) e^{-ikr}, \tag{1.14}$$

est intimement lié à la corrélation et que l'on a $\hat{C}_f(k) = |\hat{f}(k)|^2$. Concrètement l'analyse est souvent faite en terme de fonctions de structure d'ordre deux $S_2(r) = \langle [\delta f(r)]^2 \rangle = 2\langle f^2 \rangle - 2C_f(r)$, où $\delta f(r) = f(x+r) - f(x)$ est l'incrément de la fonction f.

[6] Dans le chapitre A, on définit précisement les différents spectres utilisés (1D, 2D, etc.).

Transformée de Fourier et opérateurs non-linéaires Bien sûr, les écoulements stratifiés évoluent dans un espace à trois dimensions. On utilisera donc majoritairement la transformée de Fourier 3D et le chapeau ($\hat{}$) signifiera la plupart du temps cette transformation. Ainsi, $\hat{\mathbf{u}} = TF_{3D}[\mathbf{u}]$ est la série de Fourier 3D de la vitesse $\mathbf{u}$. On va appliquer maintenant cette transformation au système d'équations (1.8-1.9).

Les opérateurs linéaires s'expriment très simplement dans l'espace de Fourier avec en particulier $\widehat{\partial_m f} = ik_m \hat{f}$. Ainsi la condition d'incompressibilité s'exprime simplement de façon géométrique $\mathbf{k} \cdot \hat{\mathbf{u}} = 0$. Le champ de vitesse est dit solénoïdal, ce qui signifie que dans l'espace de Fourier, il est orthogonal au vecteur d'onde et peut être décrit par seulement deux composantes.

Par contre il n'en va pas de même des termes non-linéaires car l'on a $\widehat{fg} = \hat{f} * \hat{g}$, où $*$ symbolise la convolution, opérateur intégral pour lequel il n'existe pas d'algorithme rapide similaire à la FFT. Numériquement, il est plus avantageux de calculer les termes non-linéaires en revenant dans l'espace physique, c'est-à-dire en utilisant la formule

$$TF[fg] = TF\left[TF^{-1}[\hat{f}]TF^{-1}[\hat{g}]\right]. \tag{1.15}$$

Les codes numériques utilisant cette stratégie de calcul sont dits pseudo-spectraux. L'algorithme FFT est central dans ce type de code et il devra être correctement optimisé pour obtenir de bonnes performances. Pour plus de concision, on définit deux quantités non-linéaires $\mathbf{nl} \equiv \mathbf{u} \cdot \boldsymbol{\nabla}\mathbf{u}$ et $nl_P \equiv \mathbf{u} \cdot \boldsymbol{\nabla}\zeta$. L'équation d'évolution des modes de Fourier de la vitesse s'écrit

$$\partial_t \hat{\mathbf{u}} + \widehat{\mathbf{nl}} = -i\mathbf{k}\hat{p} - N^2\hat{\zeta}\boldsymbol{e_z} - \nu\mathbf{k}^2\hat{\mathbf{u}}. \tag{1.16}$$

Notons que certains termes de cette équation ne sont pas perpendiculaires au vecteur d'onde. Pour respecter la condition d'incompressibilité $\mathbf{k} \cdot \hat{\mathbf{u}} = 0$, la pression s'adapte instantanément et de façon non-locale[7] et l'on a

$$i|\mathbf{k}|^2\hat{p} = -\mathbf{k} \cdot (\widehat{\mathbf{nl}} + N^2\hat{\zeta}\boldsymbol{e_z}). \tag{1.17}$$

Ainsi, si l'on ne s'intéresse pas en soit à la pression, on peut oublier ces termes et ne considérer que les composantes perpendiculaires au vecteur d'onde. On utilise pour cela le tenseur $P_\perp = \boldsymbol{\delta} - \boldsymbol{e_k} \otimes \boldsymbol{e_k}\cdot$, où $\boldsymbol{\delta}$ est la matrice identité et $\boldsymbol{e_k}$ le vecteur unitaire colinéaire à $\mathbf{k}$, de projection sur le plan perpendiculaire au vecteur d'onde. Avec ces notations, le système d'équations (1.8-1.9) devient dans l'espace de Fourier

$$\partial_t \hat{\mathbf{u}} = P_\perp[-\widehat{\mathbf{nl}} - N^2\hat{\zeta}\boldsymbol{e_z}] \qquad -\nu|\mathbf{k}|^2\hat{\mathbf{u}}, \tag{1.18}$$

$$\partial_t \hat{\zeta} = \quad -\widehat{nl_P} + \hat{w} \qquad -\kappa|\mathbf{k}|^2\hat{\zeta}. \tag{1.19}$$

Remarquons que cette formulation ne fait pas intervenir la pression, que l'on ne calcule donc pas explicitement.

[7] Ce résultat étrange est lié à l'approximation d'incompressibilité. En réalité, les ondes de pression se propagent à une vitesse finie, la vitesse du son.

1.3 Turbulence dans les fluides non-stratifiés, 3D et 2D

Dans cette section on présente quelques résultats majeurs concernant la turbulence classique, c'est-à-dire non influencée par un effet structurant comme la stratification. La turbulence est un problème fondamental de l'hydrodynamique et plus généralement de l'étude des systèmes non-linéaires et multi-échelles. C'est un domaine très étudié pour son intérêt pratique (une très grande part des écoulements aux échelles humaines et supérieures ont de fortes tendances à la turbulence) mais aussi pour son intérêt théorique. On va ici brosser un tableau très rapide, en se focalisant sur ce qui va nous intéresser pour la suite du manuscrit. On se cantonne au cas incompressible décrit par l'équation de Navier-Stokes incompressible (équation (1.8) sans le terme de flottabilité). On s'intéresse d'abord au cas classique tridimensionnel.

1.3.1 Turbulence 3D

Cascade de Richardson et invariance du flux d'énergie entre échelles

Au début du chapitre 1, on a déjà introduit le concept de cascade de Richardson. Précisons cette notion dans le cas de la turbulence statistiquement stationnaire tridimensionnelle. Un mécanisme d'injection d'énergie force des structures hydrodynamiques de grande échelle, i.e. associées à un grand nombre de Reynolds et donc faiblement influencées par la dissipation. Le taux d'injection d'énergie est d'ordre $P \sim U^2/T \sim U^3/L$ (unité d'énergie massique par unité de temps), où U, T et L sont respectivement la vitesse, le temps et la taille caractéristiques des plus grandes structures de l'écoulement (échelle dite intégrale). L'énergie ne peut pas être dissipée à l'échelle de forçage et les grandes structures hydrodynamiques évoluent sur un temps long, de l'ordre de quelques temps caractéristiques T. Ainsi, les mécanismes inertiels non-linéaires, c'est-à-dire d'interactions entre échelles, ont le temps de transférer efficacement l'énergie vers des petites échelles. Ce processus se répète sur toute une gamme d'échelles de manière relativement invariante avec un certain flux d'énergie entre échelles $\Pi(l) \sim u(l)^3/l$, où l correspond à une échelle de la cascade et $u(l)$ la vitesse caractéristique associée. Considérons deux échelles proches dans la cascade l_1 et $l_2 < l_1$ telles que l'échelle l_1 transfert son énergie vers l'échelle l_2. Si $\Pi(l_2) < \Pi(l_1)$, l'énergie s'accumule à l'échelle l_2 et $\Pi(l_2) \sim u(l_2)^3/l_2$ augmente (la turbulence n'est pas statistiquement stationnaire). Un équilibre dynamique statistiquement stationnaire est atteint lorsque le flux est égal pour chaque échelle. On a alors $\Pi = P$ sur toute la cascade et $u(l) = (\Pi l)^{1/3}$ (Taylor, 1935).

Au fur et à mesure de la cascade, l'énergie est contenue dans des structures hydrodynamiques liées à des nombres de Reynolds $Re(l) \sim u(l)l/\nu \sim \Pi^{1/3}l^{4/3}/\nu$ de plus en plus petits. A une certaine échelle appelée échelle de Kolmogorov, les gradients sont si importants que l'énergie est dissipée en chaleur avec un certain taux de dissipation d'énergie massique ε. Si l'on postule l'invariance d'échelle et la stationnarité statistique, on obtient une version qualitative d'un résultat tout à fait fondamental, l'égalité entre le taux d'injection, de transfert et de dissipation d'énergie :

$$P = U^3/L = \Pi = u(l)^3/l = \varepsilon. \tag{1.20}$$

Ce résultat, valable pour un nombre de Reynolds suffisamment important, implique que la dissipation est invariante par modification de la viscosité du fluide. C'est seulement la taille des structures dissipatives, c'est-à-dire l'échelle de Kolmogorov, qui est modifiée. On peut évaluer cette échelle η, pour laquelle $Re(\eta) \sim 1$ et on trouve $\eta = (\nu^3/\varepsilon)^{1/4} \sim LRe^{-3/4}$.

Limitation à une description statistique, probabiliste

Nous avons vu qu'un système d'équations de formulation relativement simple décrit parfaitement la dynamique de la turbulence incompressible. Pourtant on vient de voir qu'un des résultats clés est d'ordre statistique. Nous sommes limités à une telle description par des difficultés d'ordre fondamental et pratique. Elles sont liées en particulier à deux ingrédients présents : les non-linéarités et la non-localité induite par le terme de pression. D'abord, il n'existe pas de solution analytique correspondant à un champ de vitesse turbulent. De toute façon, la non-linéarité implique des comportements chaotiques, avec sensibilité aux conditions initiales et divergence des trajectoires dans l'espace des phases. La turbulence est aussi caractérisée par une superposition de structures hydrodynamiques d'échelles très différentes. On est donc dans le cas de chaos à très grand nombre de degrés de liberté[8].

Ainsi la description de l'état d'un écoulement turbulent demande une très grande quantité d'informations ce qui mène à des difficultés concrètes considérables. En première approximation, ce nombre de degrés de liberté peut être quantifié par le nombre de points numériques nécessaires à la simulation d'un écoulements turbulent. Avec un point par volume de Kolmogorov η^3, il faut pour résoudre un volume caractéristique d'échelle intégrale L^3, de l'ordre de $(\eta/L)^3 \sim Re^{9/4}$ points de colocation. Cette loi d'échelle mène très vite pour des écoulements réels à grand nombre de Reynolds à des quantités de points de calcul nécessaires totalement hors de portée même des ordinateurs les plus puissants. Néanmoins les progrès techniques sont remarquables et des simulations à très hautes résolutions ont été réalisées. En 2011, les plus grosses simulations ont des résolutions de l'ordre de 4096^3. Ces calculs représentent de véritables exploits techniques et ouvrent des horizons nouveaux en terme d'analyse et de compréhension de la dynamique des écoulements turbulents. La taille mémoire d'un champ de vitesse donne une petite idée de la difficulté de ce type de calculs (et des traitements des données). Avec la précision nécessaire (8 octets par valeur numérique), un champ vectoriel en trois dimensions représente approximativement $8 \times 3 \times 4096^3 \sim 1650$ Go à manipuler[9].

Pour toutes ces raisons théoriques et pratiques, et alors qu'aucun effet non classique (relativiste et/ou quantique) n'entre en jeu, nous sommes fondamentalement réduits à une description statistique et probabiliste de la turbulence. Ainsi, l'étude de la turbulence est intimement liée à la science du traitement statistique des signaux. Certains outils complexes sont utilisés (par exemple les ondelettes ou les fractales) mais

[8] En opposition au chaos à petits nombres de degrés de liberté qui caractérise certains systèmes très simples mais fortement non-linéaires, par exemple le pendule double.

[9] A comparer à la taille mémoire des plus gros disques durs disponibles au grand public, de l'ordre de 1000 Go.

dans ce travail de thèse, on se limite à quelques concepts classiques. Après la moyenne et l'écart type, une des quantités statistiques la plus simple et facilement accessible dans l'expérience est la fonction de structure d'ordre 2 des incréments de vitesse $S_2(r) = \langle [\delta \mathbf{u}]^2 \rangle$ (reliée simplement aux corrélations de vitesse). On a vu que sous des hypothèses d'invariance par translation (ou de périodicité), la transformation de Fourier était très utile. Il existe alors un parallélisme parfait entre les deux descriptions spatiale et spectrale qui sont liées par la relation $\hat{C}_{\mathbf{u}}(\mathbf{k}) = |\hat{\mathbf{u}}|^2(\mathbf{k})$ (cf. paragraphe d'introduction de la transformée de Fourier plus haut).

Dans ce cadre statistique, les difficultés inhérentes aux non-linéarités apparaissent avec le problème fondamental de fermeture des équations statistiques. Les équations d'évolution des quantités d'ordre 2 (fonctions de structure d'ordre 2, corrélations et spectres, liés à la répartition de l'énergie entre les échelles spatiales) sont fonctions de quantités d'ordre 3, et ainsi de suite sans fin. Pour fermer les équations il n'y a pas d'autres solutions que de faire des approximations consistant à exprimer de façon *ad-hoc* une quantité d'un certain degré en fonction d'une quantité d'ordre inférieur (par exemple avec une approche de type EDQNM[10]).

Comme souvent en physique, les piliers pour l'analyse proviennent des symétries : d'abord avec les quantités conservées, liées à des invariances des équations, par exemple l'énergie associée à l'invariance par translation temporelle des équations ; ensuite avec les symétries du milieu et des conditions limites. En particulier, la turbulence statistiquement homogène et isotrope a une importance fondamentale qui va bien au delà des cas où le forçage est lui même homogène et isotrope. En effet, les processus de cascade entre échelles ont tendance à faire perdre la mémoire de la forme précise du forçage. Lorsque le nombre de Reynolds est suffisamment grand et la cascade est suffisamment profonde ($L/\eta \gg 1$), la turbulence devient localement statistiquement homogène et isotrope, et finalement "universelle" : la structure et la dynamique de la turbulence ne dépendent plus de la forme du forçage à grande échelle (pour une discussion sur ce point, voir par exemple Mininni *et al.*, 2006).

Lois de Kolmogorov pour la turbulence homogène isotrope

Kolmogorov (1941b) a dérivé un ensemble de résultats fondateurs, dont en particulier une loi exacte dans la limite d'un très grand nombre de Reynolds. Comme la relation dimensionnelle (1.20), cette loi exacte, dite "loi des 4/5", exprime l'égalité entre flux d'énergie dans la cascade et dissipation. Elle a pour expression classique

$$\langle [\delta v_L(\mathbf{r})]^3 \rangle = -\frac{4}{5}\varepsilon r, \tag{1.21}$$

où $\delta v_L(\mathbf{r}) = (\mathbf{u}(\mathbf{x}+\mathbf{r}) - \mathbf{u}(\mathbf{x})) \cdot \mathbf{r}/r$ est l'incrément de vitesse longitudinale. Cette loi relie une quantité d'ordre 3 associée aux transferts d'énergie entre échelles à la dissipation. On discute de ce sujet de façon plus approfondie dans l'introduction du chapitre 5. Le flux d'énergie à travers les échelles (dans le domaine spectral) obtenu pour une simulation numérique d'écoulement turbulent forcé est représenté sur la figure 1.8. On

[10] Eddy-Damped Quasi-Normal Markovian, voir Sagaut & Cambon (2008).

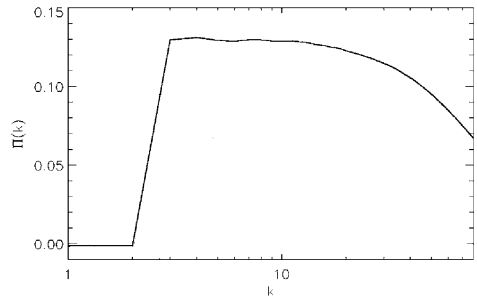

FIGURE 1.8: Flux d'énergie entre les échelles en fonction du module du vecteur d'onde. Tiré de Mininni *et al.* (2006).

voit que cette quantité est pratiquement constante dans le domaine inertiel (domaine dans lequel l'inertie domine et la dissipation est très faible), ce qu'exprime la loi des 4/5 dans l'espace physique.

De la loi exacte des 4/5 (ou de la relation dimensionnelle 1.20), on tire sous l'hypothèse de normalité (distribution de probabilité gaussienne) des prédictions pour la forme des fonctions de structure d'ordre 2 et des spectres

$$\langle [\delta v_L(\mathbf{r})]^2 \rangle = C' \varepsilon^{2/3} r^{2/3}, E(k) = C \varepsilon^{2/3} k^{-5/3}, \tag{1.22}$$

où C' et C sont des constantes universelles dites de Kolmogorov. Ces relations, qualifiées de lois des 2/3 et des 5/3 respectivement, sont vérifiées expérimentalement et numériquement avec un bon accord. Notamment, une variation du spectre en $k^{-5/3}$ est une caractéristique particulièrement robuste de nombreux écoulements turbulents (voir la figure 1.9). Dans l'annexe A, on précisera les définitions de différents types de spectres. On pourra alors donner des valeurs numériques des constantes de Kolmogorov associées.

Remarquons qu'en s'intéressant aux variations des moments supérieurs de la distribution des incréments de vitesse, on a montré que l'hypothèse de normalité n'était pas valide (Oboukhov, 1962; Kolmogorov, 1962). La turbulence est très intermittente avec des probabilités d'événements forts déviant significativement de la loi gaussienne (voir par exemple Chevillard *et al.*, 2006).

Structures cohérentes, mécanismes de la cascade turbulente et vorticité

Même si la caractérisation globale de la turbulence est statistique, on peut apprendre beaucoup en étudiant la dynamique dans l'espace physique des structures cohérentes (tourbillons, nappes de cisaillement, etc.). Dans cette introduction, on ne discute pas des mécanismes possiblement à l'origine de la cascade turbulente en milieu non-stratifié. On pourrait notamment se baser sur une analyse des instabilités agissant sur des structures de base de l'écoulement, par exemple l'instabilité elliptique sur un tourbillon ou l'instabilité de cisaillement (dite de Kelvin-Helmholtz) sur une nappe de

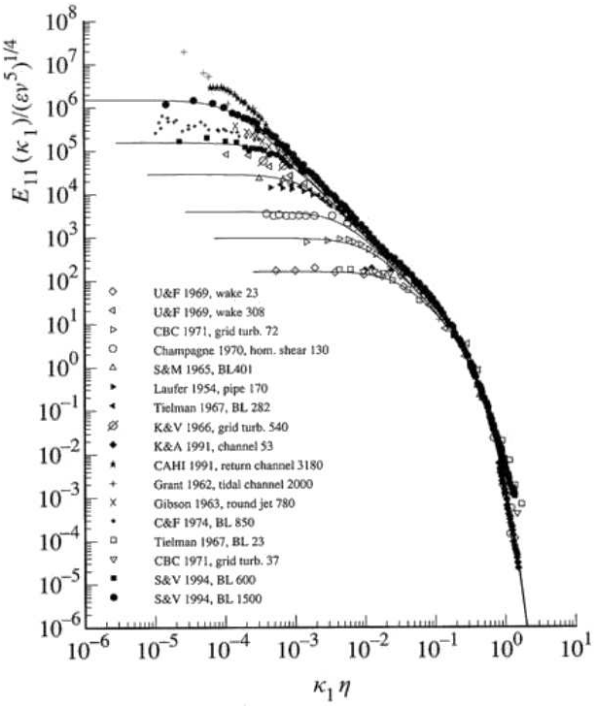

FIGURE 1.9: Spectres de vitesse d'écoulement turbulent. Tiré de Saddoughi & Veeravalli (1994) où les références des différentes expériences sont données.

cisaillement. Ces instabilités mènent à des transferts d'énergie vers des petites échelles et finalement à la transition à la turbulence. La figure 1.10 illustre le cas de l'instabilité cisaillement (dite de Kelvin-Helmholtz dans le cas stratifié).

Ici, on va se limiter à montrer comment la grandeur vorticité $\boldsymbol{\omega} = \boldsymbol{\nabla} \times \mathbf{u}$ qui caractérise la rotation locale d'une particule fluide permet d'interpréter des processus hydrodynamiques à la base de la cascade turbulente. L'équation d'évolution de la vorticité

$$\frac{d\boldsymbol{\omega}}{dt} = \boldsymbol{\omega} \cdot \boldsymbol{\nabla}\mathbf{u} + \nu \boldsymbol{\nabla}^2 \mathbf{u}, \tag{1.23}$$

comporte trois termes : elle est advectée par le champ de vitesse (terme de gauche), étirée et inclinée par les gradients de vitesse (terme $\boldsymbol{\omega} \cdot \boldsymbol{\nabla}\mathbf{u}$) et enfin dissipée par la viscosité. Aux effets visqueux près, sa dynamique est identique à celle d'un vecteur reliant deux points matériels advectés par l'écoulement. Nous allons montrer que le terme d'étirement de la vorticité est fondamental pour la cascade d'énergie vers les petites échelles.

Dans un premier temps, notons qu'une cascade turbulente est liée à une forte concentration de la vorticité aux petites échelles de l'écoulement. On peut quantifier cette concentration en considérant la dissipation moyenne. Localement la dissipation

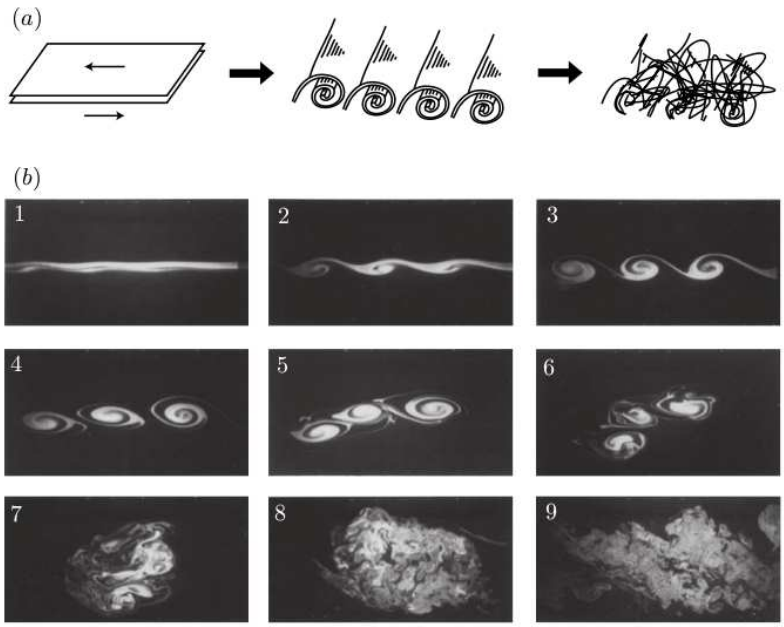

FIGURE 1.10: Destabilisation d'une couche de cisaillement par l'instabilité de Kelvin-Helmholtz. Des tourbillons d'axe horizontal sont formés lors de l'évolution non-linéaire de l'instabilité menant finalement à la transition à la turbulence. Le schéma (a) est tiré de Morize (2006) et l'expérience de Falkovich & Sreenivasan (2006).

$\varepsilon(\mathbf{x}) = 2\nu S_{ij}S_{ij}$ est liée aux déformations, donc aux gradients symétriques de vitesse $S_{ij} = (\partial_i u_j + \partial_j u_i)/2$. Mais dans un fluide incompressible, on peut relier la dissipation moyenne au champ de vorticité $\varepsilon = \langle\varepsilon(\mathbf{x})\rangle = 2\nu Z$, où $Z = \langle|\boldsymbol{\omega}|^2/2\rangle$ est l'enstrophie, la quantité quadratique associée à la vorticité. On en déduit que pour respecter l'invariance de la dissipation par variation de la viscosité, on doit avoir $Z \sim (U/L)^2 Re$. Ainsi, plus le nombre de Reynolds est grand, plus la vorticité se concentre aux petites échelles.

On peut par exemple considérer un processus de transition à la turbulence à partir d'une grande structure hydrodynamique laminaire. Une telle transition à la turbulence implique une série d'instabilités menant *in fine* au développement de structures dissipatives de très petites tailles (voir figure 1.10). Ce processus est associé à une augmentation de l'enstrophie saturant finalement à une valeur de l'ordre de $(U/L)^2 Re$ puisqu'alors l'écoulement est fortement dissipatif et la turbulence décline rapidement.

A partir de l'équation (1.23), on montre que

$$\frac{dZ}{dt} = \langle\boldsymbol{\omega}\cdot(\boldsymbol{\omega}\cdot\boldsymbol{\nabla})\mathbf{u}\rangle - \nu\langle\partial_i\omega_j\partial_i\omega_j\rangle \tag{1.24}$$

ce qui prouve qu'une telle augmentation de l'enstrophie ne peut être due qu'au terme

d'étirement de la vorticité. Ainsi, cet effet physique est fondamental pour la cascade d'énergie vers les petites échelles menant à une forte dissipation.

1.3.2 Turbulence 2D

Lorsqu'elle est plaquée sur une surface bidimensionnelle, la dynamique de la turbulence change radicalement. Puisqu'en 2D le mécanisme d'étirement de la vorticité est géométriquement inopérant, la vorticité et l'enstrophie sont conservées aux effets visqueux près. A partir de la fin des années 1960 (Kraichnan, 1967, 1971), ce type particulier de turbulence a suscité un grand intérêt. En effet, la turbulence 2D n'est pas seulement un cas modèle pour les théoriciens. Des systèmes physiques observables en laboratoire comme par exemple les bulles de savon ou de fines couches de fluide (voir par exemple Cardoso *et al.*, 1994) sont le substrat d'une telle turbulence dans certaines conditions. De plus, dans une certaine gamme de paramètres, la dynamique de la turbulence géophysique est similaire à la celle de la turbulence 2D.

Nous orientons l'axe $\mathcal{O}z$ selon la direction d'invariance. L'évolution de la seule composante de viscosité non nulle, ω_z, est régie par l'équation

$$\frac{d\omega_z}{dt} = \cancelto{0}{\omega_z \partial_z w} + \nu \boldsymbol{\nabla}_h^2 \omega_z, \tag{1.25}$$

où $\boldsymbol{\nabla}_h$ est la projection de l'opérateur vectoriel $\boldsymbol{\nabla}$ selon l'horizontale et w est la vitesse verticale, nulle (ou au moins invariante selon la direction z) en 2D.

Quelles sont les conséquences des conservations de la vorticité et de l'enstrophie ? Elles interdisent la cascade d'énergie vers les petites échelles ! Avant de le montrer, remarquons que la conservation d'une quantité supplémentaire n'implique pas en soit l'interdiction de la cascade d'énergie vers les petites échelles. En turbulence 3D, il existe des quantités conservées par la dynamique non visqueuse (appelées "casimirs"). Par exemple, l'hélicité $\mathbf{u} \cdot \boldsymbol{\omega}$ est conservée au cours du mouvement. Bien sûr cette conservation n'interdit pas la cascade vers les petites échelles. Il y a donc une subtilité qu'il va être utile pour la suite de préciser.

En vertu de la relation de Parseval, les quantités quadratiques s'expriment comme des sommes dans l'espace de Fourier et on a le couple de relations suivant

$$E = \langle |\mathbf{u}_h|^2/2 \rangle = \sum_{\mathbf{k}_h} |\hat{\mathbf{u}}_h|^2/2 = \sum_{\mathbf{k}_h} \hat{E}(\mathbf{k}_h), \tag{1.26}$$

$$Z = \langle |\omega_z|^2/2 \rangle = \sum_{\mathbf{k}_h} |\hat{\omega}_z|^2/2. \tag{1.27}$$

Le point clé est que l'enstrophie est proportionnelle à l'énergie dans l'espace de Fourier : $|\hat{\omega}_z|^2/2 = |\mathbf{k}_h \times \hat{\mathbf{u}}_h|^2/2 = |\mathbf{k}_h|^2 \hat{E}(\mathbf{k}_h)$ et il vient

$$E = \sum_{\mathbf{k}_h} \hat{E}(\mathbf{k}_h), \tag{1.28}$$

$$Z = \sum_{\mathbf{k}_h} |\mathbf{k}_h|^2 \hat{E}(\mathbf{k}_h). \tag{1.29}$$

(a) Spectre de vitesse. (b) Champ de la vorticité.

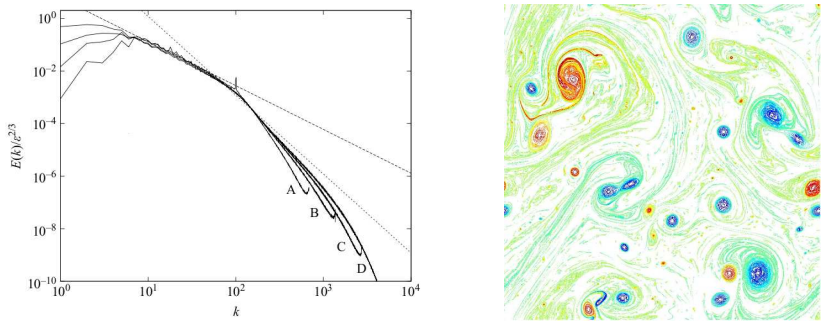

FIGURE 1.11: Deux représentations d'un écoulement bidimensionnel turbulent. (*a*) tiré de Vallgren (2010) et (*b*) tiré de Boffetta (2007). Les deux lignes droites représentent les pentes $k^{-5/3}$ et k^3.

Considérons à nouveau le cas d'une transition à la turbulence à partir d'un écoulement laminaire à grande échelle. L'énergie et l'enstrophie sont réparties dans les modes associés aux petits vecteurs d'onde. Si l'énergie est globalement transférée vers les petites échelles associées à de grands nombres d'onde, on voit que la somme correspondant à l'enstrophie va augmenter, comme en turbulence 3D. Ainsi, les relations (1.28) et (1.29) montrent très clairement qu'une cascade d'énergie vers les petites échelles est interdite par la conservation de l'enstrophie (Fjortoft, 1953). On peut revenir sur l'exemple de l'hélicité en turbulence 3D. On a le même type de relation sauf que $\widehat{\mathbf{u}\cdot\boldsymbol{\omega}} = \hat{\mathbf{u}} * \hat{\boldsymbol{\omega}}$ et qu'il n'y a pas de proportionnalité dans l'espace de Fourier entre l'hélicité et l'énergie, alors que cette proportionnalité est un élément clé du raisonnement présenté ci-dessus.

En turbulence 2D, l'énergie ne peut pas cascader vers les petites échelles. La cascade d'énergie a lieu vers les grandes échelles (cascade dite "inverse"). Le même type de loi d'échelle qu'en turbulence 3D s'applique et les spectres sont aussi en $k_h^{-5/3}$. Mais il existe aussi une cascade d'enstrophie vers les petites échelles. Aux échelles concernées, la répartition d'énergie est fixée par la constance du flux d'enstrophie $\eta \sim {\omega_z}^2/T \sim {\omega_z}^3$ à travers les échelles et le spectre d'énergie associé est en $\eta^{2/3}k_h^{-3}$. La figure 1.11(a) montre un spectre d'énergie obtenu par une simulation numérique directe de turbulence 2D. Les deux gammes inertielles sont bien visibles. Dans l'espace physique, on peut lier la cascade inverse d'énergie au mécanisme d'appariements des tourbillons et la cascade directe d'enstrophie à la filamentation de la vorticité par les grands tourbillons (voir figure 1.11b).

1.4 Eléments sur la dynamique des écoulements en milieu stratifié tournant

Après le détour par la turbulence en milieu non stratifié, nous revenons aux écoulements influencés par une stratification en densité et une rotation d'ensemble.

1.4.1 Quantités conservées : énergie et enstrophie potentielle

Energie massique moyenne $E = E_K + E_P$

La dynamique décrite par le système d'équations (1.8-1.9) conserve aux effets dissipatifs près une énergie moyenne totale, somme d'une énergie cinétique $E_K = \langle |\mathbf{u}|^2/2 \rangle$ et potentielle[11] $E_P = \langle N^2 \zeta^2/2 \rangle$. Les équations d'évolution des deux types d'énergie s'écrivent sous la forme

$$\frac{dE_K}{dt} = P_K \quad - B \quad - \varepsilon_K, \tag{1.30}$$

$$\frac{dE_P}{dt} = P_P \quad + B \quad - \varepsilon_P, \tag{1.31}$$

$$\tag{1.32}$$

où $\varepsilon_K = -\nu \langle \partial_j u_i \partial_j u_i \rangle$ et $\varepsilon_P = -\kappa \langle |\boldsymbol{\nabla} \zeta|^2 \rangle$ sont les termes de dissipation respectivement cinétique[12] et potentielle, P_K et P_P les termes d'injection d'énergie respectivement cinétique et potentielle, et $B = N^2 \langle \zeta w \rangle$ est le terme d'échange entre les deux réservoirs d'énergie. Dans la suite, les quantités sans indice désignent la somme des quantités cinétique et potentielle : on a $E = E_K + E_P$, $P = P_K + P_P$ et $\varepsilon = \varepsilon_K + \varepsilon_P$.

Le mélange est directement lié à la dissipation de l'énergie potentielle. On définit classiquement un coefficient d'efficacité du mélange $\Gamma = \varepsilon_P/\varepsilon_K$ et un nombre de Richardson de flux $Ri_f = B/P$. Dans le cas statistiquement stationnaire ($\varepsilon = P$) et forcé en vitesse ($P_P = 0 \Rightarrow B = \varepsilon_P$), on a $Ri_f = \varepsilon_P/\varepsilon = \Gamma/(\Gamma + 1)$. La capacité d'un écoulement à mélanger peut être quantifiée grâce à une diffusivité effective D, souvent exprimée en terme de nombre de Cox, $Cox = D/\kappa$. La quantification de la diffusion turbulente a un intérêt pratique important en océanographie. Une approximation très classique permet de calculer cette quantité en fonction du gradient vertical de la vitesse horizontale (quantité accessible par les mesures) :

$$D \simeq \frac{\varepsilon_P}{N^2} \simeq \frac{B}{N^2} \simeq \frac{\Gamma \varepsilon_K}{N^2} \simeq \frac{\Gamma}{N^2} \frac{15}{2} \nu \langle (\partial_z u_x)^2 \rangle. \tag{1.33}$$

La relation $D \simeq \varepsilon_P/N^2$ a été proposée par Osborn & Cox (1972) (voir aussi Lindborg & Brethouwer, 2008, et le chapitre 2). Dans cette approche, le coefficient d'efficacité du mélange Γ est pris constant et égal à 0.2. L'égalité $\varepsilon_K \simeq 15/2 \nu \langle (\partial_z u_x)^2 \rangle$ s'obtient en postulant l'isotropie de la dissipation.

[11] Comme N est constant, on peut montrer que E_P correspond au différentiel d'énergie potentielle avec l'état au repos, noté APE (available potential energy).

[12] La dissipation cinétique locale est bien liée aux déformations et donnée par la relation $\varepsilon_K(\mathbf{r}) = -2\nu S_{ij} S_{ij}$. Cela implique plusieurs expressions pour la dissipation moyenne $\varepsilon_K = \langle \varepsilon_K(\mathbf{r}) \rangle$ dont celle donnée dans le texte.

Evolution de la vorticité en milieu stratifié tournant, terme barocline

La stratification et la rotation d'ensemble influent sur la dynamique de la vorticité dont l'équation d'évolution devient en prenant en compte ces deux effets :

$$\frac{d\boldsymbol{\omega}}{dt} = (\boldsymbol{\omega} + 2\boldsymbol{\Omega}) \cdot \boldsymbol{\nabla}\mathbf{u} - \boldsymbol{e_z} \wedge \boldsymbol{\nabla}(N^2\zeta) + \nu\boldsymbol{\nabla}^2\boldsymbol{\omega}, \tag{1.34}$$

On retrouve l'équation (1.23), avec en plus un terme d'étirement-inclinaison de la rotation d'ensemble et un terme dit "barocline" lié à la flottabilité.

Théorème d'Ertel : conservation de la vorticité potentielle (PV)

Dans un fluide stratifié tournant, la conservation de la circulation, ou théorème de Kelvin, ne s'applique pas. Par contre, dans le référentiel non-tournant, la conservation de la circulation sur des contours le long des surfaces isodensités s'applique. Dans le référentiel tournant, on peut associer à cette conservation une quantité scalaire conservée, la vorticité potentielle $q = (\boldsymbol{\omega} + 2\boldsymbol{\Omega}) \cdot \boldsymbol{\nabla}\rho_{tot}$.

Pour comprendre le sens physique associé à cette conservation, on considère les équations non visqueuses. Dans une première étape, on peut examiner la conséquence du théorème de Kelvin en terme de quantités conservées scalaires dans le cas non stratifié et non tournant. On a vu que dans ce cas, la vorticité a une dynamique identique à un vecteur reliant deux points matériels. Ce résultat est le pendant du théorème de Kelvin en terme de vorticité. On peut exprimer cette idée en terme de quantités conservées : on montre que toute quantité sous la forme $\boldsymbol{\omega} \cdot \boldsymbol{\nabla}C$ est conservée si $C(\mathbf{x})$ est un champ scalaire advecté par l'écoulement. On a $dC/dt = 0 \Rightarrow d\boldsymbol{\nabla}C/dt = -\partial_i u_j \partial_j C$ et on trouve bien

$$\frac{d}{dt}(\boldsymbol{\omega} \cdot \boldsymbol{\nabla}C) = \frac{d\boldsymbol{\omega}}{dt} \cdot \boldsymbol{\nabla}C + \boldsymbol{\omega} \cdot \frac{d}{dt}\boldsymbol{\nabla}C = 0. \tag{1.35}$$

Revenons au cas stratifié tournant. L'évolution de la vorticité est donnée en terme de densité totale ρ_{tot} par (cf. les équations (1.7) et (1.34))

$$\frac{d\boldsymbol{\omega}}{dt} = (\boldsymbol{\omega} + 2\boldsymbol{\Omega}) \cdot \boldsymbol{\nabla}\mathbf{u} - \frac{g}{\rho_0}\boldsymbol{e_z} \wedge \boldsymbol{\nabla}\rho_{tot}. \tag{1.36}$$

Cette formulation montre clairement que la composante de la vorticité localement perpendiculaire à l'isodensité n'est pas influencée par le terme barocline. On choisit donc $C = \rho_{tot}$ et on s'intéresse à l'évolution de la fonction scalaire $q = (\boldsymbol{\omega}+2\boldsymbol{\Omega})\cdot\boldsymbol{\nabla}\rho_{tot}$. Puisque la densité totale est conservée, il vient

$$\frac{dq}{dt} = \frac{d}{dt}\left[(\boldsymbol{\omega} + 2\boldsymbol{\Omega}) \cdot \boldsymbol{\nabla}\rho_{tot}\right] = \frac{d\boldsymbol{\omega}}{dt} \cdot \boldsymbol{\nabla}\rho_{tot} + (\boldsymbol{\omega} + 2\boldsymbol{\Omega}) \cdot \frac{d}{dt}\boldsymbol{\nabla}\rho_{tot} = 0. \tag{1.37}$$

Ainsi la vorticité potentielle q est conservée au cours du mouvement aux effets diffusifs près. Finalement, elle s'exprime en fonction de la variable ζ comme

$$q = (2\boldsymbol{\Omega} + \boldsymbol{\omega}) \cdot \boldsymbol{\nabla}\rho_{tot} = -N^2(2\boldsymbol{\Omega} + \boldsymbol{\omega}) \cdot (\boldsymbol{e_z} - \boldsymbol{\nabla}\zeta). \tag{1.38}$$

(a) Milieu stratifié. (b) Milieu stratifié tournant.

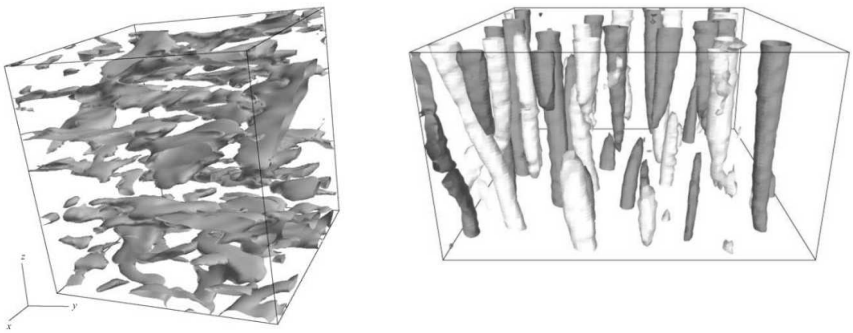

FIGURE 1.12: (*a*) Isosurfaces de gradient vertical de vitesse horizontale dans une simulation de turbulence stratifiée en déclin (Godeferd & Staquet, 2003). (*b*) Isosurfaces de vorticité verticale dans une expérience de turbulence de grille dans un fluide stratifié en rotation (Praud *et al.*, 2006).

1.4.2 Quelle échelle verticale ? Compétition rotation-stratification

Observations qualitatives

On a vu que la stratification et la rotation brisent l'isotropie et que la direction verticale est une direction particulière de l'écoulement. Les observations dans la nature, les mesures en laboratoire et les résultats numériques, montrent que l'anisotropie des structures est un élément fondamental. Les vitesses et tailles caractéristiques verticales et horizontales sont très différentes. En milieu stratifié, les structures hydrodynamiques sont en général très aplaties (structures en forme de pancake, cf. Riley & Lelong, 2000, et figure 1.12*a*) alors qu'en milieu tournant elles ont tendance à être très allongées (structures en colonnes, voir figure 1.12*b*). Voyons comment on explique ces observations. Puisque l'anisotropie des structures est un effet fondamental, on va maintenant différencier clairement les échelles verticale et horizontale. Il faut donc aussi considérer séparément les nombres de Froude horizontal $F_h = U/(NL_h)$ et vertical $F_v = U/(NL_v)$ qui vont avoir des significations physiques très différentes.

Loi d'échelle non-visqueuse dans le cas purement stratifié

On va voir que dans le cas stratifié, une échelle verticale particulière émerge naturellement. Considérons le cas d'une particule fluide ayant une vitesse U et associée à un déplacement nul des isodensités, $\zeta = 0$. Si par une transformation particulière toute son énergie cinétique $E_K = U^2/2$ est transférée en énergie potentielle $E_P = N^2\zeta^2/2$, le déplacement des isodensités va être $\zeta = U/N$. L'échelle correspondante, $L_b = U/N$ est appelée échelle de flottabilité. Ainsi, le rapport du déplacement des isodensités ζ sur la grande échelle horizontale L_h est de l'ordre du nombre de Froude horizontal $\zeta/L_h \sim F_h$. Mais qu'en est-il de la taille caractéristique verticale des couches ? Pour

répondre à cette question, on va devoir étudier quels sont les termes dominants des équations non visqueuses lorsque la stratification domine.

On s'inspire ici de raisonnements développés par Billant & Chomaz (2001). Soit un écoulement caractérisé par une certaine vitesse horizontale U et une certaine taille horizontale L_h. On laisse libre la taille caractéristique verticale L_v et on note le rapport d'aspect $\alpha = L_v/L_h$. Le terme dominant de la dérivée convective $d/dt \sim \mathbf{u}_h \cdot \boldsymbol{\nabla}_h$ est d'ordre U/L_h. En séparant la vitesse en vitesse horizontale $\mathbf{u}_h$ et verticale w, on a

$$\frac{d\mathbf{u}_h}{dt} = -\boldsymbol{\nabla}_h p \Rightarrow p \sim U^2, \tag{1.39}$$

$$\frac{dw}{dt} = -\partial_z p - N^2\zeta \Rightarrow ?\,, \tag{1.40}$$

$$\frac{d\zeta}{dt} = w \Rightarrow \frac{\zeta}{L_h} \sim \frac{w}{U}. \tag{1.41}$$

On voit que la première équation fixe l'ordre de grandeur de la pression alors que la troisième relie les ordres de grandeurs de w et ζ. La conclusion à tirer de la seconde équation est moins directe car il y a trois termes. A partir de la relation entre w et ζ, on montre que le ratio du terme d'advection de la vitesse verticale sur le terme de flottabilité est d'ordre ${F_h}^2$:

$$\frac{dw/dt}{N^2\zeta} \sim \frac{Uw}{L_h N^2 \zeta} \sim {F_h}^2. \tag{1.42}$$

L'équilibre à l'ordre dominant en nombre de Froude horizontal est donc un équilibre entre le gradient vertical de pression et la force verticale due aux fluctuations de densité. C'est l'équilibre hydrostatique. On a une illustration directe de cet équilibre lorsqu'on voit la surface séparant de l'eau en mouvement et de l'air (une discontinuité de densité) se déformer au cœur d'un tourbillon. Cet endroit est associé dans l'eau à une dépression liée au mouvement du fluide. Cette dépression aspire du fluide et déforme la surface isodensité de manière à avoir un équilibre hydrostatique et une pression continue à la surface (aux effets de tension de surface près). Avec l'équilibre hydrostatique, on peut préciser la loi d'échelle pour les variables ζ et w

$$\frac{\zeta}{L_h}(\sim \frac{w}{U}) \sim \frac{\partial_z p}{L_h N^2} \sim \frac{U^2}{{L_h}^2 N^2}\frac{L_h}{L_v} \sim \frac{{F_h}^2}{\alpha}. \tag{1.43}$$

On peut maintenant réécrire le système en fonction des variables adimensionnées. Insistons sur le fait que dans ce manuscrit, sauf précision, on gardera la même notation pour les variables dimensionnées et adimensionnées. Il n'y aura pas de confusion possible puisque dans les équations adimensionnées interviennent des nombres sans dimension. Par exemple, la dérivée convective s'exprime avec les variables dimensionnées comme $d/dt = \partial_t + \mathbf{u}_h \cdot \boldsymbol{\nabla}_h + w\partial_z$ et devient après adimensionnement

$$\frac{d}{dt} = \partial_t + \mathbf{u}_h \cdot \boldsymbol{\nabla}_h + \left(\frac{F_h}{\alpha}\right)^2 w\partial_z. \tag{1.44}$$

Avec les variables adimensionnées, le système d'équation s'écrit simplement

$$\frac{d\mathbf{u}_h}{dt} = -\boldsymbol{\nabla}_h p, \tag{1.45}$$

$${F_h}^2 \frac{dw}{dt} = -\partial_z p - \zeta, \tag{1.46}$$

$$\frac{d\zeta}{dt} = w. \tag{1.47}$$

A cette étape, deux choix sont possibles. Soit on est certain que $F_h/\alpha \ll 1$ et que $w\partial_z < 1$ tout le temps et on peut négliger les termes d'advection verticale. Soit le rapport d'aspect est laissé libre et la dynamique du système tend vers l'équilibre dominant, l'état du système tel que les plus grands termes non-fixés (ici les termes d'ordre F_h/α) s'équilibrent avec les autres termes. On a alors $\alpha \sim F_h$ ce qui signifie que la taille verticale des couches est de l'ordre de l'échelle de flottabilité, $L_v \sim L_b$ et que l'énergie potentielle est du même ordre de grandeur que l'énergie cinétique, $E_P \sim E_K$.

Nous venons d'expliquer de manière qualitative et avec un raisonnement de type "équilibre dominant"[13] pourquoi les structures hydrodynamiques sont aplaties dans les milieux stratifiés. Cela peut se justifier de manière rigoureuse en montrant que le système d'équation (1.45-1.47) devient dans l'approximation hydrostatique indépendant de F_h/α si l'on fait le changement de variable $z' = zF_h/\alpha$, $w' = w\alpha/F_h$ et $\zeta' = \zeta\alpha/F_h$. Bien sûr un tel raisonnement ne précise pas par quels mécanismes le système tend vers l'équilibre dominant, dans notre cas vers un écoulement structuré en couches minces de taille verticale caractéristique de l'ordre de l'échelle de flottabilité. Il ne précise pas non plus totalement quelles sont les conséquences dynamiques d'une telle structuration notamment en terme d'instabilités secondaires.

Cas purement tournant

Dans le cas purement tournant, rappelons qu'à l'ordre 0 en nombre de Rossby, l'écoulement est caractérisé par un équilibre selon l'horizontale appelé équilibre géostrophique. Le gradient de pression horizontal équilibre la force de Coriolis :

$$f\boldsymbol{e_z} \wedge \mathbf{u}_h = -\boldsymbol{\nabla}_h p. \tag{1.48}$$

Si cet équilibre est réalisé exactement, on montre que l'écoulement est invariant selon la verticale (c'est le théorème de Taylor-Proudman), ce qui explique l'existence de structures en colonnes.

Cas stratifié tournant

Pour un écoulement influencé à la fois par la stratification et par la rotation d'ensemble, on peut anticiper l'existence d'un équilibre entre les deux tendances contradictoires des écoulements en milieux purement stratifiés et purement tournants. La sous-section

[13] En anglais "dominant balance".

suivante présente la dynamique de ce cas mixte, le régime quasi-géostrophique. Par ailleurs, rappelons que si $N/f = Ro/F_h \gg 1$, une certaine gamme d'échelles est fortement influencée par la stratification et faiblement par la rotation comme dans l'atmosphère et les océans.

1.4.3 Turbulence quasi-géostrophique

Le régime quasi-géostrophique (QG) concerne les grandes échelles (dites synoptiques) des océans et de l'atmosphère. Charney (1971) a montré qu'un écoulement dans un milieu rapidement tournant et fortement stratifié a une dynamique très particulière similaire à une dynamique bidimensionnelle. Les explications données dans les livres sont souvent soit très rapides, soit assez lourdes car différentes subtilités (concrètement très importantes) des milieux naturels sont prises en compte. Dans ce manuscrit, on s'intéresse au cas quasi-géostrophique pour la comparaison avec le cas purement stratifié. Ainsi, on va faire un détour sur ce régime, mais en se limitant au strict nécessaire, c'est-à-dire le cas d'un fluide parfait incompressible dans l'approximation de Boussinesq avec une stratification constante et une rotation d'ensemble selon la verticale. Dans ce cas, les équations d'évolution des champs sont

$$\frac{d\mathbf{u}_h}{dt} + f\boldsymbol{e_z} \wedge \mathbf{u}_h = -\boldsymbol{\nabla}_h p, \tag{1.49}$$

$$\frac{dw}{dt} = -\partial_z p - N^2\zeta, \tag{1.50}$$

$$\frac{d\zeta}{dt} = w, \tag{1.51}$$

$$\boldsymbol{\nabla}_h \cdot \mathbf{u}_h + \partial_z w = 0, \tag{1.52}$$

où $d/dt = \partial_t + \mathbf{u}_h \cdot \boldsymbol{\nabla} + w\partial_z$ est la dérivée convective.

Quels sont les termes dominants de ces équations lorsque la rotation et la stratification sont fortes ? Ils sont liés aux deux équilibres de forces vus précédemment : l'équilibre géostrophique selon l'horizontale et l'équilibre hydrostatique selon la verticale. On a donc les ordres de grandeur suivant $p \sim fL_hU$ et $p \sim L_vN^2\zeta$ qui donnent

$$\frac{\zeta}{L_h} \sim \frac{w}{U} \sim \frac{{F_h}^2}{Ro\alpha}. \tag{1.53}$$

En fonction des variables adimensionnées, la dérivée convective est donnée par

$$\frac{d}{dt} = \partial_t + \mathbf{u}_h \cdot \boldsymbol{\nabla} + \frac{{F_h}^2}{Ro\alpha^2} w\partial_z = \partial_t + \mathbf{u}_h \cdot \boldsymbol{\nabla} + \epsilon w\partial_z, \tag{1.54}$$

où l'on a introduit le nombre sans dimension $\epsilon \equiv {F_h}^2/(Ro\alpha^2)$ qu'on va supposer a

priori petit. Le système d'équation s'écrit en fonction des variables adimensionnées

$$Ro\frac{d\mathbf{u}_h}{dt} + \boldsymbol{e_z} \wedge \mathbf{u}_h = -\boldsymbol{\nabla}_h p, \tag{1.55}$$

$${F_h}^2 \frac{dw}{dt} = -\partial_z p - \zeta, \tag{1.56}$$

$$\frac{d\zeta}{dt} = w, \tag{1.57}$$

$$\boldsymbol{\nabla}_h \cdot \mathbf{u}_h + \epsilon \partial_z w = 0. \tag{1.58}$$

A l'ordre 0 de tous les petits paramètres : F_h, Ro et ϵ, on trouve

$$\boldsymbol{e_z} \wedge \mathbf{u}_h^{(0)} = -\boldsymbol{\nabla}_h p^{(0)}, \tag{1.59}$$

$$\zeta^{(0)} = -\partial_z p^{(0)}, \tag{1.60}$$

$$d_{ht}^{(0)} \zeta^{(0)} = w^{(0)}, \tag{1.61}$$

$$\boldsymbol{\nabla}_h \cdot \mathbf{u}_h^{(0)} = 0, \tag{1.62}$$

où $d_{ht}^{(0)} = \partial_t + \mathbf{u}_h^{(0)} \cdot \boldsymbol{\nabla}_h$ est la dérivée convective par la vitesse $\mathbf{u}_h^{(0)}$. On voit qu'à cet ordre du développement, la vitesse horizontale est non-divergente. On utilise donc un formalisme typiquement 2D pour paramétrer ce champ de vitesse par une fonction de courant $\psi^{(0)}$ telle que $\mathbf{u}_h^{(0)} = -\boldsymbol{\nabla}_h \times \psi^{(0)} \boldsymbol{e_z}$. En introduisant cette relation dans l'équation (1.59), on trouve que $\psi = p$ et donc $\zeta^{(0)} = -\partial_z \psi^{(0)}$. De plus, la vorticité verticale est donnée par $\omega_z^{(0)} = \boldsymbol{\nabla}_h^2 \psi^{(0)}$. La connaissance de la fonction de courant permet le calcul de toutes les variables, à l'exception de la vitesse verticale $w^{(0)}$. Ainsi, le système d'équation à l'ordre 0 n'est pas fermé puisque l'équation d'évolution pour la fonction de courant est

$$d_{ht}^{(0)} \partial_z \psi^{(0)} = -w^{(0)}, \tag{1.63}$$

et que $w^{(0)}$ reste indéterminée. Il faut trouver une équation supplémentaire. On doit aller au delà de l'équilibre géostrophique et c'est pour cela que le régime est dit quasi-géostrophique.

On pourrait poursuivre le développement au premier ordre des petits paramètres. C'est en fait plus simple de s'appuyer sur l'équation d'évolution de la vorticité verticale

$$\frac{d\omega_z}{dt} = (f\boldsymbol{e_z} + \boldsymbol{\omega}) \cdot \boldsymbol{\nabla} w, \tag{1.64}$$

dont la version adimensionnée est

$$\epsilon^{-1}[d_{ht}^{(0)} + \epsilon w \partial_z]\omega_z = Ro^{-1} \partial_z w + \boldsymbol{\omega} \cdot \boldsymbol{\nabla} w. \tag{1.65}$$

Les deux termes dominants de cette équation sont la dérivée advective par la vitesse $\mathbf{u}_h^{(0)}$ d'ordre ϵ^{-1} et l'étirement de la rotation d'ensemble par les gradients verticaux de vitesse verticale, d'ordre Ro^{-1}. Cet équilibre dominant fixe le paramètre libre du

système de telle sorte que ces deux termes s'équilibrent. On a donc $\epsilon = Ro \Rightarrow \alpha = F_h/Ro = f/N$. Cette loi d'échelle est compatible avec l'équilibre anticipé entre la stratification et la rotation pour fixer l'échelle verticale caractéristique. Il est intéressant de noter que, comme dans le cas purement stratifié, la loi d'échelle pour l'échelle verticale découle simplement d'un équilibre dominant. Enfin, on conclut à partir de l'équation (1.65) que

$$d_{ht}^{(0)} \left[\partial_z \zeta^{(0)} - \omega_z^{(0)} \right] = -d_{ht}^{(0)} \boldsymbol{\nabla}^2 \psi^{(0)} = 0, \tag{1.66}$$

où $\boldsymbol{\nabla}^2$ est le laplacien 3D. Cette équation détermine complètement l'évolution du système. C'est en fait la version à l'ordre dominant en Ro et F_h de la conservation de la vorticité potentielle $q = (f\boldsymbol{e_z} + \boldsymbol{\omega}) \cdot (g/\rho_0 \boldsymbol{\nabla} \rho_{tot}) = -N^2 (f\boldsymbol{e_z} + \boldsymbol{\omega}) \cdot (\boldsymbol{e_z} - \boldsymbol{\nabla}\zeta)$ donnée en version adimensionnée par

$$q = -1 - Ro\omega_z + \epsilon \partial_z \zeta + \frac{F_h^2}{\alpha} \boldsymbol{\omega} \cdot \boldsymbol{\nabla} \zeta. \tag{1.67}$$

Avec la loi d'échelle quasi-géostrophique, on a bien $q \simeq -1 + Ro(\partial_z \zeta - \omega_z) = -1 - Ro(\partial_{zz} + \boldsymbol{\nabla}_h^2)\psi^{(0)}$.

Les équations obtenues ont une forme très similaire à celles de la turbulence 2D mais la structure de l'écoulement est bien tridimensionnelle. Charney (1971) prédit une certaine isotropie de l'écoulement après mise à l'échelle de la coordonnée verticale par un facteur N/f. On a vu qu'un élément fondamental pour la turbulence 2D est la relation de proportionnalité dans le domaine spectral entre l'enstrophie et l'énergie. Avec les lois d'échelle stratifiées tournantes, l'énergie s'écrit en version adimensionnée $E = E_K + (\epsilon/Ro)E_P$. Avec la loi d'échelle quasi-géostrophique $\epsilon \sim Ro$, les deux formes d'énergie sont du même ordre et on trouve à l'ordre 0 $E^{(0)} = E_K^{(0)} + E_P^{(0)} = |\boldsymbol{\nabla}\psi^{(0)}|^2/2$. L'enstrophie potentielle est bien proportionnelle à l'énergie totale dans le domaine spectral et la dynamique quasi-géostrophique est de type 2D.

1.4.4 Ondes internes de gravité

Un fluide stratifié de façon stable et non-tournant est un milieu qui supporte des ondes internes de gravité. Ces ondes permettent la propagation d'énergie sur de longues distances par un mécanisme linéaire. Elles sont largement observées dans les océans et l'atmosphère et ont des effets très importants (voir par exemple Fritts & Alexander, 2003). Elles ont une dynamique remarquablement différente d'autres types d'ondes plus connues, avec une forme particulière et inhabituelle de la relation de dispersion (Gostiaux & Dauxois, 2004)

$$\left(\frac{\omega}{N}\right)^2 = \sin^2 \Phi = \frac{{k_h}^2}{{k_h}^2 + {k_z}^2}. \tag{1.68}$$

La pulsation ne dépend que de l'angle Φ entre le vecteur d'onde et la verticale (cf. figure 1.13) et pas du module du vecteur d'onde. Ces différents éléments font que les ondes internes ont inspiré et inspirent de très nombreuses études.

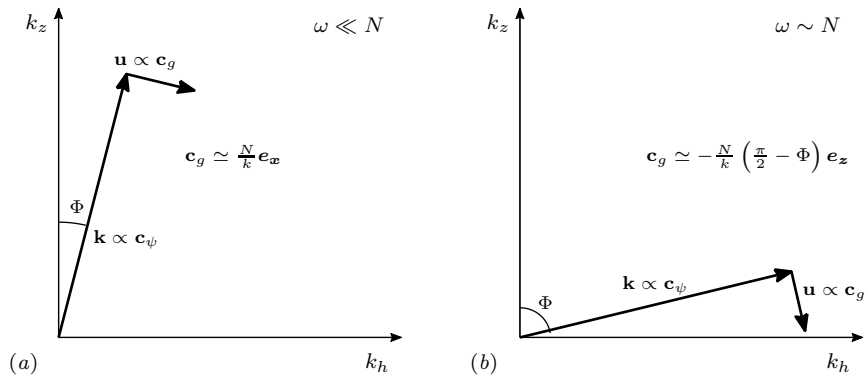

FIGURE 1.13: Caractéristiques de deux ondes linéaires planes de pulsations différentes.

Conséquences de la relation de dispersion anisotrope. D'abord, on montre que la vitesse de phase $\mathbf{c}_\psi = (\omega/k)\boldsymbol{e_k}$ est perpendiculaire à la vitesse de groupe $\mathbf{c}_g = \boldsymbol{\nabla}_\mathbf{k}\omega = (N/k)\cos\Phi(\cos\Phi \boldsymbol{e_h} - \sin\Phi \boldsymbol{e_z})$, c'est-à-dire que l'on a $\mathbf{c}_\psi \propto \mathbf{k} \perp \mathbf{c}_g \propto \mathbf{u}$.

Ensuite, notons qu'il existe un continuum d'ondes dans l'intervalle de pulsation $[0\ N]$ avec des dynamiques différentes entre les deux extrêmes. D'une part (figure 1.13a), les ondes de très faible pulsation $\omega \ll N$ qui ont un rapport d'aspect très petit (échelles verticales très petites par rapport aux échelles horizontales) se propagent rapidement et quasiment horizontalement $\mathbf{c}_g \simeq (N/k)\boldsymbol{e_x}$. D'autre part (figure 1.13b), les ondes de pulsation d'ordre N qui ont un rapport d'aspect très grand (échelles verticales très grandes par rapport aux échelles horizontales) se propagent lentement et quasiment verticalement $\mathbf{c}_g \simeq -(N/k)(\pi/2 - \Phi)\boldsymbol{e_z}$. Notons que les ondes internes dans l'atmosphère et l'océan sont dominées par les ondes du premier type de rapport d'aspect très petit (Garrett & Munk, 1979; Dewan, 1997; Lindborg & Brethouwer, 2007).

Enfin, du fait de la relation de dispersion particulière, les ondes de gravité ont un comportement singulier par rapport à des ondes plus classiques (par exemple sonores, de surface ou électromagnétiques) en terme de réflexion, diffusion, dispersion, etc.

Nombres sans dimension et ondes internes. On a présenté une analyse dimensionnelle basée sur une distinction entre les nombres de Froude horizontal et vertical. Dans le cas des ondes, cette différentiation n'est pas adoptée. Pour faire le lien avec les approches que nous employons dans ce travail de thèse, nous mentionnons l'analyse dimensionnelle des équations non-linéaires autour d'une onde linéaire caractérisée par une certaine pulsation ω et une certaine vitesse caractéristique U. Associés à ces deux caractéristiques, on peut introduire deux nombres sans dimension : un nombre de Froude de pulsation $F_\omega = \omega/N = \sin\Phi$ mesurant les effets linéaires et un paramètre de pente ("steepness" en anglais) quantifiant les non-linéarités $S = U_h k_h/\omega = U_h/c_{\psi h} = U_z k_z/\omega = U_z/c_{\psi z}$, où $c_{\psi h}$ et $c_{\psi v}$ sont respectivement les composantes horizontale et verticale de la vitesse de phase. Exprimé en terme de variables adimensionnées avec les lois d'échelle fixées par les termes linéaires, le système

d'équations non-linéaire s'écrit

$$\frac{d\mathbf{u}_h}{dt} = -\boldsymbol{\nabla}_h p \tag{1.69}$$

$$F_\omega{}^2 \frac{dw}{dt} = -(1 - F_\omega{}^2)\partial_z p - \zeta \tag{1.70}$$

$$\frac{d\zeta}{dt} = w \tag{1.71}$$

où la dérivée convective a pour expression $d/dt = \partial_t + S\mathbf{u}\cdot\boldsymbol{\nabla}$. Les termes de transport horizontal et vertical sont du même ordre quelque soit F_ω.

Remarquons enfin que dans les études sur les ondes, plusieurs nombres sans dimension sont couramment employés. Le nombre de Richardson

$$Ri \equiv \frac{-\frac{g}{\rho_0}\frac{\partial \rho_{tot}}{\partial z}}{|\partial_z \mathbf{u}_h|^2} = \frac{N^2(1-\partial_z\zeta)}{|\partial_z \mathbf{u}_h|^2}. \tag{1.72}$$

compare localement le cisaillement vertical de la vitesse horizontale à la stratification. Dans le cas d'un écoulement parallèle, non-visqueux et stationnaire, Miles (1961) et Howard (1961) ont montré que la condition $Ri < 1/4$ à un endroit de l'écoulement est une condition nécessaire mais pas suffisante pour le développement de l'instabilité de cisaillement (instabilité dite de Kelvin-Helmholtz consistant en l'enroulement de la nappe de cisaillement). Les nombres de "Froude" (en fait nombre de Froude vertical) $Fr = U/(NH)$ ou de Long $Lo = 1/Fr$, où H est une taille caractéristique verticale du problème, sont plus utilisés pour les problèmes dans lesquels une onde interagit avec la topographie. Ces différents nombres peuvent être reliés par les relations $Fr \sim Ri^{-1/2} \sim Sk_z/k$ et on obtient dans la limite de faible F_ω où $k \simeq k_z$, $Fr \simeq S$.

Décomposition poloïdale-toroïdale et interactions ondes-tourbillons. De manière générale, le champ de vitesse d'un écoulement incompressible peut être décomposé de manière unique (à un écoulement horizontalement invariant près) en deux parties distinctes définies par des caractéristiques cinématiques : une partie poloïdale liée à la divergence de la vitesse horizontale et à la vitesse verticale et une partie toroïdale liée à la vorticité verticale (Craya, 1958; Herring, 1974; Riley & Lelong, 2000; Cambon, 2001; Lindborg & Brethouwer, 2007). Cette décomposition dite aussi de Craya-Herring est toujours possible. Par contre, une interprétation dynamique liant la vitesse poloïdale aux ondes internes et la vitesse toroidale aux tourbillons est valable seulement si $F_v \ll 1$. Cette limite n'est pas valable en général, même pour des écoulements très fortement stratifiés.

Précisons le sens cinétique de la décomposition poloïdale-toroïdale, d'abord, dans l'espace réel. Un champ de vecteur peut toujours être décomposé en un champ non-divergent et un champ irrotationnel. On applique cette décomposition, dite de Helmholtz, à la vitesse horizontale :

$$\mathbf{u}_h = -\boldsymbol{\nabla}_h \times \psi_h \boldsymbol{e_z} + \boldsymbol{\nabla}_h \Phi_h. \tag{1.73}$$

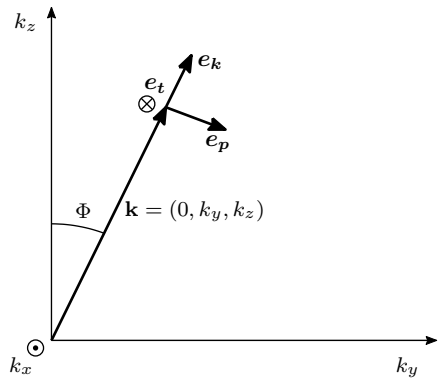

FIGURE 1.14: Représentation graphique dans l'espace spectral de la décomposition poloïdale-toroïdale de la vitesse. On a choisi pour plus de clarté un vecteur d'onde dans le plan Oyz.

ψ_h et Φ_h sont respectivement la fonction de courant et la fonction potentielle de la vitesse horizontale. La vitesse toroïdale $\mathbf{u}_t$ est la vitesse associée à la vorticité verticale ω_z. Elle est horizontale et égale à $\mathbf{u}_t = -\boldsymbol{\nabla}_h \times \psi_h \boldsymbol{e_z}$. De façon complémentaire, la vitesse poloïdale $\mathbf{u}_p$ est associée à la divergence horizontale. Elle est donnée par la somme $\mathbf{u}_p = +\boldsymbol{\nabla}_h \Phi_h + w\boldsymbol{e_z}$. Pour résumer, les vitesses poloïdale et toroïdale vérifient les propriétés suivantes :

$$\boldsymbol{\nabla}_h \times \mathbf{u}_p = 0, \qquad \boldsymbol{\nabla}_h \cdot \mathbf{u}_p = \boldsymbol{\nabla}_h \cdot \mathbf{u}, \tag{1.74}$$

$$\boldsymbol{\nabla}_h \times \mathbf{u}_t = \omega_z, \qquad \boldsymbol{\nabla}_h \cdot \mathbf{u}_t = 0. \tag{1.75}$$

Comme la vitesse est solénoïdale ($\mathbf{k} \cdot \hat{\mathbf{u}} = 0 \Rightarrow \hat{\mathbf{u}} \perp \mathbf{k}$), la décomposition poloïdale-toroïdale s'exprime dans l'espace spectral de manière géométrique (cf. figure 1.14). Puisque les directions verticale et du vecteur $\mathbf{k}$ sont deux directions particulières du problème, on utilise la base orthonormale associée aux coordonnées sphériques ($\boldsymbol{e_k}$, $\boldsymbol{e_p}$, $\boldsymbol{e_t}$), avec $\boldsymbol{e_k} = \mathbf{k}/|\mathbf{k}|$, $\boldsymbol{e_t} = \boldsymbol{e_z} \times \boldsymbol{e_{k_h}}$ et $\boldsymbol{e_p} = \boldsymbol{e_t} \times \boldsymbol{e_k}$.

Nous présentons maintenant les fondements et limites du sens dynamique associé à la décomposition poloïdale-toroïdale. Les équations linéarisées autour d'un état au repos s'écrivent en fonction des composantes de vitesse poloïdale $\hat{u}_p = \boldsymbol{e_p} \cdot \hat{\mathbf{u}}$ et toroïdale $\hat{u}_t = \boldsymbol{e_t} \cdot \hat{\mathbf{u}}$ comme

$$\partial_t \hat{u}_t = 0, \tag{1.76}$$

$$\partial_t \hat{u}_p = -N^2 \hat{\zeta} \sin\Phi, \tag{1.77}$$

$$\partial_t \hat{\zeta} = \hat{u}_p \sin\Phi. \tag{1.78}$$

Nous voyons que la vitesse toroïdale n'a pas de comportement ondulatoire et que les ondes linéaires correspondent à des échanges d'énergie entre les réservoirs potentiels et poloïdaux. Cette propriété de la décomposition poloïdale-toroïdale, exacte dans la limite linéaire, a été fortement mise en avant, au point que l'appellation "décomposition

ondes-tourbillons" est parfois utilisée (le mot tourbillon désignant alors des structures associées à de la vorticité verticale et à de la vorticité potentielle, plus loin on dira tourbillons de PV). Il est classique de définir une onde dynamiquement comme une structure propagative et ondulatoire. Sa pulsation caractéristique est, au moins dans les cas faiblement non-linéaires, proche de la pulsation donnée par la relation de dispersion linéaire (1.68). Notons au contraire que la vorticité potentielle n'a pas de comportement ondulatoire (Staquet & Riley, 1989). Une décomposition ondes-tourbillons de PV (propagatif-non propagatif) a donc un sens dynamique précis. Nous allons voir que si la relation $F_v \ll 1$ n'est pas vérifiée, la décomposition cinétique poloïdale-toroïdale ne partage pas les caractéristiques dynamiques d'une décomposition ondes-tourbillons de PV.

Considérons le cas modèle d'un écoulement constitué de tourbillons de PV de vitesse toroïdale caractéristique U_t. Nous allons quantifier le rapport entre la vitesse horizontale divergente et la vitesse toroidale en fonction du nombre de Froude vertical. Le tourbillons de PV déforment les surfaces iso-densités sur une distance verticale de l'ordre de l'échelle de flottabilité $L_b = F_h L_h$ ce qui induit des vitesses verticales d'ordre $W \sim F_h U$. Finalement, la vitesse horizontale poloïdale liée aux tourbillons de PV est d'ordre $\boldsymbol{e_h} \cdot \mathbf{u}_p \sim (L_h/L_v)W \sim (L_h/L_v)F_h U_t \sim F_v U_t$. Alors que l'écoulement modèle considéré n'est pas constitué d'ondes, la vitesse poloïdale n'est négligeable que sous la condition $F_v \ll 1$. C'est donc seulement dans la limite $F_v \ll 1$ que l'on peut décomposer un écoulement par la méthode cinématique de décomposition poloïdale-toroïdale en partie propagative et partie non propagative.

Un autre écoulement modèle met en défaut l'interprétation dynamique de la décomposition poloïdale-toroïdale. Lorsque le nombre de Richardson est d'ordre 0.25 et inférieur, un gradient vertical de vitesse horizontale mène par l'enroulement de la nappe de vorticité à la formation de tourbillons d'axe horizontal. Cette instabilité dite de Kelvin-Helmholtz est typique de la limite $F_v \sim 1$ puisque $F_v \sim Ri^{-1/2}$. Notons que les tourbillons de Kelvin-Helmholtz ne sont clairement pas des ondes. Pourtant la vitesse est uniquement poloïdale avec une vitesse toroïdale associée nulle. Cet exemple confirme la conclusion précédente : dans la limite $F_v \sim 1$ une part potentiellement importante de la vitesse poloïdale n'est pas associée à des structures propagatives. Dans la limite $F_v \sim 1$, on peut quand même détecter des ondes en s'appuyant sur le fait que la vorticité potentielle n'a pas de comportement ondulatoire (Staquet & Riley, 1989) ou sur les caractéristiques des ondes linéaires (relation de dispersion et déphasages entre les différentes variables, cf. Fofonoff, 1969; Cho *et al.*, 1999; Jacobitz *et al.*, 2005; Lindborg & Brethouwer, 2007).

Ce résultat sur l'interprétation dynamique de la décomposition poloïdale-toroïdale doit être relié à un autre résultat sur la dynamique des ondes et des tourbillons de PV associé aux limites $F_h \ll 1$, $F_\omega \sim 1$ ou $F_h \ll 1$, $F_v \ll 1$, où F_h et F_v sont les nombres de Froude associés aux tourbillons de PV et F_ω le nombre de Froude associé aux ondes. Le rapport de la fréquence caractéristique des tourbillons de PV sur celle des ondes est d'ordre $(U_t/L_h)/\omega \sim F_h/F_\omega$. Si l'on postule que les ondes et les tourbillons de PV ont des tailles caractéristiques verticale et horizontale similaires, on obtient $(U_t/L_h)/\omega \sim F_v$. Dans les limites mentionnées, les deux modes propagatif et non-propagatif interagissent donc faiblement. Par contre, dans la limite $F_v \sim 1$, les

ondes et les tourbillons de PV peuvent interagir fortement.

Dans cette présentation générale de la dynamique des écoulements stratifiés, nous avons mis en avant deux modes d'écoulement très différents, les ondes de gravité propagatives et les tourbillons de PV non-propagatifs. Nous avons aussi souligné l'importance des deux limites $F_v \ll 1$ et $F_v \sim 1$ associées à des dynamiques très différentes. Nous proposons maintenant dans le chapitre 2 une revue sur la turbulence en milieu stratifié. Nous allons voir que les problématiques liées aux différences entre ondes et tourbillons de PV et entre les deux lois d'échelle pour le nombre de Froude vertical seront centrales.

Chapter 2

Introduction on turbulence in stratified fluids

We now focus on the main subject of this thesis, the dynamics of turbulent flows strongly influenced by a stable density stratification. In chapter 1, we have presented our motivations: the understanding and modeling of atmospheric and oceanic hydrodynamic processes. We have underlined that turbulence and stratification are ubiquitous in nature. In particular, the modeling of the mixing processes and of the unresolved small scales in numerical simulations strongly rely on the understanding of turbulence in stratified fluids. We have presented the typical anisotropic spectra that are commonly observed in the oceans and atmosphere, with horizontal spectra scaling like $E(k_h) \propto \varepsilon^{2/3} k_h^{-5/3}$ and vertical spectra like $E(k_z) \propto N^2 k_z^{-3}$ (see table 2.1 for definitions). We have introduced many basic concepts dealing with turbulence, stratification and rotation. Let us now consider purely stratified (i.e. without rotation) turbulence.

N	Brunt-Väisälä frequency
ε, ε_K, ε_P	total, kinetic and potential energy dissipation rates
Re	Reynolds number
F_h, F_v	horizontal and vertical Froude numbers
$\mathcal{R}$	buoyancy Reynolds number
Ri	Richardson number
$\mathbf{u}_h$, w	horizontal and vertical velocities
U, W	typical horizontal and vertical velocities
ζ	local vertical displacement of fluid particles
L_h, L_v	horizontal and vertical characteristic length scales
$\alpha = L_v/l_h$	aspect ratio
$L_b = U/N$	buoyancy length scale
k_h, k_z	horizontal and vertical wavenumbers

Table 2.1: Notations already defined in chapter 1.

2.1 Notion of turbulence in stratified fluids

In the context of stratified fluids, the word "turbulence" refers to many different processes, observations and flow regimes. In this manuscript, we focus on one particular regime: the strongly stratified and strongly non-linear turbulent regime. This regime is first put into perspective and an overview of issues linked to "turbulence" in stratified fluids is given.

Earliest strategy, à la Kolmogorov

The earliest strategy to predict geophysical spectra consisted in adapting the point of view of Kolmogorov (1941b) to a stratified fluid (Lumley, 1964; Ozmidov, 1965). In the inertial range, the spectra is assumed to depend only on the mean energy dissipation rate ε and on the Brunt-Väisälä frequency N. The proposed theories are also based on physical interpretations but let us remark that by dimensional arguments, one obtains the following expression:

$$E(k) = C_\varepsilon \varepsilon^{2/3} k^{-5/3} + C_N N^2 k^{-3} = C_\varepsilon \varepsilon^{2/3} k^{-5/3} (1 + (l_o k)^{-4/3} C_N / C_\varepsilon), \qquad (2.1)$$

where C_ε and C_N are constants, k is a wave vector and $l_o = (\varepsilon/N^3)^{1/2}$ is the Ozmidov length scale. The law (2.1) predicts both $k^{-5/3}$ and k^{-3} power laws with a transition at l_o (e.g. Lumley, 1964; Ozmidov, 1965). Later, Holloway (1983) derived interesting scaling laws following similar ideas. In particular, he underlined the importance of the ratio of Ozmidov length scale over the Kolmogorov length scale. These theories do not focus on the anisotropy of the spectra but simply on the transition between different scaling laws. Recently, Dewan (1997) and Brethouwer *et al.* (2007) developed similar dimensional arguments and predicted a similar expression but only for the vertical spectrum. However, the physical interpretations behind these studies are very different.

Wakes in stratified fluids

Many experiments have considered the wake of cylinder or sphere in the presence of a density stratification (see Lin & Pao (1979) for a review or Diamessis *et al.* (2011) for a recent study). Of course, late wake dynamics is closely related to the decay of stratified turbulence. Because the wake becomes less energetic, the influence of stratification increases and a transition happens. Internal waves are generated and propagate away while the three-dimensional wake collapses toward quasi-horizontal meandering motions. The late time flow is thought to be dominated by vertical vorticity with low horizontal divergence. It is associated to potential vorticity $q = (g/\rho_0)\boldsymbol{\omega} \cdot \nabla \rho_{tot}$ and is generally structured in thin horizontal layers, with vortices with low aspect ratio $\alpha = L_v/L_h$, where L_v and L_h are respectively their vertical and horizontal characteristic length scales (see e.g. Riley & Lelong, 2000). As pointed out by Godeferd & Cambon (1994), the term quasi-two-dimensional is misleading in this context because the motion is quasi-two-component but strongly varying along the vertical.

Lilly (1983) first introduced the term "stratified turbulence" to refer to the resulting meandering quasi-two-component flows dominated by potential vorticity (PV). In section 2.3 this type of flow is presented in detail.

Gravity waves and PV

These observations suggest that waves and flows linked to PV decouple and evolve independently. Implicitly considering a weakly anisotropic flow, Riley, Metcalfe, & Weissman (1981) explained the dynamical decoupling with a scaling analysis. They showed that under the condition that the Froude number Fr is small (where $Fr \equiv F_h$ or $F_r \equiv F_v$, hence $F_h \sim F_v \ll 1$), the two parts of the flow evolve over different time scales (fast propagating waves and slow non-propagating horizontal vortices). The latter vortices, i.e. the "stratified turbulence" is governed by a set of reduced equations, which describe layers of horizontal, horizontally non-divergent and fully non-linear motion coupled along the vertical by viscosity only. Many studies and interpretations are based on this result and so focus on the dynamics of either waves or quasi-horizontal vortices. When both types of flow are considered together, the assumption of weak interaction is often made. However, we will see that these approaches are questionable.

Let us note that, in general it is not trivial to decompose a flow into waves and horizontal vortices associated to PV (propagating and non-propagating motions). Different methods have been employed in purely stratified flows. The Craya-Herring decomposition (Craya, 1958; Herring, 1974) also known as the poloidal-toroidal decomposition (Cambon, 2001) has been presented in chapter 1. It is a purely kinematic method that decomposes waves and PV in the limit $F_v \ll 1$ only (i.e. when the deformations of the isopycnals are negligible compared to the characteristic vertical length scale). Staquet & Riley (1989) extended this method for small, but finite, F_v when there is no overturning. The Craya-Herring is then modified by replacing the horizontal planes by the slightly tilted isopycnals. Another method exploits the particular phase shift between density and velocity for linear waves (see e.g. Fofonoff, 1969; Cho *et al.*, 1999; Jacobitz *et al.*, 2005). Recently, Lindborg & Brethouwer (2007) have used frequency spectra of spectral modes to detect waves.

Gravity waves and turbulence

We saw in chapter 1 that the linearised Boussinesq Navier-Stokes equations describe internal gravity waves. It is therefore natural to base the interpretations on these linear coherent structures. Moreover, internal waves have been widely observed in the oceans and atmosphere. This propagating motion has been extensively studied in the laboratory and in nature. Here, we just provide an insight of some issues related to waves and stratified turbulence. Theories involving waves have been proposed to explain the observed anisotropic spectra (for a review see Waite & Bartello, 2006a).

Garrett & Munk (1979) interpret many different statistical oceanic measures by considering a continuous superposition of waves and by computing the associated anisotropic spectra. It has to be pointed out that they do not give any physical argument about the energetic repartition over the different waves, which is fixed by

fitting the data (see also Munk, 1981). At large vertical scales, the vertical spectrum scales like k_z^{-2} whereas it steepens at lower scales (1 m $\lesssim k_z^{-1} \lesssim$ 100 m) and scales like k_z^{-3} before shallowing toward $k_z^{-5/3}$ (Gargett *et al.*, 1981; Gregg, 1987). Garrett & Munk (1979) interpret the k_z^{-2} and k_z^{-3} slopes as the result of waves. The $k_z^{-5/3}$ inertial range is explained by "small-scale turbulence".

The concept of "wave saturation" has been used to explain the universality of the spectra (see Fritts, 1984, for a review). All waves are marginally stable, i.e. nearly "breaking", which fixes the energy distribution. The physical explanation of the saturation is however unclear: Dewan & Good (1986) and Smith *et al.* (1987) invoke linear instabilities while Hines (1991) and Dewan (1997) proposed non-linear processes. In fact, it is known that most of the waves are strongly non-linear in the oceans and atmosphere (Fritts & Alexander, 2003; Lindborg & Riley, 2007). The non-linear (triadic) interaction between waves, the related instabilities and eventually the wave breaking producing "small-scale turbulence" have been extensively studied (see e.g. Staquet & Sommeria, 2002; Lelong & Dunkerton, 1998a, and many papers by Fritts and co-workers).

Finally, "wave turbulence" or "weak turbulence" refer to a theoretical approach considering the non-linear interaction between small amplitude waves (see e.g. Caillol & Zeitlin, 2000; Lvov & Tabak, 2001). In the stratified case, this approach is questionable because waves in the oceans and atmosphere are not weak (see e.g. Holloway, 1980; Lindborg & Riley, 2007). Moreover, Lelong & Riley (1991), Godeferd & Cambon (1994) and Bartello (1995) have shown that resonant interactions between waves and vortical motion are more efficient than three-wave interactions at transferring wave energy (see Waite & Bartello, 2006a).

Mixing and shear layer

The mixing of stratified fluids by turbulent flows is fundamental and widely studied (for reviews, see Gregg, 1987; Peltier & Caulfield, 2003; Ivey *et al.*, 2008). The shear layer in a stratified fluid is an elementary flow to understand the basics of mixing (see e.g. Smyth & Moum, 2000b,a; Smyth *et al.*, 2001; Jacobitz *et al.*, 2005; Brucker & Sarkar, 2007). The effect of the stratification on a shear layer (initially turbulent or not) is studied for different values of the Froude number (quantifying the influence of the stratification on the flow) and of the Richardson number (comparing the stratification to the shear). It has to be pointed out that an interesting regime corresponds to the case when $Ri \simeq 0.25$ (i.e. of order unity) wherein shear instabilities can develop and lead to an energy transfer from the mean shear flow to the turbulent fluctuations. In that case, the stationary state is roughly characterised by $Ri \sim 1$ and $F_h \sim 1$ and the resulting turbulence is not strongly influenced by stratification. In this sense, it is different from the strongly stratified regime that we are concerned about here.

"Strongly stratified turbulence" and related issues

In this manuscript, we stress on the importance of a strongly stratified, strongly non-linear turbulent regime. The flow is strongly influenced by the stratification with very

low horizontal Froude number $F_h \ll 1$. Therefore the dynamics at large scales is hydrostatic. But the flow is also strongly anisotropic, with an aspect ratio $\alpha = L_v/L_h$ of the order of the horizontal Froude number F_h (Billant & Chomaz, 2001, see section 1.4). Thus the vertical Froude number F_v is of order unity and this scaling law corresponds to vertical displacement ζ and vertical characteristic length scale L_v of the order of the buoyancy length scale $L_b = U/N$. We will see that this strongly non-linear regime is radically different of the classical $F_h \sim F_v \ll 1$ regime considered by Riley *et al.* (1981). We will present arguments that show why this particular regime is an attractor for many strongly stratified flows at very high Re and why it is geophysically relevant.

This thesis fits into the scheme of former studies on flows with potential vorticity. But we would like to point out that we are led to consider together strongly coupled and strongly non-linear vortices and waves. Indeed, Lindborg & Brethouwer (2007) have shown that strongly stratified turbulence presents a degree of universality, i.e. is relatively invariant whatever the type of forcing, with waves or PV.

New findings on strongly stratified turbulence are conflicting with older theories and clearly question some older approaches. For instance, the cascade is now known to be direct whereas it was predicted to be inverse. Hereafter, we present a (necessarily involved) version of the state of understanding of stratified turbulence. We are going to focus on the following important issues:

- What are the fundamental scaling laws? In particular, for the vertical length scale?
- What are the mechanisms of vertical decorrelation and length scale selection that are active in a stratified flow?
- How can we decompose a flow between a propagating part (internal waves) and a non-propagating part (PV flows)?
- What is the dynamics and the direction (forward or backward) of the cascade in stratified turbulence?

2.2 Dominant balance and buoyancy Reynolds number $\mathcal{R}$

Before the beginning of the 21th century, the attention was focused on the small vertical Froude number F_v dynamics. The flows produced in laboratory and simulated in numerical studies were indeed associated to small F_v. It is somehow contradictory with the result presented in chapter 1 about the scaling analysis for inviscid stratified fluid which leads to the scaling law $F_v \sim 1$ (Billant & Chomaz, 2001). In this section, we explain this apparent contradiction. Due to the strong anisotropy of stratified flows, the diffusive effects can play an important role even at large Re. Billant & Chomaz (2001) argued that the quantity $ReF_h{}^2$ should be considered as a "modified Reynolds number". Hereby, we follow Godoy-Diana, Chomaz, & Billant (2004) and Brethouwer, Billant, Lindborg, & Chomaz (2007) to show how the strongly stratified scaling is modified by the introduction of diffusive effects. We restrict to the

Boussinesq approximation with a constant Brunt-Väisälä frequency N. Using the strongly stratified scaling presented in chapter 1, the diffusive equations are written in non-dimensional form as

$$\begin{aligned}
\frac{d\mathbf{u}_h}{dt} &= -\boldsymbol{\nabla}_h p + \frac{1}{Re\alpha^2}(\partial_{zz} + \alpha^2\boldsymbol{\nabla}_h^2)\mathbf{u}_h, && (2.2)\\
{F_h}^2\frac{dw}{dt} &= -\partial_z p - \zeta + \frac{1}{Re\alpha^2}(\partial_{zz} + \alpha^2\boldsymbol{\nabla}_h^2)w, && (2.3)\\
\frac{d\zeta}{dt} &= +w + \frac{1}{ScRe\alpha^2}(\partial_{zz} + \alpha^2\boldsymbol{\nabla}_h^2)\zeta, && (2.4)\\
\boldsymbol{\nabla}_h\cdot\mathbf{u}_h + \frac{{F_h}^2}{\alpha^2}\partial_z w &= 0. && (2.5)
\end{aligned}$$

where $Sc = \nu/\kappa$ is the Schmidt number, $\alpha = L_v/L_h$ is the aspect ratio and $d/dt = \partial_t + \mathbf{u}_h\cdot\boldsymbol{\nabla}_h + (F_h/\alpha)^2 w\partial_z$. If we keep only the dominant terms when $F_h \to 0$, it yields

$$\begin{aligned}
(\partial_t + \mathbf{u}_h\cdot\boldsymbol{\nabla}_h + \frac{{F_h}^2}{\alpha^2}w\partial_z)\mathbf{u}_h &= -\boldsymbol{\nabla}_h p + \frac{1}{Re\alpha^2}\partial_{zz}\mathbf{u}_h, && (2.6)\\
0 &= -\partial_z p - \zeta && (2.7)\\
(\partial_t + \mathbf{u}_h\cdot\boldsymbol{\nabla}_h + \frac{{F_h}^2}{\alpha^2}w\partial_z)\zeta &= +w + \frac{1}{ScRe\alpha^2}\partial_{zz}\zeta, && (2.8)\\
\boldsymbol{\nabla}_h\cdot\mathbf{u}_h + \frac{{F_h}^2}{\alpha^2}\partial_z w &= 0. && (2.9)
\end{aligned}$$

At this stage, we have to know which are the dominant terms between the dissipative terms of the order $1/(Re\alpha^2)$ and the advective terms of the order ${F_h}^2/\alpha^2 = {F_v}^2$. This depends on the value of the buoyancy Reynolds number $\mathcal{R} \equiv Re{F_h}^2 = (L_b/L_\nu)^2$, where $L_b = U/N$ is the buoyancy length scale and $L_\nu = \sqrt{\nu L_h/U}$ the dissipative length scale associated to the large structures.

If $\mathcal{R} = (L_b/L_\nu)^2 \gg 1$, the vertical transport dominates and the dominant balance leads to $F_v \sim 1 \Rightarrow L_v \sim L_b$. The system of equations becomes

$$\begin{aligned}
(\partial_t + \mathbf{u}_h\cdot\boldsymbol{\nabla}_h + w\partial_z)\mathbf{u}_h &= -\boldsymbol{\nabla}_h p, && (2.10)\\
0 &= -\partial_z p - \zeta, && (2.11)\\
(\partial_t + \mathbf{u}_h\cdot\boldsymbol{\nabla}_h + w\partial_z)\zeta &= +w, && (2.12)\\
\boldsymbol{\nabla}_h\cdot\mathbf{u}_h + \partial_z w &= 0. && (2.13)
\end{aligned}$$

This set of inviscid strongly stratified reduced equations has been already described in chapter 1 for the inviscid case. A fundamental fact is that the Froude number does not appear anymore. This means that different flows with different stratifications are identical up to a scaling factor. In particular, the vertical length scales associated to all strongly stratified inviscid processes are proportional to the buoyancy length scale.

These results are very general. However, it must be pointed out that these equations describe the dynamics of strongly stratified large structures neglecting the presence of smaller scales, and hence do not describe all the scales of strongly stratified

turbulence. Nevertheless, we will see in section 2.6 that important results about stratified turbulence can be deduced from this scaling analysis. When considering strongly stratified isolated large structures, care must be taken while using the proportionality relation $L_v \propto L_b$. Indeed, there are strongly stratified instabilities whose vertical wavelength of the dominant mode is strictly zero $k_z = 0$, for example, the instability of a horizontal shear (Deloncle *et al.*, 2007)[1]. In this case, the relation of proportionality does not imply the scaling $L_v \sim L_b$. Moreover, the strongly stratified inviscid dynamics can lead to instabilities for which the reduced equations do not apply anymore, as for example the gravitational instability linked to non-hydrostatic processes.

If $\mathcal{R} = (L_b/L_\nu)^2 \ll 1$, the vertical dissipation dominates and the dominant balance leads to $\alpha^2 \sim Re \Rightarrow L_v \sim L_\nu$. The system of equations becomes

$$(\partial_t + \mathbf{u}_h \cdot \boldsymbol{\nabla}_h)\mathbf{u}_h = -\boldsymbol{\nabla}_h p + \partial_{zz}\mathbf{u}_h, \tag{2.14}$$

$$0 = -\partial_z p - \zeta, \tag{2.15}$$

$$(\partial_t + \mathbf{u}_h \cdot \boldsymbol{\nabla}_h)\zeta = +w + Sc^{-1}\partial_{zz}\zeta, \tag{2.16}$$

$$\boldsymbol{\nabla}_h \cdot \mathbf{u}_h = 0. \tag{2.17}$$

This system has been derived by Riley *et al.* (1981) with a scaling analysis based on a condition of small "Froude number", i.e. based on the conditions $F_h \ll 1$ and $F_v \ll 1$, and with no condition on the Reynolds number. Since the flow is dominated by horizontally quasi-non-divergent horizontal motion, the convective derivatives are quasi-two-dimensional and the dynamics has similarities with two-dimensional dynamics. However, the horizontal layers are strongly coupled by dissipative effects with strong vertical gradients.

To conclude, the dissipation prevents the development of small vertical scales and opposes the tendency of the flow to go toward order unity F_v. At relatively small $\mathcal{R}$, the attractor is linked to a dynamics at low F_v that is strongly influenced by dissipative effects linked to vertical gradients. This is the reason why stratified flows with $F_v \ll 1$ have been widely observed in laboratory experiments or numerical simulations and why the corresponding limit $F_v \ll 1$ was thought to be more general than it is.

2.3 "Lilly's stratified turbulence", a brief historical review

This section presents a theory proposed by Lilly (1983) about the meandering quasi-horizontal flows observed in stratified fluids (for a review, see Riley & Lelong, 2000). The expression "stratified turbulence" was first introduced by Lilly (1983) to refer to this particular kind of disordered non-propagative motions. Here, we propose a brief review about Lilly's theory and related works in the light of the results of the last section.

Riley *et al.* (1981) presented scaling analysis and numerical simulations of stratified flows. Due to the coarse numerical resolution available at that time (only 32^3), the

[1] However, Deloncle *et al.* (2007) showed that the cut off of the range of unstable vertical wavelength scales like L_b. This tendency of a horizontal shear flow to select small vertical scales is also observed in DNS by Basak & Sarkar (2006) and Arobone & Sarkar (2010).

Reynolds numbers of the simulated flows were relatively low. This leads to very low buoyancy Reynolds number, lower than those typically obtained in laboratory experiments. The authors implicitly assumed weak anisotropy and derived the system of equations (2.14-2.17) linked to the dissipative regime. Besides, Gage (1979) gave an observational argument showing a similarity between atmospheric stratified turbulence and 2D turbulence. The ratio between the longitudinal and the transverse structure functions has been found to approximately correspond to the 2D case. However, this observation has been shown to be invalid by Lindborg (1999).

These works led Lilly (1983) to introduce the concept of "stratified turbulence" in order to refer to the vortical flows described by Riley's equations. Inspired by the quasi-geostrophic case (QG), Lilly (1983) stated that the stratified turbulence is dynamically similar to 2D turbulence. In chapter 1, we showed that a crucial property of 2D turbulence is the proportionality between the energy and the enstrophy in spectral space. In the limit $F_v \ll 1$, the condition of proportionality is fulfilled because PV is simply proportional to vertical vorticity, $q \simeq -N^2\omega_z$. Eventually, Lilly (1983) proposed that the observed atmospheric spectra could be explained by an inverse cascade of energy due to stratified turbulence.

However, these reasonings neglected the dissipative effects which are fundamental in the limit obtained for $\mathcal{R} \ll 1$. Actually, we now know that in this regime the stratified pancakes are strongly dissipative and that an inverse cascade cannot develop. Nevertheless, at that time, the fundamental aspect of the importance of the dissipative terms linked to vertical gradients was not understood. Lilly (1983) stated that at large Reynolds number, dissipation is negligible and that the system consists in fully decoupled horizontal layers. He predicted that the shear will grow, leading eventually to the development of shear instabilities and to the production of small-scale turbulence.

We see that Lilly's theory has a dual aspect. On the one hand, an inverse cascade is predicted. On the other hand, strong shear that leads to Kelvin-Helmholtz instability, which is a mechanism of forward cascade, is predicted. This is linked to an internal contradiction of Riley's scaling when the Reynolds number is large enough (actually when $\mathcal{R} > 1$). If we assume that $F_v \ll 1$, the horizontal layers are nearly decoupled. This leads to an increase of the vertical gradients and of the vertical Froude number that is inconsistent with the assumption of small F_v. Eventually, it was argued that the small scale turbulence can be modeled with a turbulent viscosity and that the dynamics of the large strongly stratified scales would not be fundamentally modified by the increase of Reynolds number (as stated for example in Praud *et al.*, 2005).

Much of the theoretical framework for strongly stratified flows has been developed for the limit $F_v \ll 1$. In that particular and restrictive limit, waves and PV interact weakly. Moreover, it is possible to decompose a flow in two propagative and non-propagative parts with the kinetic poloidal-toroidal decomposition (see chapter 2 for technical details). Indeed, different theories that consider either waves or PV, were put forward to explain the geophysical spectra. Hopefully, these two very different interpretations lead to opposite predictions: wave theories predict a forward cascade, while vortex Lilly's theory predicts a backward cascade. Thus, at that time, one can thought that results on the direction of the cascade would have resolved this

controversy.

Within the framework of Lilly's assumption, some numerical studies have been carried out to test the backward energy cascade theory. Metais & Herring (1989) performed simulations of decaying stratified flows inspired by the experiment of Itsweire *et al.* (1986). Herring & Metais (1989) also presented simulations of forced stratified flows but in both studies no cascade (neither inverse nor direct) was clearly observed. Unfortunately, the numerical resolution was very limited (64^3) at that time and the flows were strongly influenced by dissipation. Other numerical studies, Metais *et al.* (1996) (with higher resolution, 128^3 and rotation) and Vallis *et al.* (1997) (with a meteorological code), have investigated the subject but their results were not conclusive. Eventually, Lilly *et al.* (1998) reviewed these different studies and presented new meteorological simulations showing a rapid increase in larger-scale energy. They noted that some results are conflicting and concluded that further observations were needed.

The generation of slow large scales in forced rotating stratified turbulence has been reported by Smith & Waleffe (2002). Actually, these large scales are "shear modes" developing in the numerical box of a pseudo-spectral code with periodic boundary conditions. Shear modes correspond to horizontally invariant shear flows which can exist in such numerical method. Smith & Waleffe (2002) interpreted this transfer as an inverse cascade. Lindborg (2006) later showed that the continuous growth of shear modes is a diffusive effect. However, large shear modes are found in many (or maybe all) forced stratified turbulence simulations, even at large buoyancy Reynolds number, when the dissipative effects are weak. The cause of this type of motion and its effects on the global turbulence are not fully understood.

The diffusive stratified regime has been observed in many other experimental and numerical studies. Among others, Lienhard & Van Atta (1990) and Yoon & Warhaft (1990) studied the decay of grid-generated turbulence influenced by thermal stratification. After the collapse of the nearly isotropic turbulence, the large scales are strongly influenced by dissipative effects. Staquet & Godeferd (1998) and Godeferd & Staquet (2003) numerically reproduced this type of flow at Reynolds number typical of the laboratory experiment with DNS at moderate resolution (256^3). These simulations were used to precisely test a new anisotropic EDQNM model[2] whose results compare remarkably well with those of DNS. The initial states for the stratified simulations are final flows of non-stratified isotropic turbulence simulations with random density perturbations (with a relatively high initial potential energy). It has to be pointed out that these non-balanced initial conditions (without the stratified phase coherence between poloidal velocity, toroidal velocity and density perturbations) are not adapted to study strongly stratified turbulence. In the physical laboratory situation of the decay of a non-stratified turbulence, the flow experiences first a state that is weakly influenced by stratification. The flow becomes strongly influenced by stratification only when a non-negligible part of the energy has been dissipated or transfered to small scales by the three-dimensional weakly stratified turbulence. Because the initial turbulence has to fit into the numerical mesh, the obtained strongly stratified flow is characterized by too low buoyancy Reynolds number, and thus corresponds to the

[2]Eddy-Damped Quasi-Normal Markovian, see e.g. Sagaut & Cambon (2008).

viscosity affected stratified regime (Godoy-Diana *et al.*, 2004; Brethouwer *et al.*, 2007). It has to be pointed out that even the most recent experimental studies in this field (e.g. Fincham *et al.*, 1996; Praud *et al.*, 2005) concern flows associated with relatively low $\mathcal{R}$ and hence strongly influenced by the dissipation due to vertical gradients.

Let us finally note that the term turbulence is actually not appropriate to qualify the strongly diffusive stratified regime obtained when $\mathcal{R} < 1$. Indeed, there is neither scale superposition nor inertial range in this regime because the dissipation acts mainly through the large structures.

2.4 The dynamics in the limit $F_h \ll 1$, $F_v \ll 1$ leads to $F_v \sim 1$

Vertical decorrelation and length scale selection

In this section, we deal with the mechanisms leading to the structure in thin layers. We neglect the diffusive effects which are not actively involved in the layering. Let us consider a flow characterized by a relatively important vertical correlation, i.e. with small vertical (and horizontal) Froude number leading to very flat isopycnals compared to the characteristic vertical length scale ($\zeta \ll L_v$). Vertically invariant structures (2D-2C flows) are the classical simple model case used to study the layering processes. However, the results should apply for any vortical flows with a vertical length scale much larger than the buoyancy length scale (which is very small for strongly stratified flows). In particular, it should apply for relatively isotropic structure with $L_v \sim L_h \gg L_b$.

Dynamics of decoupled horizontal layers

A first step could be to consider a flow with an infinite stratification, i.e. with $F_h = F_v = 0$. In this limit, vertical velocity and vertical displacement are zero and, in the inviscid case, the horizontal layers are fully decoupled. The 2D dynamics of the layers naturally leads to an increase of the vertical gradients. Lilly (1983) stated that "*both the inherent instability of turbulent flows and the existence of any mean vertical shear will decorrelate the vertical flow structure [...]*". The concept of toroidal cascade introduced by Cambon (2001) synthesizes these ideas. It is, however, important to note that there is no inviscid scale selection since the stratification is infinite (leading to zero vertical transfer terms). Thus, all vertical scales grow in average at the same growth rate.

Interaction between layers and zigzag instability

This first step contains some physics (the dynamics of horizontal 2D flows) but all interactions between the horizontal layers have been neglected. They correspond to very small terms of order ${F_v}^2$ and it could be relevant to neglect them for a nearly vertically invariant flow strongly influenced by stratification. Actually, the limit $F_v \to 0$ is singular and even when $F_v \ll 1$, these interactions can strongly influence the dynamics. In some flows, when several vertical columnar (or nearly columnar with

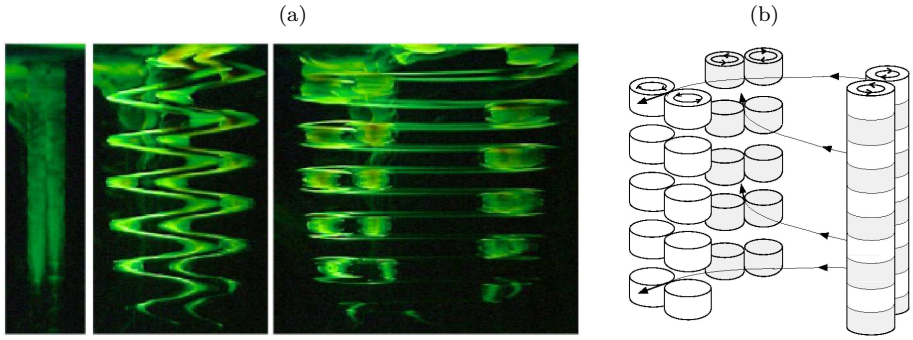

Figure 2.1: (a) Photographies of the evolution of the zigzag instability on two columnar counter rotating vortices. The dipole propagates initially toward the reader. Taken from Billant & Chomaz (2000a). (b) Schema of the non-linear evolution of the zigzag instability illustrating the creation of pancake vortices.

$L_v \gg L_b$) vortices are interacting, the small terms of order ${F_v}^2$ are implied in the mechanism of an instability that spontaneously creates layers.

This instability, called the zigzag instability, has first been identified on the simple case of two columnar counter-rotating vortices. The phenomenon has been observed experimentally by Billant & Chomaz (2000a) in a stratified tank filled with salt water. The vortices are created by a dipole generator composed of two rotating vertical plates. The columnar dipole propagates and the zigzag instability bends and twists it along the vertical with very weak horizontal deformations as shown in figure 2.1. The unstable perturbation consists at leading order both in a vertically modulated rotation $\phi(z,t)$ (twisting) and translation $\eta(z,t)$ of the vortex pair perpendicular to the propagation direction (bending). Billant & Chomaz (2000b,c) explained the instability via analytical and numerical linear instability analysis of the Lamb-Chaplygin[3] vortex pair. These studies showed that the maximum growth rate scales like the strain $\sim U/L_h$ and that the vertical length scale of the dominant mode scales like the buoyancy length scale U/N. Indeed, the zigzag instability selects a vertical deformation with a vertical Froude number of order unity.

Analysis of the zigzag instability in the limits $F_h \ll 1$ and $F_v \ll 1$

The analytical results are derived by a multiple-scale expansion analysis for $F_h \ll 1$ and $F_v \ll 1$. Equations governing the evolution of the phase variables describing the zigzag instability are derived. At leading order, the linear governing equation for the translation, $\dot{\eta} = U\phi$, reflects only a kinematic effect: if the angle of propagation of a dipole is vertically modulated, the propagation of the dipole in the different layers increases the translation. This toroidal effect does not cancel out in the limit $F_v = 0$.

[3]The appendix B recalls the definitions of some model vortices and dipoles, including the Lamb-Chaplygin dipole.

The second equation giving the time derivative of the rotation (equation (1.3) in Billant & Chomaz, 2000b) is associated to more subtle effects of higher order in F_v. A qualitative explanation of the physical understanding of the instability mechanism is given by Billant & Chomaz (2000b): "*If the columnar vortex pair is vertically bent in the y-direction* [perpendicular to the propagation direction]*, the resulting vertical pressure gradient distorts by hydrostatic balance the isopycnal surfaces. In response, a vertical velocity field is generated in order to conserve density* [which imposes that the fluid particles follow the isopycnals]. *This vertical velocity field stretches the basic vertical vorticity and induces secondary horizontal motions in order that mass be conserved. These two effects induce a twisting of the vortex pair which modifies the travelling direction in such a way as to increase the initial bend, thus leading to instability.*" This theory is confirmed by a numerical study providing a comprehensive description and understanding of the zigzag instability in the case of two counter-rotating vortices strongly influenced by a stratification.

Generality of the zigzag instability

From these arguments, one can anticipate that the instability mechanism is not particular to the case of counter-rotating vortices. The zigzag instability could potentially develop on any horizontal flows that are able to linearly increase an infinitesimal vertical decorrelation by horizontal evolution of the different layers. Indeed, the zigzag instability has been shown to be a generic instability. It also acts in the cases of a pair of co-rotating vortices (Otheguy *et al.*, 2006b) and vortex arrays (Deloncle, Billant, & Chomaz, 2011). However, its development depends on the 2D-2C base state flow[4] and the zigzag instability is stable in the cases of 2D Taylor-Green flow (a three-dimensional periodical array of horizontal vortices, see Riley & de Bruyn Kops, 2003), a single row of co-rotating vortices (Deloncle *et al.*, 2011) and of vertically invariant horizontal jet (Deloncle *et al.*, 2007).

Analysis of the zigzag instability in the limit of small vortex core

Recently, Billant (2010) have presented a general study on the three-dimensional bending instabilities on flows with two columnar vortices influenced by stratification and rotation (including the zigzag, tall-column and Crow instabilities). The analysis is performed under the assumptions of long vertical wavelength and of large separation between the vortices (small core) but, contrary to previous theoretical studies, it is valid over a wide range of rotation and stratification (going from weakly stratified to strongly stratified). The theory is further generalized formally to any basic flow consisting of an arbitrary number of vortices in stratified and rotating fluids. Billant *et al.* (2010) present comparisons between the theoretical predictions and numerical computations. A very good agreement is generally found, thereby providing a comprehensive description of the zigzag instability. Some particular results on the maximum growth rate and the most amplified wavelength are given in appendix B.

[4]This dependence of the decorrelation process on the existence and the location of some coherent structures (on phase coherence in spectral space) is not taken into account in the EDQNM approach.

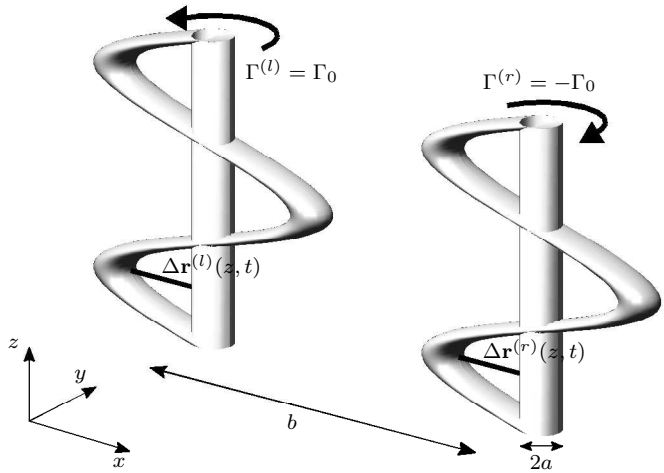

Figure 2.2: Schematic representation of two counter-rotating vortices bended with the antisymetric neutral mode corresponding to the zigzag instability with $\Delta\mathbf{r}^{(l)}(z,t) = \Delta\mathbf{r}^{(r)}(z,t)$. The two vortices of radius a are separated by a distance b.

Following Billant (2010), we can provide an insight on the mechanisms of the zigzag instability. We consider the particular case of a counter-rotating vortex pair, with two columnar vertical vortices of circulation $\Gamma^{(l)} = \Gamma_0$ and $\Gamma^{(r)} = -\Gamma_0$, and separated by a distance b as sketched in figure 2.2. The theory is formulated in terms of bending waves of each vortex, $\Delta\mathbf{r}^{(l)}(z,t)$ and $\Delta\mathbf{r}^{(r)}(z,t)$. Note that a bending wave is not an internal wave but only a bending perturbation of a columnar vortex.

The evolution of the bending mode of a vortex (let us say of the right vortex) is due to the self-induction and to the action of the companion bent vortex (the left vortex). The effect of the companion vortex is further decomposed in two terms, namely, (i) "strain" effect: it comes from the velocity gradient induced by the columnar basic left vortex. It is expressed as a function of the displacement of the right vortex $\Delta\mathbf{r}^{(r)}$; and (ii) "mutual induction": it is the effect of the perturbation of the companion vortex and is expressed as a function of the associated displacement $\Delta\mathbf{r}^{(l)}$. For neutral displacements such as $\Delta\mathbf{r}^{(l)}(z,t) = \Delta\mathbf{r}^{(r)}(z,t)$, i.e. corresponding to the zigzag instability, and under the assumption of long vertical wavelength and of large separation between the vortices, these two effects cancel out because of the translation invariance. In that case, the evolution of the bending modes only depends on the self-induction.

The critical point is that self-induction reverses when stratification increases. This can be understood easily by comparing the non-stratified and quasi-geostrophic cases. In both flows, the motion of a modulated vortex line can be derived from the Biot-Savart law as sketched in figure 2.3. But in the quasi-geostrophic case, the Biot-Savart law is modified and the total vorticity is replaced by $\omega_z \boldsymbol{e_z}$ (figure 2.3*b*). We see that the self-induction is negative in the non-stratified case (with bending mode rotating opposite to the vortex rotation) and positive in the QG case (bending mode and vortex

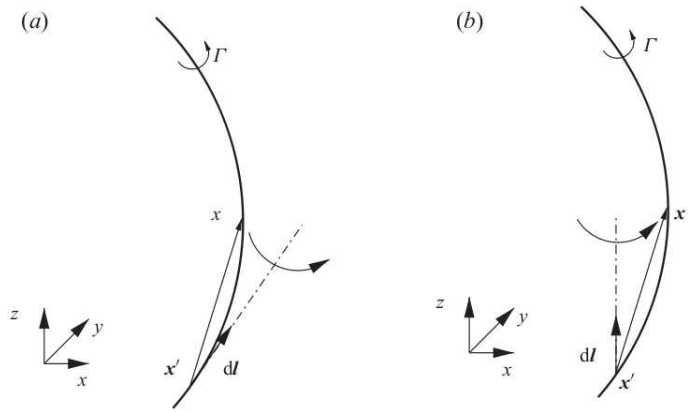

Figure 2.3: Graphical interpretation of the Biot-Savart law in non-stratified fluid (a) and quasi-geostrophic fluid (b). Taken from Billant (2010).

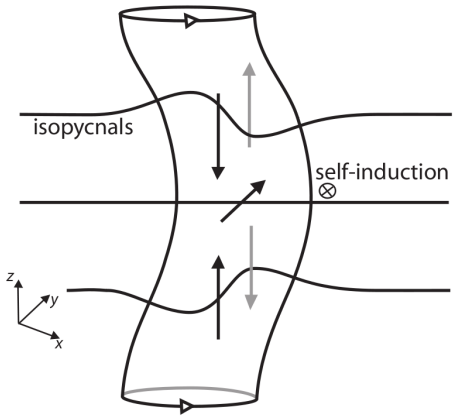

Figure 2.4: Schematic representation of the mechanism of self-induction for the purely stratified case. The isopycnal lines are taken along the centre of the vortices. Black and grey arrows represent poloidal velocity. Grey arrows correspond to vertical velocity in the back of the vortex. In that case, the horizontal poloidal velocity goes backward, leading to a positive self-induction, with the bending mode rotating in the same way as the vortex.

rotate together).

The result in purely stratified fluids is similar to the QG case, but since the circulation of the vortex is not conserved, no simple Biot-Savart formulation applies and the global vortex 3D dynamics has to be considered. Figure 2.4 is a schematic representation of the mechanisms involved in purely stratified fluids. For the interpretation, the reader can refer to the cited paragraph from Billant & Chomaz (2000b). The bending

of the columnar vortex leads to vertical pressure gradients which distort the isopycnal surfaces. In the case of the hydrostatic equilibrium, they tend to be deformed toward low pressure regions, i.e. toward the centre of the vortex. Since the fluid particles follow the isopycnals, they go up and down rotating around the vortex. The poloidal horizontal velocity due to the vertical gradients of vertical velocity pushes the bended vortex such as the self-induction is positive, as in the QG case. Finally, the stretching of vertical vorticity due to vertical gradients of vertical velocity also drives a positive self-induction.

Finally, figure 2.5 summarises the mechanism of the zigzag instability. In figure 2.5(a), the dipole is bended with an antisymmetric neutral mode without twisting. The (stratified) self-induction twists the bended dipole (figure 2.5b) so that the bending is amplified by the propagation of the dipole (figure 2.5c). These two effects couple together in a positive feedback and drive an exponential increase of the bending.

Conclusive remarks

Let us now summarize the main points of this section : (i) The 2D dynamics of decoupled horizontal layers (the toroidal cascade) leads to an increase of the vertical gradients. (ii) The limit $F_v \to 0$ is singular and the zigzag instability can be efficient (but depending on the 2D flow) to create horizontal layers characteristed by vertical Froude number of order unity (with a growth rate of the order of the horizontal characteristic frequency of the 2D flow). (iii) In all cases, the increase of the vertical gradients is limited either by dissipative effects if $\mathcal{R} \lesssim 1$ (leading to relatively low vertical gradients and vertical Froude number), or by other instabilities like the shear and the gravitational instabilities if $\mathcal{R} \gtrsim 1$. As already mentioned in chapter 2, these instabilities tend to select vertical length scale of the order of the buoyancy length scale corresponding to a vertical Froude number of order unity.

2.5 Data analysis support the forward energy cascade hypothesis

Before focusing on the $F_v \sim 1$ dynamics, let us present some recent results about geophysical turbulence on Earth. We have presented in chapter 1 the anisotropic spectra typically observed both in the atmosphere and oceans (Nastrom & Gage, 1985; Gage & Nastrom, 1986; Garrett & Munk, 1979; Gargett *et al.*, 1981). Later, many geophysical measurements and analysis on turbulence brought further informations. For instance, the direction of the energy cascade in the atmosphere has been measured by Lindborg (1999); Cho & Lindborg (2001); Lindborg & Cho (2001). The third order structure functions are shown to be proportional to negative r, where r is the separation distance, which implies a downscale energy cascade. This tends to show that the energy spectra can not be explained by a two-dimensional dynamics and thus gives credit to the wave theories that predict a downscale energy cascade. However, Lindborg (2007a) computed the horizontally divergent and rotational spectra from aircraft signals and showed that these two spectra are nearly equal in the stratified

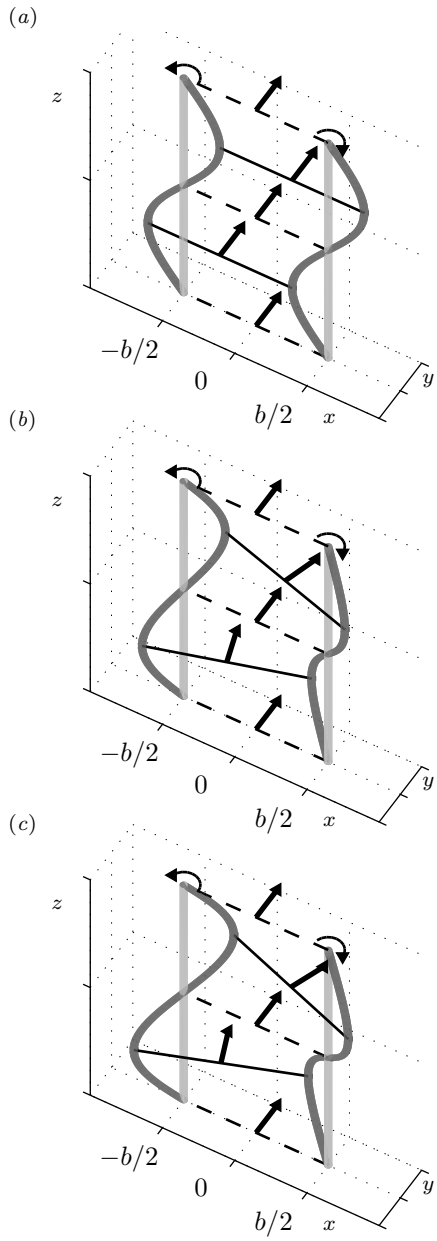

Figure 2.5: Qualitative explanation of the zigzag instability. In (a) a pure bending mode is applied to a columnar dipole. The self-induction twists the bended dipole (b). The bending is thereby amplified by the propagation of the dipole (c). The arrows represent the propagation velocity of the dipole in the different layers.

inertial range. This is not consistent with the interpretation of a dynamics dominated by waves.

2.6 Dynamics in the limit $F_h \ll 1$, $\mathcal{R} \gg 1 \Rightarrow F_v \sim 1$

In the previous sections, we have given theoretical arguments showing that the scaling $F_v \sim 1$ characterizes the attractor flow when $F_h \ll 1$ and $\mathcal{R} \gg 1$. We now focus on the dynamics in this range of parameters and present results which can be interpreted in the framework of the inviscid strongly stratified scaling introduced by Billant & Chomaz (2001). In this case, the non-linearities are intrinsically three-dimensional.

Waves and potential vorticity strongly interact

Billant & Chomaz (2001) pointed out that in the limit $F_v \sim 1$, waves and PV have equal characteristic times and thus can strongly interact together. It is then not possible to consider separately weakly interacting waves and pancake vortices.

Interpretation of poloidal velocity as waves only is no more valid

When $F_v \sim 1$, the vertical gradients are so large that the toroidal velocity interact fully non-linearly with the poloidal velocity. Both velocity components are of the same order. A part of the poloidal velocity is associated to PV and therefore does not propagate and does not correspond to waves.

Besides, when $F_v \sim 1$, the shear and the gravitational instabilities possibly act. These instabilities are associated to relatively high local vertical (and poloidal) velocity. It has to be pointed out that Kelvin-Helmholtz billows are strongly non-linear structures with relatively high characteristic frequency compared to the local Brunt-Väisälä frequency $N(\mathbf{x})$ (taken into account the total density, i.e. including the density perturbation). Indeed, they develop from a shear flow with a local Richardson number $Ri \sim N(\mathbf{x})^2/|\boldsymbol{\omega}_h|^2 \lesssim 1/4$, and the characteristic horizontal vorticity $\boldsymbol{\omega}_h$ is therefore at least of the order of $N(\mathbf{x})$. But the non-linearities dominate the wavy behavior and these structures can not be considered as weakly non-linear waves. To conclude, firstly, poloidal velocity does not necessary correspond to wave motion only and secondly, poloidal and toroidal velocity strongly interact together.

When $\mathcal{R} > 1$, the scaling $L_v \sim U/N$ applies for turbulence

Waite & Bartello (2004) have performed numerical simulations of strongly stratified turbulence initialized with small random noise and forced with a random vertically invariant vortical forcing. The advantage of such forcing is that it does not contain any characteristic vertical length scale. The vertical structure of the flow emerges only through the flow dynamics. The authors showed that, for the highest Reynolds numbers achieved, the vertical microscale goes like the buoyancy length scale. This result is consistent with earlier studies which also report such behaviour (Riley & de Bruyn Kops, 2003; Godeferd & Staquet, 2003).

Coupling of the horizontal layers and overturnings

Riley & de Bruyn Kops (2003) studied the transition to turbulence from a horizontal Taylor-Green flow with an imposed vertical structure in a stratified fluid. They carried out direct numerical simulations with Newtonian dissipation at relatively high resolution ($512^2 \times 256$) and large Reynolds number. A strong increase of the vertical shear is observed. It is then limited by the coupling between adjacent layers. The Richardson number is shown to be quite small ~ 0.25 and some events of shear instability producing patches of turbulence are observed. This process is associated to a direct cascade and the horizontal spectra tend to show a $k_h^{-5/3}$ inertial range.

Hebert & de Bruyn Kops (2006a) developed the idea proposed by Billant & Chomaz (2001) and Riley & de Bruyn Kops (2003) on a condition for the appearance of small scale turbulence. They showed that the typical Richardson number is simply related to the buoyancy Reynolds number with $Ri^{-1} \sim \mathcal{R}$ and that the condition $\mathcal{R} \gtrsim 1$ can be used *a priori* to predict the development of overturning and small scale turbulence. The turbulent buoyancy Reynolds number $\mathcal{R}^t = \varepsilon/(\nu N^2) = (l_o/\eta)^{4/3}$ and the buoyancy Reynolds number $\mathcal{R}$ are shown to be the same to within a multiplicative constant. With the same simulations, Hebert & de Bruyn Kops (2006b) examined the effect of the increase of the buoyancy Reynolds number on the structure of the dissipation. There is a transition from a strongly anisotropic dissipation at low $\mathcal{R}$ toward a nearly isotropic dissipation at larger $\mathcal{R}$.

Laval, McWilliams, & Dubrulle (2003) carried out forced stratified turbulence simulations using hyperviscosity, anisotropic mesh and moderate resolution ($256^2 \times 128$). Their interpretations and conclusions are very similar to those of Riley & de Bruyn Kops (2003). Moreover, they suggested that the shear instability transfers energy toward a horizontal scale of the order of the buoyancy length scale.

These papers introduce a fundamental result: whatever the importance of the stratification, if the Reynolds number is large enough, the shear grows until the shear instability acts, leading to small scale turbulence. In this interpretation, the shear instability is central (Laval *et al.*, 2003, even if the gravitational instability is also mentioned in).

Secondary instabilities on the zigzag instability

Recently, Deloncle, Billant, & Chomaz (2008) and Waite & Smolarkiewicz (2008) have performed numerical simulations of the non-linear evolution of the zigzag instability of a pair of counter-rotating vertical vortices in a stratified fluid. Both studies report the development of a small scale secondary instability when the vortices are strongly bent if the Reynolds number Re is sufficiently high. However, the two papers provide different explanations for the nature of this secondary instability: it is a shear instability according to Deloncle *et al.* (2008) and a gravitational instability according to Waite & Smolarkiewicz (2008). They also largely disagree about the condition for the onset of the secondary instability: $\mathcal{R} = {ReF_h}^2 > O(1)$ in Deloncle *et al.* (2008) or $ReF_h > 80$ in Waite & Smolarkiewicz (2008). We address and solve this contradiction in the paper of section 3.1.

Strongly stratified forward cascade

Here, we focus on a slightly different approach based on the analysis of the consequences of the inviscid strongly stratified scaling for stratified turbulence. Because the potential enstrophy is non-linear and the convective derivative is fully three dimensional, Lindborg (2002) proposed that strongly stratified turbulence would be a special type of turbulent motion associated to a cascade toward small scales.

This hypothesis has been investigated through a numerical study by Lindborg (2006). The forcing is vortical and vertically invariant in order not to introduce any characteristic vertical length scale. Thin anisotropic boxes with height proportional to the horizontal Froude number were used such as a relatively large but constant number of layers is simulated for all simulations. Thus, one can be confident that the thickness of the boxes does not influence the results as later confirmed by Lindborg & Brethouwer (2007). The numerical mesh is strongly anisotropic ($\Delta x \gg \Delta z$) with an anisotropic hyperviscosity to dissipate along the horizontal direction at scales $\sim \Delta x$ and along the vertical direction at scales $\sim \Delta z$. Thus, these simulations are not DNS and can be considered as highly resolved Large Eddy Simulations (LES with typically $512^2 \times 64$ numerical points), even if the dissipative scheme is much more simple than those currently employed in classical LES. Lindborg (2006) showed that when the Ozmidov length scale is approximately resolved along the vertical direction ($\Delta z \sim 7 l_o$), a strongly stratified forward cascade is obtained with a clear $k_h^{-5/3}$ horizontal spectra. He suggested that this dynamical regime can be the origin of the anisotropic $k_h^{-5/3}$ and $N^2 k_z^{-3}$ spectra observed in nature.

These simulations can be compared to geophysically relevant simulations for which the primitive equations are resolved with strongly anisotropic mesh. The recent global circulation numerical models (GCM) and regional models now resolve the mesoscale range associated to stratified but weakly rotating flows. It is striking to see that these models (e.g. Koshyk & Hamilton, 2001; Skamarock, 2004; Hamilton *et al.*, 2008) are now able to reproduce the global horizontal spectra with both the quasi-geostrophic range and the mesoscale range. But overturning motions in general, and shear instability in particular are not resolved or only poorly resolved because of the strongly anisotropic mesh. Theoretically, it is an indication about the physical mechanisms of the cascade. This tends to show that the shear instability is less fundamental for the strongly stratified forward cascade than expected. Thus, a mechanism different from the shear instability contributes to downscale energy transfer in stratified turbulence (Kitamura & Matsuda, 2010). Lindborg (2006) pointed out the importance of a balanced hydrostatic strongly stratified forward cascade (which does not exclude non-hydrostatic small-scale events).

Theoretical expressions for the spectra are derived via a dimensional analysis under the assumption of strong stratification $F_h \ll 1$. Lindborg (2006) assumed both a forward energy cascade along the horizontal direction (leading to the classical estimate $u(l_h) \sim (\varepsilon l_h)^{1/3}$ by Taylor, 1935) and an approximate equality between potential and kinetic energies $E_P \sim E_K$ (due to the inviscid strongly stratified scaling $F_v \sim 1$). Then, one deduces that the strongly stratified forward cascade is associated to a

$k_h^{-5/3}$ and $N^2 k_z^{-3}$ spectra. Two universal proportionality constants corresponding to the Kolmogorov and Obukhov-Corrsin constants of three-dimensional turbulence have to be introduced to express the spectra as

$$E_K(k_h) = C_1 \varepsilon_K^{2/3} k_h^{-5/3}, \tag{2.18}$$

$$E_P(k_h) = C_2 \varepsilon_K^{2/3} k_h^{-5/3} \frac{\varepsilon_P}{\varepsilon_K}, \tag{2.19}$$

with $C_1 \simeq C_2 \simeq 0.51 \pm 0.02$. Given the dependency in $k_h^{-5/3}$ for both kinetic and potential spectra, the relation $E_P/E_K = \varepsilon_P/\varepsilon_K$ is quite intuitive. It would be therefore astonishing that the two constants C_1 and C_2 were not equal. Later, the value 0.5 has been slightly modified to fit the data from simulations with more numerical points (Lindborg & Brethouwer, 2007, give the value $C_1 = C_2 \simeq 0.47$). Furthermore, it has to be noted that the value $C_1 \simeq 0.5$ is remarkably different from the equivalent Kolmogorov constant for the non-stratified isotropic case, which is approximately equal to 1 (see appendix A.1 for details and references).

The results of Lindborg (2006) have been confirmed and extended by Brethouwer *et al.* (2007) with direct numerical simulations with Navier-Stokes viscosity at high resolution (typically $1024^2 \times 192$). This study investigates the influences of Re and F_h on strongly stratified flows thanks to the scaling analysis already exposed in section 2.2 whose conclusion is that the buoyancy Reynolds number $\mathcal{R} = ReF_h{}^2$ is the main control parameter. The authors pointed out that $\mathcal{R} \gg 1$ is a necessary condition to obtain the strongly stratified turbulent regime. A remarkable difference with the results presented by Lindborg (2006) is the precise shape of horizontal spectra. The spectra from the DNS approximately follow a $k_h^{-5/3}$ scaling law but with a bumpy shape at the highest wave number (a bottleneck, but no hyperviscosity is used). This bump was proposed to be caused by Kelvin-Helmholtz instabilities generating more classical three-dimensional turbulence at small scales.

Degree of universality and waves

Most simulations mentioned in this section are initalized or forced with vortical (toroidal) motions. One may wonder whether the strongly stratified turbulent regime is particular to these flows or whether it is an universal regime. We have already pointed out that in the traditional limit $F_v \ll 1$, waves and PV motions only weakly interact. Thus, the vertical $N^2 k_z^{-3}$ spectra is classically explained via a set of linear or weakly non-linear waves (Dewan, 1997). But when $F_v \sim 1$, waves and PV motions strongly interact. Moreover, horizontal poloidal velocity and toroidal velocity should be of the same order (but poloidal velocity does not only correspond to waves). These results tend to support the universality of strongly stratified turbulence.

Simulations forced with isotropic (i.e. with $k_z = k_h$) large scale waves were carried out by Waite & Bartello (2006a). Their results differ from similar simulations forced with vortical motions presented in Waite & Bartello (2004). In particular, when the flow is forced with waves, the scaling $F_v \sim 1$ is not reached and the $N^2 k_z^{-3}$ spectrum is not reproduced.

Lindborg & Brethouwer (2007) performed a set of simulations forced either with vortical motions, or with waves. The vortically forced runs confirm the results presented in Lindborg (2006). It is shown that the poloidal and toroidal two-dimensional spectra are approximately equal in the inertial range. Furthermore, waves are detected using an appropriate method, still valid for $F_v \sim 1$, based on toroidal, poloidal and potential frequency spectra for particular spectral modes. A wave has a null toroidal spectrum and appears as two equal peaks in the poloidal and potential frequency spectra at the frequency given by the linear dispersion relation. Such peaks are clearly observed at large scales with no corresponding peak in the toroidal spectra. However, there are fewer waves in the inertial range as the cascade goes downscales. In the most dynamically important low-aspect-ratio modes, there are no waves at all and toroidal and poloidal spectra perfectly superimpose. The runs forced with waves are quite different from those presented in Waite & Bartello (2006a). Indeed, the variation of the vertical wavenumber of the forced waves is investigated (giving a constant horizontal wavenumber) and it has been shown to be a crucial parameter. When the forced waves are associated to approximately $F_v \sim 1$, strongly stratified turbulence is obtained with a dynamics very similar to the one of the vortically forced flows. In contrast, no stationary state is reached if the forced waves are associated to very small vertical Froude number.

Both papers (Waite & Bartello, 2006a; Lindborg & Brethouwer, 2007) clearly prove that the dynamics of waves and vortices are very different when $F_v \ll 1$. Through the mechanisms presented in section 2.4, the toroidal motions lead to vertical Froude number of order unity. In contrast, the waves dynamics at $F_v \ll 1$ does not effectively lead to the scaling $F_v \sim 1$. However, if $F_v \sim 1$, waves and vortices strongly interact and the same strongly stratified cascade is obtained for both type of forcing. This universality of the strongly stratified turbulence has important consequences in the geophysical context because in nature, many processes force waves.

Some other issues will be not discussed in details in this indroduction. We just mentioned that it has been demonstrated that the strongly stratified turbulence regime can be obtained with relatively weak rotation (Lindborg, 2005; Waite & Bartello, 2006b). Furthermore, Riley & Lindborg (2008) argued that the strongly stratified turbulent regime could be the basis of a possible interpretation of some geophysical turbulence measurements. The consequences of the strongly stratified turbulence for the mixing have been also investigated by Lindborg & Brethouwer (2008). They show that the strongly stratified turbulence gives some theoretical basis to the classical Osborn & Cox (1972) model for vertical diffusion with an effective diffusivity $D = \varepsilon_P/N^2$. The predictions of the model have been verified and their consequences have been investigated recently (Brethouwer & Lindborg, 2008, 2009; Lindborg & Fedina, 2009). As a matter of fact, for vertical length scale much larger than the buoyancy length scale, the effect of mixing through stratified turbulence could be modeled with a simple diffusion model. Finally, Diamessis *et al.* (2011) have recently carried out simulations of the wake of a sphere in stratified fluid at resolution sufficient to show clear departure from what was classically observed in late wake dominated by vertical dissipation. The dynamics at vertical Froude number of order unity and the strongly stratified forward cascade also apply in the old problem of the wake decay.

2.7 Scientific issues and objectives

The global presentation given in this chapter has raised several important issues for the study of stratified turbulence which will be considered in the following:

- We have seen that there is a controversy about secondary instabilities for coherent structures as pancake dipole and their thresholds. We elucidate this contradiction in section 3.1. Besides, we do not know what happens in the corotating case (see chapter 6).
- We have seen that the strongly stratified turbulent regime (or even shear instability in stratified turbulence as observed in the numerical simulations of Riley & de Bruyn Kops, 2003) has never been obtained in a laboratory experiment. A new experiment of forced stratified disordered flows presented in section 4.1 exhibits such events.
- Both Ozmidov length scale and buoyancy length scale have been presented as the larger scale at which overturning could happen. However, they are distinct physical scales with $l_o/L_b \sim {F_h}^{1/2}$ (Waite, 2011). This issue is discussed in sections 3.2 and 4.2.
- Both shear and gravitational instabilities generate non-local transfers in the spectral space. We do not know the relative importance of these transfers compared to local transfers. It is not clear at which scales they occurs (buoyancy length scale, Ozmidov length scale or diffusive length scale). Sections 3.2 and 4.2 address this issue.
- Some results have been interpreted with a forward cascade involving hydrostatic structures. However, we do not know the detailed mechanisms of this special type of cascade. The dynamics of forced strongly stratified turbulence is discussed in section 4.2.
- We have listed some mechanisms of vertical decorrelation and of length scale selection. Nevertheless, the balance between these different mechanisms is still unclear. An appendix of section 4.2 addresses this issue.
- In chapter 1, we have stressed the importance of the 4/5s law for isotropic homogeneous turbulence. But there is no counterpart law known for strongly stratified turbulence. Such law is derived for this anisotropic turbulent regime in chapter 5.

Chapter 3

About the secondary instabilities on the zigzag instability

3.1 Onset of secondary instabilities

Onset of secondary instabilities on the zigzag instability in stratified fluids

Pierre Augier and Paul Billant
LadHyX, CNRS, École Polytechnique, 91128 Palaiseau Cedex, France

Published in J. Fluid Mech. (2011), **662**, 120-131.

Recently, Deloncle, Billant, & Chomaz (2008) and Waite & Smolarkiewicz (2008) have performed numerical simulations of the nonlinear evolution of the zigzag instability of a pair of counter-rotating vertical vortices in a stratified fluid. Both studies report the development of a small scale secondary instability when the vortices are strongly bent if the Reynolds number Re is sufficiently high. However, the two papers are at variance about the nature of this secondary instability: it is a shear instability according to Deloncle *et al.* (2008) and a gravitational instability according to Waite & Smolarkiewicz (2008). They also profoundly disagree about the condition for the onset of the secondary instability: $ReF_h{}^2 > O(1)$ in Deloncle *et al.* (2008) or $ReF_h > 80$ in Waite & Smolarkiewicz (2008), where F_h is the horizontal Froude number.

In order to understand the origin of these discrepancies, we have carried out Direct Numerical Simulations of the zigzag instability of a Lamb-Chaplygin vortex pair for a wide range of Reynolds and Froude numbers. The threshold for the onset of a secondary instability is found to be $ReF_h{}^2 \simeq 4$ for $Re \gtrsim 3000$ and $ReF_h = 80$ for $Re \lesssim 1000$ in agreement with both previous studies. We show that the scaling analysis of Deloncle *et al.* (2008) can be refined to obtain a universal threshold: $(Re - Re_0)F_h{}^2 \simeq 4$, with $Re_0 \simeq 400$, which works for all Re. Two different regimes for the secondary instabilities are observed: when $(Re-Re_0)F_h{}^2 \gtrsim 4$ only the shear instability develops while when $(Re - Re_0)F_h{}^2 \gg 4$, both shear and gravitational instabilities appear almost simultaneously in distinct regions of the vortices. However, the shear instability seems to play a dominant role in the breakdown into small scales in the range of parameters investigated.

3.1.1 Introduction

Strongly stratified flows are anisotropic and generally exhibit a layered structure (Riley & Lelong, 2000). Layers can arise spontaneously through an instability, the zigzag instability, when several vertical vortices are interacting. This has been shown in the cases of pairs of counter- or co-rotating vortices (Billant & Chomaz, 2000a; Otheguy, Chomaz, & Billant, 2006b) and vortex arrays (Deloncle, Billant, & Chomaz, 2011). The study of such elementary flows is convenient to identify and understand some of the fundamental mechanisms at work in more complicated flows such as stratified turbulence.

The zigzag instability exists for low horizontal Froude number $F_h = U/(Na)$, where U is the typical horizontal velocity of the vortices, a the vortex radius and N

the Brunt-Väisälä frequency. Its originates from the coupling between vortex bending waves and the strain exerted by companion vortices [Otheguy, Billant, & Chomaz (2007); Billant (2010); Billant *et al.* (2010)]. The instability bends the vortices with a growth rate scaling like the strain and a vertical wavelength scaling like $L_b b/a$, where $L_b = U/N$ is the buoyancy length and b the vortex separation distance.

In the laboratory, the zigzag instability of a counter-rotating vortex pair has been observed to grow to a very large amplitude producing high vertical shear and leading to the formation of thin but laminar layers (Billant & Chomaz, 2000a). Recently, Deloncle *et al.* (2008) and Waite & Smolarkiewicz (2008) have carried out numerical simulations of the nonlinear evolution of the zigzag instability at higher Reynolds number $Re = Ua/\nu$ (where ν is the viscosity) than in the laboratory. They have both observed that small scales develop leading to a transition to turbulence when the zigzag instability is fully developed and the Reynolds number sufficiently large.

Deloncle *et al.* (2008) attributed this breakdown into small scales to the onset of the Kelvin-Helmholtz instability by showing that it develops in regions where the Richardson number becomes lower than 1/4. In contrast, Waite & Smolarkiewicz (2008) have shown that small scales emerge when density perturbations generated by the zigzag instability become gravitationally unstable.

In addition to this difference of interpretation about the nature of the secondary instabilities, Deloncle *et al.* (2008) and Waite & Smolarkiewicz (2008) also disagree about the threshold for their onsets. Deloncle *et al.* (2008) have shown that the exponential growth of the zigzag instability is not saturated by nonlinear effects but by viscous effects due to the vertical shear when there is no secondary instability. This occurs when the vertical length scale L_v has decreased down to the viscous length scale $L_v \sim a/\sqrt{Re}$. At that time, the Richardson number is $Ri \simeq N^2/|\partial \mathbf{u}_h/\partial z|^2 \propto N^2 L_v^2/U^2 \propto 1/({ReF_h}^2)$, where $\partial \mathbf{u}_h/\partial z$ is the vertical gradient of horizontal velocity. Therefore, when ${ReF_h}^2$ is large, the Richardson number can be lower than 1/4 before viscous saturation of the zigzag instability. Deloncle *et al.* (2008) have shown that this criterion predicts well the occurence of the shear instability in their simulations. In contrast, Waite & Smolarkiewicz (2008) reported that the gravitational instability occurs when $ReF_h > 80$. However, this threshold is empirical and no theoretical justification has been provided by Waite & Smolarkiewicz (2008).

Deloncle *et al.* (2008) and Waite & Smolarkiewicz (2008) have speculated that the discrepancies between their conclusions might come from the different initial conditions: Waite & Smolarkiewicz (2008) used a Lamb-Chaplygin vortex pair while Deloncle *et al.* (2008) used a pair of counter-rotating gaussian vortices with a separation distance $b = 2.5a$. In order to check this hypothesis, we have reconsidered the problem and performed DNS of a Lamb-Chaplygin vortex pair for a wide range of Reynolds number Re and Froude number F_h.

3.1.2 Numerical method and initial conditions

The numerical procedure is the same as in Deloncle *et al.* (2008) except that the vortex pair consists of a Lamb-Chaplygin dipole instead of a pair of adapted counter-rotating Lamb-Oseen vortices. The incompressible Navier Stokes equations under

the Boussinesq approximation are solved by means of a pseudo-spectral method with periodic boundary conditions (see Deloncle *et al.* (2008) for details). The velocity field $\mathbf{u}$ and the density perturbation ρ' are initialized as:

$$[\mathbf{u},\ \rho'](x,y,z,t=0) = [\mathbf{u_{2D}}(x,y),\ 0] + \varepsilon\cos(2\pi z/\lambda_z)[\mathbf{u_p},\ \rho'_p](x,y) \tag{3.1}$$

where $(x,\ y,\ z)$ are Cartesian coordinates with z along the vertical, $\mathbf{u_{2D}}$ is the velocity field of a Lamb-Chaplygin dipole in the co-moving frame like in Waite & Smolarkiewicz (2008). This dipole is a steady solution of the Euler equation given by $\mathbf{u_{2D}} = -\boldsymbol{\nabla}\times\psi_0\mathbf{e_z}$, with

$$\psi_0(r,\theta) \equiv \begin{cases} \dfrac{2UR}{\mu_1 J_0(\mu_1)} J_1(\mu_1 r/R)\cos\theta & \text{if } r < R, \\ \\ Ur\left(1-\dfrac{R^2}{r^2}\right)\cos\theta & \text{if } r \geqslant R, \end{cases} \tag{3.2}$$

where (r,θ) are cylindrical coordinates with $(x = r\cos\theta,\ y = r\sin\theta)$, U the velocity of propagation in the laboratory frame, R the dipole radius, J_0 and J_1 are the zeroth- and first-order Bessel functions and $\mu_1 \simeq 3.8317$ is the first root of J_1.

The second term in the right-hand side of (3.1) is a small perturbation with $[\mathbf{u_p},\ \rho'_p]$ the most unstable eigenmode of $\mathbf{u_{2D}}$ determined by a numerical linear stability analysis, λ_z its vertical wavelength and ε a small amplitude.

The Reynolds number Re and the Froude number F_h are based on the initial conditions: $Re = UR/\nu, F_h = U/(NR)$, where ν is the kinematic viscosity and $N = \sqrt{-(g/\rho_0)(d\bar{\rho}/dz)}$ the Brunt-Väisälä frequency (assumed constant), where g is the gravity, ρ_0 a reference density and $\bar{\rho}(z)$ the basic density profile. The total density is given by $\rho_{tot} = \rho_0 + \bar{\rho}(z) + \rho'$. The Schmidt number $Sc = \nu/D$, where D is the mass diffusivity, is set to unity in all runs. For simplicity and without loss of generality, R and R/U are taken respectively as length and time units, i.e. are fixed to unity. The density perturbations are non-dimensionalized by $R|d\bar{\rho}/dz|$. The same symbols are kept for the non-dimensional variables.

The parameters of the main runs are summarized in table 3.1. The value of the Froude number is kept below the threshold $F_h = 0.2$ where the zigzag instability is dominant in the case of the Lamb-Chaplygin dipole (Billant & Chomaz, 2000c). For each Froude number investigated, only the runs with the highest and lowest Reynolds numbers are listed in table 3.1. For the runs with intermediate values of Re, the resolution and time step have been chosen between these two limiting cases. The height of the computational domain is set to the most amplified wavelength of the zigzag instability $\mathcal{L}_z = \lambda_z$. The horizontal size of the box $\mathcal{L}_x = \mathcal{L}_y = 10R$ is taken sufficiently large compared to the dipole radius R in order to have negligible effects of the periodic boundary conditions. Several additional runs have been performed with different domain size and numerical resolution in order to check the accuracy and convergence of the results presented.

Run	F_h	Re	$\mathcal{R} = ReF_h{}^2$	$\mathcal{L}_x \times \mathcal{L}_y \times \mathcal{L}_z$	$N_x \times N_y \times N_z$	δt
Fh0.15Re500	0.15	400	9	$10 \times 10 \times 1.5$	$256 \times 256 \times 64$	0.01
Fh0.15Re1000	0.15	1000	22.5	$10 \times 10 \times 1.5$	$256 \times 256 \times 64$	0.01
Fh0.1Re600	0.1	600	6	$10 \times 10 \times 1.0$	$256 \times 256 \times 64$	0.01
Fh0.1Re2500	0.1	2500	25	$10 \times 10 \times 1.0$	$512 \times 512 \times 96$	0.005
Fh0.05Re1500	0.05	1500	3.75	$10 \times 10 \times 0.5$	$384 \times 384 \times 64$	0.006
Fh0.05Re4000	0.05	4000	10	$10 \times 10 \times 0.5$	$768 \times 768 \times 96$	0.003
Fh0.03Re4500	0.03	4500	4.05	$10 \times 10 \times 0.3$	$768 \times 768 \times 96$	0.003
Fh0.03Re6000	0.03	6000	5.4	$10 \times 10 \times 0.3$	$768 \times 768 \times 96$	0.003

Table 3.1: Overview of the physical and numerical parameters of the simulations with highest and lowest Re for each F_h. The number of nodes in the x-, y- and z-direction are denoted, respectively, N_x, N_y and N_z. The time step is δt. We recall that the length and time units are R and R/U respectively.

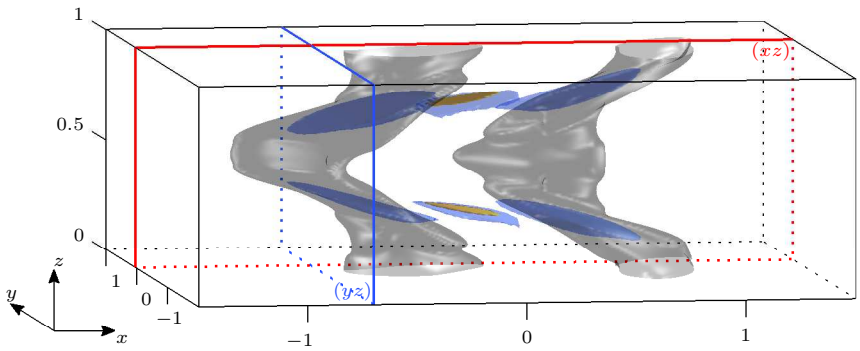

Figure 3.1: Three-dimensional contours of the vertical vorticity of the dipole for $F_h = 0.1$ and $Re = 2500$ at time $t = 3.8$. The grey surfaces are iso-surfaces of vertical vorticity $|\omega_z| = 0.7 \max(\omega_z)$. The blue surfaces correspond to iso-values of the Richardson number equal to $1/4$ (indication of the possibility of shear instability) and the orange surfaces correspond to iso-values $\partial \rho_{tot}/\partial z = 0$ (instability condition for the gravitational instability). The red and blue lines indicate the position of the vertical cross-sections (xz) and (yz) displayed in figure 3.2(ab).

3.1.3 Description to the transition to small scales

We first describe a simulation for $F_h = 0.1$ and $Re = 2500$ for which the nonlinear evolution of the zigzag instability leads to a transition to small scales. Since the development of the zigzag instability has been already described in details by Waite & Smolarkiewicz (2008) and Deloncle *et al.* (2008), we start our description at the time where the zigzag instability is mature and the transition to small scales is incipient. Our main purpose is to determine the nature of the underlying secondary instabilities.

Figure 3.1 displays in grey the iso-surfaces of vertical vorticity at $t = 3.8$. As can be seen, the zigzag instability has reached a finite amplitude and the vortices are fully bent but small scales have not yet developed. Even if the growth of the zigzag

instability is still exponential at that time, the bending deformation of the vortices is no longer purely sinusoidal: one can see that the vortices tend to be vertically aligned at the extrema of the bending deformation, i.e. at $z = 0$ and $z = 0.5$, while in between the vortices tend to be more inclined than for a pure sinusoid. In order to identify regions susceptible to the shear instability, we have plotted in blue the isosurfaces where the local Richardson number

$$Ri = \frac{-\partial\rho_{tot}/\partial z}{{F_h}^2|\partial \mathbf{u}_h/\partial z|^2} \tag{3.3}$$

is equal to $1/4$, where $\partial\rho_{tot}/\partial z$ is the non-dimensional vertical gradient of total density, i.e. $\partial\rho_{tot}/\partial z = -1 + \partial\rho'/\partial z$. The condition $Ri < 1/4$ somewhere in the flow is a necessary but not sufficient condition for the shear instability of a steady parallel inviscid shear flow (Miles, 1961; Howard, 1961). It is therefore not rigorously applicable to the present flow but we expect that the application of this condition will be meaningful if the flow is sufficiently parallel and evolves sufficiently slowly compared, respectively, to the characteristic length scale and time scale of the shear instability. As seen in figure 3.1, there are six distinct regions where $Ri < 1/4$. Four of these regions are located close to the iso-vorticity surfaces, i.e. inside the vortex cores at the vertical levels where they are most slanted. The two other regions are located approximately at the same vertical levels but right in the middle between the two vortex cores. Quite strikingly, an orange surface, corresponding to the isovalue $Ri = 0$, is embedded within each of the two latter regions. This means that the vertical gradient of the total density is positive inside these regions so that they are prone to a convective instability. Interestingly, the conditions for the shear and gravitational instabilities can be also satisfied simultaneously for inertia-gravity waves (see for example Fritts & Alexander, 2003; Lelong & Dunkerton, 1998b). However, we emphasize that here these two conditions are fulfilled for distinct physical reasons: the regions where $0 < Ri < 1/4$ appear in the vortex cores because the bending of the vortices enhances the vertical shear (Deloncle *et al.*, 2008). In contrast, the regions where $Ri < 0$ (connected to small regions where $Ri < 1/4$) appear because the bending of the low-pressure vortex cores produce high vertical pressure gradient and so high density perturbations by hydrostatic balance (Waite & Smolarkiewicz, 2008).

The precise position of these regions can be seen more clearly in figures 3.2(a) and 3.2(b) which show the color contours of the Richardson number in the vertical cross-sections yz and xz indicated respectively in blue and red in figure 3.1. These figures show also the contours of total density. The subsequent time evolution of these quantities is shown in figures 3.2(c-j). Note that the y position of the xz cross-sections (figure 3.2$bdfhj$) is displaced with time in order to always cut through the mean position of the two vortex centres. At $t = 4.4$ (figure 3.2cd), we see that the regions where $0 < Ri < 1/4$ and $Ri < 0$ have widened and intensified but no secondary instability is yet visible. At $t = 5$ (figure 3.2ef), Kelvin-Helmholtz rolls are clearly formed in the regions where $0 < Ri < 1/4$. These rolls can be seen in both yz and xz cross-sections because they are oblique with respect to the x direction as observed by Deloncle *et al.* (2008). This creates gravitationally unstable regions as seen by the yellow contours. We stress that the billows in the xz cross-section (figure 3.2f)

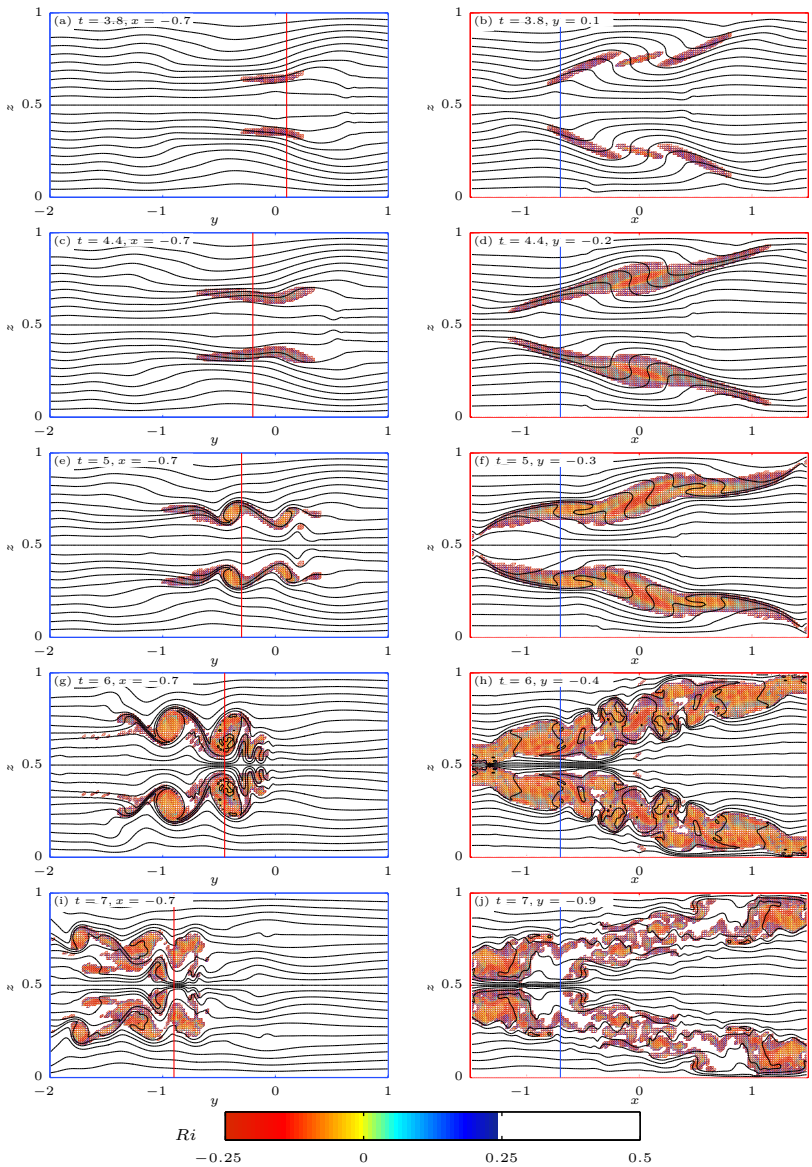

Figure 3.2: Time evolution of the total density in the vertical cross-sections yz (a, c, e, g, i) and xz (b, d, f, h, j) indicated in blue and red, respectively, in figure 3.1. The colour contours indicate the Richardson number where $Ri < 1/4$. The red vertical lines indicate the location of the xz cross-sections. Conversely, the blue vertical lines indicate the location of the yz cross-sections. The contour interval of total density is equal to $1/22$. A movie is available with the electronic version of the paper.

develop in the regions where the condition $Ri < 1/4$ is satisfied because the shear is enhanced and not because the vertical gradient of the total density decreases. In contrast, the overturning of the isopycnals is steeper in the regions where $Ri < 0$ (red regions, figure 3.2*f*) but no instability is yet apparent there. At $t = 6$, the Kelvin-Helmholtz billows have grown up to a large size (figure 3.2*g*). In the xz cross-section (figure 3.2*h*), there is an abrupt breakdown into small scales leading to large areas of mixed fluid (figure 3.2*j*) as described by Waite & Smolarkiewicz (2008). However, this breakdown occurs everywhere in the regions where the Richardson number was below 1/4 not only where $Ri < 0$. In addition, the shear instability develops faster and over a wider region than the gravitational instability. Thus, the breakdown seems mostly due to the Kelvin-Helmholtz instability and not due solely to the gravitational instability as argued by Waite & Smolarkiewicz (2008). It is likely that there is a coupling between the two instabilities since they develop in neighbouring regions. In particular, the perturbations generated by the shear instability may trigger the gravitational instability. The shear present in the statically unstable regions may also affect the gravitational instability (see Fritts & Alexander, 2003).

Figure 3.3 shows similar time series as figure 3.2 but for a lower Reynolds number $Re = 1000$. For such intermediate values of Re, we have observed another scenario where only the shear instability operates. Indeed, figures 3.3(*abcd*) are very similar to the corresponding figures 3.2(*abef*) except that the Kelvin-Helmholtz billows are less intense. A rolling-up of the isopycnals is also visible in the xz cross-section (figure 3.3*d*) but this occurs in the regions unstable to the shear instability (blue regions at $t = 5$, figure 3.3*b*). In contrast, the size of the gravitationally unstable regions (red) near $x = 0$ decreases with time after $t = 6.5$ (figures 3.3*dfh*) without any development of the gravitational instability. Note that the other red regions which appear at $t = 6.5$ in figures 3.3(*dfh*) are due to the overturnings created by the Kelvin-Helmholtz billows. The gravitational instability does not develop probably because its growth rate is not sufficiently high compared to the characteristic time scale of the zigzag instability or compared to the diffusive time scale.

When the Reynolds number is close to the threshold for the onset of secondary instabilities, the minimum Richardson number still drops below 1/4 for a short time period but the shear instability does not appear. It is likely that the growth rate of the shear instability is then too small for the instability to develop over this time period.

3.1.4 Flow regimes in the parameter space $[Re, F_h]$

Figure 3.4 summarizes all the different runs in the parameter space $[Re, F_h]$. As already mentioned, only the range $F_h < 0.2$ has been explored since the zigzag instability is most unstable only in this range in the case of the Lamb-Chaplygin vortex pair (Billant & Chomaz, 2000c). The different symbols distinguish the simulations with gravitational and shear instabilities ($*$), from those with only the shear instability ($\times$) and those with no secondary instability ($\circ$). The triangle symbols ($\triangle$) indicate an intermediate case for which undulations of the isopycnals are observed but Kelvin-Helmholtz rolls do not really develop.

The red dashed line shows the threshold $ReF_h{}^2 = \mathcal{R}_c$ derived by Deloncle *et al.*

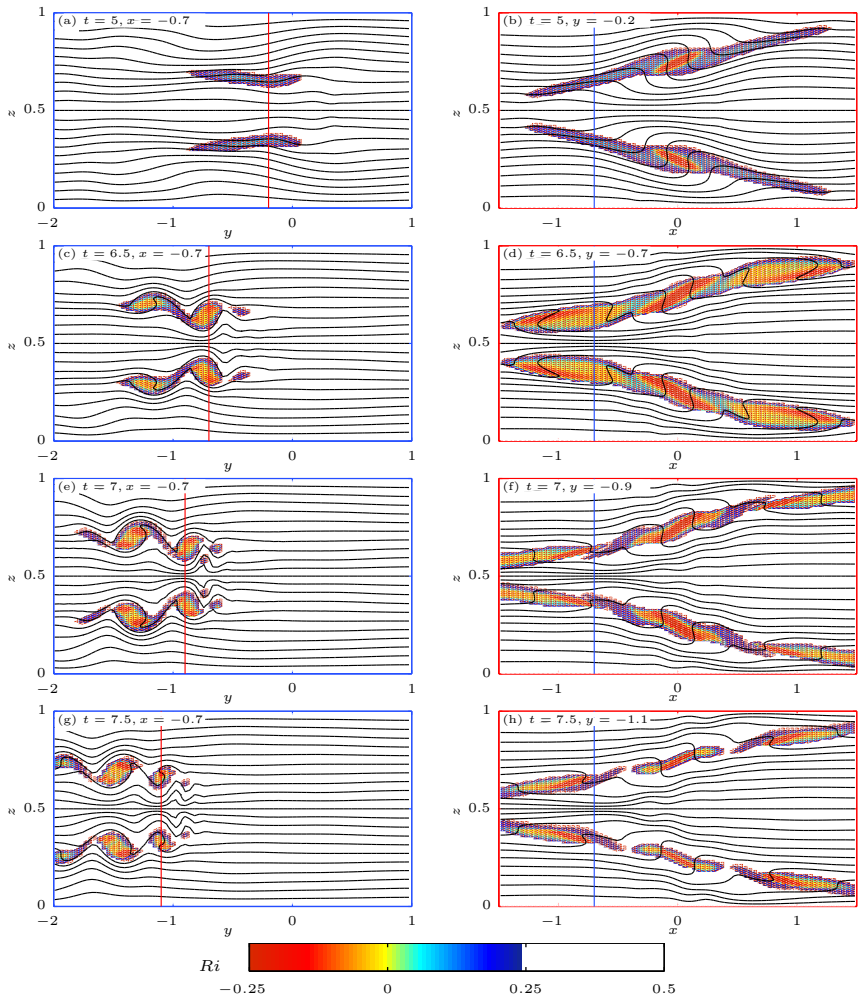

Figure 3.3: Same as in figure 3.2 but for $Re = 1000$. A movie is available with the electronic version of the paper.

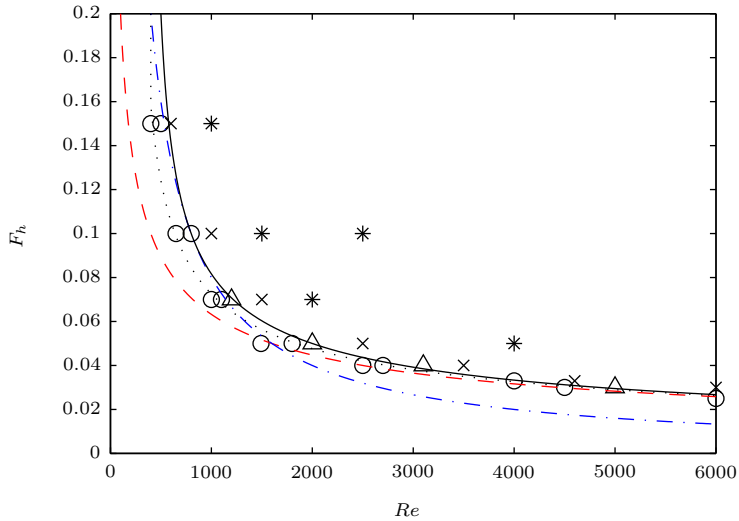

Figure 3.4: Summary of all the runs in the parameter space $[Re, F_h]$. The asterisks indicate runs in which both Kelvin-Helmholtz and gravitational instabilities are observed. The crosses correspond to runs where Kelvin-Helmholtz rolls are observed but no gravitational instability is observed. Triangles are intermediate cases for which the shear instability creates undulations but roll-up does not fully develop. The circles denote the runs where no secondary instability is observed. The blue dashed dotted and red dashed lines corresponds respectively to the criterion $ReF_h = 80$ and $ReF_h{}^2 = \mathcal{R}_c$, with $\mathcal{R}_c = 4$. The black solid and dotted lines correspond to the criterion $(Re - Re_0)F_h{}^2 = \mathcal{R}_c$, with respectively $Re_0 = 400$ and $Re_0 = 240$.

(2008) for the onset of the shear instability. Note that the critical value $\mathcal{R}_c$ depends on the properties of the vortex pair and has been empirically found to be $\mathcal{R}_c \simeq 4$ in the present case. The alternative threshold $ReF_h = 80$ proposed by Waite & Smolarkiewicz (2008) is indicated by the blue dashed dotted line. We can see that the threshold proposed by Deloncle *et al.* (2008) works well for large Reynolds number $Re \gtrsim 3000$ but not below. Alternatively, the threshold proposed by Waite & Smolarkiewicz (2008) is in good agreement for $Re \lesssim 1000$ but departs from the observations for larger Re. The black line shows the threshold $(Re - Re_0)F_h{}^2 = \mathcal{R}_c$, with $Re_0 = 400$, which works remarkably well for any Reynolds number. In particular, it is as good as the threshold $ReF_h = 80$ for $Re \lesssim 1000$, even if it has not the same functional dependence with F_h.

This universal threshold can be justified by refining the analysis of Deloncle *et al.* (2008). These authors observed that the zigzag instability causes an exponential growth of the total horizontal enstrophy per unit of vertical wavelength: $Z_h = (1/\mathcal{L}_z)\int_{\mathcal{V}} d\mathcal{V}|\boldsymbol{\omega}_h|^2/2$, where $\boldsymbol{\omega}_h$ is the horizontal vorticity. This growth saturates only when Z_h is of the order of the Reynolds number, i.e. $Z_{hmax} \propto Re$. Since

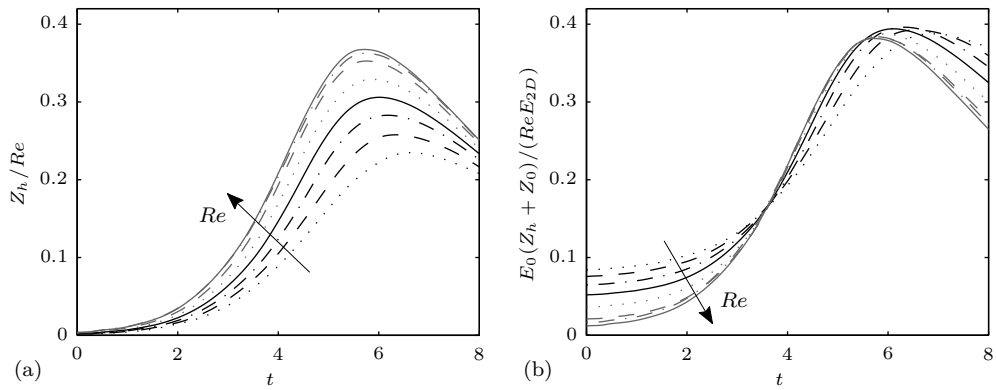

Figure 3.5: Time evolution of (a) the horizontal enstrophy Z_h rescaled by Re and of (b) the quantity $(Z_h(t) + Z_0)/Re\ E_0/E_{2D}(t)$ for different Froude and Reynolds numbers: ($Re = 600$, $F_h = 0.14$, black dotted line), ($Re = 670$, $F_h = 0.12$, black dashed line), ($Re = 790$, $F_h = 0.10$, black dashed dotted line), ($Re = 1000$, $F_h = 0.08$, black solid line), ($Re = 1480$, $F_h = 0.06$, grey dotted line), ($Re = 2800$, $F_h = 0.04$, grey dashed line), ($Re = 4000$, $F_h = 0.03$, grey dashed dotted line) and ($Re = 6000$, $F_h = 0.025$, grey solid line).

the flow is strongly stratified, the vertical velocity is small and vertical gradients are large so that the horizontal enstrophy Z_h is a direct measure of the mean vertical shear of the horizontal velocity, i.e. $Z_h \simeq (1/\mathcal{L}_z)\int_{\mathcal{V}} d\mathcal{V}|\partial \mathbf{u}_h/\partial z|^2/2$. Thus, by assuming that the maximum local shear is proportional to the mean shear, Deloncle *et al.* (2008) obtained the following estimate for the minimum Richardson number: $Ri_{min} \simeq 1/[F_h^2 \max(|\partial \mathbf{u}_h/\partial z|^2)] \propto 1/[F_h^2 Re]$. Hence, the condition for the shear instability, i.e. $Ri < 1/4$, is equivalent to $ReF_h^2 > \mathcal{R}_c$.

The scaling law $Z_{hmax} \propto Re$ is at the heart of this reasoning. In order to check its validity, we have plotted in figure 3.5(a) the horizontal enstrophy Z_h scaled by the Reynolds number for several simulations covering a wide range of parameters: $0.025 < F_h < 0.16$ and $600 < Re < 6000$. Note that these runs are all below the threshold for the onset of secondary instabilities in order that the development of small scales, which tends to be less affected by the stratification and thus more isotropic, do not introduce any bias on the maximum of the horizontal enstrophy. We see in figure 3.5(a) that all the curves of Z_h/Re collapse remarkably well when the Reynolds number is large: $Re \gtrsim 2800$. However, when the Reynolds numbers is moderate: $Re \lesssim 1500$, there is a significant decrease of Z_{hmax}/Re when Re decreases and the collapse deteriorates.

In order to understand this discrepancy, it is interesting to consider the equation for the total energy per unit of vertical length in non-dimensional form following Deloncle *et al.* (2008):

$$\frac{dE}{dt} = -2\frac{Z}{Re} - \frac{1}{ReSc}\frac{\int_{\mathcal{V}} d\mathcal{V}|\boldsymbol{\nabla}\rho'|^2}{{F_h}^2\mathcal{L}_z} \tag{3.4}$$

The potential energy dissipation (last term in the right-hand side) remains small in all cases (less than 10 % of the total dissipation) so that it can be neglected as a first approximation. The equation (3.4) shows that viscous effects (first term in the right-hand side) will be able to dissipate the energy, i.e. to saturate the development of the zigzag instability, when the total enstrophy is of the order of the Reynolds number: $Z_{max} = Z_{hmax} + Z_{vmax} = CRe$, where C is a constant of order unity. Since the vertical enstrophy Z_v is observed to decrease from its initial value (which is of order unity by virtue of the non-dimensionalisation), this implies $Z_{hmax} \sim CRe$ when $Re \gg 1$ (Deloncle *et al.*, 2008). However, for moderate Reynolds number, the accuracy of this approximation is no longer ensured since Z_{hmax} is no longer very large compared to Z_{vmax}. A better estimate is therefore $Z_{hmax} \sim CRe - Z_0$ where the vertical enstrophy has been assumed to be approximately constant: $Z_{vmax} \sim Z_0$.

In addition, one has to remark that the equation (3.4) is non-dimensionalized based on the initial velocity U and radius R of the dipole. Thus, the relation $Z_{max}/Re = C$ implicitly assumes that the energy of the dipole $E(t_{max})$ at the time t_{max} of the enstrophy peak, is approximately the same as at $t = 0$: $E(t_{max}) \sim E_0$. Again, this assumption is valid for large Reynolds number but is more questionable at moderate Reynolds number. The energy of the dipole indeed significantly decays owing to two-dimensional viscous diffusion before the zigzag instability has reached a finite amplitude. This effect can be taken into account by considering the energy $E_{2D}(t_{max})$ that the dipole would have at t_{max} if the dynamics were purely two-dimensional. This energy can be estimated by $E_{2D}(t) \simeq E_0 - 2(Z_0/Re)t$ since the enstrophy Z_0 remains almost constant for 2D flows.

All together, we see that the relation $Z_{hmax} = CRe$ for $Re \gg 1$ should become for moderate Reynolds number:

$$Z_{hmax} + Z_0 = CReE_{2D}(t_{max})/E_0 \tag{3.5}$$

where the right-hand side has been normalised by E_0 in order to be consistent with the relation for $Re \gg 1$. In order to test the validity of this scaling law, we show in figure 3.5(b) the quantity

$$\frac{Z_h(t) + Z_0}{Re} \frac{E_0}{E_0 - 2(Z_0/Re)t} \tag{3.6}$$

for the same set of Froude and Reynolds numbers as in figure 3.5a. We see that the maxima of each curve are now almost equal confirming the above reasoning.

Using the relation (3.5) and the assumption $\max(|\partial \mathbf{u}_h/\partial z|^2) \propto Z_{hmax}$, it is now a simple matter to deduce that the minimum Richardson number scales like $Ri_{min} = 1/[F_h^2 \max(|\partial \mathbf{u}_h/\partial z|^2)] \propto 1/[F_h^2(Re - Re_0)]$ where $Re_0 = 2Z_0 t_{max}/E_0 + Z_0/C$ is approximately a constant since t_{max} is almost independent of Re. For the Lamb-Chaplygin dipole (3.2) in the computational box, we have $Z_0 \simeq 46.1$ and $E_0 \simeq 5.5$. Using these values and the empirical values of $C \simeq 0.38$ and $t_{max} \simeq 7$ obtained from figure 3.5(b), we obtain $Re_0' \simeq 240$. In figure 3.4, we see that the criterion $(Re - Re_0')F_h^2 = \mathcal{R}_c$ (dotted line) is in better agreement with the data for low Re than the threshold $ReF_h^2 = \mathcal{R}_c$. However, an even better agreement can be obtained by using the empirical value $Re_0 = 400$ shown by the black line in figure 3.4.

In summary, the constant Re_0 takes in account two features which were neglected in the analysis of Deloncle *et al.* (2008): the viscous dissipation of the base flow and the fact that the vertical enstrophy is actually not so small compared to the maximum horizontal enstrophy when the Reynolds number is moderate.

3.1.5 Conclusion

We have performed direct numerical simulations of the nonlinear development of the zigzag instability of a Lamb-Chaplygin dipole for a large range of Reynolds numbers Re and Froude numbers F_h in order to understand the discrepancies between the previous studies of Deloncle *et al.* (2008) and Waite & Smolarkiewicz (2008).

Secondary instabilities produce a transition to small-scales when $(Re - Re_0){F_h}^2 \geqslant \mathcal{R}_c$, where $Re_0 \simeq 400$ and $\mathcal{R}_c \simeq 4$. This threshold, which has been obtained by refining the analysis of Deloncle *et al.* (2008), is valid for any Reynolds number. It agrees with the threshold derived by Deloncle *et al.* (2008) for large Reynolds number and with the one of Waite & Smolarkiewicz (2008) for moderate Reynolds number. Just above the threshold, a shear instability develops in the most bent region of the vortex cores. Further above the threshold, there are simultaneously two types of secondary instabilities: the shear instability mentioned above and a gravitational instability which develops in the middle between the two vortices. However, the shear instability develops faster and seems to play a dominant role in the transition to small scales in all the simulations that have been performed. Our study therefore clarifies and reconciles the different results reported by Deloncle *et al.* (2008) and Waite & Smolarkiewicz (2008). Some further simulations have been carried out in the case of two counter-rotating Lamb-Oseen vortices like in Deloncle *et al.* (2008). They agree qualitatively with the present conclusions and are therefore not shown.

The transition to small scales has important implications for our understanding of stratified turbulence. As pointed out by Deloncle *et al.* (2008), the shear instability generates small billows whose size L_{KH} scales like the buoyancy length scale $L_b = U/N$. There is therefore a direct transfer from the large scales to a small horizontal scale L_{KH} instead of a local cascade. Deloncle *et al.* (2008) associated L_{KH} to the Ozmidov length scale $l_o = \sqrt{\varepsilon/N^3}$, where ε is the mean kinetic dissipation rate per unit mass, because the corresponding Froude number is unity if the typical velocity of the billows is assumed to be U, i.e. the same as the velocity of the large scale vortices. However, it would be more appropriate to call this length scale the buoyancy length scale. As shown recently by Waite (2011), the Ozmidov and buoyancy length scales are indeed distinct physical scales even if they both correspond to a Froude number of order unity. As a final point, it would be interesting to study also the scale selected by the gravitational instability and its implications for stratified turbulence.

We would like to thank A. Deloncle for his invaluable help with the numerical code, D. Guy for technical assistance and the referees for their helpful comments and suggestions. This work is supported by IDRIS (CNRS) for computational facilities under project No. 61722.

About the secondary instabilities on the zigzag instability

3.2 Spectral analysis of the transition to turbulence

Spectral analysis of the transition to turbulence from a dipole in stratified fluids

Pierre Augier, Jean-Marc Chomaz and Paul Billant
LadHyX, CNRS, École Polytechnique, 91128 Palaiseau Cedex, France

In preparation for submission to *J. Fluid Mech.*

We investigate the spectral properties of the turbulence generated during the nonlinear evolution of a Lamb-Chaplygin dipole in a stratified fluid for a high Reynolds number $Re = 28000$ and a wide range of horizontal Froude number $F_h \in [0.0225\ 0.135]$ and buoyancy Reynolds number $\mathcal{R} = ReF_h{}^2 \in [14\ 510]$. The simulations are quasi-DNS with weak hyperviscosity. After the nonlinear development of the zigzag instability, both shear and gravitational instabilities develop and lead to the transition to small scales. A spectral analysis shows that this transition is dominated by two kinds of transfers: first, the shear instability induces a direct non-local transfer toward horizontal wavelength of the order of the buoyancy scale $L_b = U/N$, where U is the characteristic horizontal velocity of the dipole and N the Brunt-Väisälä frequency; Second, the destabilization of the Kelvin-Helmholtz billows and the gravitational instability lead to small-scale weakly stratified turbulence. Horizontal spectrum of kinetic energy exhibits a ${\varepsilon_K}^{2/3}k_h^{-5/3}$ power law (where k_h is the horizontal wavenumber and ε_K is the dissipation of kinetic energy) from $k_b = 2\pi/L_b$ to the dissipative scales, with an energy deficit between the integral scale and k_b and an excess around k_b. The vertical spectrum of kinetic energy can be expressed as $E(k_z) = C_N N^2 k_z^{-3} + C{\varepsilon_K}^{2/3}k_z^{-5/3}$ where C_N and C are two constants of order unity and k_z is the vertical wavenumber. It is therefore very steep near the buoyancy scale with a $N^2k_z^{-3}$ shape and approaches the ${\varepsilon_K}^{2/3}k_z^{-5/3}$ spectrum for $k_z > k_o$, k_o being the Ozmidov wavenumber which is the crossover between the two scaling laws. A decomposition of the vertical spectra conditioned on the associated horizontal wavenumber value shows that the $N^2k_z^{-3}$ power law is associated to large horizontal scales $|\mathbf{k}_h| < k_b$ and the ${\varepsilon_K}^{2/3}k_z^{-5/3}$ to $|\mathbf{k}_h| > k_b$.

3.2.1 Introduction

Our understanding of the dynamics of strongly stratified flows has made an major step with the realization of the importance of the anisotropy and of the "buoyancy" scaling law which states that the vertical length scale of a structure should scale as the buoyancy length scale $L_b = U/N$, where U is the typical velocity of the structure and N is the Brunt-Väisälä frequency. This scaling law is valid in the inviscid limit as soon as the horizontal Froude number $F_h = U/(NL_h)$ (where L_h is the typical horizontal length scale) is small and implies that the potential energy is of the same order as the kinetic energy. Theoretically, it comes from the invariance of the Boussinesq Euler equations under the hydrostatic approximation with respect to variation of the stratification (Billant & Chomaz, 2001).

From the turbulence point of view, this scaling law leads to the hypothesis of a direct energy cascade (Lindborg, 2002, 2006). Such cascade and the importance of the buoyancy length scale in strongly stratified turbulence has been observed in many numerical studies (Godeferd & Staquet, 2003; Laval *et al.*, 2003; Riley & de Bruyn Kops, 2003; Waite & Bartello, 2004; Lindborg, 2006; Hebert & de Bruyn Kops, 2006a; Brethouwer *et al.*, 2007; Lindborg & Brethouwer, 2007).

As soon as the buoyancy Reynolds number $\mathcal{R} = ReF_h{}^2$ is very large (where Re is the usual Reynolds number, $Re = UL_h/\nu$, with ν the viscosity), it exists an universal regime of strongly stratified turbulence associated to a horizontal kinetic energy spectrum of the form $C_1{\varepsilon_K}^{2/3}k_h^{-5/3}$, with $C_1 = 0.5$ an universal constant (Lindborg, 2006; Brethouwer *et al.*, 2007).

Actually, this $k_h^{-5/3}$ horizontal energy spectrum for strongly stratified turbulence is followed by a weakly stratified cascade at small scales (Brethouwer *et al.*, 2007). The strongly stratified inertial range has been predicted to exhibit vertical spectra of the form $N^2k_z^{-3}$. On the contrary, the weakly stratified cascade is nearly isotropic and thus associated to a ${\varepsilon_K}^{2/3}k_z^{-5/3}$ vertical spectrum. The transition between the two regimes happens at the Ozmidov length scale $l_o = \sqrt{\varepsilon_K/N^3}$, for which the horizontal Froude number $F_h(l_o) = u(l_o)/(Nl_o)$ is of order unity, where $u(l_o) = {\varepsilon_K}^{1/3}l_o^{-1/3}$ is the characteristic velocity associated to the length scale l_o.

However, numerous numerical simulations of stratified turbulence report mixing events due to the shear instability (Riley & de Bruyn Kops, 2003; Laval *et al.*, 2003; Hebert & de Bruyn Kops, 2006a; Brethouwer *et al.*, 2007). The inverse of the buoyancy Reynolds number is an estimate of the minimum value of the Richardson number that can be reached when vertical diffusion balances horizontal transport. Thus, Riley & de Bruyn Kops (2003) and Hebert & de Bruyn Kops (2006a) interpret the condition $\mathcal{R} > 1$ as a condition for the development of the shear instability in stratified turbulence. In addition, the Richardson number is related to the vertical Froude number $Ri \sim (NL_v/U)^2 \sim 1/{F_v}^2$ so that overturnings might develop already at vertical length scales L_v of the order of the buoyancy length scale L_b, i.e. at scales larger than the Ozmidov length scale l_o.

The evolution of a counter-rotating vortex pair in a stratified fluid has been extensively studied, in particular because it is one of the simplest flow on which the zigzag instability develops and from which the buoyancy length scale naturally emerges as the vertical length (Billant & Chomaz, 2000b). Recently, Deloncle *et al.* (2008), Waite & Smolarkiewicz (2008) and Augier & Billant (2011) have investigated the nonlinear development of the zigzag instability at high buoyancy Reynolds number. They have shown that both the shear and gravitational instabilities appear when the zigzag instability has a finite amplitude leading to a transition to turbulence. This simple flow is interesting to unfold the nonlinear processes and instabilities since they occur successively in a time sequence whereas they all occur simultaneously in stratified turbulence.

In this paper, we continue the numerical study of the transition to turbulence in this particular case of a dipole. In contrast to previous studies, we adopt a statistical point of view and look at spectra and transfers. In section 3.2.2 we describe the

initial conditions and the numerical methods. The evolution of the spectra for a moderate horizontal Froude number is described in details in section 3.2.3. The effect of the horizontal Froude number is studied in section 3.2.4 and those of the Reynolds number in section 3.2.5. A statistical analysis of the non-linear transfers is presented in section 3.2.6. Finally, conclusions are offered in the last section.

3.2.2 Methods

The methods are similar to those employed in Augier & Billant (2011). The flow is initialized by a Lamb-Chaplygin columnar dipole weakly perturbed by the dominant mode of the zigzag instability. The incompressible Navier-Stokes equations under the Boussinesq approximation are solved by means of a pseudo-spectral method with periodic boundary conditions (see Deloncle *et al.* (2008) for details).

The Reynolds number Re and the horizontal Froude number F_h are based on the initial conditions: $Re = UR/\nu, F_h = U/(NR)$, where U and R are respectively the velocity of translation and the radius of the Lamb-Chaplygin dipole and ν is the kinematic viscosity. The Schmidt number $Sc = \nu/\kappa$, where κ is the mass diffusivity, is set to unity in all runs. The Brunt-Väisälä frequency is given by $N = \sqrt{-(g/\rho_0)(d\bar{\rho}/dz)}$, where g is the gravity, ρ_0 a reference density and $\bar{\rho}(z)$ the basic density profile. The total density is given by $\rho_{tot} = \rho_0 + \bar{\rho}(z) + \rho'$, where ρ' is the classical perturbations. For simplicity and without loss of generality, R and R/U are taken respectively as length and time units. The density perturbations are non-dimensionalized by $Rd\bar{\rho}/dz$. The vertical length of the numerical box $\mathcal{L}_z$ is taken equal to the vertical wavelength of the dominant mode of the zigzag instability $\lambda_{zz}/R \simeq 10F_h$ (Billant & Chomaz, 2000c). In the sequel, the buoyancy length scale will be taken to be this natural length scale $L_b = \lambda_{zz} = 10U/N$.

Most of the simulations are performed with the same Reynolds number $Re = 28000$. In contrast, the Froude number will be varied over a wide range: from strongly stratified ($F_h = 0.0225$) to moderately stratified ($F_h = 0.135$). Thus a large range of buoyancy Reynolds number is covered going from 14 to 510, i.e. always well above the threshold for the shear and gravitational instabilities $\mathcal{R}_c \simeq 4.1$ (Augier & Billant, 2011). The parameters of the runs are summarized in table 3.2.

In order to achieve such high Reynolds number, our methods differ from those employed in Augier & Billant (2011) in four main points: first, the horizontal size of the box is $\mathcal{L}_h = 4$ instead of $\mathcal{L}_h = 10$. We have verified that the development of the zigzag and shear and gravitational instabilities are weakly affected by this stronger lateral confinement due to the periodic boundary conditions. Only the late wake evolution differs since the pancake dipoles issued from the zigzag instability have then travelled more than a box size and the amplitude of the zigzag instability is larger than the box size. Therefore, the dipoles interact with their images due to the periodicity. Second, we use an adaptable time step procedure which maximizes the time step over a Courant-Friedrichs-Lewy condition (Lundbladh *et al.*, 1999).

Third, in order to reduce the computational cost, the resolution in the x and y directions is increased during the run so as to adapt to the smallest scales of the flow. We start with a horizontal resolution $N_x \times N_y = 384 \times 384$. At the time the zigzag

Run	F_h	$\mathcal{R} = ReF_h{}^2$	${\mathcal{L}_h}^2 \times \mathcal{L}_z$	${N_h}^2 \times N_z$	ν_4	$\max_t \left(\frac{\varepsilon_{\nu_4}(t)}{\varepsilon(t)}\right)$	$\max_t(\varepsilon_K(t))$
Fh0.0225S	0.0225	14	$4^2 \times 0.225$	$384^2 \times 24$	1.8×10^{-18}	0.63	0.088
Fh0.0225M	0.0225	14	$4^2 \times 0.225$	$768^2 \times 48$	9.3×10^{-21}	0.40	0.082
Fh0.0225L	0.0225	14	$4^2 \times 0.225$	$1024^2 \times 64$	1.1×10^{-21}	0.31	0.082
Fh0.045S	0.045	57	$4^2 \times 0.45$	$384^2 \times 48$	1.8×10^{-18}	0.71	0.075
Fh0.045M	0.045	57	$4^2 \times 0.45$	$768^2 \times 96$	9.3×10^{-21}	0.50	0.088
Fh0.045L	0.045	57	$4^2 \times 0.45$	$1024^2 \times 128$	1.1×10^{-21}	0.38	0.087
Fh0.09S	0.09	227	$4^2 \times 0.9$	$384^2 \times 96$	1.8×10^{-18}	0.73	0.066
Fh0.09M	0.09	227	$4^2 \times 0.9$	$768^2 \times 192$	9.3×10^{-21}	0.49	0.070
Fh0.09L	0.09	227	$4^2 \times 0.9$	$1024^2 \times 256$	1.1×10^{-21}	0.36	0.069
Fh0.09L2	0.09	227	$4^2 \times 0.9$	$1280^2 \times 320$	1.7×10^{-22}	0.25	0.069
Fh0.135S	0.135	510	$4^2 \times 1.35$	$384^2 \times 144$	1.8×10^{-18}	0.73	0.063
Fh0.135M	0.135	510	$4^2 \times 1.35$	$768^2 \times 288$	9.3×10^{-21}	0.49	0.063
Fh0.135L	0.135	510	$4^2 \times 1.35$	$1024^2 \times 384$	1.1×10^{-21}	0.36	0.062

Table 3.2: Overview of the physical and numerical parameters of the simulations. For all simulations $Re = 28000$. The number of nodes in the x-, y- and z-direction are denoted, respectively, N_x, N_y and N_z. We recall that the length and time units is R and R/U respectively. $\varepsilon_{\nu_4}(t)$, $\varepsilon(t)$ and $\varepsilon_K(t)$ denote respectively the hyperviscous dissipation, the total dissipation and the dissipation of kinetic energy.

instability becomes nonlinear ($t = 3$), the resolution is increased to 768×768 and when the secondary instabilities develop ($t = 3.7$), it reaches 1024×1024. The runs for these 3 different resolutions are labelled S, M and L respectively (table 3.2). For each horizontal resolution, the number of numerical points over the vertical N_z is chosen to have a nearly isotropic mesh $N_z \simeq (\mathcal{L}_z/\mathcal{L}_h)N_x$. For $F_h = 0.09$, a additional simulation with an even higher resolution $1280 \times 1280 \times 320$ (labeled L2, see table 3.2) has been performed. Finally, to ensure the numerical stability, we have used added to the classical dissipation an isotropic hyperviscosity $-\nu_4|\mathbf{k}|^8$, where $\mathbf{k}$ is the wavenumber and ν_4 a constant coefficient. From the lowest to the highest resolution, the value of the hyperviscosity ν_4 is decreased such as only the modes with the highest wavenumbers significantly contribute to the hyperviscous dissipation. For each resolution, the hyperdissipation rate $\varepsilon_{\nu_4}(t)$ is observed to suddenly increase at a particular time when the highest wavenumber modes start to be filled. The resolution is increased before this time, i.e. before that the hyperviscosity affects the flow (except for the highest resolution).

The lack of resolution can be quantified by the temporal maxima (which is at the maximum of dissipation) of the ratio $\varepsilon_{\nu_4}(t)/\varepsilon(t)$, where $\varepsilon(t)$ is the total energy dissipation rate. This quantity would tend to 0 if the resolution were increased enough to perfectly resolve the Kolmogorov length scale. In table 3.2, the value of this parameter is reported for each run (note that all simulations are continued largely after the maximum of dissipation). It is around 0.3-0.4 for the largest simulations. A careful comparison of the run Fh0.09L and Fh0.09L2 corresponding to the same set of parameters but to two different resolutions does not show any differences in physical and spectral space apart from the width of the dissipative range. Indeed, the maximum of the ratio $\varepsilon_{\nu_4}(t)/\varepsilon(t)$ has decreased from 0.36 to 0.25. This indicates that, when the

resolution is large enough, the non-dissipative part of the flow starts to be independent of the resolution and of the associated hyperviscosity suggesting that it would also be the same if a DNS were carried. Because we do not seek to study the detailed structure of the dissipative range, we can use such hyperviscosity to decrease the width of the dissipation range and achieve higher Reynolds number values, i.e. increase the width of the inertial range.

3.2.3 Global description of a simulation with $F_h = 0.09$

At the beginning of the simulation, the zigzag instability linearly bends the dipole. With the chosen initial amplitude of the zigzag dominant mode, the evolution of the zigzag instability begins to be strongly non-linear roughly at time $t = 3.3$ but no secondary instability are yet active (Augier & Billant, 2011). Thus, we start the description of the flow at this time $t = 3.3$.

Figures 3.6(*a,d,g,j*) present the time evolution of the density field for $F_h = 0.09$ in a horizontal cross-section at the level at which the shear instability appears $z = 0.66\mathcal{L}_z$. At $t = 3.8$, small scale wiggles can be seen. They are associated to the roll up of Kelvin-Helmholtz (KH) billows with an horizontal axis as described by Deloncle *et al.* (2008) and Augier & Billant (2011). At time $t = 4.2$ (figure 3.6g), the destabilization of the KH billows generate disordered small scales. Eventually, just after the maximum of dissipation, i.e. at $t = 4.9$, small scale perturbation invades the whole domain (figure 3.6j).

To analyze the proprieties of the small scales that appears, we first use the poloidal toroidal decomposition (Cambon, 2001) also known as the Craya-Herring decomposition (Craya, 1958; Herring, 1974) which expresses simply in Fourier space as $\hat{\mathbf{u}} = \hat{\mathbf{u}}_p + \hat{\mathbf{u}}_t$ for each wavenumber, where $\hat{\mathbf{u}}_p = -\boldsymbol{e_\theta} \times (\boldsymbol{e_\theta} \times \hat{\mathbf{u}})$ with $\boldsymbol{e_\theta}$ the unit vector parallel to $\boldsymbol{e_z} \times \mathbf{k}$ and $\hat{\mathbf{u}}_t = (\boldsymbol{e_\theta} \cdot \hat{\mathbf{u}})\boldsymbol{e_\theta}$. In the limit of small vertical Froude number, the poloidal velocity $\hat{\mathbf{u}}_p$ is associated to gravity wave and the toroidal velocity $\hat{\mathbf{u}}_t$ to potential vorticity modes. It has to be pointed out that in the present case this interpretation based on linear approximation is not legitimate since potential vorticity motion reaches order unity vertical Froude number. The zigzag, KH and Rayleigh Taylor instabilities induce an increase of the poloidal kinetic energy $\hat{E}_{Kp}(\mathbf{k}) = |\hat{\mathbf{u}}_p|^2/2$ and of the potential energy $\hat{E}_P(\mathbf{k}) = |\hat{\rho'}|^2/(2{F_h}^2)$ even if there is no waves (see e.g. Staquet & Riley, 1989). However, in the sequel the toroidal poloidal decomposition is used as a convenient formal decomposition enlighting the occurrence of vertical velocity without over interpreting its meaning in term of waves and vortices. Since the poloidal velocity does not correspond to vertical vorticity, its representation allows to follow in Fourier space both the development of the non-linear zigzag instability with the strongly deformed dipole and the Kelvin-Helmholtz instability. From the energy in Fourier mode $\hat{E}_{Kp}(\mathbf{k})$, we define a two-dimensional poloidal energy spectral density

$$\tilde{E}_{Kp}(\kappa_h, k_z) = \frac{1}{\delta\kappa_h \delta k_z} \sum_{\mathbf{k} \in \delta\Omega_{[\kappa_h, \pm k_z]}} \hat{E}_{Kp}(\mathbf{k}), \tag{3.7}$$

where $\delta k_z = 2\pi/\mathcal{L}_z$, $\delta\kappa_h = 2\pi/\mathcal{L}_h$ and $\delta\Omega_{[\kappa_h, \pm k_z]}$ is a volume made of two rings

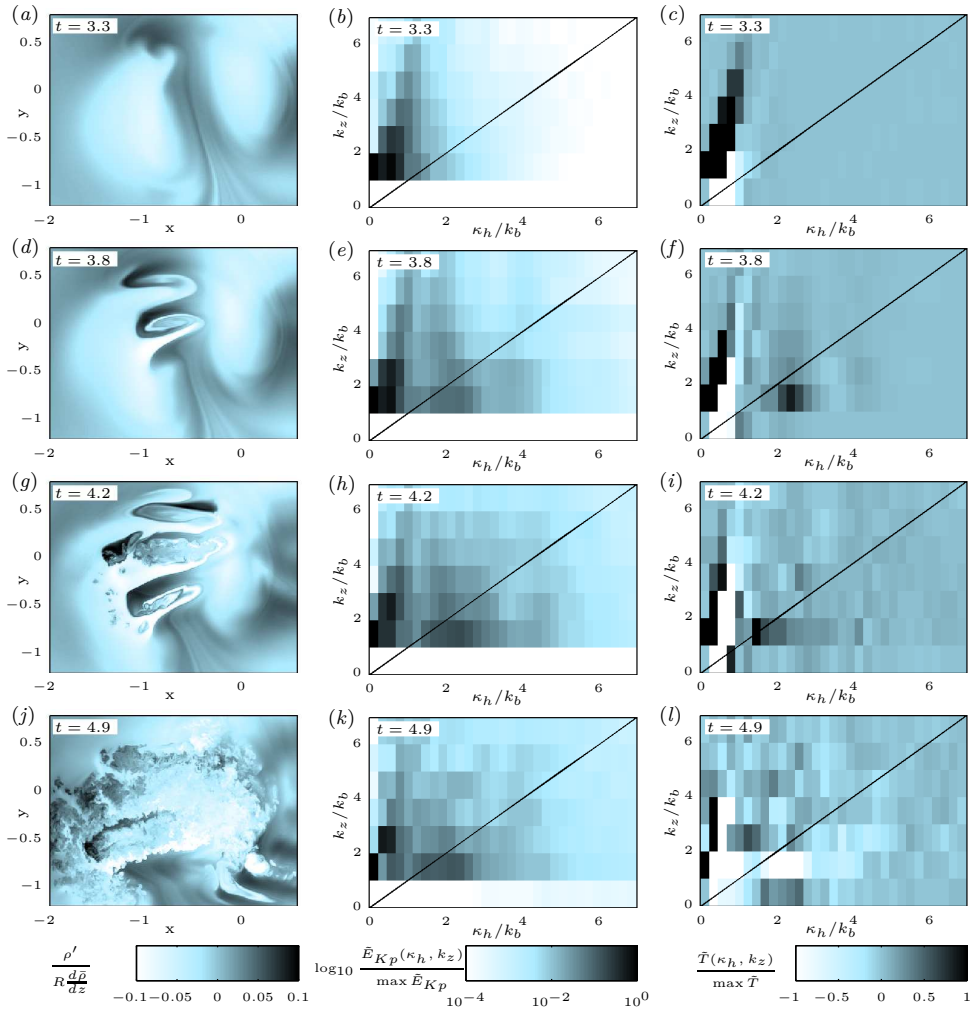

Figure 3.6: Description of four different characteristic times: $t = 3.3$ (a,b,c), $t = 3.8$ (d,e,f), $t = 4.2$ (g,h,i) and $t = 4.9$ (j,k,l) for $F_h = 0.09$. (a,d,g,j) show horizontal cross-sections of the density field at the level at which the shear instability begin to develop $z = 0.66\mathcal{L}_z$; (b,e,h,k) show the spectrum of poloidal energy $\tilde{E}_{Kp}(\kappa_h, k_z)$ and (c,f,i,l) display the total nonlinear energy transfer $\tilde{T}(\kappa_h, k_z)$.

($k_z = \pm|k_z|$) defined by the relation ${\kappa_h}^2 \leqslant {k_x}^2 + {k_y}^2 < (\kappa_h + \delta\kappa_h)^2$.

Figures 3.6(*b,e,h,k*) show for the same instants as figures 3.6(*a,d,g,j*) the poloidal energy density $\tilde{E}_{Kp}(\kappa_h, k_z)$. Both vertical and horizontal wavenumbers are scaled by $k_b = 2\pi/L_b = 2\pi/\mathcal{L}_z$ which corresponds to the lowest non-zero vertical wavenumber and to the most amplified wavenumber of the zigzag instability. At $t = 3.3$, the poloidal energy is concentrated at $k_z = k_b$ and $\kappa_h \simeq 0$-k_0, where k_0 is the leading horizontal wavenumber of the 2D base flow. This feature is associated to the zigzag instability that has a finite amplitude. The energy is spread out at higher vertical wavenumbers than k_b as a result of the nonlinear development of the zigzag instability.

Figure 3.6(*c,f,i,l*) show the two-dimensional spectral density of total nonlinear energy transfers defined by the relation

$$\tilde{T}(\kappa_h, k_z) = \frac{1}{\delta\kappa_h \delta k_z} \sum_{\mathbf{k} \in \delta\Omega_{[\kappa_h, \pm k_z]}} \hat{T}(\mathbf{k}), \tag{3.8}$$

where $\hat{T}(\mathbf{k}) = -\Re[\hat{\mathbf{u}}^*(\mathbf{k}) \cdot (\widehat{\mathbf{u} \cdot \boldsymbol{\nabla}\mathbf{u}})(\mathbf{k}) + F_h^{-2} \hat{\rho'}^*(\mathbf{k})(\widehat{\mathbf{u} \cdot \boldsymbol{\nabla}\rho'})(\mathbf{k})]$, $\Re$ denoting the real part and the star the complex conjugate. The factor F_h^{-2} in front of the second term comes from the non-dimensionalisation of the density perturbations. In all the light regions, the transfer is negative meaning that these modes are loosing energy at the benefit of the wavenumbers in the dark regions. At $t = 3.3$ (figure 3.6*c*), the lost is maximum for the 2D mode $k_z = 0$, $\kappa_h = k_0$ and the gain is maximum at $k_z = k_b$, $\kappa_h \simeq 0$-k_0. This indicates that the zigzag instability is the leading mechanism extracting energy from the 2D base flow at that time. The black region extends vertically nearly up to $k_z \sim 6k_b$ and $\kappa_h \simeq k_b$. This confirms that the nonlinear zigzag instability before the secondary instability is transferring energy to harmonic modes of the initial preferred wavenumber corresponding to small vertical scales but not to small horizontal scales smaller than the buoyancy length scale. Figure 3.6(*c*) also shows transfer toward the modes $k_z = k_b$ and $\kappa_h = 0$ which are the so-called "shear modes" introduced by Smith & Waleffe (2002).

At $t = 3.8$, the energy transfer (figure 3.6*f*) exhibits a new peak close to $k_z \simeq k_b$ and $\kappa_h \simeq 2k_b$ (just below the diagonal isotropic line $\kappa_h = k_z$), linked to the appearance of the KH instability which starts when the local Richardson number is small enough $Ri \lesssim 1/4$ (Deloncle *et al.*, 2008). The wavenumber selected by the KH instability scales like the shear thickness which is proportional to the buoyancy length L_b when Ri is close to the critical value for instability. Therefore, the horizontal wavenumber selected by the secondary KH instability scales like k_b like the vertical wavenumber selected by the primary zigzag instability. Poloidal energy (figure 3.6*e*) presents then a secondary peak around the wavenumber of the KH instability just below the "isotropic" diagonal ($\kappa_h = k_z$). At $t = 4.2$, the appearance of small scales due to the destabilization of the KH billows (figure 3.6*g*), corresponds to positive transfers (figure 3.6*i*) toward high wavenumbers and a lost of energy at low horizontal wavenumbers. The energy spectrum exhibits a more isotropic shape with energy distributed nearly uniformly along the semi-circular lines ${k_z}^2 + {\kappa_h}^2 = const$ (figure 3.6*h*). At $t = 4.9$ (figure 3.6*l*), there are eventually transfers toward very small scales and all the scales corresponding to the earlier development of the KH billows are now loosing energy (bright region). It

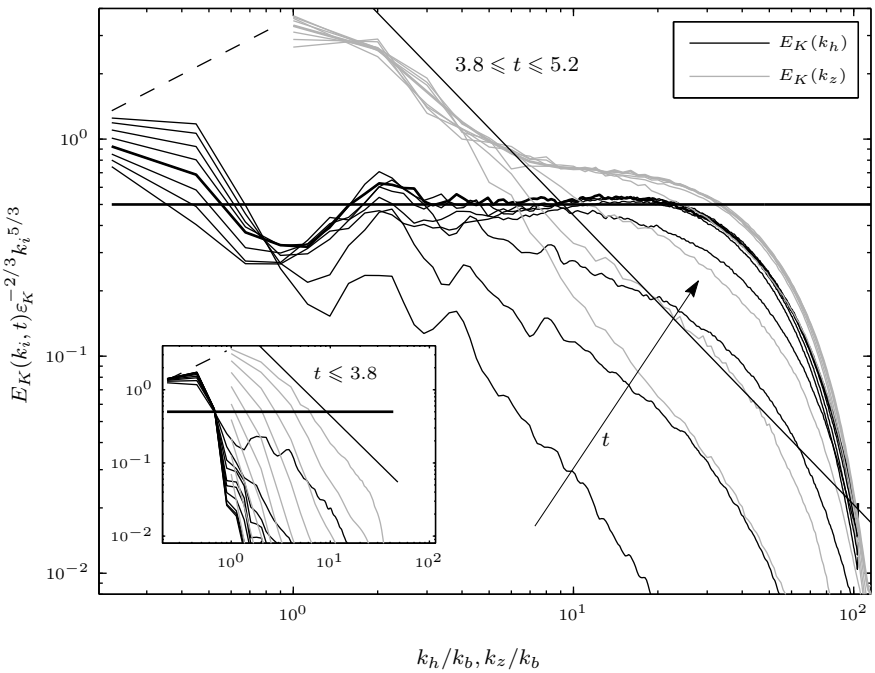

Figure 3.7: Time evolution of the horizontal and vertical compensated 1D spectra for $F_h = 0.09$ and $Re = 28000$. In the main plot, the spectra are shown for $t = 3.8$ to 5.2 with a time increment equal to 0.2. The inset plot shows the spectra for $t = 0.2$ to 3.8 with a time increment of 0.4. The thick curves correspond to the time for which the dissipation is maximum. The thin straight lines indicate the k_z^{-3} power law and the horizontal thick lines the $C_1\varepsilon_K^{2/3}k^{-5/3}$ law, with $C_1 = 0.5$. The dashed lines show a k^{-1} power law.

can be notice that during all this process, the modes $k_z \simeq k_b$-$3k_b$ and $\kappa_h \simeq k_0$ are still gaining energy indicating that the primary zigzag instability remains active despite the development of the secondary shear and gravitational instabilities.

In figure 3.7, we have plotted several horizontal (black curves) and vertical (grey curves) instantaneous compensated unidimensional spectra $E_K(k_h)\varepsilon_K^{-2/3}{k_h}^{5/3}$ and $E_K(k_z)\varepsilon_K^{-2/3}{k_z}^{5/3}$, respectively, where ε_K is the maximum kinetic dissipation. The horizontal unidimensional spectra are the mean value of the unidimensional spectra $E(k_x)$ and $E(k_y)$, in the same way as in Lindborg (2006). For the time $3.8 \leqslant t \leqslant 5.2$ corresponding to the development and the destabilization of the KH billows. The inset plot shows also the sprectra for $t \leqslant 3.8$, i.e. prior to the development of the shear instability. The thin straight lines indicate the k^{-3} power law and the horizontal thick lines display the $C_1\varepsilon_K^{2/3}k^{-5/3}$ law, with $C_1 = 0.5$, corresponding to the horizontal kinetic spectra of forced strongly stratified turbulence (Lindborg, 2006; Brethouwer

et al., 2007). The dashed lines mark the k^{-1} slope which should rely two points of the horizontal and vertical spectra associated with the same anisotropic structure, i.e. with same horizontal velocity U but different horizontal and vertical characteristic length scales and with spectra scaling like $E(k) \simeq U^2 k^{-1}$.

In the inset plot, we see that during the early evolution of the zigzag instability, the horizontal spectra does not vary at large scales. Only after $t > 3.2$, does the energy at wavenumbers larger than the buoyancy wavenumber k_b start increasing. In sharp contrast, the level of the vertical spectra increases nearly linearly in time in this logarithmic representation since the energy in the first mode grows exponentially owing to the development of the zigzag instability. For the penultimate time of the inset $t = 3.4$, the slope of the vertical spectra approaches k_z^{-3} even if only the zigzag instability has developed at that time. This indicates that this characteristic slope is mainly due to the vertical deformation of the dipole due to the non-linear deformation induced by the zigzag instability.

Starting at $t = 3.4$, we can see a peak in the horizontal spectra around $k_h/k_b = 2$ and its harmonics at $k_h/k_b = 4$ and 8. This is due to the appearance of the secondary KH instability. We observe a dip in the horizontal spectra between the small horizontal wavenumber k_0 corresponding to the initial dipole and $k_h/k_b = 2$. This is consistent with the observation of figure 3.6 where a direct transfer from the $[\kappa_h, k_z] \simeq [k_0, k_b]$ modes to the $[\kappa_h, k_z] \simeq [2k_b, k_b]$ modes due to the KH instability was evidenced. Beyond $t = 4.4$, energy eventually cascades toward the small horizontal scales with a slope close to $k_h^{-5/3}$ over approximately one decade. Remarkably, the horizontal spectra nearly perfectly collapse on the $C_1 {\varepsilon_\kappa}^{2/3} k_h^{-5/3}$, with $C_1 = 0.5$, as observed in forced strongly stratified turbulence (Lindborg, 2006; Brethouwer *et al.*, 2007). However, the particular value of this constant is here not meaningful since it depends on the horizontal size of the computational domain compared to the dipole size. This is because the turbulence is concentrated around the vortices and is not homogeneous along the horizontal directions. Therefore, the observed agreement with the theory of strongly stratified turbulence is fortuitous. Quite remarkably, small vertical scales develop at the same time as the horizontal scales and, after $t = 4.4$, the vertical spectra exhibit a break in the slope around $k_z/k_b = 8$ where the slope goes from k_z^{-3} to $k_z^{-5/3}$. The $k_z^{-5/3}$ power law begins when the vertical spectrum k_z^{-3} approaches the horizontal one indicating a return to isotropy.

On figure 3.8, instantaneous toroidal (black), poloidal (light grey) and potential (dark grey), horizontal (figure 3.8*a*) and vertical (figure 3.8*b*) spectra are presented for $t = 4.6$ which correspond to the time where the dissipation is maximum. The large horizontal scales are dominated by the toroidal part while the peak at horizontal scales $\kappa_h = 2k_b$ is largely dominated by the poloidal and the potential parts. At smaller horizontal scales, the toroidal and poloidal spectra approach each other. In figure 3.8(b), we see that the large vertical scales are also dominated by the toroidal spectra which confirms that the nearly k_z^{-3} slope in figure 3.7 is due to the non-linear deformation generated by the zigzag instability.

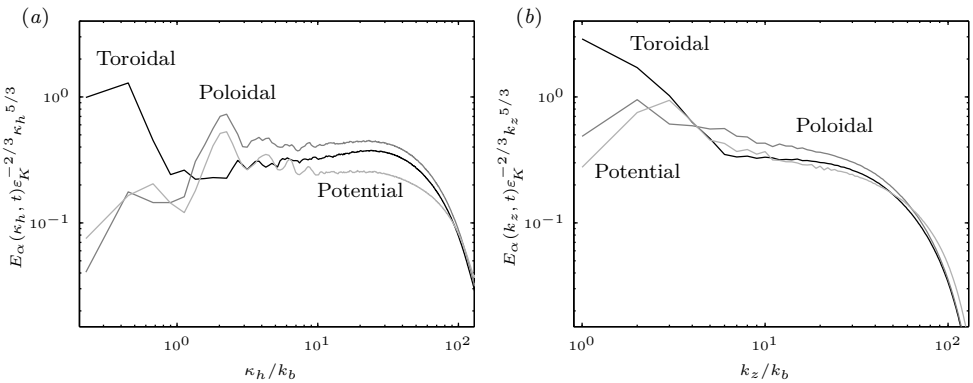

Figure 3.8: Horizontal (a) and vertical (b) compensated two-dimensional spectra of toroidal, poloidal and potential energy for $F_h = 0.09$ and $Re = 28000$ at $t = 4.6$. Black, dark grey and light grey curves correspond respectively to toroidal, poloidal and potential energies.

3.2.4 Variation of F_h and $\mathcal{R}$

Figure 3.9 presents horizontal (continuous curves) and vertical (dashed curves) compensated kinetic spectra $E_K(k_h)\tilde{\varepsilon_K}^{2/3}{k_h}^{5/3}$ and $E_K(k_z)\tilde{\varepsilon_K}^{2/3}{k_z}^{5/3}$ obtained from simulations with different values of F_h but the same Reynolds number $Re = 28000$. The spectra have been time-averaged over $\Delta t = 0.3$ around the time where the total dissipation is maximum.

In order to rescale quantities, we use the maximum kinetic dissipation rate for $F_h = 0.09$: $\tilde{\varepsilon}_K = 0.069$. This is equivalent to consider $\tilde{\varepsilon}_K$ to be equal to the energy injection rate and to assume it does not vary with F_h, the early development of the zigzag instability being similar for all simulations since the initial state is identical. The plot would have been very similar if each curve were scaled by its maximum dissipation rate ε_K since ε_K varies only weakly with F_h (see table 3.2).

Since the wavenumbers are scaled by k_b, all the vertical spectra begin at the same dimensionless wavenumber $k_z/k_b = 1$, because the vertical size of the numerical box is adjusted to the dominant wavelength of the zigzag instability. While Re is the same for all runs, the dissipative ranges move to the right when F_h is increased because k_b decreases with F_h. For the same reason the horizontal spectra also extend to larger values of k_h/k_b when F_h increases since the lowest horizontal wavenumber is the same for all the simulations. We see again the peak or more precisely the end of the trough corresponding to the KH billows in the horizontal spectra at $k_h \simeq 2k_b$. For $F_h = 0.0225$ (black continuous thin line), the bump is of smaller amplitude and occurs at a slightly smaller wavenumber probably because of the lower value of the buoyancy Reynolds number ($\mathcal{R} = 14$). For $F_h = 0.135$, the bump is nearly not visible and is located at a slightly larger dimensionless wavenumber. This is probably due to a weaker anisotropy since the stratification is moderate, the wavelength of

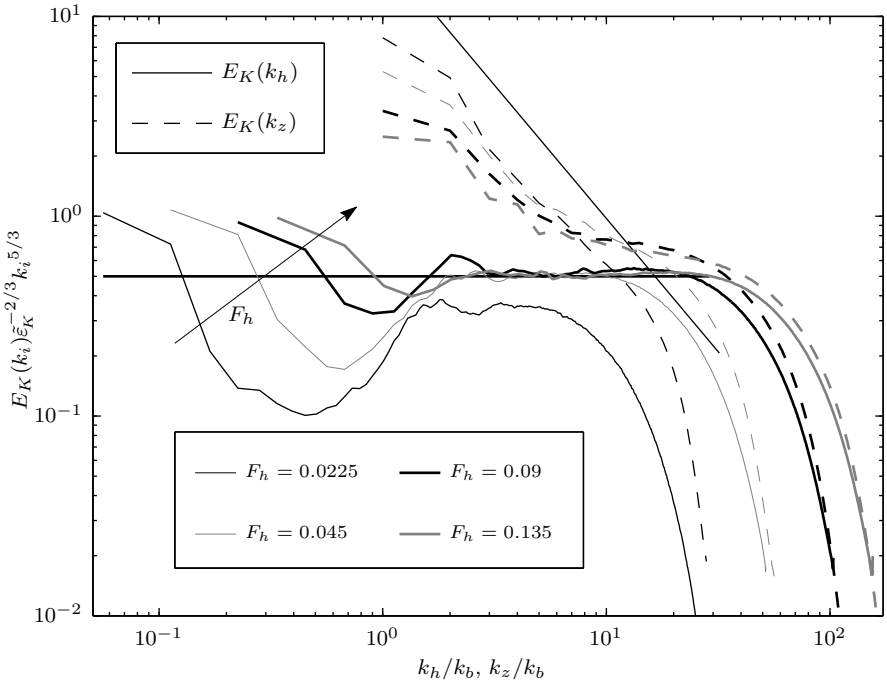

Figure 3.9: Horizontal and vertical compensated spectra $E_K(k_i)\tilde{\varepsilon}_K^{-2/3}{k_i}^{5/3}$ as a function of the dimensionless wavenumber k_i/k_b for four runs with different values of the Froude number $F_h = 0.0025$, 0.045, 0.09 and 0.135 but the same Reynolds number $Re = 28000$. Each curve is the average over time interval $\Delta t = 0.3$ near the maximum of the dissipation. The thin straight line indicates the k_z^{-3} power law and the horizontal thick line the $C_1{\tilde{\varepsilon}_K}^{2/3}k^{-5/3}$ law, with $C_1 = 0.5$.

the zigzag instability is indeed as large as the radius of the Lamb-Chaplygin dipole $\lambda_{zz} = 1.35R$. For all the Froude numbers, the spectra are depleted in energy between the small horizontal wavenumbers and $k_h = k_b$. Remarkably, all the runs except for $F_h = 0.0225$ present for higher wavenumbers $k_h \gtrsim 2k_b$, a flat compensated horizontal spectra (corresponding to a $k_h^{-5/3}$ power law) collapsing at a value approximately equal to 0.5. As already mentioned the buoyancy Reynolds number is probably too low for $F_h = 0.0225$.

The vertical spectra are very steep near $k_z = k_b$ and show a tendency to follow a k_z^{-3} slope. They flatten when approaching the horizontal spectra at large wavenumber and their slope tends to $k_z^{-5/3}$ except for the highest stratification $F_h = 0.0025$, where the two curves approach each other only in the dissipation range (i.e. the Ozmidov scale is of the order of the Kolmogorov scale).

Figure 3.10(a) presents compensated vertical spectra $E_K(k_z)N^{-2}{k_z}^3$ versus k_z/k_b averaged over the same time interval. All the curves collapse to $E_K(k_z)N^{-2}{k_z}^3 =$

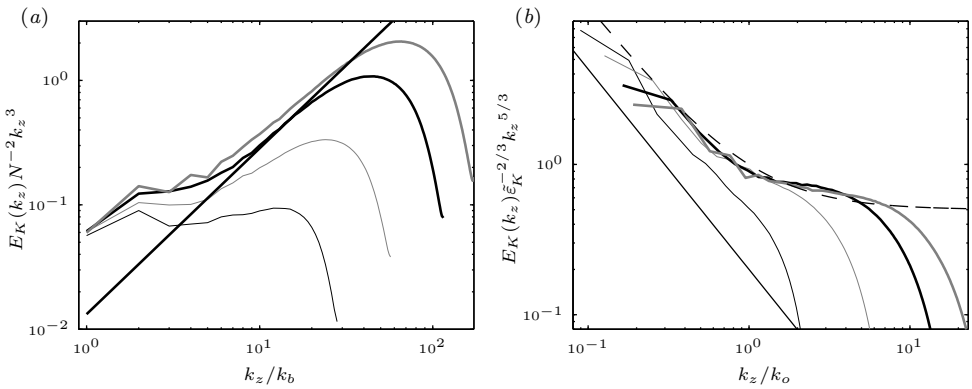

Figure 3.10: Vertical dimensionless average spectra already presented in figure 3.9 plotted in (a) as $E_K(k_z)N^{-2}k_z{}^3$ versus k_z/k_b and in (b) as $E_K(k_z)\tilde{\varepsilon}_K^{-2/3}k_z{}^{5/3}$ versus k_z/k_o. In (a), the thick straight line indicates the $k_z^{-5/3}$ power law. In (b), the thin straight line indicates the k_z^{-3} power law and the dashed line represents the theoretical expression (3.9).

$C_N \simeq 0.1$ for $k_z = k_b$ corresponding to the dominant mode of the zigzag instability. However, the curves depart rapidly from this constant when k_z increases all the more than F_h is large. This is because the transition to the $k_z^{-5/3}$ power law occurs at a lower vertical wavenumber when F_h increases.

Spectra scaling like $N^2k_z^{-3}$ are widely observed in nature (see e.g. Garrett & Munk, 1979; Gregg, 1987) and many authors (e.g. Lumley, 1964; Holloway, 1983; Dewan, 1997; Brethouwer *et al.*, 2007; Riley & Lindborg, 2008) have predicted with dimensional analysis based on different theories that the spectra in stratified fluid should express as the sum of a balanced strongly stratified spectra and an inertial spectra, i.e. as

$$E_K(k_z) = C_N N^2 k_z^{-3} + C\varepsilon_K^{2/3}k_z^{-5/3} = ((k_z/k_o)^{-4/3} + 1)C\varepsilon_K^{2/3}k_z^{-5/3} \tag{3.9}$$

where C is a constant of order unity and $k_o = 2\pi/l_o$ with $l_o = 2\pi(C/C_N)^{3/4}(\varepsilon_K/N^3)^{1/2}$ the Ozmidov length scale. In figure 3.10(b), the compensated vertical spectra are plotted as a function of k_z/k_o. Apart the Froude number $F_h = 0.0225$, all the curves collapse over a large range of vertical wavenumbers and in particular near the wavenumber of transition between the k_z^{-3} and the $k_z^{-5/3}$ power laws. This indicates that the change of slope occurs at the Ozmidov length scale as predicted for strongly stratified turbulence (Brethouwer *et al.*, 2007). We can see that the spectrum (3.9) with $C_N = 0.08$ and $C = 0.56$ (dashed line) describes remarkably well the observed spectra except of course near the dissipative range. It has to be pointed out that the constant $C = 0.56$ associated to small scale turbulence is smaller than the classical Kolmogorov constant for homogeneous isotropic turbulence and unidimensional kinetic energy spectrum $C_K \simeq 1$ (Sreenivasan, 1995; Monin & Yaglom, 1975; Gotoh *et*

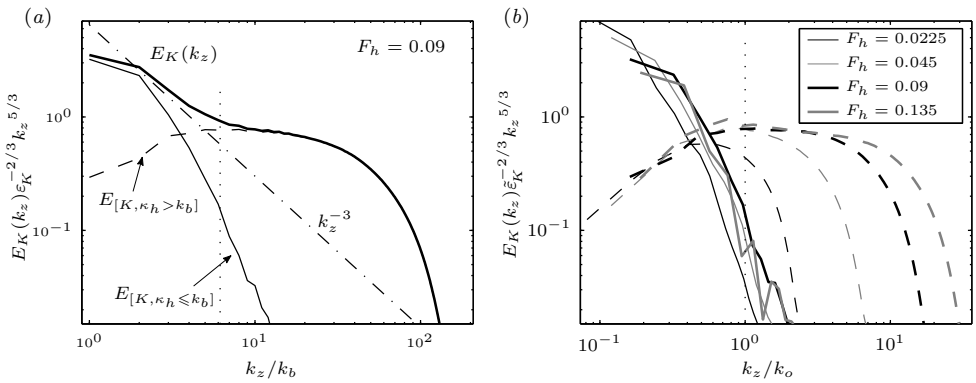

Figure 3.11: Decomposition of the vertical compensated spectra for $F_h = 0.09$ (a) and for all Froude numbers (b) shown in figure 3.9. In (a), the black thin curve correspond to the vertical spectrum $E_{[K,\kappa_h\leqslant k_b]}(k_z)$ computed with modes for which $\kappa_h \leqslant k_b$ and the dashed curve to the spectrum $E_{[K,\kappa_h>k_b]}(k_z)$ computed with modes for which $\kappa_h > k_b$. The dotted lines indicate the Ozmidov wavenumber $k_z = k_o$. The dotted dashed lines show the k_z^{-3} power law. In (b), the solid curves correspond to the spectra $E_{[K,\kappa_h\leqslant k_b]}(k_z)$ and the dashed curves to the spectra $E_{[K,\kappa_h>k_b]}(k_z)$.

al., 2002). However, the precise value of the constant C is here not meaningful and depends of the horizontal size of the numerical box because the turbulence does not invade all the computational domain.

Figure 3.11(a) presents a decomposition of the vertical compensated spectra $E_K(k_z)\varepsilon_K^{-2/3}k_z{}^{5/3}$ for $F_h = 0.09$ shown in figure 3.9. The continuous thin curve corresponds to conditional vertical spectrum $E_{[K,\kappa_h\leqslant k_b]}(k_z)$ computed with modes for which $\kappa_h \leqslant k_b$. As shown in figure 3.6, these modes correspond to the dipole deformed by the zigzag instability. This conditional vertical spectrum is very steep for both Froude numbers and clearly dominates the total spectrum at the largest vertical scales where the $N^2k_z^{-3}$ power law is observed. The dashed curve corresponds to conditional vertical spectrum $E_{[K,\kappa_h>k_b]}(k_z)$ computed with modes for which $\kappa_h > k_b$. We have shown in figure 3.6 that these scales are generated mostly through the KH instability. We see that this conditional vertical spectrum is nearly flat from $k_z \simeq 3k_b$ to the dissipative range, i.e. the range corresponding to a $k_z^{-5/3}$ power law. This spectrum do not show any tendency to steepen at the largest vertical scales. This indicates that the structures generated by the shear instability are relatively isotropic and lead to a transition to turbulence with a $k^{-5/3}$ inertial range. This feature is hidden in the total vertical kinetic energy spectra at the large vertical scales between the buoyancy and the Ozmidov length scales owing to the dominance of the $N^2k_z^{-3}$ spectra associated to the large horizontal scales. The conditional spectra for all Froude number are plotted in figure 3.11(b) as a function of k_z/k_o. This shows that the beginning of the $k_z^{-5/3}$ inertial range associated to small horizontal scales $\kappa_h > k_b$ scales with the

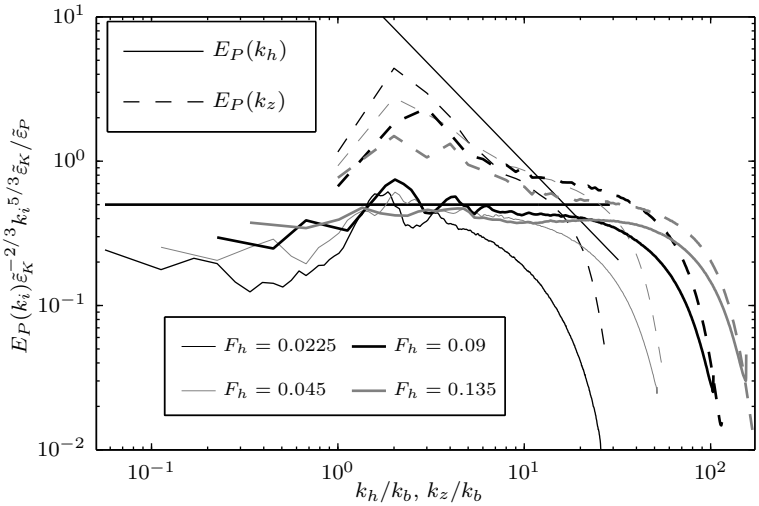

Figure 3.12: Similar to figure 3.9 except that it is the spectra of potential energy. The horizontal thick line shows the $0.5\tilde{\varepsilon_K}^{2/3} k^{-5/3} \varepsilon_P/\varepsilon_K$ law.

Ozmidov wavenumber.

Figure 3.12 presents the horizontal (continuous lines) and vertical (dashed lines) compensated spectra $E_P(k_i)\tilde{\varepsilon_K}^{2/3} {k_i}^{5/3} \varepsilon_K/\varepsilon_P$ of potential energy corresponding to the kinetic energy spectra shown in figure 3.9. An average over the same time interval has been performed. The potential spectra are very similar to the kinetic spectra but with less energy at large horizontal scales since the initial dipole has no potential energy. More pronounced bumps around the buoyancy length scale can be also seen. Like the horizontal compensated kinetic energy spectra $E_K(k_h)\tilde{\varepsilon_K}^{2/3} {k_h}^{5/3}$ (figure 3.9), the horizontal compensated potential energy spectra $E_P(k_h)\tilde{\varepsilon_K}^{2/3} {k_h}^{5/3} \varepsilon_K/\varepsilon_P$ present a flat range corresponding to a $k_h^{-5/3}$ power law from the buoyancy wavenumber to the dissipative wavenumber and nearly collapse at a value approximately equal to 0.5. This means that the relation $E_P(k_h)/\varepsilon_P = E_K(k_h)/\varepsilon_K$ approximatelly holds as observed in forced strongly stratified turbulence (Lindborg, 2006; Brethouwer *et al.*, 2007). However, the compensated spectra are slightly lower than predicted and slightly decrease over the inertial range before the dissipative range.

The total dissipation is plotted versus time on figure 3.13(a). For all Froude numbers, we see an increase at $t \simeq 3.7$ linked to the development of the KH instability. The dissipation before this time is mostly due to the vertical shear resulting from the non-linear development of the zigzag instability. It is thus approximately proportional to the inverse of the buoyancy Reynolds number. When the horizontal Froude number is increased, the period of strong dissipation tends to last a longer time, with slower increase and decrease of the dissipation. This might be explained by considering the proprieties of the KH billows as a function of F_h. We will show in section 3.2.5

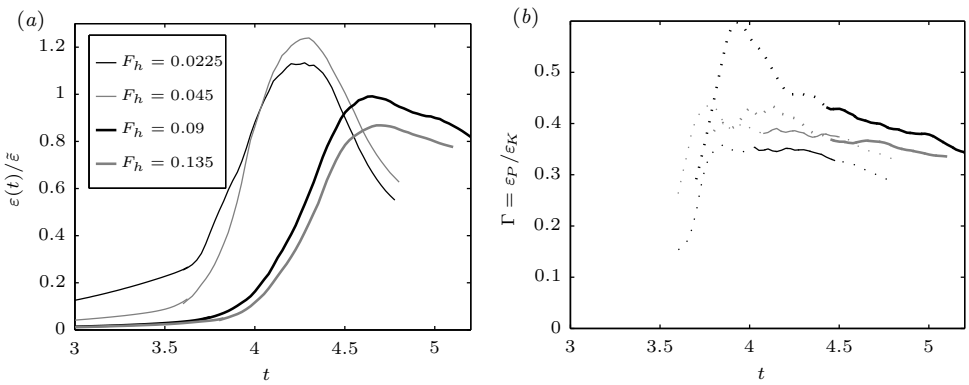

Figure 3.13: Temporal evolution of (a) the total dissipation rate $\varepsilon(t)$ for $F_h = 0.0025$, $F_h = 0.0045$, $F_h = 0.09$, $F_h = 0.135$ scaled by $\tilde{\varepsilon}$ the maximum dissipation rate for $F_h = 0.09$ and (a) the mixing efficiency $\Gamma = \varepsilon_P(t)/\varepsilon_K(t)$ (continuous lines are used when the dissipation rate is high $\varepsilon(t) > 0.8 \max \varepsilon(t)$).

that when the buoyancy Reynolds number is large enough, the shear instability is only weakly influenced by dissipation. In this explanation, we neglect the dissipation even if this assumption is not valid for the smallest Froude number $F_h = 0.0225$ for which $\mathcal{R} = 14$. The vertical Froude number of the KH billows $F_{vKH} = \omega_h/(2N) \simeq (4Ri)^{-1/2}$, where ω_h is the dimensional horizontal vorticity, is of order unity for all F_h since $Ri \simeq 1/4$ at the onset of the shear instability. Since the dominant mode of the Kelvin-Helmholtz instability is characterized by a horizontal wavelength scaling like the shear thickness and a growth rate scaling like the shear (Hazel, 1972), the shear instability transfers energy from the dipole with an horizontal scale R and characteristic time R/U toward small fast quasi-isotropic KH billows with characteristic length scale of order $U/N = F_h R$ and characteristic time of order $\omega_h^{-1} \sim N^{-1} = F_h R/U$. This may explain why the duration of the strong dissipation tends to decrease with the stratification.

Figure 3.13(b) presents the temporal evolution of the instantaneous mixing efficiency $\Gamma(t) \equiv \varepsilon_P(t)/\varepsilon_K(t)$. We see that the mixing efficiency is around 0.4 and weakly varies with the stratification and with the time period during which the dissipation is strong. We have also looked at the isotropy of the dissipation by considering the ratio $\varepsilon_z(t)/\varepsilon(t)$ where ε_z is the dissipation due to vertical gradients. The maximum value of $\varepsilon_z/\varepsilon$ increases with $\mathcal{R}$ and tends to $1/3$ which corresponds to an isotropic dissipation (not shown) even if a weak isotropic hyperviscosity is used.

3.2.5 Effect of the Reynolds number and of the resolution for $F_h = 0.09$

We now focus on the effects of the variation of the Reynolds number and of the resolution. Two supplementary simulations have been carried out for $F_h = 0.09$ and

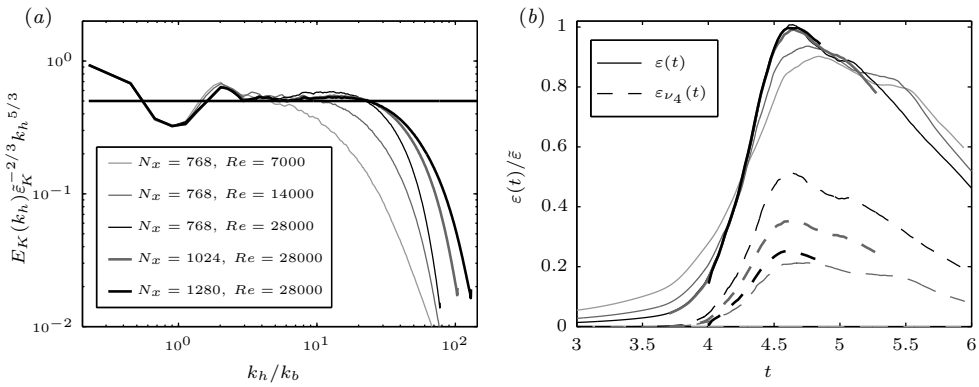

Figure 3.14: (a) Horizontal compensated spectra $E_K(k_h)\tilde{\varepsilon_K}^{2/3}{k_h}^{5/3}$ for five runs for different values of the Reynolds number and of resolution but for the same Froude number $F_h = 0.09$. Each curve is the average over time interval $\Delta t = 0.3$ near the maximum of the dissipation. The horizontal thick line shows the $0.5\tilde{\varepsilon_K}^{2/3}k_h^{-5/3}$ law. (b) Temporal evolution of the total dissipation rate $\varepsilon(t)$ (continuous lines) and of the hyper-dissipation rate $\varepsilon_{\nu_4}(t)$ (dashed lines) scaled by $\tilde{\varepsilon}$ the maximum dissipation rate for $Re = 28000$ and for the maximum resolution $N_h = 1280$ for the same runs.

for the same resolution as for the simulation Fh0.09M, i.e. $N_h = N_x = N_y = 768$ and $N_z = 192$, but for different values of the Reynolds number $Re = 14000$ and $Re = 7000$. Figure 3.14(a) displays the horizontal compensated spectra $E_K(k_h)\tilde{\varepsilon_K}^{2/3}{k_h}^{5/3}$ for these two simulations with a lower Reynolds number and for the simulations Fh0.09M, Fh0.09L and Fh0.09L2 for which $Re = 28000$ (see table 3.2). We see that the width of the inertial range largely decreases when the Reynolds is decreased. However, the bump corresponding to the shear instability is nearly not affected meaning that, when the Reynolds number and the buoyancy Reynolds number are large enough, the horizontal wavelength of the shear instability continues to scale with the buoyancy length scale. Besides, as already stated, there is nearly no differences between the two spectra for $N_h = 1024$ and $N_h = 1280$ apart at the smallest scales of the dissipative range, validating the use of a weak isotropic hyperviscosity.

The total dissipation (continuous lines) and the hyper-dissipation (dashed lines) are plotted versus time for the same runs on figure 3.14(b). We see that despite the important variation of resolution, the total dissipation curves for $Re = 28000$ (black thick and thin lines and grey thick line) are quite close, especially for the two largest simulations Fh0.09L and Fh0.09L2 (thick lines). On the contrary, the hyper-dissipation strongly decreases when the resolution is increased indicating that the Kolmogorov scale becomes nearly resolved. For the lowest Reynolds number $Re = 7000$, there is no need for hyperviscosity and the simulation is a real DNS. The total dissipation curves for the different Reynolds numbers slightly differ. For lower Re, the dissipation is more important during the non-linear evolution of the zigzag instability

before the development of the secondary instabilities occurring after $t = 3.7$. The increase corresponding to the development of the secondary instabilities is less fast leading to a slightly lower maximum of total dissipation of the order of $0.9\tilde{\varepsilon}$ for $Re = 7000$ and $0.94\tilde{\varepsilon}$ for $Re = 14000$. However, the global evolution of the total dissipation rate is only weakly affected by the variation of the Reynolds number. This shows that, for these values of buoyancy Reynolds number and of Reynolds number, the first mechanisms of the transition to turbulence, namely the non-linear evolution of the zigzag instability and the secondary instabilities, are only weakly influenced by dissipation.

3.2.6 Decomposition of the horizontal fluxes for $F_h = 0.09$

The evolution equations of the kinetic and potential energies $\hat{E}_K(\mathbf{k}) = |\hat{\mathbf{u}}|^2/2$ and $\hat{E}_P(\mathbf{k}) = |\hat{\rho'}|^2/(2{F_h}^2)$ of a wavenumber $\mathbf{k}$ can be expressed as

$$\frac{d\hat{E}_K(\mathbf{k})}{dt} = \hat{T}_K - \hat{b} - \hat{D}_K, \tag{3.10}$$

$$\frac{d\hat{E}_P(\mathbf{k})}{dt} = \hat{T}_P + \hat{b} - \hat{D}_P, \tag{3.11}$$

and where $\hat{T}_K = -\Re[\hat{\mathbf{u}}^*(\mathbf{k}) \cdot (\widehat{\mathbf{u} \cdot \boldsymbol{\nabla}\mathbf{u}})(\mathbf{k})]$ and $\hat{T}_P = -F_h^{-2}\Re[\hat{\rho'}^*(\mathbf{k})(\widehat{\mathbf{u} \cdot \boldsymbol{\nabla}\rho'})(\mathbf{k})]$ are the kinetic and potential nonlinear transfers, $\hat{D}_K(\mathbf{k}) = |\mathbf{k}|^2|\hat{\mathbf{u}}|^2/Re$ and $\hat{D}_P(\mathbf{k}) = |\mathbf{k}|^2|\hat{\rho'}|^2/({F_h}^2 ReSc)$ are the kinetic and potential mean energy dissipation and $\hat{b}(\mathbf{k}) = F_h^{-2}\Re[\hat{\rho'}^*(\mathbf{k})\hat{w}(\mathbf{k})]$ is the conversion of kinetic energy into potential energy. When (3.10) and (3.11) are summed over the wavenumbers inside a vertical cylinder Ω_{κ_h} of radius κ_h in spectral space, we obtain,

$$\frac{dE_K(\kappa_h)}{dt} = -\Pi_K(\kappa_h) - B(\kappa_h) - \varepsilon_K(\kappa_h), \tag{3.12}$$

$$\frac{dE_P(\kappa_h)}{dt} = -\Pi_P(\kappa_h) + B(\kappa_h) - \varepsilon_P(\kappa_h). \tag{3.13}$$

$E_K(\kappa_h) = \sum_{|\mathbf{k}_h| \leqslant \kappa_h, k_z} \hat{E}_K(\mathbf{k})$, $\Pi_K(\kappa_h)$ the kinetic flux going outside of Ω_{κ_h}, $B(\kappa_h)$ the conversion of kinetic energy into potential energy inside Ω_{κ_h} and $\varepsilon_K(\kappa_h)$ the kinetic dissipation inside Ω_{κ_h}. The quantities with the subscript P are the same but for the potential energy. In order that the fluxes of the shear modes be not located at $-\infty$ in logarithmic plots, the horizontal wavenumber κ_h is discretized as $\kappa_h = \delta\kappa_h/2 + \delta\kappa_h l$, where $\delta\kappa_h = 2\pi/\mathcal{L}_h$ and l is the discretization integer.

These energy fluxes, conversion and dissipation rates are plotted versus κ_h for four particular times on figure 3.15 for $F_h = 0.09$. All the curves have been scaled by $\tilde{\varepsilon}$, the maximum of the total instantaneous dissipation. The plot for $t = 3.3$ (figure 3.15*a*) corresponds to a time where the zigzag instability evolves nonlinearly but the shear instability has not yet developed. At this time all the quantities are small compared to $\tilde{\varepsilon}$. The dissipation (dashed lines) is negligible. There is only a weak kinetic energy flux (black continuous line) of order $0.2\tilde{\varepsilon}$ toward horizontal wavenumbers slightly larger

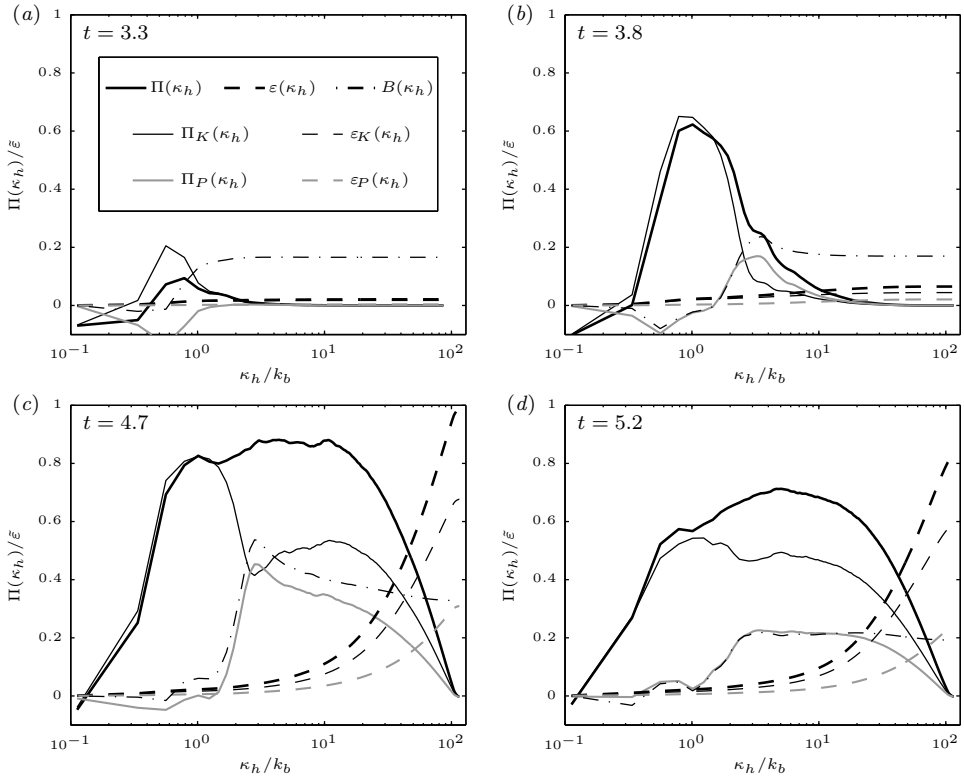

Figure 3.15: Fluxes going out from a vertical cylinder Ω_{κ_h} of radius κ_h in spectral space and dissipations inside this cylinder. The continuous black thin, grey and black thick curves are respectively the kinetic $\Pi_K(\kappa_h)$, potential $\Pi_P(\kappa_h)$ and total horizontal fluxes through the surface of Ω_{κ_h}. The dashed black thin, grey and black thick curves are respectively the kinetic $\varepsilon_K(\kappa_h)$, potential $\varepsilon_P(\kappa_h)$ and total dissipations inside the volume Ω_{κ_h}. The dotted dashed black curve is $B(\kappa_h)$ the sum inside the volume Ω_{κ_h} of $\hat{b}(\mathbf{k})$ the local conversion of kinetic energy into potential energy. The lowest wavenumber corresponds to the shear modes.

than the leading horizontal wavenumber of the 2D base flow k_0 (which is of order $0.4k_b$ for the particular stratification $F_h = 0.09$). Let's note that we have observed by looking at the flux for other F_h that the horizontal wavenumbers in which kinetic energy is transfered at this time do not scale as the buoyancy wavenumber but as k_0. The weakness of the transfer along the horizontal when only the zigzag instability is active is consistent with figure 3.6 which shows that the zigzag instability produces strong transfers along the vertical toward large vertical wavenumber of order k_b but only with weak transfers along the horizontal. At wavenumbers slightly larger than k_0, $B(\kappa_h)$ increases from zero to approximately $0.17\tilde{\varepsilon}$ indicating a total conversion of kinetic into potential energies. Let's note that since $B(\kappa_h) = \sum_{|\mathbf{k}_h|\leqslant\kappa_h,k_z} \hat{b}(\mathbf{k})$, an increase (respectively decrease) of $B(\kappa_h)$ indicate positive (respectively negative) local conversion of kinetic into potential energies. The local conversion at wavenumber $\kappa_h \simeq k_0$ is due to the bending of the vortices. Remarkably, there is also a backward potential energy flux (grey continuous line) toward the smallest horizontal wavenumbers of the numerical box. However, the potential energy flux toward the horizontally invariant "shear modes" (located at the first point $\kappa_h \simeq 0.1k_b$ as explained previously) is zero. In contrast, kinetic energy flux is negative for the smallest wavenumber $\kappa_h \simeq 0.1k_b$, indicating a transfer of order $0.06\tilde{\varepsilon}$ to shear modes.

The time $t = 3.8$ (figure 3.15b) corresponds to the development of the KH billows before the transition to turbulence. As for $t = 3.3$ the dissipation (dashed lines) is negligible and there is a weak kinetic energy flux toward shear modes. The potential flux is still negative at large horizontal scales $0.1 \leqslant \kappa_h/k_b \lesssim 1$ and is now balanced by the energy conversion. Kinetic energy flux becomes positive at $\kappa_h \simeq 0.3k_b$ (second point), reaches a maximum around $\kappa_h = 0.8k_b$ and drops down to nearly zero around $\kappa_h \simeq 3k_b$. This means that the kinetic energy is transferred from the large scales $\kappa_h \simeq k_0$ toward horizontal scales around $\kappa_h = 2k_b$. This transfer appears as a peak and not as a plateau because the ratio $2k_b/k_0$ is not large but only moderate for $F_h = 0.09$. However, the other runs for lower F_h (not plotted) show that this non-local transfer appears as a plateau with a width $2k_b/k_0$ proportional to F_h^{-1}. The conversion of kinetic into potential energies (grey dashed dotted curve) becomes positive at horizontal wavenumber $\kappa_h \simeq 1.5k_b$, reaches its maximum at $\kappa_h \simeq$ 3-4k_b and then slightly decreases and stays constant around 0.2ε for smaller scales. Again, the increase of $B(\kappa_h)$ at k_b is due to the development of the KH billows which convert kinetic energy into potential energy at the buoyancy length scale. The slight decrease of $B(\kappa_h)$ at smaller scales corresponds to a weak conversion of potential energy back into kinetic energy.

Figure 3.15(c) corresponds to the time $t = 4.7$ when the dissipation is maximum. The total dissipation $\varepsilon(\kappa_h)$ (black thick dashed line) reaches the value $\tilde{\varepsilon}$ for the largest κ_h. The potential dissipation is approximately one third of the total dissipation. The kinetic energy flux at large scales is similar to the one for $t = 3.8$ with even a stronger flux from large scales toward $\kappa_h \simeq 2k_b$. The peak at large scales corresponding to the development of the KH billows has reached a value close to unity just before at $t = 4.5$. The conversion of kinetic into potential energies at wavenumbers $\kappa_h \simeq 2k_b$ is now much stronger indicating that the KH billows are efficient to displace isopycnals.

At the wavenumber $\kappa_h \simeq 3k_b$, kinetic and potential fluxes are nearly equal. In contrast to figure 3.15(a), the total flux, equal to $0.8\tilde{\varepsilon}$ between k_0 and $2k_b$, does not drop to zero but reach another plateau close to $\Pi(\kappa_h)/\varepsilon = 0.9$ down to the dissipation range. Let's note that the value of total fluxes corresponding to the two plateaus rapidly evolve with time with different dynamics. This positive flux at small scales is due to the destabilization of the KH billows and to the gravitational instability. At small scales, there is a conversion of potential energy back into kinetic energy (the dotted dashed curve goes down) which is driven by these instabilities and the associated transition to turbulence. This conversion leads to an increase of the kinetic energy flux and a decrease of potential energy flux (grey continuous curve) with a nearly constant total energy flux. Besides, the upscale energy fluxes at large scales have significantly decreased.

At later time $t = 5.2$ (figure 3.15c), dissipation is still close to $0.8\tilde{\varepsilon}$ but the plateau of kinetic energy flux has decreased to $0.5\tilde{\varepsilon}$. The new feature is that the total transfer at small scales is now dominated by the kinetic energy flux, the potential energy flux being nearly 2 times smaller. This may be the sign of a restratification with weaker overturning events. Moreover, the potential flux is remarkably flat from $\kappa_h \simeq 3k_b$ to the dissipative range and there is no energy conversion. This may indicate that the density at small scales is passively advected during the late decay.

Since the initial flow has no potential energy and since the energy conversion at large scales is weak during the life time of the dipole, no potential energy is available at large scales and the cascade of potential energy toward small scales should exist at the expense of the kinetic energy. This is evidenced by the fact that potential energy transfer $\Pi_P(\kappa_h)$ is almost always equal to the conversion of kinetic energy into potential energy $B(\kappa_h)$. Remarkably, $B(\kappa_h)$ always becomes positive when $\kappa_h \gtrsim k_b$, i.e. in the range of scales created by the development of secondary instabilities.

3.2.7 Summary and conclusions

We have presented a statistical analysis of the transition to turbulence from a columnar dipole in a stratified fluid. A series of instabilities and non-linear processes occurs in a particular and well-known time sequence leading to a breakdown into small-scale turbulence.

We have shown that the transition to turbulence occurring during the nonlinear evolution of the zigzag instability has a two-step dynamics. First, a shear instability feeds quasi-isotropic and fast Kelvin-Helmholtz billows with a vertical Froude number of order unity $F_{vKH} \sim 1$ and a typical scale of the order of the buoyancy scale, i.e. larger that the Ozmidov length scale. Second, the destabilisation of these structures and the gravitational instability generate a turbulence from the buoyancy scale to the dissipative range. This turbulent regime is weakly stratified because the associated larger structures are linked to vertical Froude number of order unity and are roughly isotropic, with horizontal and vertical characteristic length scales of the same order. Moreover, significant vertical motions due to overturnings exist in this regime.

The spectra have been shown to be strongly anisotropic. The horizontal spectra exhibit a $k_h^{-5/3}$ inertial range. Nevertheless, there is a deficit of energy in the range

between the large scales associated to the dipole and the buoyancy length scale. In contrast, there is an excess of energy at the buoyancy length scale. Remarkably, at smaller scales and down to the dissipative scales, the kinetic and potential energy horizontal spectra approximatively collapse respectively on the $0.5{\varepsilon_K}^{2/3}k_h^{-5/3}$ and $0.5{\varepsilon_K}^{2/3}k_h^{-5/3}\varepsilon_P/\varepsilon_K$ spectra. Thus the relation $E_P(k_h)/\varepsilon_P = E_K(k_h)/\varepsilon_K$ approximately holds as measured in numerical simulations of forced stratified turbulence. The vertical kinetic spectrum follows at large vertical scales a $C_N N^2 k_z^{-3}$ law, with $C_N \simeq 0.08$. For the largest values of the buoyancy Reynolds number $\mathcal{R}$, it presents a transition at the Ozmidov length scale l_o toward a $C{\varepsilon_K}^{2/3}k^{-5/3}$ spectrum, with $C \simeq 0.56$.

Thus, the anisotropic spectra share many characteristics with those obtained from numerical simulations of forced stratified turbulence and from measurements in the atmosphere and in the ocean. This is quite surprising because the initial flow is very simple and not turbulent. Moreover, the fundamental difference between a transition toward turbulence and developed turbulence has to be stressed. With only two vortices interacting, the dynamics at large horizontal scales is dominated by the nonlinear zigzag instability and there is no strongly stratified cascade. This contrasts with numerical simulations of forced stratified turbulence which exhibit a forward strongly stratified cascade but for which the overturning motions at the buoyancy length scale and beyond are not resolved or only weakly resolved due to the use of strongly anisotropic numerical meshes (see e.g. Koshyk & Hamilton, 2001; Lindborg, 2006; Waite, 2011).

Since the transition in the vertical spectra happens at the Ozmidov length scale, it is tempting to conclude that the overturning motions at the buoyancy scale are strongly anisotropic. However, this is not the case. Indeed, we have shown that the very steep vertical spectrum is mainly due to the large horizontal scales of the dipole strongly deformed by the zigzag instability. In contrast, the vertical spectrum computed with spectral modes with horizontal wavenumbers larger than the buoyancy wavenumber k_b does not present any k_z^{-3} power law but exhibits a $k_z^{-5/3}$ power law from a vertical wavenumber scaling like the Ozmidov wavenumber k_o down to the dissipative range.

In this paper, we have stressed the qualitative difference between the buoyancy length scale L_b and the Ozmidov length scale l_o. However, quantitatively, the ratio L_b/l_o scales like $F_h^{-1/2}$ and is therefore not very large for $F_h = O(0.1)$. In the present case, we can compute precisely the Ozmidov wavenumber

$$k_o = \left(\frac{C_N}{C}\right)^{3/4}\left(\frac{N^3}{\varepsilon_K}\right)^{1/2} = F_h^{-3/2}\left(\frac{C_N}{C}\right)^{3/4}\left(\frac{U^3}{\varepsilon_K R}\right)^{1/2}\frac{1}{R}, \tag{3.14}$$

and the buoyancy wavenumber $k_b = 2\pi/(10F_h)$. The ratio is therefore

$$\frac{k_o}{k_b} = F_h^{-1/2}\left(\frac{C_N}{C}\right)^{3/4}\left(\frac{U^3}{\varepsilon_K R}\right)^{1/2}\frac{10}{2\pi} \simeq 1.4F_h^{-1/2}, \tag{3.15}$$

and varies from 9.3 to 3.8 when F_h increases from 0.0225 to 0.135.

It has to be pointed out that recent results highlight the importance of the buoyancy length scale on forced stratified turbulence (Waite, 2011). Finally, we can conjecture that such nonlocal transfers linked to secondary instabilities act as a leak from the strongly stratified turbulent cascade toward a weakly stratified turbulence at and beyond the buoyancy scale. However, the horizontal scales larger than the buoyancy length scale dominate the vertical spectra down to the Ozmidov length scale.

Chapter 4

Studies of stratified turbulence forced with columnar dipoles

4.1 Experimental study of a forced stratified turbulent-like flow

Stratified turbulence forced with columnar dipoles. Part 1. Experimental study, on the edge of the strongly stratified turbulent regime

Pierre Augier, Paul Billant,
M. Eletta Negretti and Jean-Marc Chomaz
LadHyX, CNRS, École Polytechnique, 91128 Palaiseau Cedex, France

In preparation for submission to *J. Fluid Mech.*

Recent results show that strongly stratified turbulence has a three dimensional dynamic. A direct cascade associated with a $k_h^{-5/3}$ horizontal kinetic energy spectrum has been predicted when the buoyancy Reynolds number $\mathcal{R} = ReF_h{}^2$ is sufficiently large (Lindborg, 2006; Brethouwer *et al.*, 2007), where F_h is the horizontal Froude number and Re the classical Reynolds number. In order to check experimentally this hypothesis, we investigate a forced stratified turbulent-like flow generated by 12 vortex generators (flaps) placed on the side of a large stratified tank. The interactions of the randomly produced vortex pairs give rise to a statistically stationary disordered flow with a low horizontal Froude number and a buoyancy Reynolds number of order unity. PIV measurements in vertical cross-sections show that the flow organises itself into horizontal layers. When $\mathcal{R}$ is increased, we observe a transition from vertically sheared quasi-two dimensional flow dominated by large scale dissipation to a very different dynamic with vertical Froude number of order one, overturning events and abundant small scales. However, even for the largest $\mathcal{R}$ reached, horizontal compensated second order structure functions only exhibit a flattening when $\mathcal{R}$ is increased which we interpret as the first indication of the inertial range that is predicted at large $\mathcal{R}$. This suggests that experiments with a larger size are needed in order to acheive higher buoyancy Reynolds numbers and to test the direct cascade hypothesis.

4.1.1 Introduction

Atmospheric mesoscales are weakly influenced by rotation and strongly influenced by stable density stratification. These scales are characterized by a relatively large Rossby number and a low horizontal Froude number $F_h = U/(NL_h)$, with U and L_h representing the characteristic horizontal velocity and length scale, and N the Brunt-Väisälä frequency. Riley & Lindborg (2008) argue that these characteristics concern a large range of scales in the atmosphere (1 m $\lesssim L_h \lesssim$ 100 km) and in the oceans (1 m $\lesssim L_h \lesssim$ 1 km). They show that many geophysical data are compatible with a strongly stratified turbulent regime associated with a direct energy cascade.

The structure of stratified flows is characterized by thin horizontal layers (Riley & Lelong, 2000). This strong anisotropy implies that vertical gradients are high and play an important role in the dynamics. Vertical advective transport and vertical viscous diffusion act with two different characteristic length scales: respectively, the buoyancy

length scale $L_b = U/N$ and the viscous length scale $L_\nu = \sqrt{\nu L_h/U}$, where ν is the viscosity. The ratio between these two length scales is related to the buoyancy Reynolds number $\mathcal{R} = (L_b/L_\nu)^2 = ReF_h{}^2$, where $Re = UL_h/\nu$ is the classical Reynolds number Billant & Chomaz (2001); Hebert & de Bruyn Kops (2006a); Brethouwer *et al.* (2007). For geophysical flows, the buoyancy Reynolds number is typically very high even if F_h is small whereas it is difficult to establish a high buoyancy Reynolds number in laboratory experiments of strongly stratified flows (Praud *et al.*, 2005).

The layered structure can arise spontaneously through a generic instability, the zigzag instability, when several vertical vortices interact (Billant & Chomaz, 2000a; Billant, 2010; Billant *et al.*, 2010). This instability slices columnar vortices into "pancake" vortices with a vertical length scales L_v of the order of the buoyancy length scales so that their aspect ratio L_v/L_h scales like F_h.

Theoretically, the scaling law $F_v = U/(NL_v) \sim 1$ is linked to an invariance of the hydrostatic Boussinesq Euler equations that are valid in the limits $F_h \ll 1$ and $\mathcal{R} \gg 1$ (Billant & Chomaz, 2001). It implies that the potential and kinetic energies are of the same order and any wave-vortex separation is dynamically meaningless. This scaling law also suggests the possible development of instabilities. For example, the associated Richardson number $Ri \simeq 1/F_v{}^2$ is of order one, which means that pancake structures are potentially unstable to the shear instability. Similarly, the density perturbations are of the same order as the mean density gradient when $F_v \sim 1$ meaning that regions gravitationally unstable may appear.

Deloncle *et al.* (2008); Waite & Smolarkiewicz (2008) and Augier & Billant (2011) have shown that both shear and gravitational instabilities are active in the particular case of the non-linear development of the zigzag instability of a pair of counter-rotating vortices. More generally, this tendency to overturning and local shear instability could explain the local patches of turbulence observed in geophysical flows Gregg (1987) and numerical simulations (Hebert & de Bruyn Kops, 2006a).

It has to be noted that the governing equations in the limit $F_h \ll 1$ and $\mathcal{R} \gg 1$ are fully three-dimensional, in the sense that vertical and horizontal advections are of the same order of magnitude. The scaling law $F_v \sim 1$ means also that the potential vorticity is fully nonlinear, in contrast to quasi-geostrophic flows where its conservation implies an inverse energy cascade as in two-dimensional turbulence. Lindborg (2006) proposed an universal regime of strongly stratified turbulence associated with a stratified forward energy cascade. At each scale l_h, the structures are in a balanced state, meaning that their vertical length scale l_v is of the order of the associated buoyancy length scale $l_v \sim l_b \sim u(l_h)/N$, where $u(l_h)$ is the corresponding characteristic horizontal velocity. This implies that the vertical kinetic energy spectra goes like $E(k_v) \sim N^2 k_v^{-3}$, with k_v the vertical wavenumber (Billant & Chomaz, 2001). The hypothesis of local forward energy transfer implies that at each horizontal scale l_h, the kinetic energy flux $\Pi_K(l_h) \simeq u(l_h)^3/l_h$ is of the order of the kinetic dissipation ε_K. Thus, the horizontal kinetic energy spectra is equal to $E(k_h) = C_1 \varepsilon_K{}^{2/3} k_h^{-5/3}$, where k_h is the horizontal wavenumber and $C_1 \simeq 0.5$ is an universal constant (Lindborg, 2006).

According to this phenomenological theory, the energy goes through the scales

from the injection length scale L_h to the Kolmogorov length scale η via two kinds of forward cascades: via strongly stratified turbulence at large horizontal scales such that $F_h(l_h) < 1$ and via classical isotropic turbulence at smaller horizontal scales such that $F_h(l_h) > 1$. The transition between the two regimes defines the Ozmidov scale l_o for which $F_h(l_o) = \varepsilon_K^{1/3}/(N{l_o}^{2/3}) = 1$. Under the conditions of small horizontal Froude number and large turbulent buoyancy Reynolds number $\mathcal{R}_t = \varepsilon_K/(\nu N^2)$, the scales L_h, l_o and η are well separated: $l_o/L_h \sim F_h(L_h)^{3/2} \ll 1$ and $l_o/\eta \sim {\mathcal{R}_t}^{3/4} \gg 1$.

This theory of strongly stratified turbulence is attractive because of its simplicity and its ability to explain many numerical results (Riley & de Bruyn Kops, 2003; Waite & Bartello, 2004; Hebert & de Bruyn Kops, 2006a; Lindborg, 2006; Brethouwer *et al.*, 2007; Lindborg & Brethouwer, 2007) and in-situ observations (Riley & Lindborg, 2008). However, it does not explain all the observations such as for example the bump in the horizontal spectra observed at relatively small scales (Brethouwer *et al.*, 2007; Waite, 2011). A deep understanding of the mechanisms involved in the stratified cascade is not yet achieved. In particular, the role of the zigzag instability is not very well understood and the action of the shear and gravitational instabilities remains unclear. Finally, most of the simulations on forced stratified turbulence are performed using pseudo-spectral methods with periodic boundary conditions, characterised by the lack of walls. In these simulations, a large amount of energy accumulates in horizontally invariant, vertically sheared modes called "shear modes" (Smith & Waleffe, 2002). Lindborg (2006) argues that the continuous increase of the energy in the shear modes observed in many numerical simulations is linked to a viscous effect. Nevertheless, even for the simulations with large $\mathcal{R}$, the portion of energy in those modes is quite high, for example it represents $\sim 25\%$ of the total energy in the study of Brethouwer *et al.* (2007). Thus, it is likely that these shear modes influence all the cascade via highly non-local interactions. As a consequence, the numerical simulations need to be supported by experiments.

The main challenge to reproduce stratified turbulence in the laboratory is the fact that dissipation at large horizontal scales is important even if the Reynolds number is large. For example, Praud *et al.* (2005) have shown that experimental decaying grid turbulence in a strongly stratified fluid consists of quasi-horizontal motions in a sea of weak internal gravity waves. The dynamics which does not depend on the ambient stratification, is found to be dominated by a balance between the horizontal advective motion and the dissipation due to strong vertical shear. These results can be understood in the framework of the strongly dissipative, small vertical Froude number regime described in Godoy-Diana *et al.* (2004) and Brethouwer *et al.* (2007). Furthermore, most of the previous experiments consist in decaying turbulence generated by a grid (Itsweire *et al.*, 1986; Lienhard & Van Atta, 1990; Yoon & Warhaft, 1990; Fincham *et al.*, 1996; Praud *et al.*, 2005). During the decay, both Re and F_h decrease and the turbulence collapses into a strongly stratified flow. However, the time period during which both conditions $F_h < 1$ and $\mathcal{R} > 1$ are fulfilled is short and the flow is rapidly strongly influenced by the viscous effects due to vertical shear. Thus, it remains a challenge to obtain a strongly stratified fully turbulent flow in a laboratory experiment.

We present here a new experimental set-up of stratified disordered flows forced with columnar vortices. This set-up allowed us to obtain a buoyancy Reynolds number $\mathcal{R}$ of order unity during long time periods compared to previous experimental studies of decaying turbulence.

The paper is organised as follow. In Sec. 4.1.2, we describe the experimental setup. The flow is described in details in Sec. 4.1.3. First, we present the flow obtained for the highest buoyancy Reynolds number achieved. Then, we focus on the transition obtained when $\mathcal{R}$ is decreased. Finally, conclusions are offered in the last section.

4.1.2 Experimental design

Experimental setup

The experiments are carried out in a tank of 1 m $\times$ 2 m and 0.6 m deep filled with salt-stratified water. Since the purpose is to investigate strongly stratified turbulence, with a small horizontal Froude number together with the largest possible Reynolds number, we have set the strongest stratification possible with salt: at the surface, the water is fresh with a density equal to one and at the bottom of the tank, it is saturated with a density nearly equal to 1.2 leading to a constant Brunt-Väisälä frequency $N = \sqrt{-(g/\rho_0)(d\bar{\rho}/dz)}$ of 1.7 rad/s in all experiments, where g is the gravity, ρ_0 the mean density and $\bar{\rho}$ the basic density profile. The stable linear stratification is established by the well-known two tanks method by means of two computer-controlled volumetric pumps. The density profile is obtained by measuring with a densitometer the density of several small samples of fluid taken along the vertical. The comparison between results obtained before and after a set of experiments allowed us to verify that the density profile was not modified by the mixing. The kinematic viscosity ν slightly decreases from the bottom to the top from 1.6×10^{-6} m^2/s to 1.0×10^{-6} m^2/s. In the sequel, we neglect this variation and consider the viscosity at the middle depth $\nu \simeq 1.1\times10^{-6}$ m^2/s. The Schmidt number $Sc = \nu/D$ is around 700, where D is the diffusivity of salt.

As depicted in Fig. 4.1(a), the flow is generated by 12 dipole generators placed on the side of a large stratified tank. A generator is composed of two symmetric vertical plates whose closing create a counter-rotating vertical columnar vortex pair (Fig. 4.1b) as described by Billant & Chomaz (2000a). One motor drives two dipole generators as shown in Fig. 4.1(c). However, the 6 motors are independent and, hence, are run with random phases. Thus, each pair of generators produces periodically and independently pairs of dipoles which propagate toward the central part of the tank. Fig. 4.1(c) presents the driving device of two coupled dipole generators. The motor drives a cam with a pulley that pushes two levers fixed on the gears. The particular setting of the levers are chosen such that the dipole generators are closed slowly and smoothly and remain closed during some seconds. Then, they open slightly slower and remains again open for same time period before closing. By this way, the dipole are not perturbed by the subsequent opening of the flaps. Note also that the vortices created during the opening are trapped inside the generators and do not perturb the propagating dipoles. The only parameter that can be varied with this system is

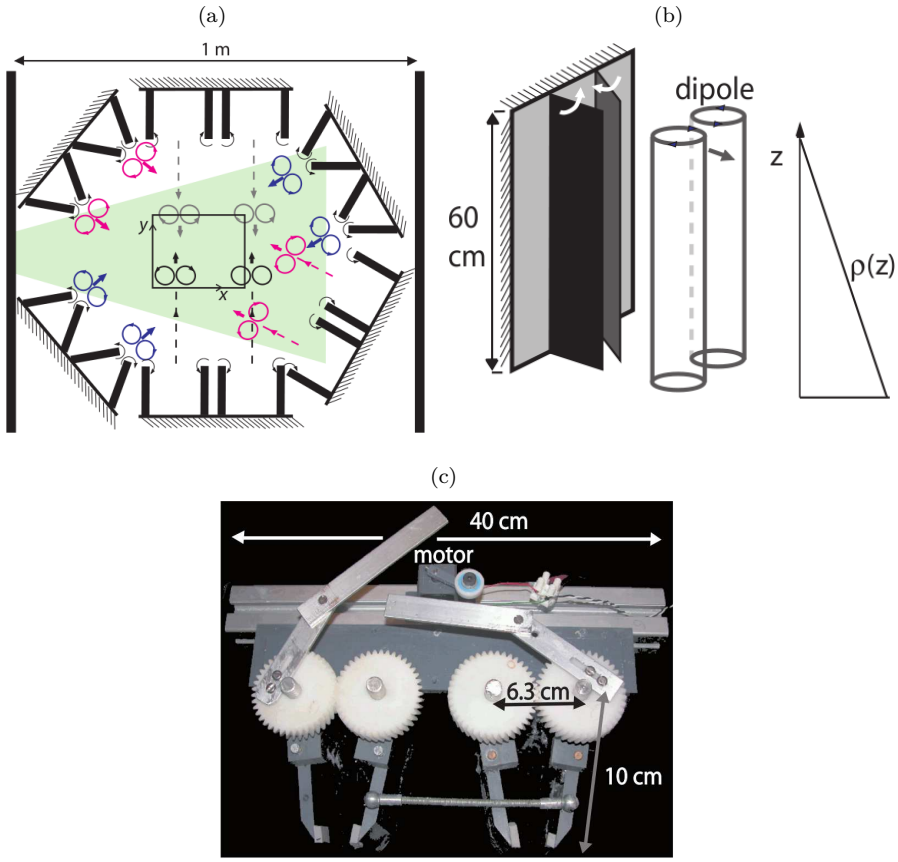

Figure 4.1: Sketch of the experimental apparatus. (a) Top view of the set-up from above. The dashed square indicates the field of view of the PIV. (b) Sketch of one dipole generator. (c) View from above of the motor and system driving a pair of vortex generators.

therefore the frequency of dipole generation f_i. When f_i is increased, not only the time interval between two successive dipoles decreases but the strength of the dipole increase as well. The frequency f_i has been varied between 0.03 and 0.07 Hz, i.e. one dipole is created by one flap every 14 s in the fastest cases and every 33 s in the slowest experiments.

Measurements of the velocity field have been obtained by Particle Image Velocimetry using FlowMaster software by LaVision. The image acquisition is made by a double-frame camera with resolution of 1280×1024 pixels. The laser sheet was produced by a 50mJ pulsed Nd:YAG dual head laser. As shown in Fig. 4.1(a), the field of view is located in the central part of the fluid volume encircled by the flaps. Velocity fields in vertical cross-section have been also measured by setting the laser sheet vertical. The fluid was seeded with particles made of ion-exchange resin (Purolite). We select particles with an adapted size (~ 50 μm) with filtrations through sieves. Only particles with a density distribution close to the density of the fluid are kept. The particles concentration is a crucial parameter: it should be large enough to achieve good PIV calculations but not too large to prevent a significant damping of the laser light. A concentration of approximately 0.1 particles by pixel has been found to be optimal.

The thickness of the light sheet was adjusted to 3 mm in the field of view in order to minimize the rate of particles that come in or escape the light sheet between two laser pulses. This thickness is not negligible compared to the velocity gradients and in some paires of images, particles with different velocities can be seen at the same location. However, most of the corresponding velocity vectors are eliminated during the PIV post-processing and thus not used to compute the velocity structure functions. In practice, it is easier to obtain the velocity field in horizontal cross-sections than in vertical ones. First, the mean vertical velocity is smaller than the mean horizontal velocity and second, it is easier to seed the fluid with an homogeneous spreading of the particles in horizontal cross-sections than in vertical ones. Thus, the quality of velocity fields is better in the horizontal direction than in the vertical direction. Since the forcing consists only in horizontal motions and the flow is strongly stratified, the vertical velocity is generally sufficiently small so that the variations of the refractive index are weak. Nevertheless, in order to obtain accurate measurements despite the variations of the refractive index due to small-scale mixing, each vector is calculated using a relatively large interrogation window of 64×64 pixels corresponding to physical dimensions of 6.8 mm for vertical cross-sections and 9.6 mm for horizontal cross-sections. Since there is a 50% overlapping this leads to a resolution of the velocity field of respectively 3.4 mm and 4.8 mm. In addition, no interpolation is used in order to have a measurement at the location where erroneous vectors have been eliminated. For this reason, only structure functions have been computed and not spectra since their computations would have required regularly spaced data.

Flow characteristics and relevant parameters

In order to characterize the vortices produced by the vortex generators, we have first carried out several experiments with only one module, i.e. one pair of dipole generator

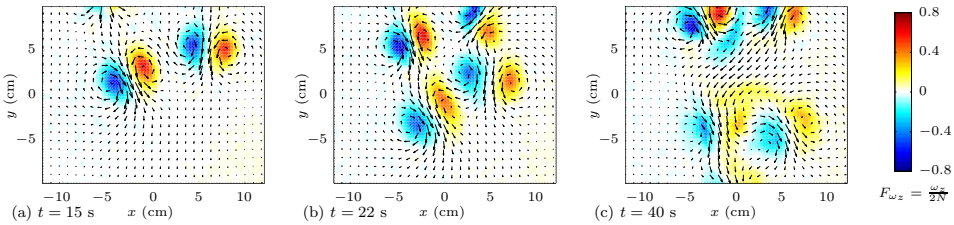

Figure 4.2: Horizontal cross-sections of the velocity field after switching on one module at $t = 0$ from rest. The vector fields are measured at $t = 15$s, 22s, 40s. The background colours represent the vertical vorticity scaled by twice the Brunt-Väisälä frequency, i.e. the local horizontal Froude number $F_{\omega_z} = \omega_z/(2N)$. The frequency of injection is $f_i = 0.05$ Hz and the corresponding non-dimensional numbers associated to the vortices are $Re = 290$, $F_h = 0.59$ and $\mathcal{R} = 100$.

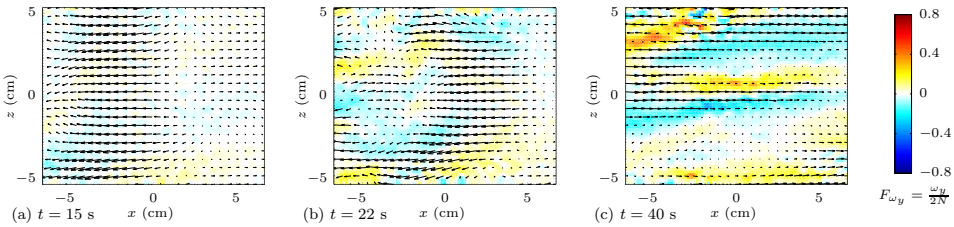

Figure 4.3: Vertical cross-sections of the velocity field after switching on one module at $t = 0$ from rest. Background colours represent the local vertical Froude number $F_{\omega_y} = \omega_y/(2N)$. Same times as in Fig. 4.2 but for $Re = 210$, $F_h = 0.41$ and $\mathcal{R} = 35$.

running. Fig. 4.2 shows one example of the flow evolution in a horizontal cross-section starting from a fluid at rest. The first two dipoles move obliquely toward the center of the tank and toward each other because of their mutual induction (Fig. 4.2a). At $t = 22$ s (Fig. 4.2b), two new dipoles have been created and start to interact with the first ones. Later on, at $t = 40$ s, another pair of dipoles has been created while the four dipoles generated previously have strongly interacted producing a disordered flow.

The characteristics of the dipole can be obtained by fitting the first vortices that are created (Fig. 4.2a) to pair of Lamb-Oseen vortices with vorticity:

$$\omega_z = \sum_{i=1,2} \frac{\Gamma_i}{\pi a^2} e^{\frac{-(x-x_i)^2-(y-y_i)^2}{a^2}} \tag{4.1}$$

where $(x_i,\ y_i)$ is the center of each vortex, Γ_i the circulation, a the vortex radius and $b = \sqrt{(x_1 - x_2)^2 + (y_1 - y_2)^2}$ is the separation distance between the 2 vortices of a dipole. Table 4.1 gives the parameters of the dipoles as a function of the frequency of dipole generation f_i (i.e. one flap produces one dipole every $1/f_i$ time period). The shape of the dipole, i.e. the vortex radius $a \simeq 18$ mm and the separation distance

f_i (Hz)	Ω (Hz)	Re	F_h	$\mathcal{R} = ReF_h{}^2$
0.031	0.4	120	0.24	7
0.040	0.7	210	0.41	35
0.052	1.0	290	0.59	100
0.062	1.27	370	0.75	210
0.071	1.45	430	0.85	310

Table 4.1: Overview of the non-dimensional parameters characterising the dipoles generated by the flaps as a function of the frequency of generation f_i.

$b \simeq 2a$, is almost independent of f_i as observed previously by Leweke & Williamson (1998) and Billant & Chomaz (2000a). In contrast, the maximum angular velocity of one vortex $\Omega = |\Gamma_i|/(2\pi a^2)$ increases approximately linearly with f_i as can be seen in Table 4.1. Based upon these parameters, we define the horizontal Froude number and Reynolds number as follows (Deloncle *et al.*, 2008):

$$F_h = \frac{\Omega}{N}, \qquad Re = \frac{\Omega a^2}{\nu}. \tag{4.2}$$

Since only Ω varies, the Froude and Reynolds numbers both increase linearly with f_i (Table 4.1). Another convenient definition of the horizontal Froude number has been also used:

$$F_{\omega_z} = \frac{\omega_z}{2N}, \tag{4.3}$$

where ω_z is the vertical vorticity. This local Froude number is shown in Fig. 4.2 as color contours. As can be seen, its maximum value is around 0.6 in agreement with the corresponding value of $F_h = 0.59$ for $f_i = 0.05$ (Table 4.1).

The maximum horizontal Froude number, obtained for the largest frequency f_i, is equal to 0.85. This value have to be compared to the threshold $F_h = 1$ above which the zigzag instability becomes damped by a critical layer (Billant, 2010; Billant *et al.*, 2010). Hence, the value 0.85 ensures that the zigzag instability should be fully active when the vortices interact. The growth rate of the zigzag instability scales with the strain exerted on a vortex by their companion. Its vertical wavelength λ_{ZZ} scales like $F_h b$. In the case of dipoles similar to those generated in this study, Billant & Chomaz (2000a) report a vertical wavelength of the zigzag instability around 6 cm. Vertical cross-sections of a similar flow but for $f_i = 0.04$ Hz are plotted in Fig. 4.3. We observe a transition from a state with a vertically invariant columnar vortex (Fig. 4.3a) to a flow organized in horizontal layers (Fig. 4.3c) through a bending of the vortex (Fig. 4.3b), which is the signature of the zigzag instability. Background colour represents the local vertical Froude number $F_{\omega_y} = \omega_y/(2N)$. We see that the process of vertical decorrelation leads to the formation of nearly horizontal vorticity sheets with a local vertical Froude number of order unity (Fig. 4.3c).

Another important non-dimensional parameter is the buoyancy Reynolds number $\mathcal{R} = ReF_h{}^2$ (Billant & Chomaz, 2001; Brethouwer *et al.*, 2007; Riley & de Bruyn Kops, 2003). This number measures the importance of viscous effects due to the vertical shear and it controls also the onset of small-scale instabilities (Deloncle *et al.*, 2008;

Waite & Smolarkiewicz, 2008; Augier & Billant, 2011). As indicated in Table 4.1, the maximum buoyancy Reynolds number reached for the fastest flow is equal to 310. This value can be compared to the threshold for the transition to small scales via the development of the shear instability found to be $\mathcal{R}_c = 340$ by Deloncle *et al.* (2008) for an isolated Lamb-Oseen dipole with $b/a = 2.5$. All the experiments are below this particular critical value so that an isolated dipole should not be subjected to the shear instability. However, the highest buoyancy Reynolds number achieved approaches the threshold and the ratio b/a is here lower. Furthemore, the interactions between dipoles should be another important source of small-scale instabilities.

In the next section, we shall present the results obtained with all the six modules switched on. After a transient flow looking like the flow described just before, the interactions between the periodically produced vortex pairs give rise to a statistically stationary disordered stratified flow. The only difference between the five flows presented is the value of the injection frequency f_i.

f_i (Hz)	U_h (mm/s)	P (mm^2/s^3)	Re_t	F_{ht} $\times 10^{-2}$	$\mathcal{R}_t$
0.031	2.1	0.04	450	0.5	0.01
0.04	3.4	0.15	800	0.8	0.05
0.052	4.5	0.4	900	1.2	0.1
0.062	5.3	0.8	900	1.7	0.25
0.071	6.0	1.2	1000	1.9	0.4

Table 4.2: Overview of the parameters characterising the turbulent-like flows in the statistically steady regime.

In order to characterized these turbulent-like flows, it is convenient to define also turbulent Froude, Reynolds and buoyancy Reynolds numbers as

$$F_{ht} = \frac{P}{{U_h}^2 N},\ Re_t = \frac{{U_h}^4}{P\nu} \text{ and } \mathcal{R}_t = \frac{P}{\nu N^2}, \tag{4.4}$$

respectively, where P is the mean energy injection rate and $U_h = \langle (u_x^2 + u_y^2)/2 \rangle_{xyt}^{1/2}$ the square root of the horizontal kinetic energy, the brackets $\langle \cdot \rangle_{xyt}$ denote an average over the horizontal cross-section x, y and time t. While it is easy to measure the characteristic horizontal velocity U_h for each frequency f_i, the total mean injection rate P needs to be estimated. We consider that 12 columnar dipoles are produced every $1/f_i$ seconds and that the kinetic energy of each dipole $\sim H\pi a^2 (a\Omega)^2$ spreads over the total volume $H\pi {R_h}^2$, where $R_h \simeq 0.4$ m is the radius of the fluid volume encircled by the flaps and H is the total water depth. These considerations lead to the following approximation for the mean injection rate $P \simeq 12 f_i \left(a/R_h\right)^2 \left(a\Omega\right)^2$. Since the flows are statistically stationary the total mean injection rate is of the order of the total dissipation rate ε. Thus, these global non-dimensional numbers can be compared to those employed in many numerical studies and in particular by Brethouwer *et al.* (2007). Table 4.2 summarizes the values of the parameters characterising the turbulent-like flows. Although one should not place importance

on the exact values, the orders of magnitude are consistent with the previous non-dimensional numbers associated to the injected vortices: the turbulent horizontal Froude number goes from very low to moderate values whereas the largest turbulent buoyancy Reynolds, $\mathcal{R}_t \simeq 0.4$, is not far from unity.

4.1.3 Description of the statistically stationary stratified flows

In this section, we present the results of the experiments with the 12 vortex generators running continuously. We first describe the turbulent-like flow obtained for the highest buoyancy Reynolds number $\mathcal{R} = 310$.

Description of the flow for the buoyancy Reynolds number $\mathcal{R} = 310$

Figs. 4.4 and 4.5 show the statistically stationary velocity fields at two different times for $\mathcal{R} = 310$ in horizontal and vertical cross-sections, respectively. The time interval between two snapshots is equal to 2 s, i.e. approximately one half of the Brunt-Väisälä period. The field of view is in the central region between the flaps (see Fig. 4.1a). The representation is the same as in Fig. 4.2 and 4.3 with horizontal and vertical local Froude number represented by the background colour. Each vector is calculated over an interrogation window of 32×32 pixels, corresponding to a resolution of 4.8 mm and 3.4 mm in Figs. 4.4 and 4.5 respectively. For the vertical cross-sections, a post-processing treatment has been used to fill the missing data (incorrect vectors) by interpolation using the neighbouring correct vectors. This method is used only here in order to show a nicer figure.

In Fig. 4.4 we see that there is a mean flow moving to the left at this particular depth. Because the horizontal Froude number is moderate for this flow, $F_h = 0.85$, the local horizontal Froude number F_{ω_z} associated to large scale structures can reach values just below unity. In the vicinity of the dipole generators, there are small scale structures associated to even larger F_{ω_z} as we can see for example in the bottom right corner of Fig. 4.4(a). Nevertheless, the typical size of the structures looks quite large.

In contrast, the vertical cross-sections in Fig. 4.5 show that the flow is strongly three-dimensional and organised into horizontal layers with small scales structures superimposed. A strong shear linked to a local vertical Froude number F_{ω_x} of order unity is visible in the middle of the cross-sections. This value corresponds to a Richardson number

$$Ri = \frac{-(g/\rho_0)(\partial \rho_{tot}/\partial z)}{|\partial \mathbf{u}_h/\partial z|^2} \simeq \frac{1}{4{F_{\omega_x}}^2}, \tag{4.5}$$

with ρ_{tot} the total density, of order 1/4 above which the shear instability could develop for an inviscid parallel stratified flow. Interestingly, we see small scale structures with quite large vertical velocity indicating that some energy is transferred from the large forced scales toward small scales. Actually, these small-scale structures could also be due to internal waves.

In order to further check the presence of gravity waves, Fig. 4.6 presents a spatio-temporal diagram of the vertical and horizontal velocity at a particular horizontal location $y = -0.2$ of Fig. 4.5. In the case of vertical velocity (Fig. 4.6a), we see

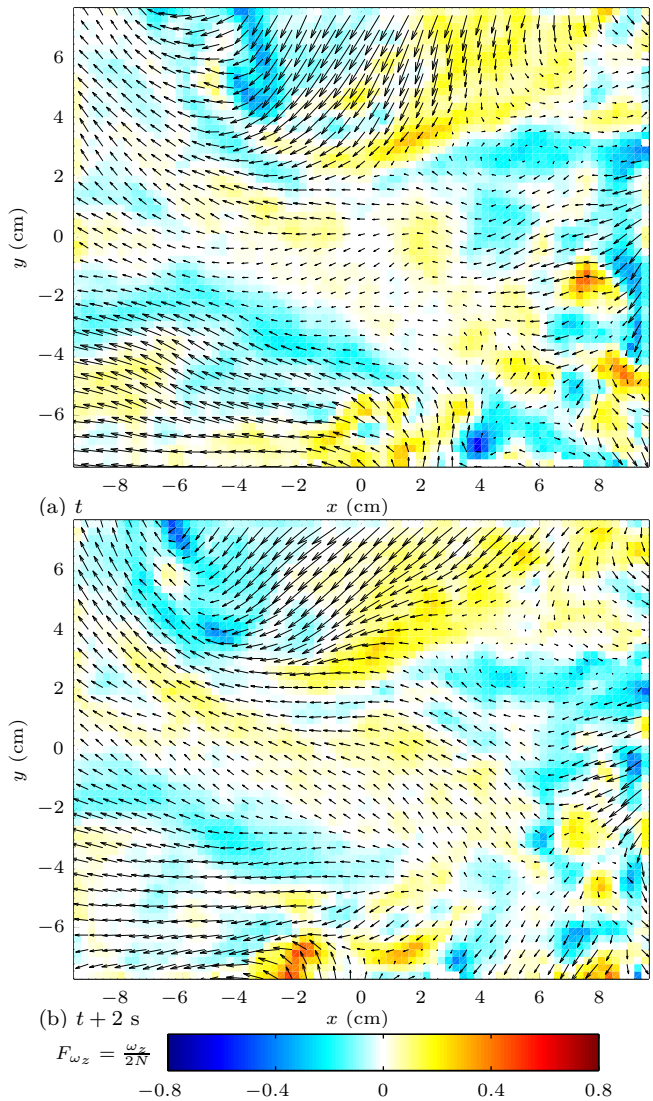

Figure 4.4: Velocity fields in a horizontal cross-section for $\mathcal{R} = 310$ at two different times: t (a), $t + 2$ s (b). The PIV resolution is 4.8 mm (each vector is calculated over a window of 32×32 pixels). Only half of the vectors are shown. The background color shows the horizontal Froude number F_{ω_z}.

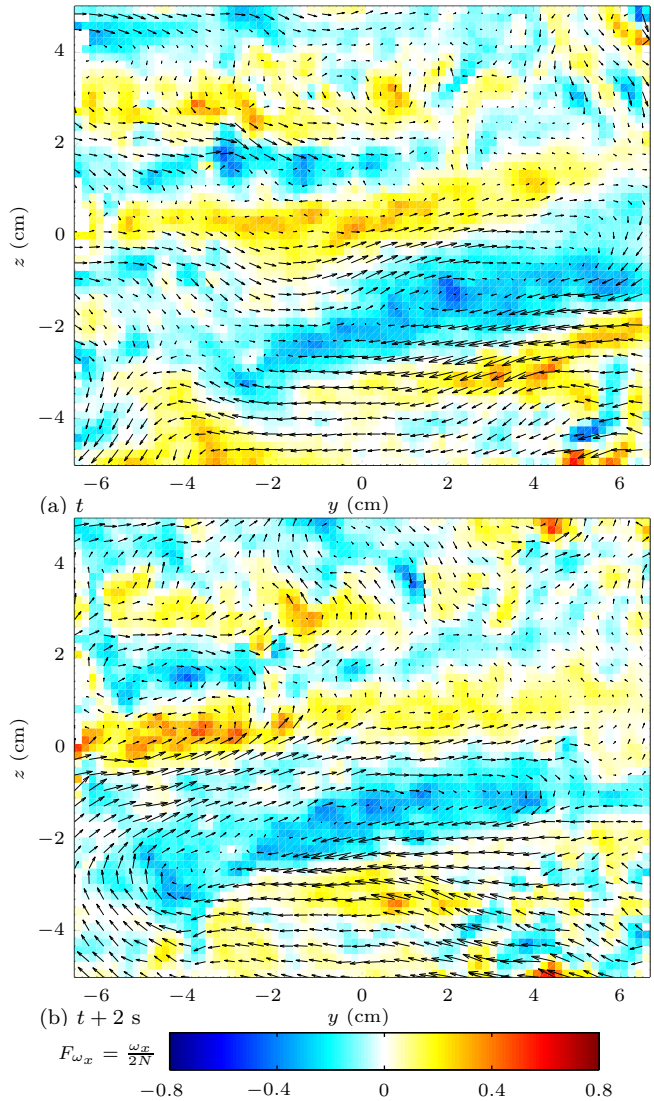

Figure 4.5: Velocity fields in a vertical cross-sections for $\mathcal{R} = 310$ at different instants: t (a), $t+2$ s (b). The PIV resolution is 3.4 mm (each vector is calculated over a window of 32×32 pixels). A post-processing treatment has been used to fill the missing data by means of an interpolation based on the correct vectors. Only one in two vectors are plotted.

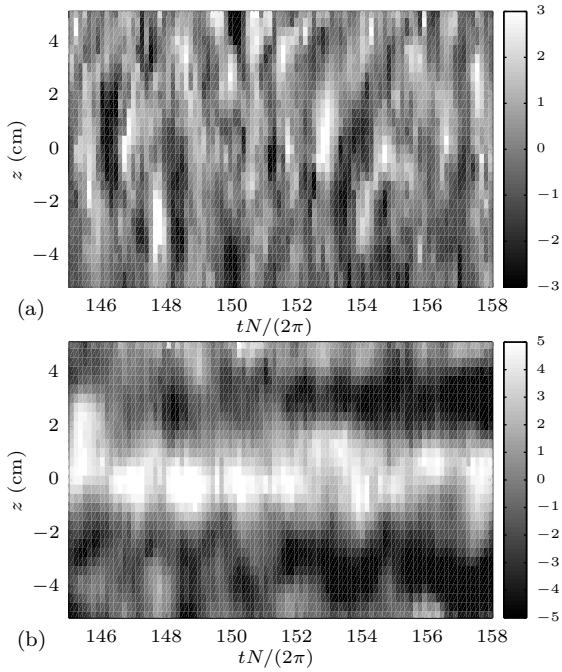

Figure 4.6: Spatio-temporal diagram of the vertical velocity $u_z(y = -0.2, z, t)$ (a) and of the horizontal velocity $u_y(y = -0.2, z, t)$ (a) as a function of the vertical coordinate and of time for $\mathcal{R} = 310$. The spatial resolution is 6.8 mm and the acquisition frequency is 2 Hz.

vertical strips alterning with a characteristic time scale of the order of the Brunt-Väisälä period. This indicates that there are some gravity waves in the experiment. However, we see also smaller motions with higher frequency linked to the presence of the small scale overturning motions. The horizontal velocity shown in Fig. 4.6(b) is dominated by sheared motions due to horizontal layering. However, some oscillations with a period $O(2\pi/N)$ are also visible. It has to be pointed out that in the limit $F_v \sim 1$, gravity waves and pancake vortices strongly interact together.

In Fig. 4.7, the mean horizontal velocity $U_y = \langle {u_y}^2 \rangle_{yz}^{1/2}$ and mean vertical velocity $U_z = \langle {u_z}^2 \rangle_{yz}^{1/2}$ averaged over the vertical cross-section y, z are plotted as a function of time. The recording starts five minutes after the time when the vortex generators have been switched on and last more than 15 minutes. Both mean velocities present no mean trend and seem to be statistically stationary. However, high fluctuations typical of turbulent flows can be seen. The mean vertical velocity is much lower than the mean horizontal velocity despite that the horizontal Froude number is of order unity ($F_h = 0.85$).

Fig. 4.8(a) shows the mean flow $\mathbf{U}_h = \langle \mathbf{u}_h \rangle_t$ in a horizontal cross-section obtained by averaging over 100 instantaneous velocity fields with a frequency of acquisition of

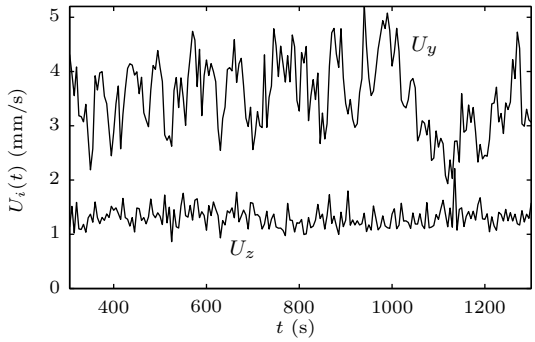

Figure 4.7: Horizontal and vertical averaged velocities as a function of time for $\mathcal{R} = 310$. For each time the velocities are obtained by averaging over the total vertical field of view.

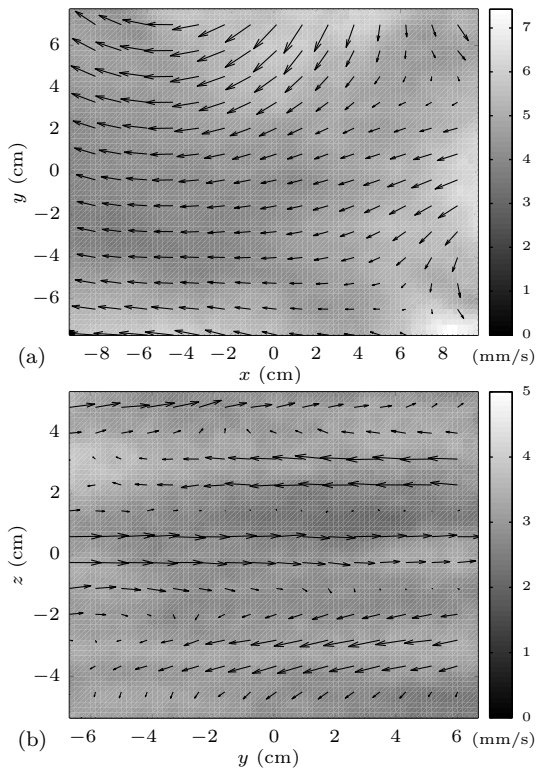

Figure 4.8: Horizontal cross-section of mean flow (vectors) and rms of the velocity fluctuations for $\mathcal{R} = 310$. The maximum mean velocity is 12 mm/s in (a) and 4 mm/s in (b).

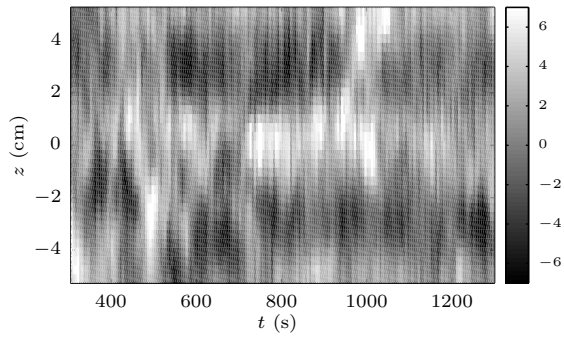

Figure 4.9: Space-time representation of the horizontal velocity averaged over the y direction, $\langle u_y \rangle_y$.

0.5 Hz (i.e. over a time period of 200 s). The vectors correspond to the mean flow and the grey contours represent the rms of velocity fluctuations $\langle |\mathbf{u}_h - \mathbf{U}_h|^2/2 \rangle_t^{1/2}$. We see that the mean flow is non zero with maximum values 12 mm/s. Such mean velocity is quite large since the instantaneous velocity is of the order of 20 mm/s. The mean flow goes leftward toward the open zone where the laser sheet go through and where there is no vortex generator (see Fig. 4.1a). The velocity fluctuations are also inhomogeneous with rms values approximatively twice larger near the dipole generators than in the less energetic central regions. This inhomogeneity is a drawback of the present forced flow compared to grid decaying turbulence. The maximum rms of velocity fluctuations is approximately twice smaller than the maximum mean flow velocity. Fig. 4.8(b) presents the same type of velocity decomposition but in a vertical cross-section. Horizontal flow in alternating direction and vertically sheared are clearly visible The mean velocity is smaller than in the horizontal cross-section with maximum values of 4 mm/s because the mean flow visible in Fig. 4.8(a) is oriented along the x direction.

In order to check the presence of horizontally invariant vertically sheared flow analogous to the "shear modes" frequently observed in numerical simulations of stratified turbulence, the horizontal velocity $\langle u_y \rangle_y$ averaged over the y direction is shown in Fig. 4.9 as a function of time and vertical coordinate. We see that such mean flow is not negligible with velocity up to 7 mm/s. The mean flow evolves slowly compared to the forcing time scale. For example, the white regions in the middle of Fig. 4.9 last for more than 200 s. The vertical characteristic wavelength is approximatively equal to 5 cm, which is of the order of the wavelength selected by the zigzag instability for a single dipole. This mean flow is only an indication of the presence of shear modes since real shear modes would correspond to a non-zero mean horizontal flow vertically sheared over the whole volume of the experiment whereas we have access only to a cross-section in the central part of the experiment. In addition, real shear modes are expected to be nearly zero in the experiment because of the presence of the vortex generators even if some fluid may escape through the spaces between them.

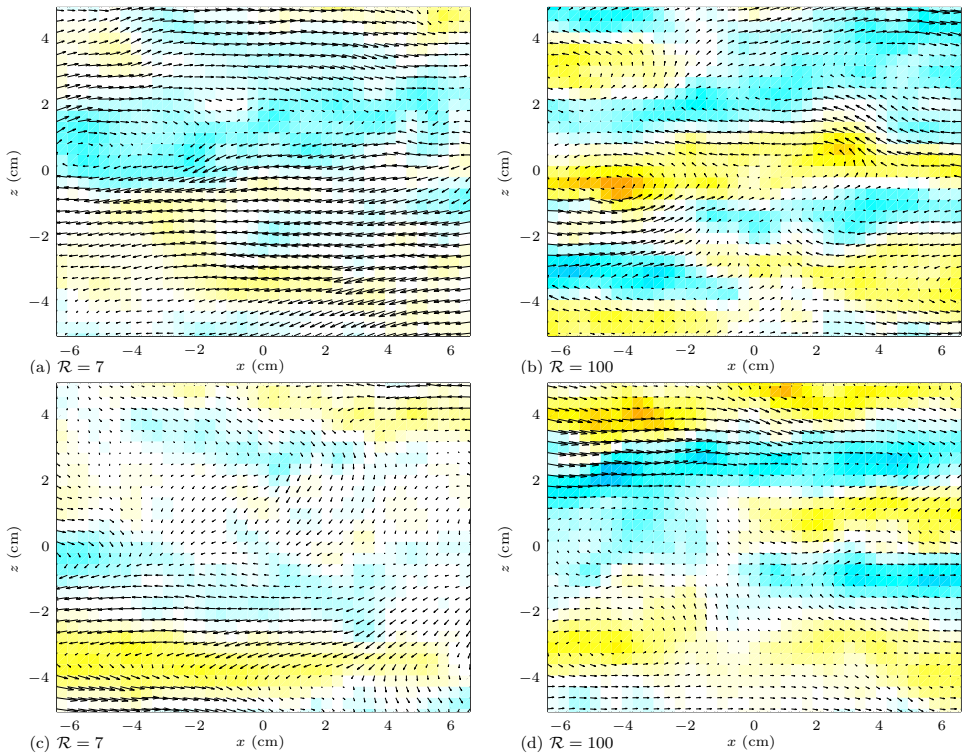

Figure 4.10: Vertical cross-sections of the velocity field for two different buoyancy Reynolds number $\mathcal{R} = 18$ (a, c), $\mathcal{R} = 100$ (b, d). For each $\mathcal{R}$, two snapshots separated by approximately 1 min are displayed. The representation is the same as in Fig. 4.3. Each vector is obtained from an interrogation window of 64×64 pixels, leading to a resolution of 6.8 mm.

Transition for decreasing buoyancy Reynolds number

Vertical structure

In this subsection, we focus on the effect of the buoyancy Reynolds number. Fig. 4.10 shows vertical cross-sections of two flows with buoyancy Reynolds numbers lower than in Fig. 4.5: $\mathcal{R} = 18$ and $\mathcal{R} = 100$. Unlike in Fig. 4.5, the fields are obtained from a PIV processing with interogation windows of 64×64 pixels, leading to a lower resolution of 6.8 mm so that the smallest scales of the flow of the order of the millimeter (see Fig. 4.5) are not resolved. However, the missing vectors are not interpolated so that all the vectors shown are correct. We can see clearly that the layers and structures are smoother when the buoyancy Reynolds number decreases. As shown by the color contours, the vertical Froude number F_{ω_x} reaches also lower maximum values when $\mathcal{R}$ decreases.

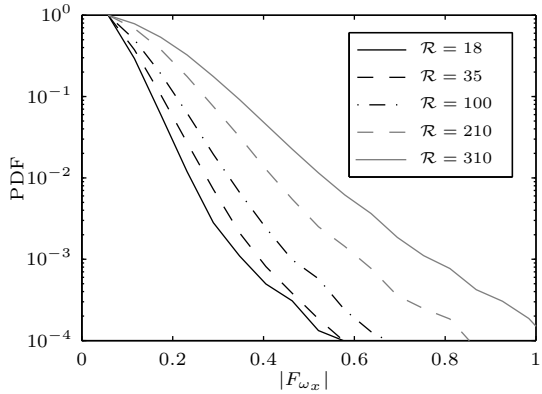

Figure 4.11: Probability density function of the local vertical Froude number $|F_{\omega_x}| = |\omega_x|/(2N) \simeq (4Ri)^{-1/2}$.

Fig. 4.11 presents probability density functions of the absolute value of the local vertical Froude number $|F_{\omega_x}| = |\omega_x|/(2N)$ for different buoyancy Reynolds numbers. We recall that this non-dimensional number is related to the local Richardson number $Ri \simeq 1/(4{F_{\omega_x}}^2)$. We see a regular increase of the maximum vertical Froude number when $\mathcal{R}$ is increased. For the highest buoyancy Reynolds number achieved $\mathcal{R} = 310$, the maximum value of $|F_{\omega_x}|$ is of order unity confirming that the shear instability should occur.

In order to quantify the vertical structure of the flow, we have computed second order transverse vertical structure functions $S_{2T}(z) = \langle[\delta u_x(z)]^2\rangle$ where $\delta u_x(z) = u_x(\mathbf{x} + z\boldsymbol{e_z}) - u_x(\mathbf{x})$, is the transverse velocity increment. Fig. 4.12(a) displays the quantity $z^{-2}S_{2T}(z)/(2{U_x}^2)$ for the five different $\mathcal{R}$. At the small dissipative scales at which the velocity is differentiable ($S_{2T} \simeq \langle[\partial_z u_x]^2\rangle z^2$), this quantity tends toward a constant equal to $1/{L_v}^2$, where L_v is the so-called microscale $L_v = (2{U_x}^2/\langle[\partial_z u_x]^2\rangle)^{1/2}$. We see that the quantity $1/{L_v}^2$ shown by the crosses in Fig. 4.12(a) varies by a factor two with $\mathcal{R}$. Note that the quantity L_v is here not exactly the real microscale of the flow since the small dissipative scales are not well resolved. Nevertheless, this length scale is expected to characterize reliably the vertical structure of the energetic vertical scales that are resolved. The evolution of this microscale when $\mathcal{R}$ is varied is shown in Figs. 4.12. Following Brethouwer *et al.* (2007), two different scaling are tested: a viscous scaling in Fig. 4.12(b) and an inviscid scaling in Fig. 4.12(c). The viscous scaling is obtained by balancing the dissipation due to vertical gradients and the horizontal advection $L_v \sim \sqrt{\nu a/U} \sim a/\sqrt{Re}$ (Godoy-Diana *et al.*, 2004). The inviscid scaling is obtained by balancing the buoyancy term to the horizontal advection so that $L_v \sim U/N \sim aF_h$ (Billant & Chomaz, 2001). Even if there are only few points with a weak variation, we see that the viscous scaling works at low $\mathcal{R}$ whereas the inviscid scaling is better at large $\mathcal{R}$. It is consistent with the interpretation of a transition from a viscous regime in which the vertical length scale is fixed by viscous

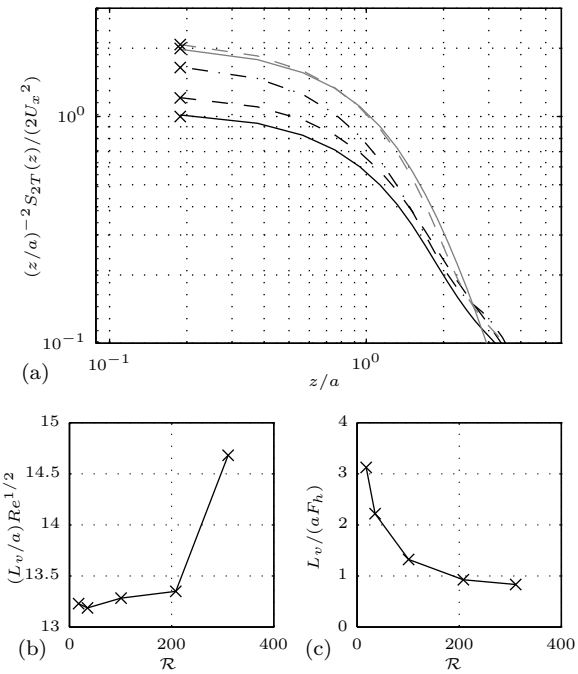

Figure 4.12: Variation of the vertical microscale L_v with $\mathcal{R}$. (a) Viscously compensated vertical structure function of order two ($(z/a)^{-2}S_{2T}(z)/(2U_x^2)$) for different $\mathcal{R}$: ($\mathcal{R}$ = 18, continuous black line), ($\mathcal{R}$ = 35, dashed black line), ($\mathcal{R}$ = 100, dashed dotted black line), ($\mathcal{R}$ = 210, continuous grey line) and ($\mathcal{R}$ = 310, dashed grey line). The crosses correspond to the inverse of the square of the calculated vertical microscales for each $\mathcal{R}$. (b) $(L_v/a)Re^{1/2}$ and (c) $L_v/(aF_h)$ as a function of $\mathcal{R}$.

effects (Godoy-Diana *et al.*, 2004), to a non-linear stratified regime for which the vertical length scale is fixed by an invariance of the hydrostatic Euler equations valid for strong stratification (Billant & Chomaz, 2001).

Horizontal structure

Fig. 4.13 displays two snapshots of the horizontal velocity field for two different values of the buoyancy Reynolds number lower than in Fig. 4.2: $\mathcal{R} = 7$ in Fig. 4.13(a) and $\mathcal{R} = 100$ in Fig. 4.13(b). The flow is dominated by larger scales than the injected scales. The central part of the tank is less energetic than the periphery near the vortex generators. In Fig. 4.13(a), we clearly see some coherent vortices interacting together. In contrast, we see much less coherent vortices in the meandering flows in Fig. 4.2 and 4.13(b). At very low buoyancy Reynolds number, the vortices that are created reach the central part of the tank while still being coherent. In contrast, at

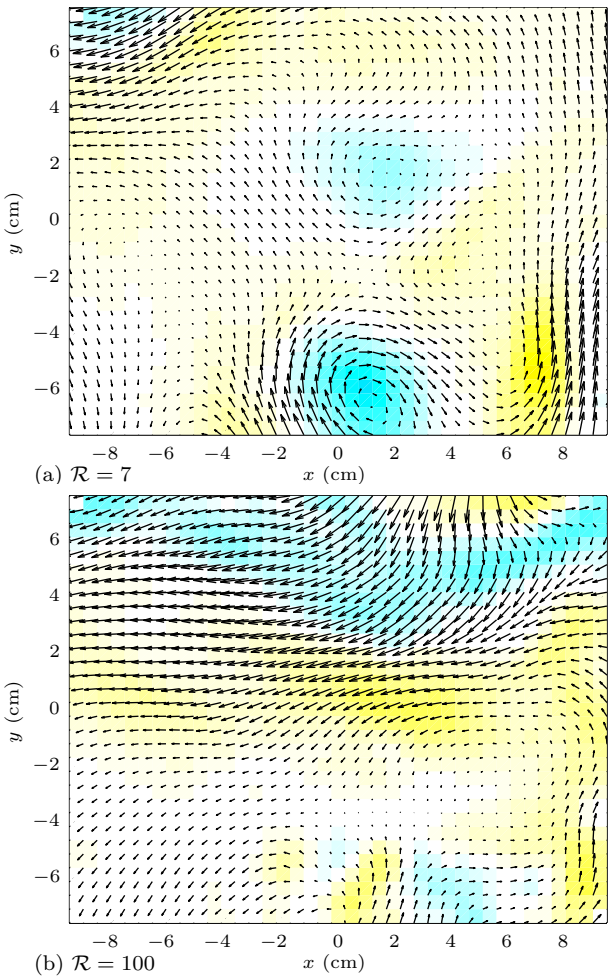

Figure 4.13: Horizontal cross-sections of the velocity field for two values of the buoyancy Reynolds numbers $\mathcal{R} = 7$ (a) and $\mathcal{R} = 100$ (b). The contours show the local horizontal Froude number and the colorbar is given in Fig. 4.2.

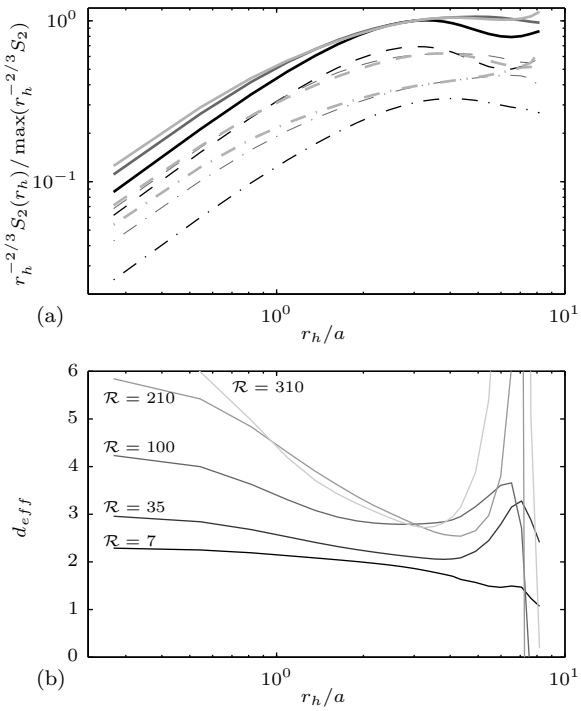

Figure 4.14: (a) Compensated total (heavy curves), transverse (dashed curves) and longitudinal (dotted dashed curves) horizontal second order structure functions for different $\mathcal{R}$: ($\mathcal{R} = 7$, black lines), ($\mathcal{R} = 100$, dark grey lines) and ($\mathcal{R} = 310$, light grey lines). (b) Effective dimension $d_{eff}(r_h) = 1 + (r_h \partial_{r_h} S_{2L})/(S_{2T} - S_{2L})$ as a function of the horizontal increment r_h scaled by a.

larger $\mathcal{R}$, the vortices are destabilized and interact with other vortices before reaching the field of view explaining why the flows look different. When the buoyancy Reynolds number is increased, the small scales are more abundant, especially in the vicinity of the vortex generators. Since the velocity vectors are obtained with large windows of 64×64 pixels, leading to a low resolution of 9.6 mm, they are reliable even in the mixed regions where the refractive index varies. These sets of data have been used to compute horizontal longitudinal $S_{2L} = \langle [\delta u_L(\mathbf{r})]^2 \rangle$ and transverse $S_{2T} = \langle [\delta u_T(\mathbf{r})]^2 \rangle$ second order structure functions plotted in Fig. 4.14(a). The thick lines correspond to the sum of compensated longitudinal and transverse structure functions $r_h^{-2/3}(S_{2T} + S_{2L})$ for three buoyancy Reynolds number: $\mathcal{R} = 7$ in black, $\mathcal{R} = 100$ in dark grey and $\mathcal{R} = 310$ in light grey. The power law at the smaller scales correspond to a r_h^{-2} slope which means that the data are globally differentiable. However, the dissipative range is not entirely resolved because of the low resolution. The differentiable propriety of the data has to be related to the PIV process: each vector corresponds to an average over a

quite large window with a 50% overlapping. A large inertial range would be associated to a structure function scaling like ${r_h}^{2/3}$ leading to a flat slope within a range of scale in Fig. 4.14(a), since the structure functions are compensated. However, we do not see such inertial range in Fig. 4.14(a), but when $\mathcal{R}$ increases, we see a flattening of the compensated structure functions at very large scales and a clear increase of the energy at the small scales. This could be the first indications of the inertial range that is predicted for large $\mathcal{R}$. The dashed and dashed dotted lines in Fig. 4.14(a) correspond to the transverse and longitudinal structure functions respectively. At large scales, S_{2T} largely dominates S_{2L} because the flow is forced by columnar vertical vortices. When $\mathcal{R}$ is varied, S_{2L} strongly increases at small scales leading to a flattening as if there were transfers from the transverse to the longitudinal functions.

This effect can be quantified and compared to isotropic turbulence in two- and three-dimensions. Assuming isotropy, the second order structure function tensor can be expressed in terms of the longitudinal and transverse second order structure functions

$$D_{ij}(r) = S_{2T}(r)\delta_{ij} + (S_{2L}(r) - S_{2T}(r))\frac{r_i r_j}{r^2},$$

where δ_{ij} is the Kronecker tensor (Frisch, 1995). Applying the incompressibility condition $\partial D_{ij}/\partial r_i = \partial D_{ij}/\partial r_j = 0$ shows that these two scalar structure functions are related by,

$$S_{2T}(r) = \left(1 + \frac{r}{d-1}\frac{\partial}{\partial r}\right) S_{2L}(r), \tag{4.6}$$

where d is the dimension of the space (Moisy *et al.*, 2009). For an anisotropic flow, we can introduce from (4.6) a so-called effective dimension,

$$d_{eff}(r_h) = 1 + \frac{r_h(\partial S_{2L})/(\partial r_h)}{S_{2T} - S_{2L}}. \tag{4.7}$$

This quantity is not a real dimension but is convenient to compare the relative behaviour of transverse and longitudinal functions. This effective dimension can be also related to the two points correlations of vertical vorticity and horizontal divergence computed by Lindborg (2007a) from atmospheric second order structure functions. In particular, the latter author shows that for an axisymmetric, incompressible, homogeneous flow, the correlation of horizontal divergence $D_h(r_h) = \langle \boldsymbol{\nabla}_h \cdot \mathbf{u}_h(\mathbf{x}) \boldsymbol{\nabla}_h \cdot \mathbf{u}_h(\mathbf{x} + \mathbf{r}_h) \rangle_{\mathbf{x}}$ is given by

$$D_h = -\frac{1}{2}\left[\frac{1}{r_h}\frac{\partial S_{2T}}{\partial r_h} - \frac{1}{{r_h}^2}\frac{\partial}{\partial r_h}\left({r_h}^2\frac{\partial S_{2L}}{\partial r_h}\right)\right]. \tag{4.8}$$

It is straightforward to rewrite this expression in terms of the effective dimension

$$D_h = \left(\frac{d_{eff} - 2}{d_{eff} - 1}\right)\frac{1}{2r_h}\frac{\partial}{\partial r_h}\left[r_h\frac{\partial S_{2L}}{\partial r_h}\right]. \tag{4.9}$$

Indeed, if $d_{eff} \simeq 2$, the correlation of horizontal divergence is negligible compared to the correlation of vertical vorticity.

The effective dimension computed for five different $\mathcal{R}$ are plotted in Fig. 4.14(b). The increase at larger scale is not physical, and originates from the non-homogeneity

of the flow and the particular forcing used. For the lowest $\mathcal{R}$ (black line), the effective dimension is close to 2 indicating that the velocity is dominated by two-dimensional horizontal flow even if there is strong vertical shear. For $\mathcal{R} = 35$ (grey line), the effective dimension goes from nearly 2 at large scale to nearly 3 at small scales. When $\mathcal{R}$ is further increased, the effective dimension goes from values near 3 at large scales to large values at the smaller resolved scales. This means that the longitudinal structure functions are larger than for isotropic turbulence. This could come from the shape of the Kelvin-Helmholtz billows which are indeed associated to very low transverse structure function. We have checked that this effect is not due to PIV errors. Similar trends are also obtained from numerical simulations of the same type of flow. These results will be reported in a forthcoming paper.

4.1.4 Summary and conclusions

We have set-up a novel experiment of continuously forced, stratified disordered flow with maximum turbulent buoyancy Reynolds number of order one and small horizontal Froude number $F_h < 1$. This set-up differs from previous experiments of stratified turbulence since the forcing consists in vertically invariant columnar vortex pairs generated intermittently. After an initial spontaneous three-dimensionalisation of the flow, a statistically stationary disordered state is reached.

The flow exhibits thin horizontal layers associated with relatively strong vertical gradients. When the frequency of dipole generation and circulation of the vortices are increased, both the buoyancy Reynolds number $\mathcal{R}$ and the horizontal Froude number increase and we observe a transition between two very different flow regimes. For very low $\mathcal{R}$ (and F_h), the flow is quasi horizontal and the structures are smooth suggesting that these experiments are in the viscosity affected stratified regime (Godoy-Diana *et al.*, 2004; Brethouwer *et al.*, 2007). On the contrary, for the largest $\mathcal{R}$ achieved, we observe small scale structures superimposed on the large scale horizontal layers, indicating that these experiments approach the strongly stratified regime (Brethouwer *et al.*, 2007). Consistently, the local vertical Froude number $F_{\omega_x} \equiv \omega_x/(2N)$ is of order unity. Vertical cross-sections show that overturnings are common features of the flow. We call this flow "stratified turbulence-like" because the maximum turbulent buoyancy Reynolds number is still quite small $\mathcal{R}_t \simeq 0.4$ compared to the values achieved in the numerical simulations where an inertial range has been observed (Brethouwer *et al.*, 2007). Thus, the horizontal second order structure functions do not exhibit any clear $r_h^{-2/3}$ slope but rather a flattening consistent with weak non-linear transfers toward small scales.

Hence, these experimental results need to be supported and extended. This can be done via two complementary ways: numerical and experimental. We are currently reproducing numerically the experimental flows with a pseudo-spectral code and a forcing very similar to the experimental one. The results globally support the experimental results. Moreover, the direct numerical simulations allows to extend the results toward higher $\mathcal{R}$ keeping F_h low and hence, to reach the strongly stratified fully turbulent regime.

Experiments with a larger size could be also carried out. Indeed, the present

experiment has a size $\sim$ 1 m only and it could be scaled up using large facilities. Thus, it seems reasonable to gain a factor 5 with vortices of radius $\sim$ 10 cm. Since the buoyancy Reynolds number $\mathcal{R} = ReF_h^2 = \Omega^3 a^2/(\nu N^2)$ goes like a^2 if Ω and N are kept constant, it should be possible to produce fully strongly stratified turbulence with a buoyancy Reynolds number of order 10, i.e. equivalent to the highest numerical resolution used by Brethouwer *et al.* (2007), and to overcome the viscous doom of stratified experiments.

We thank F. Moisy for helpful discussions. We are indebted to J.C. Boulay of Météo-France who designed and made the flaps, and to A. Garcia who assembled them.

Studies of stratified turbulence forced with columnar dipoles

4.2 Numerical study of strongly stratified turbulence

Stratified turbulence forced with columnar dipoles. Part 2. Numerical study

Pierre Augier, Paul Billant and Jean-Marc Chomaz
LadHyX, CNRS, École Polytechnique, 91128 Palaiseau Cedex, France

In preparation for submission to *J. Fluid Mech.*

This paper continues the experimental investigation of Augier *et al.* (2012b) in which a strongly stratified turbulent-like flow was forced by 12 generators of vertical columnar dipoles. These experiments report some first evidences for the existence of a strongly stratified inertial range that have been predicted for large buoyancy Reynolds number $\mathcal{R} = ReF_h{}^2$, where Re is the classical Reynolds number and F_h the horizontal Froude number. However, because of experimental constraints, the buoyancy Reynolds number could not be increased to sufficiently large values in order to fully reach the strongly stratified turbulent regime.

In order to extend the experimental results toward higher buoyancy Reynolds number, we have performed numerical simulations of forced stratified flows with a forcing similar to the one used experimentally. To reproduce the experimental vortex generators, columnar dipoles are periodically produced in spatial space at the peripheries of the computational domain. For moderate $\mathcal{R}$, these numerical simulations are able to reproduce the results obtained in the experiments, validating this particular forcing. For higher $\mathcal{R}$, the simulations show that the flow becomes turbulent as observed in Brethouwer *et al.* (2007). However, the statistically stationary flow is inhomogeneous because the dipoles are destabilized quite rapidly after their generation.

In order to produce a homogeneous turbulence, simulations have been carried out with a slightly modified forcing in which dipoles are forced at random location all over the computational domain. By means of high resolution simulations using a weak isotropic hyperviscosity, we have succeeded in achieving high turbulent buoyancy Reynolds numbers $\mathcal{R}_t = \varepsilon_K/(\nu N^2)$ of order 20, where ε_K is the mean dissipation rate of kinetic energy, ν the viscosity and N the Brunt-Väisälä frequency. The unidimensional horizontal spectra of kinetic energy and potential energy scale like $C_1\varepsilon_K^{2/3}k_h^{-5/3}$ and $C_2\varepsilon_K^{2/3}k_h^{-5/3}(\varepsilon_P/\varepsilon_K)$ respectively, with $C_1 = C_2 \simeq 0.5$. Especially for the highest values of $\mathcal{R}$, we observe a depletion in the horizontal kinetic energy spectrum for scales between the integral length scale and the buoyancy length scale and an anomalous energy excess around the buoyancy length scale probably due to direct transfers resulting from the shear and gravitational instabilities. Indeed, an abrupt increase of the horizontal buoyancy flux co-spectrum at the buoyancy scale is interpreted as a signature of the overturnings. Remarkably, the vertical kinetic energy spectrum exhibits a transition at the Ozmidov length scale from a steep spectrum scaling like $N^2k_z^{-3}$ at large scales to a spectrum scaling like $C_K\varepsilon_K^{2/3}k_h^{-5/3}$, with $C_K = 1$ the classical Kolmogorov constant.

4.2.1 Introduction

Remarkable progresses in the understanding of flows strongly influenced by stable density stratification and weakly influenced by rotation have been achieved during the first years of this century. These conditions concern in particular the meso-scales in the atmosphere and the submeso-scales in the oceans. At these scales, the spectra obtained in these two media present noticeable similarities and regularities (Garrett & Munk, 1979; Gargett *et al.*, 1981; Nastrom *et al.*, 1984; Nastrom & Gage, 1985; Riley & Lindborg, 2008). They are strongly anisotropic with different power laws along the vertical and the horizontal. The vertical spectrum of kinetic energy presents a $N^2 k_z^{-3}$ form, where N is the Brunt-Väisälä frequency and k_z the vertical wavenumber, whereas the horizontal spectrum of kinetic energy scales like ${\varepsilon_K}^{2/3} {k_h}^{-5/3}$, where ε_K is the mean kinetic energy dissipation rate and k_h the horizontal wavenumber. High resolution General Circulation models (GCM) and regional models start to resolve the meso-scales range and also to reproduce such $k_h^{-5/3}$ inertial range (Koshyk & Hamilton, 2001; Skamarock, 2004; Hamilton *et al.*, 2008). The anisotropy of the spectra is due to the strong influence of the stratification, which is expressed by a small horizontal Froude number $F_h = U/(NL_h)$, where U is a typical velocity and L_h a characteristic horizontal length scale. A ${\varepsilon_K}^{2/3} k_h^{-5/3}$ power law is an evidence for a cascade of energy but does not indicate in which direction the energy cascades. In the previous century, a direct cascade from large scales toward small scales was predicted by theories involving saturated gravity waves (Dewan & Good, 1986; Smith *et al.*, 1987; Hines, 1991; Dewan, 1997). An inverse cascade was predicted by a theory of stratified turbulence involving quasi-horizontal meandering motions of decoupled horizontal layers (Riley *et al.*, 1981; Lilly, 1983). However, Cho & Lindborg (2001) and Lindborg & Cho (2001) showed that the third-order structure function exhibits a negative linear dependence. This is an observational evidence supporting the forward energy cascade and thereby the gravity wave hypothesis. Nevertheless, Lindborg (2007a) computed spectra of vertical vorticity and horizontal divergence from aircraft data and showed that they are of the same order in the meso-scale range. This observation invalidates also the gravity wave hypothesis so that the 2 hypotheses mentioned above can not explain the anisotropic geophysical spectra.

However, in the mean time, a new theory of strongly stratified turbulence has emerged (Lindborg, 2006; Brethouwer *et al.*, 2007). This theory is quite different from the previous theories involving gravity waves or quasi-horizontal vortices. Since stratified flows exhibit thin horizontal layers (Riley & Lelong, 2000), it is fundamental to consider a second Froude number based on a vertical characteristic length scale L_v. The vertical Froude number $F_v = U/(NL_v)$ quantifies the interactions between the different horizontal layers and therefore the importance of three-dimensional processes. Many theoretical studies have been performed in the limits $F_h \ll 1$, $F_v \ll 1$ (Riley *et al.*, 1981; Lilly, 1983) whereas the scaling law $F_v \sim 1$ emerges through an invariance of the Boussinesq inviscid Euler equations under the condition $F_h \ll 1$ (Billant & Chomaz, 2001). In these limits $F_h \ll 1$, $F_v \sim 1$, propagative gravity waves and non-propagative horizontal vortices of potential vorticity (PV) strongly interact together and can not be considered separately.

Actually, the reason why the limit $F_v \ll 1$ was thought to apply to strongly stratified flows may come from a quantitative difference between the viscous effects in geophysical flows and in the flows produced experimentally or simulated numerically. The characteristic sizes of the geophysical flows are indeed so large that the Reynolds number Re is considerable and diffusive effects at these scales are negligible even if the structures are very thin with high vertical gradients. In contrast, at the laboratory scale, even the large scales of strongly stratified flows are usually influenced by dissipation. Vertical advective transport and vertical viscous diffusion act with two different characteristic length scales: respectively, the buoyancy length scale $L_b = U/N$ and the viscous length scale $L_\nu = \sqrt{\nu L_h/U}$, where ν is the viscosity. The ratio between these two length scales is related to the buoyancy Reynolds number $\mathcal{R} = (L_b/L_\nu)^2 = ReF_h{}^2$, where $Re = UL_h/\nu$ is the classical Reynolds number (Billant & Chomaz, 2001). In geophysical flows, the buoyancy Reynolds number is typically high even if F_h is small whereas it is difficult to establish a high buoyancy Reynolds number in laboratory experiments of strongly stratified flows (Praud *et al.*, 2005; Godoy-Diana *et al.*, 2004; Augier *et al.*, 2012b). In the regime of small buoyancy Reynolds number, the flow is quasi-two-dimensional with $F_v \ll 1$ and coupled along the vertical only by viscous effects (Godoy-Diana *et al.*, 2004) as originally proposed in the theory of Riley *et al.* (1981) and Lilly (1983).

Lindborg (2002, 2006) investigated the consequences for stratified turbulence of the inviscid scaling analysis of Billant & Chomaz (2001) performed for strongly stratified structures. He predicted and reported numerical simulations with highly anisotropic mesh and forced with vortical motions supporting the existence of a strongly stratified turbulent regime with a forward energy cascade and a horizontal spectrum of kinetic energy scaling like ${\varepsilon_K}^{2/3} k_h^{-5/3}$. Riley & Lindborg (2008) have argued that many geophysical data could be interpreted by this strongly stratified turbulent regime. These results have been confirmed with Direct Numerical Simulations (DNS) of stratified turbulence (Brethouwer *et al.*, 2007). These DNS show clearly that a condition on the buoyancy Reynolds number $\mathcal{R} = ReF_h{}^2 \gg 1$ or equivalently $\mathcal{R} = \varepsilon_K/(\nu N^2) \gg 1$ is fundamental to reach the strongly stratified turbulent regime characterized by $F_v \sim 1$ (Billant & Chomaz, 2001; Riley & de Bruyn Kops, 2003; Godeferd & Staquet, 2003; Waite & Bartello, 2004; Hebert & de Bruyn Kops, 2006b; Brethouwer *et al.*, 2007; Deloncle *et al.*, 2008; Augier & Billant, 2011). In this case, strong vertical shears appear. As a direct consequence, the development of Kelvin-Helmholtz instability has been observed leading to forward transfers toward small scales (Riley & de Bruyn Kops, 2003; Laval *et al.*, 2003; Hebert & de Bruyn Kops, 2006b). When the buoyancy Reynolds number is high enough, there should be also a transition to isotropic spectra at the Ozmidov length scale $l_o = (\varepsilon_K/N^3)^{1/2} \sim L_h {F_h}^{3/2}$ but no clear evidence has been reported by Brethouwer *et al.* (2007). Carnevale *et al.* (2001) reported such transition in Large Eddy Simulations (LES) of stratified flows forced with waves but their eddy damping is designed to favor the formation of a $k^{-5/3}$ range. Recently, Augier *et al.* (2012c) showed that such transition at the Ozmidov length scale occurs in the case of the breakdown into turbulence of a dipole. However, they pointed out that the characteristic size of the overturnings is of the order of the buoyancy length scale.

Waite & Bartello (2006a) and Lindborg & Brethouwer (2007) carried out numerical simulations forced with internal gravity waves. Waite & Bartello (2006a) forced the flow with isotropic waves and showed that the results differ from simulations forced with vortical motions described in Waite & Bartello (2004). In particular the scaling law $F_v \sim 1$ do not emerge from the wavy forced flows. However, Lindborg & Brethouwer (2007) showed that the strongly stratified turbulence is similar when forced with waves or with vortical motions provided that the vertical Froude number of the forced waves is of order unity.

In contrast to numerical studies, it has not yet been possible to produce strongly stratified turbulence in a laboratory experiment. The buoyancy Reynolds number in the experiments of Fincham *et al.* (1996) and Praud *et al.* (2005) is indeed typically too low. Recently, Augier *et al.* (2012b) have presented a new experimental set-up of maintained stratified disordered flows forced with columnar vortices. Such set-up enables to achieve $\mathcal{R}$ of order unity during long periods of time compared to previous experimental studies on decaying turbulence produced by towing a wake of vertical cylinders. The vertical Froude number is of order one and there are overturning events and abundant small scales for the highest buoyancy Reynolds number achieved. However, since $\mathcal{R}$ is still moderate, only the first indications of the inertial range that is predicted at large $\mathcal{R}$ have been observed. Hence, these experimental results need to be supported and extended to larger buoyancy Reynolds numbers.

In this paper, we carry out numerical simulations of strongly stratified flows forced with columnar dipole as in the experiments of Augier *et al.* (2012b). The forcing and the numerical methods are described in section 4.2.2. We first investigate a flow generated with a forcing resembling the experimental one in which dipoles are periodically produced at the periphery of the computational domain (section 4.2.3). In order to obtain larger buoyancy Reynolds number and to come closer to previous numerical studies of forced strongly stratified turbulence, we consider in section 4.2.4 a slightly different forcing in which columnar dipoles are produced randomly all over the computational domain.

4.2.2 Numerical methodology

Forcing method and definitions of the physical parameters

Disordered forced stratified flows with an uniform and stable stratification are simulated by means of a pseudo-spectral method with periodic boundary conditions solving the incompressible Navier-Stokes equations under the Boussinesq approximation (see Deloncle *et al.*, 2008, for details).

In order to reproduce the experimental vortex generators, vertical columnar counter-rotating vortex pairs are periodically produced in spatial space. Eight numerical dipole generators are placed on the side of the numerical box as shown by the grey rectangles in figure 4.15. They each produce periodically a dipole that propagates toward the central part of the box. The numerical domain is a rectangular box with sizes $\mathcal{L}_h = 30a$ in the two horizontal directions and size $\mathcal{L}_v = 12a$ in the vertical direction, where a is the radius of the vortices forced.

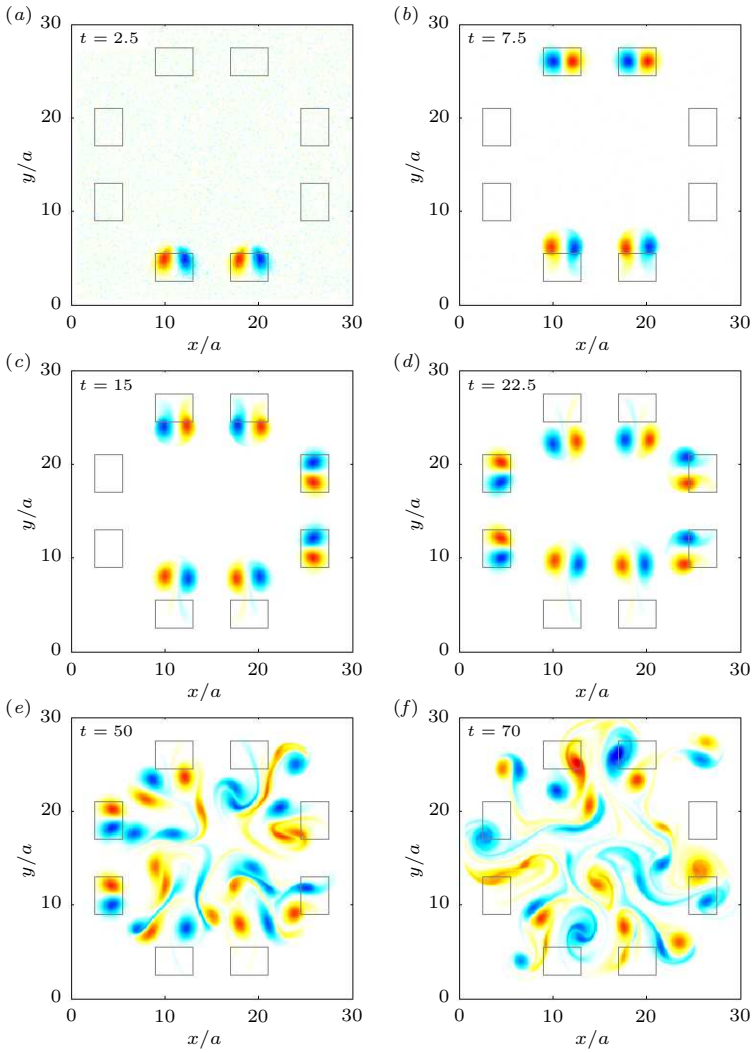

Figure 4.15: Horizontal cross-sections of the vertical vorticity field for six times at the beginning of a simulation for $Re = 600$ and $F_h = 0.85$. Two dipoles are forced every 7 time units. (a,b,c,d) correspond to the flow just after the first four forcing times $t = 0$, 7, 14, 21. (e,f) correspond to later times: $t = 50$ and $t = 70$. The grey rectangles indicate the location of the numerical dipole generators.

Figure 4.15 shows an example of horizontal cross-sections of the vertical vorticity for four times just after the beginning of a simulation and two times slightly later. At $t = 2.5$ (figure 4.15a), we see two dipoles that have been forced at the very beginning of the simulation. They have been generated by a constant force corresponding to four Lamb-Oseen vortices applied between times $t = 0$ and $t = 0.5$. This results in two dipoles very similar to the forcing field and to those observed in the experiments: each dipole can be approximated by a pair of Lamb-Oseen vortices with vorticity:

$$\omega_z = \sum_{i=1,2} \frac{\Gamma_i}{\pi a^2} e^{\frac{-(x-x_i)^2-(y-y_i)^2}{a^2}} \tag{4.10}$$

where $(x_i,\ y_i)$ is the centre of each vortex, $\Gamma_1 = -\Gamma_2$ their circulations and a their radius. For simplicity and without loss of generality, a and $\Omega^{-1} = 2\pi a^2/|\Gamma_i|$ are taken respectively as length and time units, i.e. are fixed to unity (Ω is the maximum angular velocity of the vortices). The same symbols are kept for the non-dimensional variables. This leads to the following definitions for the Froude number F_h, Reynolds number Re and buoyancy Reynolds number RR based on the forced vortices

$$F_h = \frac{\Omega}{N}, \qquad Re = \frac{\Omega a^2}{\nu}, \qquad \mathcal{R} = ReF_h{}^2, \tag{4.11}$$

where ν is the kinematic viscosity and $N = \sqrt{-(g/\rho_0)(d\bar{\rho}/dz)}$ the Brunt-Väisälä frequency (assumed constant), where g is the gravity, ρ_0 a reference density and $\bar{\rho}(z)$ the basic density profile. The total density is given by $\rho_{tot} = \rho_0 + \bar{\rho}(z) + \rho'$. The density perturbations ρ' are non-dimensionalized by $a|d\bar{\rho}/dz|$. The Schmidt number $Sc = \nu/D$, where D is the mass diffusivity, is set to unity throughout the paper.

The separation distance between the 2 vortices of a pair $b = \sqrt{(x_1 - x_2)^2 + (y_1 - y_2)^2}$ is set to $b = 2a$. Because of this relatively small separation, the vortices are slightly deformed after their generation as can be seen in figure 4.15(a).

The forcing is periodic in time with a period $\Delta t = 28$ meaning that two new dipoles are forced every $\Delta t/4 = 7$. Accordingly, we see two new dipoles at $t = 7.5$ (figure 4.15b). They have been just forced between $t = 7$ and $t = 7.5$ on the opposite side of the box. We can notice that the vortices are still almost circular. Figure 4.15(c) and (d) correspond to times $t = 15$ and $t = 22.5$ respectively, just after the forcing of the third and fourth pairs of dipoles in the right and left of the box. The forcing continues periodically exactly in the same way so that rapidly several columnar dipoles are present in the numerical box and interact together (figures 4.15e,f). Note that a white noise of small amplitude is added to the velocity field at $t = 0$ in order to allow the three-dimensionalization of the flows. In section 4.2.4, a slightly different forcing consisting in a randomly moving dipole generator will be used.

Figure 4.16(a) shows the time evolution of the kinetic energy (black continuous line) and potential energy (grey line). Figure 4.16(b) displays the total, kinetic and potential dissipation rate scaled by the mean injection rate $\bar{P}$ (continuous curves) and the injection rate $\tilde{P}(t)$ averaged over $\Delta t/4 = 7$ (grey curve). The instantaneous energy

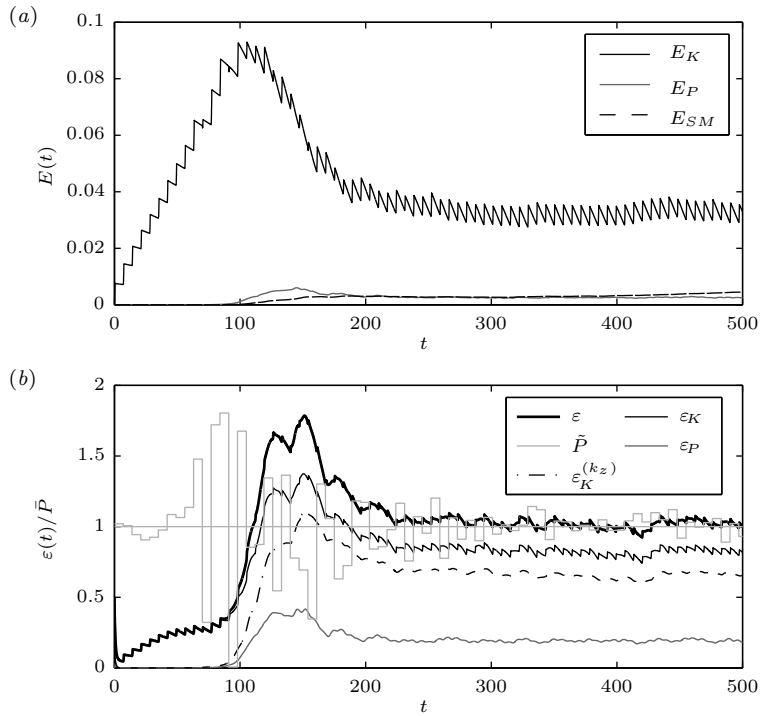

Figure 4.16: Temporal evolution of energy (a) and dissipation rate (b) for $F_h = 0.85$ and $\mathcal{R} = 450$ corresponding to the highest $\mathcal{R}$ obtained in the experiments. In (a), the dashed line corresponds to the energy associated to the shear modes. In (b), the dashed dotted line corresponds to the dissipation due to vertical gradient of horizontal velocity. The light grey staircase curve shows $\tilde{P}(t)$ the injection rate averaged over one injection period $\Delta t/4 = 7$.

injection rate $P(t)$ depends on the velocity field as (Alvedius, 1999)

$$P(t) = \frac{1}{2}\sum_{\mathbf{k}} \hat{\mathbf{f}} \cdot \hat{\mathbf{f}}^* \, dt + \frac{1}{2}\sum_{\mathbf{k}} (\hat{\mathbf{u}} \cdot \hat{\mathbf{f}}^* + \hat{\mathbf{u}}^* \cdot \hat{\mathbf{f}}), \tag{4.12}$$

where dt is the time step, * denotes the complex conjugate, $\hat{\mathbf{u}}$ is the Fourier transformed velocity, $\hat{\mathbf{f}}$ is the Fourier transformed force and the summations are taken over all wave vectors $\mathbf{k}$. The forcing used herein implies that the first term in the rhs of (4.12 is smaller than the second one in contrast to the forcing used by Lindborg & Brethouwer (2007).

Up to $t \simeq 80$, the kinetic energy increases linearly with time although staircases are present at each forcing time. For times between $t = 80$ and $t = 100$, the sharp increases become somewhat more erratic. This irregularity can be also seen in the injection rate $\tilde{P}(t)$ (figure 4.16b). Since the force is constant during the forcing events, the second

term in the rhs of (4.12) shows that the energy injection rate $P(t)$ depends directly on the velocity field at the location of the forcing. This effect is stronger when the velocity is large and when the flow is not yet fully three-dimensional. This explains why it occurs at $t \simeq 90$. Nevertheless, the forcing is able to produce coherent dipoles even when the background flow is fully turbulent.

Up to $t = 100$, the flow remains almost vertically uniform but around this time, the dissipation due to vertical gradient (dashed line in figure 4.16*b*) suddenly increases, showing that the flow is then fully three-dimensional. This process is associated to an increase of the potential energy (figure 4.16*a*) and of the potential energy dissipation (figure 4.16*b*) (grey lines). Between $t = 100$ and $t = 250$, the total dissipation rate (thick line) is larger than the injection rate such that the energy decreases. The flow reaches a nearly statistically stationary state only after $t = 250$. Although $\varepsilon/\bar{P} \simeq 1$, the flow is not exactly statistically stationary: the energy in the so-called "shear modes", i.e. the horizontally invariant modes (dashed line) slowly increases as first reported by Smith & Waleffe (2002). Lindborg (2006) argued that such growing shear modes are due to a too strong dissipation at large scales.

Choice of the physical and numerical parameters

The parameters of the main runs are summarized in table 4.3. The Froude and the Reynolds number have been varied in the ranges: $0.5 \leqslant F_h \leqslant 2$ and $120 \leqslant Re \leqslant 8000$. The Froude number range is approximately the same as in the experiments: $0.24 \leqslant F_h \leqslant 0.85$ but the Reynolds number range is significantly larger than in the experiments: $120 \leqslant Re \leqslant 430$. Like in the experiments (Augier *et al.*, 2012b), we define also turbulent Froude, Reynolds and buoyancy Reynolds numbers as follows

$$F_{ht} = \frac{\varepsilon_K}{{U_h}^2 N},\ Re_t = \frac{{U_h}^4}{\varepsilon_K \nu} \text{ and } \mathcal{R}_t = \frac{\varepsilon_K}{\nu N^2}, \tag{4.13}$$

where $U_h = \langle (u_x^2 + u_y^2)/2 \rangle^{1/2}$ is the square root of the horizontal kinetic energy and ε_K the mean kinetic dissipation rate into the statistically stationary regime.

In order to compare the numerical and experimental flows, we have performed simulations for $F_h = 0.85$ for three Reynolds number typically achieved in the experiments: $Re = 120$, 300 and 450. The corresponding values of the buoyancy Reynolds number are for $F_h = 0.85$: $\mathcal{R} = \mathcal{R}_{exp1} = 90$, $\mathcal{R} = \mathcal{R}_{exp2} = 220$ and $\mathcal{R} = \mathcal{R}_{exp3} = 330$. For each Froude number, several higher values of the Reynolds number have been investigated to extend the experimental results to high buoyancy Reynolds number. In table 4.3, the quantity $\mathcal{R}' = (Re - 400){F_h}^2$ is also indicated. As shown by Augier & Billant (2011), this parameter controls the onset of the shear and convective secondary instabilities on the zigzag instability, the critical value being $\mathcal{R}'_c = 4$.

The horizontal resolution is varied between $N_h = 192$ and $N_h = 768$ depending on the Reynolds number. The vertical resolution is chosen so that the numerical mesh is nearly isotropic. The vertical size of the numerical box $\mathcal{L}_z = 12$ is large compared to the characteristic vertical length scale of the layers developing in stratified flows. We use an adaptable time step procedure which maximizes the time step over a Courant-Friedrichs-Lewy condition (Lundbladh *et al.*, 1999). For the highest Reynolds

F_h	Re	$\mathcal{R}'$	$\mathcal{R}$	${N_h}^2 \times N_z$	F_h^t ($\times 100$)	Re_t	$\mathcal{R}_t$	ν_4 ($\times 10^{-13}$)
0.5	120	< 0	30	$192^2 \times 96$	1.6	130	0.03	0
0.5	300	< 0	80	$192^2 \times 96$	1.9	250	0.08	0
0.5	550	40	140	$256^2 \times 128$	1.9	420	0.15	0
0.5	1000	140	250	$384^2 \times 192$	2.0	680	0.27	5.0
0.5	3600	800	900	$384^2 \times 192$	1.8	2200	0.7	7.6
0.5	7900	1900	1980	$512^2 \times 256$	1.3	6900	1.2	1.4
0.66	490	40	210	$256^2 \times 128$	2.7	308	0.27	0
0.66	2200	800	970	$384^2 \times 192$	2.1	1900	0.87	6.0
0.66	4700	1900	2100	$512^2 \times 256$	1.7	5400	1.5	1.6
0.66	8000	3300	3500	$768^2 \times 192$	1.8	8600	2.7	0.066
0.85	120	< 0	90	$192^2 \times 96$	3.6	70	0.10	0
0.85	300	< 0	220	$192^2 \times 96$	3.8	170	0.23	0
0.85	450	40	330	$256^2 \times 128$	4.2	200	0.34	0
0.85	600	140	430	$256^2 \times 128$	4.0	280	0.44	0
0.85	1500	800	1080	$384^2 \times 192$	3.7	740	1.0	7.8
0.85	3000	1900	2170	$512^2 \times 256$	3.0	2000	1.7	1.1
1.0	120	< 0	120	$192^2 \times 96$	4.5	70	0.13	0
1.0	300	< 0	300	$192^2 \times 96$	4.6	150	0.32	0
1.0	436	40	440	$256^2 \times 128$	4.7	210	0.46	0
1.0	545	140	540	$256^2 \times 128$	4.7	250	0.55	0
2.0	120	< 0	480	$192^2 \times 96$	10	60	0.54	0
2.0	300	< 0	1200	$192^2 \times 96$	11	110	1.2	0
2.0	410	40	1640	$256^2 \times 128$	10	160	1.5	0
2.0	440	140	1760	$256^2 \times 128$	10	160	1.8	0

Table 4.3: Overview of the physical and numerical parameters of the simulations. The number of nodes in the horizontal and vertical directions are denoted, respectively, N_h and N_z. We recall that the length and time units is a and Ω^{-1} respectively. The numerical box has horizontal sides equal to $\mathcal{L}_h = 30$ and vertical side equal to $\mathcal{L}_z = 12$, except for the simulation for $F_h = 0.66$ and $Re = 8000$ for which the length of the vertical side is divided by 2. For all the simulations, the mean injection rate $\bar{P}$ is of the order of 0.001.

numbers, we add to the classical dissipation a weak isotropic hyperviscosity $-\nu_4\mathbf{k}^8$, where $\mathbf{k}$ is the wavenumber and ν_4 a constant coefficient (Augier *et al.*, 2012c).

The vertical size of the box is reduced to $\mathcal{L}_z = 6$ in the simulation for the largest buoyancy Reynolds achieved $\mathcal{R} = 3500$, corresponding to $F_h = 0.66$ and $Re = 8000$. This value of $\mathcal{L}_z$ is still sufficient to have several layers along the vertical.

4.2.3 Numerical forcing similar to the experimental one

In this section, we first describe the numerical simulations for the values of F_h and $\mathcal{R}$ achieved in the experiments. The simulations for much higher values of $\mathcal{R}$ are then presented.

Parameters similar to the experimental ones

Figure 4.17 displays horizontal and vertical cross-sections of the flow for $F_h = 0.85$, $\mathcal{R} = \mathcal{R}_{exp3} = 330$ and for a time $t = 475$ corresponding to the statistically stationary regime. The periphery of the numerical box has been cropped and only a central portion is shown. Four dipole generators indicated by grey lines can be seen. The colors in this figure represent the local horizontal Froude number $F_{\omega_z} = \omega_z/(2N)$, where ω_z is the vertical vorticity. As expected, the extrema of this quantity are of the same order as the global horizontal Froude number $F_h = 0.85$. Vortices are seen only in the vicinity of the vortex generators. This is because they are destroyed by instabilities before reaching the central part of the box. Such strong instability renders the flow inhomogeneous as observed in the experiments. Superposed to the large scale vortices, there are also small scale structures. The nature of these structure can be understood by looking at figure 4.17(b), where the isopycnals are plotted in black lines. We see rollings of the isopycnals typical of the shear instability (Deloncle *et al.*, 2008; Augier & Billant, 2011). In this figure, the colors correspond to the local vertical Froude number $F_{\omega_y} = \omega_y/(2N)$, where ω_y is the y-component of the vorticity. This number compares locally the horizontal vorticity (which is of the order of the vertical gradients in strongly stratified flows) to the mean stratification. This Froude number can be used to quantify approximately the local Richardson number:

$$Ri = \frac{-(g/\rho_0)(\partial\rho_{tot}/\partial z)}{|\partial\mathbf{u}_h/\partial z|^2} \simeq \frac{1}{4|F_{\omega_y}|^2}, \tag{4.14}$$

Although this relation neglects local density perturbations, it shows that a value $F_{\omega_y} \simeq 1$ correspond to a Richardson number of order $1/4$. This is exactly the critical value above which the shear instability can develop for an invicid parallel stratified flow (Miles, 1961; Howard, 1961). We see that $|F_{\omega_y}|$ is indeed high and of order unity in the regions where the rollings of the isopycnals occur. This confirms indirectly that the shear instability was operating in the experiments for the highest buoyancy Reynolds number achieved $\mathcal{R}_{exp3} = 330$.

Figure 4.18(a) shows the mean kinetic energy $\langle|\mathbf{u}|^2/2\rangle_{zt}$ averaged over the vertical coordinate z and over 20 instantaneous fields belonging to the statistically stationary regime for $F_h = 0.85$ and $\mathcal{R} = 220$. Figure 4.18(b) shows the quantity $\nu\langle|\boldsymbol{\omega}|^2\rangle_{tz}/\bar{P}$

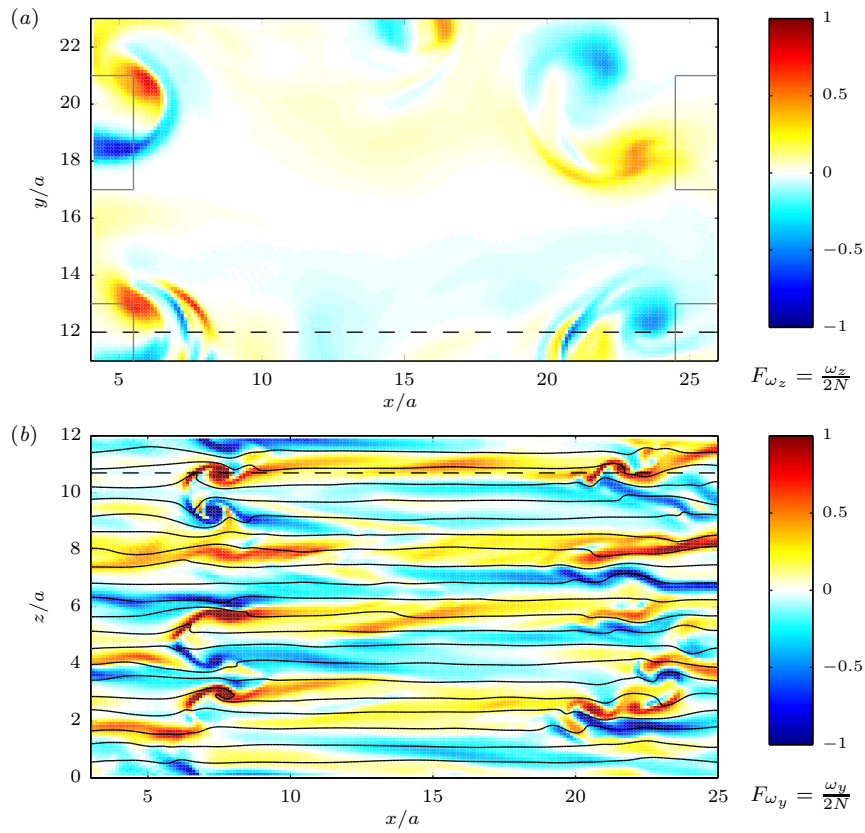

Figure 4.17: Horizontal (a) and vertical (b) cross-sections of the flow for $F_h = 0.85$ and $\mathcal{R} = 330$ and for a time $t = 475$ corresponding to the statistically stationary regime. The contours represent the local horizontal Froude number F_{ω_z} in (a) and the local vertical Froude number F_{ω_y} in (b). The dashed horizontal lines indicate the location of the cross-section in the perpendicular direction. The black lines in (b) are isopycnals. The contour interval of total density is equal to 0.6.

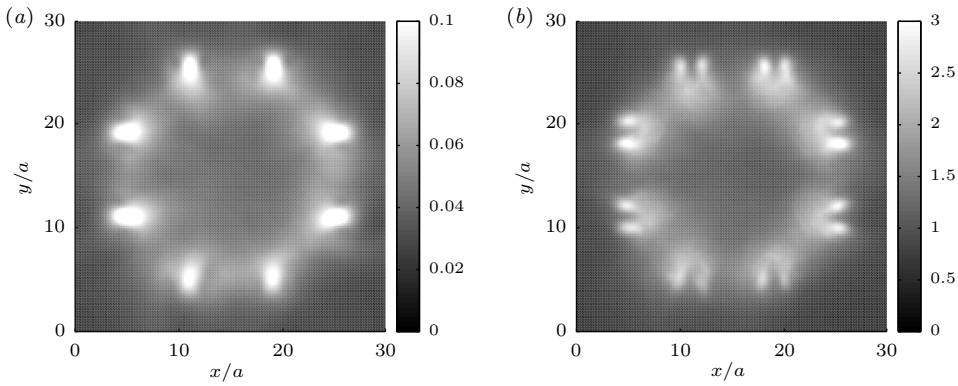

Figure 4.18: Horizontal cross-section of the mean kinetic energy $\langle |\mathbf{u}|^2/2 \rangle_{zt}$ in (a) and of the mean enstrophy scaled by $\bar{P}/\nu$ in (b) for $F_h = 0.85$ and $\mathcal{R} = 220$.

which is an estimation for the normalized local kinetic dissipation $\varepsilon_K(\mathbf{x})/\bar{P}$. We see that both the energy and the enstrophy concentrate in the vicinity of the vortex generators showing that the flow is quite inhomogeneous as in the experiments. This confirms that the dipoles are destabilized quite rapidly, so that they are not able to propagate as far as the centre of the numerical box.

In the experiments, small-scale structures and overturnings were observed only for sufficiently high buoyancy Reynolds number. In order to investigate this point, figure 4.19 displays vertical cross-sections of F_{ω_y} for three different values of the buoyancy Reynolds number $\mathcal{R} = 90$, 220 and 330 and for the same horizontal Froude number $F_h = 0.85$. The plots show close-up views in one particular region of intense overturnings. For $\mathcal{R} = 330$ (figure 4.19c), the isopycnals are clearly overturned by small billows in the region where the local vertical Froude number F_{ω_y} is of order unity. In contrast, the overturnings are weak for $\mathcal{R} = 220$ (figure 4.19b) and no overturned isopycnals are observed for $\mathcal{R} = 90$ (figure 4.19a). Accordingly, we can see that the extrema of F_{ω_y} decreases with $\mathcal{R}$. In the corresponding horizontal cross-sections (figure 4.20), we clearly see the appearance of small scales superimposed on the large scale vortices when $\mathcal{R}$ is increased.

In the experimental study (Augier *et al.*, 2012b), this transition has been quantified by measuring horizontal longitudinal $S_{2L} = \langle [\delta u_L(\mathbf{r})]^2 \rangle$ and transverse $S_{2T} = \langle [\delta u_T(\mathbf{r})]^2 \rangle$ second order structure functions, where $\delta u_L(y) = u_y(\mathbf{x} + y\boldsymbol{e_y}) - u_y(\mathbf{x})$ are the increments of longitudinal velocity and $\delta u_T(y) = u_x(\mathbf{x} + y\boldsymbol{e_y}) - u_x(\mathbf{x})$ the increments of transverse velocity. Figure 4.21(a) shows these quantities compensated by $r_h^{-2/3}$, where $r_h = y$, for four different values of the buoyancy Reynolds numbers from $\mathcal{R} = 90$ to $\mathcal{R} = 430$ and for fixed horizontal Froude number $F_h = 0.85$. The increment r_h is scaled by $R = 2b$, the characteristic length scale of the dipoles that are forced. The power law at the smaller scales correspond to a ${r_h}^2$ slope meaning that the dissipative range is resolved. An inertial range is associated to a structure function scaling like ${r_h}^{2/3}$, i.e. a flat slope for the compensated structure functions.

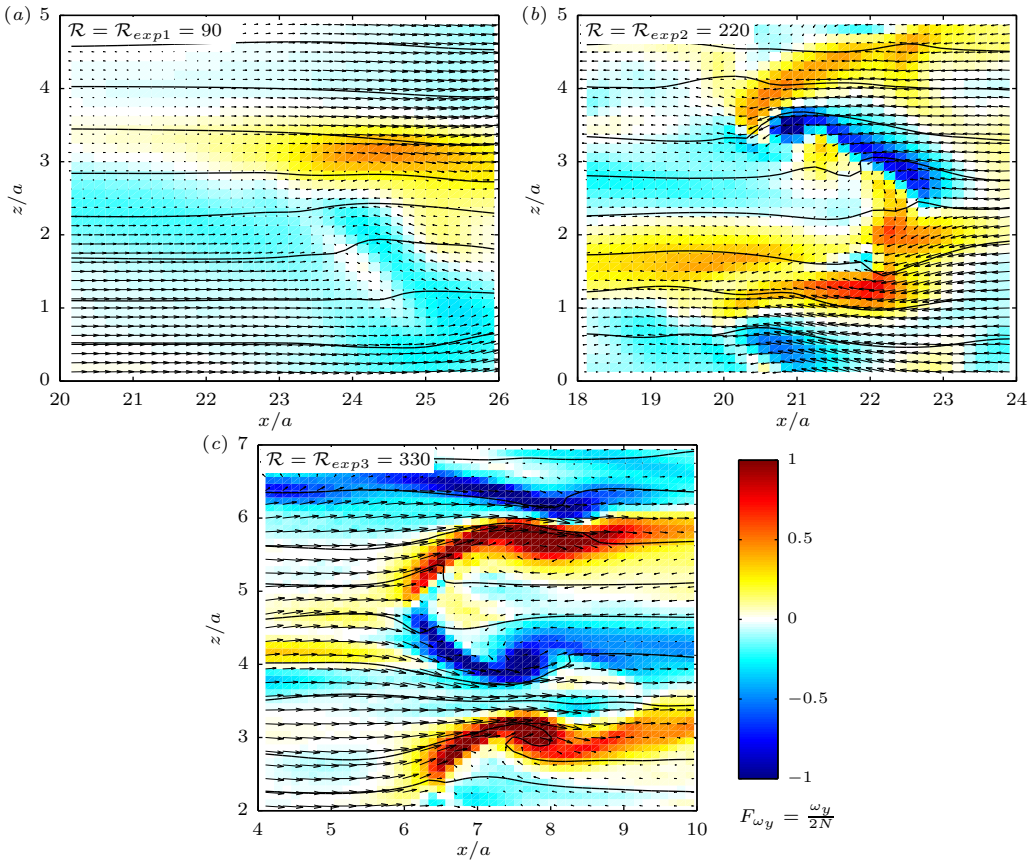

Figure 4.19: Vertical cross-section of the velocity field and $F\omega_y$ for $F_h = 0.85$ and for three different values of the buoyancy Reynolds number $\mathcal{R} = 90$ (a), 220 (b) and 330 (c). Only a small portion of the box is shown. The contours represent the local vertical Froude number. The black lines are isopycnals.

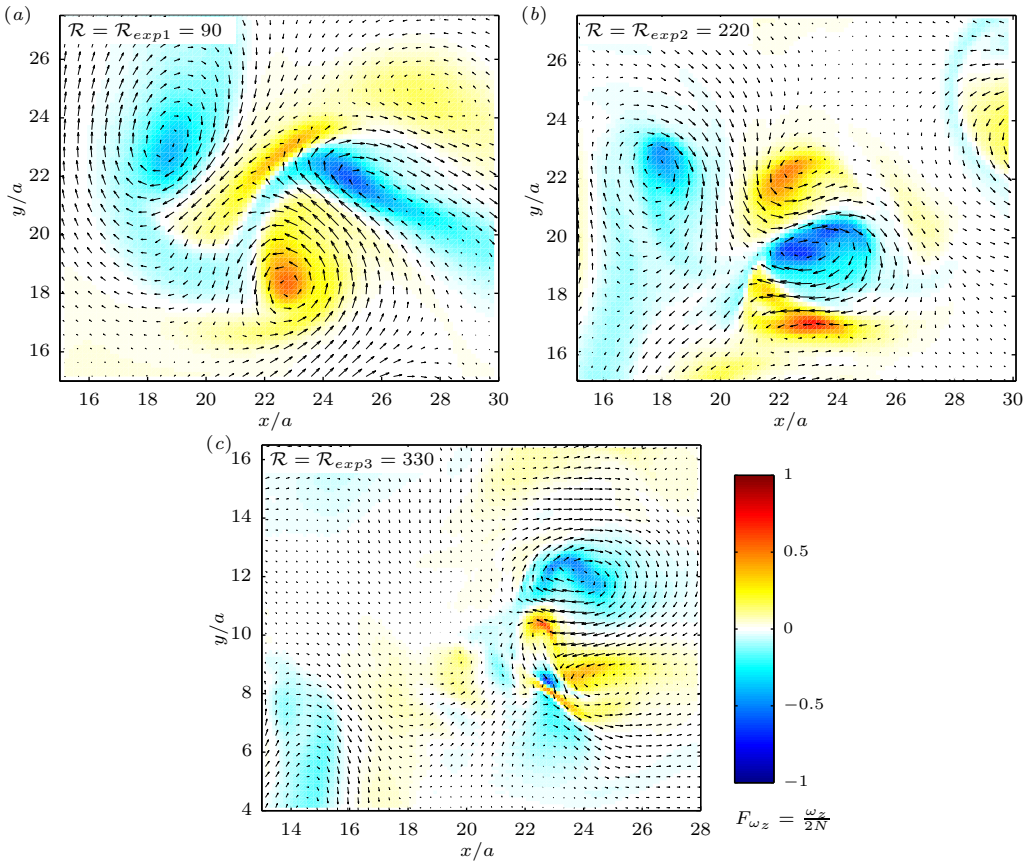

Figure 4.20: Horizontal cross-section of the velocity field and $F\omega_z$ for $F_h = 0.85$ and for three different values of the buoyancy Reynolds number $\mathcal{R} = 90$ (a), 220 (b) and 330 (c). The contours represent the local horizontal Froude number $F\omega_z$. Only a small portion of the box is shown.

We do not see such inertial range in Figure 4.21(a) even if there is a flattening of the compensated structure functions at very large scales when $\mathcal{R}$ increases. An increase of the energy at the small scales, especially for the transverse structure functions, can be also seen. This flattening was also observed in the experimental study and was interpreted as the first indications of the inertial range that is predicted for large $\mathcal{R}$. A so-called effective dimension

$$d_{eff}(r_h) = 1 + \frac{r_h(\partial S_{2L}/\partial r_h)}{S_{2T} - S_{2L}}. \tag{4.15}$$

was used to interpret the difference between longitudinal and transverse structure functions. This quantity is not a real dimension but is equal to 2 for a two dimensional isotropic flow and to 3 for a three-dimensional isotropic flow (Augier *et al.*, 2012b). It is shown in the inset of figure 4.21(a). For each buoyancy Reynolds number the effective dimension is very close to 2 at large scales reflecting the fact that the forcing is two dimensional. However for the highest value of $\mathcal{R}$, $d_{eff}(r_h)$ increases at small scales to reach a value around 3 while it remains approximatively equal to 2 for the lowest value of $\mathcal{R}$.

In figure 4.21(b), the horizontal compensated unidimensional spectra of kinetic energy $E_K(k_h)\varepsilon_K^{-2/3}{k_h}^{5/3}$ is plotted as a function of the horizontal wavenumber k_h scaled by $K = 2\pi/R$ the horizontal wavenumber corresponding to the forced dipoles. The vertical compensated spectra $E_K(k_z)\varepsilon_K^{-2/3}{k_z}^{5/3}$ is also shown with dashed lines. At horizontal wavenumbers around K, the different horizontal spectra collapse. When $\mathcal{R}$ is increased, we observe an increase of the spectra at large wavenumber $k_h > K$ and a decrease at low wavenumbers $k_h \ll K$. This indicates that there is more forward transfers toward small scales and less backward transfers toward the largest scales. This is consistent with the interpretation of a transition from a 2D dynamics dominated by viscous effect toward a 3D strongly stratified dynamics when $\mathcal{R}$ is increased. However, the compensated spectra are not flat even for the largest $\mathcal{R}$ indicating that there is no inertial range for the typical range of parameters of the experiments.

We now turn to the analysis of the energy budget. The evolution equations of the kinetic and potential energies $\hat{E}_K(\mathbf{k}) = |\hat{\mathbf{u}}|^2/2$ and $\hat{E}_P(\mathbf{k}) = |\hat{\rho'}|^2/(2{F_h}^2)$ (the factor F_h^{-2} appears because of the non-dimensionalization) of a wavenumber $\mathbf{k}$ can be expressed as

$$\frac{d\hat{E}_K(\mathbf{k})}{dt} = \hat{T}_K - \hat{b} - \hat{D}_K + \hat{\mathcal{F}}, \tag{4.16}$$

$$\frac{d\hat{E}_P(\mathbf{k})}{dt} = \hat{T}_P + \hat{b} - \hat{D}_P, \tag{4.17}$$

where $\hat{T}_K = -\Re[\hat{\mathbf{u}}^*(\mathbf{k}) \cdot (\widehat{\mathbf{u}\cdot\boldsymbol{\nabla}\mathbf{u}})(\mathbf{k})]$ and $\hat{T}_P = -F_h^{-2}\Re[\hat{\rho'}^*(\mathbf{k})(\widehat{\mathbf{u}\cdot\boldsymbol{\nabla}\rho'})(\mathbf{k})]$ are the kinetic and potential nonlinear transfers, $\hat{D}_K(\mathbf{k}) = |\mathbf{k}|^2|\hat{\mathbf{u}}|^2/Re$ and $\hat{D}_P(\mathbf{k}) = |\mathbf{k}|^2|\hat{\rho'}|^2/({F_h}^2 ReSc)$ are the kinetic and potential mean energy dissipation, $\hat{b}(\mathbf{k}) = F_h^{-2}\Re[\hat{\rho'}^*(\mathbf{k})\hat{w}(\mathbf{k})]$ is the buoyancy flux from kinetic to potential energy and $\hat{\mathcal{F}}$ is the Fourier transformed forcing term. When (4.16) and (4.17) are summed over the

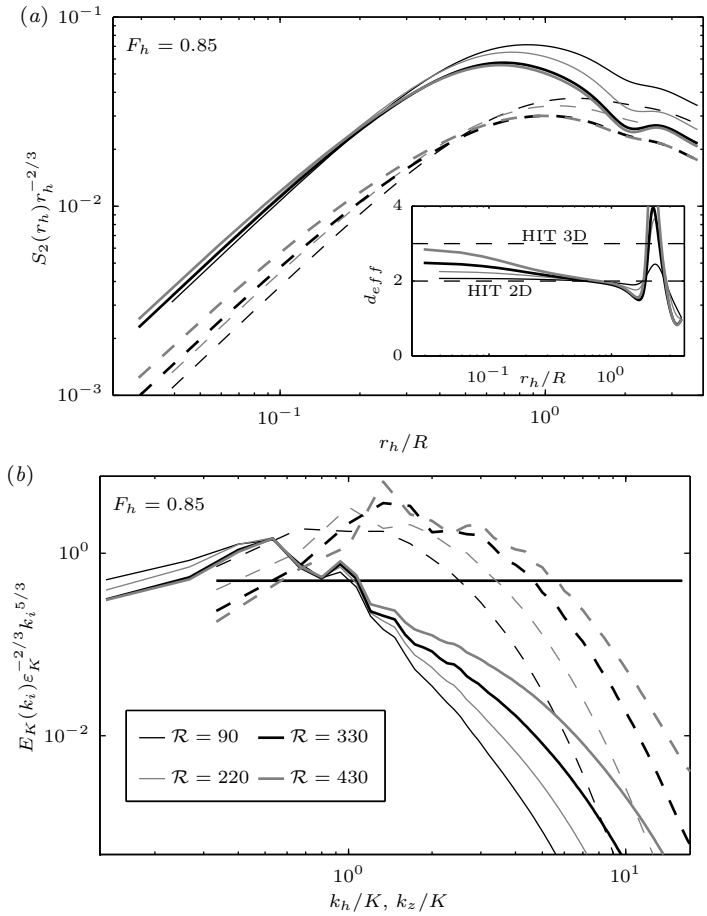

Figure 4.21: (a) Transverse and longitudinal horizontal compensated second order structure functions $S_{2L} = \langle[\delta u_L(\mathbf{r})]^2\rangle$ (continuous lines) and $S_{2T} = \langle[\delta u_T(\mathbf{r})]^2\rangle$ (dashed lines) for different buoyancy Reynolds numbers. The inset shows the effective dimension $d_{eff} = 1 + (r_h(\partial S_{2L}/\partial r_h))/(S_{2T} - S_{2L})$. ($b$) Horizontal (continuous lines) and vertical (dashed lines) compensated 1D spectra of kinetic energy $E_K(k_i)\varepsilon_K^{-2/3} k_i^{5/3}$ as a function of the scaled wavenumber k_i/K, where k_i denotes either the horizontal wavenumber k_h or the vertical wavenumber k_z.

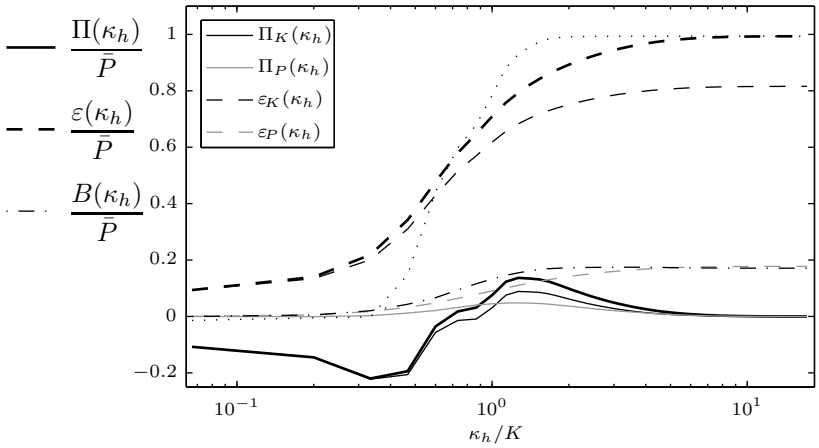

Figure 4.22: Fluxes going out from a vertical cylinder Ω_{κ_h} of radius κ_h in spectral space and dissipations inside this cylinder for $F_h = 0.85$ and $\mathcal{R} = 330$. The continuous black thin, grey curves and black thick curves are respectively the kinetic $\Pi_K(\kappa_h)$, potential $\Pi_P(\kappa_h)$ and total horizontal fluxes through the surface of Ω_{κ_h}. The dashed black thin, grey and black thick curves are respectively the kinetic $\varepsilon_K(\kappa_h)$, potential $\varepsilon_P(\kappa_h)$ and total dissipations inside the volume Ω_{κ_h}. The dotted dashed black curve is $B(\kappa_h)$ the flux of energy from kinetic to potential energies inside the volume Ω_{κ_h}. The dotted line represents the sum $\Pi(\kappa_h)+\varepsilon(\kappa_h)$ which is equal to $P(\kappa_h)$ for a statistically steady flow. The lowest wavenumber corresponds to the shear modes.

wavenumbers inside a vertical cylinder Ω_{κ_h} of radius κ_h in spectral space, we obtain,

$$\frac{dE_K(\kappa_h)}{dt} = -\Pi_K(\kappa_h) - B(\kappa_h) - \varepsilon_K(\kappa_h) + P(\kappa_h), \tag{4.18}$$

$$\frac{dE_P(\kappa_h)}{dt} = -\Pi_P(\kappa_h) + B(\kappa_h) - \varepsilon_P(\kappa_h). \tag{4.19}$$

$E_K(\kappa_h) = \sum_{|\mathbf{k}_h|\leqslant\kappa_h,k_z} \hat{E}_K(\mathbf{k})$, $\Pi_K(\kappa_h)$ the kinetic flux going outside of Ω_{κ_h}, $B(\kappa_h)$ the flux of energy going from kinetic to potential energies inside Ω_{κ_h}, $\varepsilon_K(\kappa_h)$ the kinetic dissipation inside Ω_{κ_h} and $P(\kappa_h)$ the injection rate by the forcing inside Ω_{κ_h}. The quantities with the subscript P are the same but for the potential energy. Total quantities are unsubscripted, i.e. $\Pi = \Pi_K + \Pi_P$, $\varepsilon = \varepsilon_K + \varepsilon_P$. In order that the fluxes in the shear modes appear in the logarithmic plotting, the horizontal wavenumber κ_h is discretized as $\kappa_h = \delta\kappa_h/2 + \delta\kappa_h l$, where $\delta\kappa_h = 2\pi/\mathcal{L}_h$ and l is the discretization integer.

These energy fluxes and energy dissipation rates are plotted versus κ_h in figure 4.22 for $F_h = 0.85$ for the highest value of $\mathcal{R}$ achieved in the experiments $\mathcal{R} = \mathcal{R}_{exp3} = 330$. All the curves have been averaged over the time interval $300 \leqslant t \leqslant 500$, i.e. in the statistically stationary regime (see figure 4.16) and are scaled by the mean injection

rate $\bar{P}$. The horizontal wavenumber κ_h is scaled by K the horizontal wavenumber associated to the forced dipoles.

The sum $\Pi(\kappa_h) + \varepsilon(\kappa_h)$ is shown by a dotted line. Since the flow is statistically stationary, this quantity should be equal to $P(\kappa_h)$ the mean injection rate by the forcing. Therefore, we see indirectly that $P(\kappa_h)$ increases sharply in the wavenumber range $0.3 \lesssim \kappa_h/K \lesssim 1.4$ corresponding to the wavenumbers forced by the dipole generators.

The total dissipation $\varepsilon(\kappa_h)$ (thick dashed line) is approximately equal to $0.1\bar{P}$ for the smallest wavenumbers and then, increases rapidly for the forced wavenumbers: $0.4 \lesssim \kappa_h/K \lesssim 1.4$. For $\kappa_h = 1.4$, $\varepsilon(\kappa_h)$ is already around $0.85\bar{P}$ meaning that the dissipation occurs mainly at large scales and that only a small portion of the energy is still available to be transfered to smaller scales.

The flux of total energy $\Pi(\kappa_h)$ (thick continuous line) is negative at small wavenumbers $\kappa_h \lesssim 0.4K$ indicating backward transfers but it is completely balanced by dissipation (thick dashed line). Besides the flux of potential energy (grey continuous line) is negligible at these scales. The total flux $\Pi(\kappa_h)$ becomes positive at wavenumber around $0.7K$ and increases up to $0.15\bar{P}$ at wavenumbers around 1-2K corresponding to a weak forward energy flux.

The local transfer from kinetic to potential energy $B(\kappa_h)$ (dotted dashed line) smoothly increases in the range of forced wavenumbers and then remains constant at smaller scales. Since $B(\kappa_h) = \sum_{|\mathbf{k}_h| \leqslant \kappa_h, k_z} \hat{b}(\mathbf{k})$, the increase (respectively decrease) of $B(\kappa_h)$ indicates positive (respectively negative) local transfer from kinetic energy to potential energy. This transfer from kinetic to potential energies at the forced wavenumbers is due to the bending of the dipoles and to the shear instability.

Effect of the Froude number F_h

The effect of the horizontal Froude number F_h is addressed in figure 4.23. Vertical (*a,b*) and horizontal (*c,d*) cross-sections of the flow are presented for two different horizontal Froude numbers: $F_h = 0.5$ (*a,c*) and $F_h = 2$ (*b,d*) but for similar values of the quantity $\mathcal{R}' = (Re - 400){F_h}^2$. We recall that the condition $\mathcal{R}' > 4$ should be satisfied to have the shear instability (Augier & Billant, 2011). Here, it is approximately $\mathcal{R}' \simeq 40$ like in the experiments for $\mathcal{R} = \mathcal{R}_{exp3}$. The local horizontal Froude number $F_{\omega_z} = \omega_z/(2N)$ shown by colors (figures 4.23*c,d*) has maximum values of the order of F_h. In contrast, the local vertical Froude number $F_{\omega_y} = \omega_y/(2N)$ (figures 4.23*a,b*) is of order unity. We see in figure 4.23(*a*) several rolls that seems to be due to the shear instability. Since $F_h = 2$ corresponds to a weakly stratified flow, the maximum values of $|F_{\omega_y}|$ are even higher than unity in figure 4.23(*b*). The rolls are also not small compared to the characteristic horizontal length scale in contrast to figure 4.23(*a*) for $F_h = 0.5$.

Extension to large buoyancy Reynolds number

We now increase the buoyancy Reynolds number to values much larger than those achieved in the experiments. Figure 4.24 shows horizontal cross-section of F_{ω_z} (*a*) and vertical cross-sections of F_{ω_z} (*b*) of the statistically stationary flow $\mathcal{R} = 1100$.

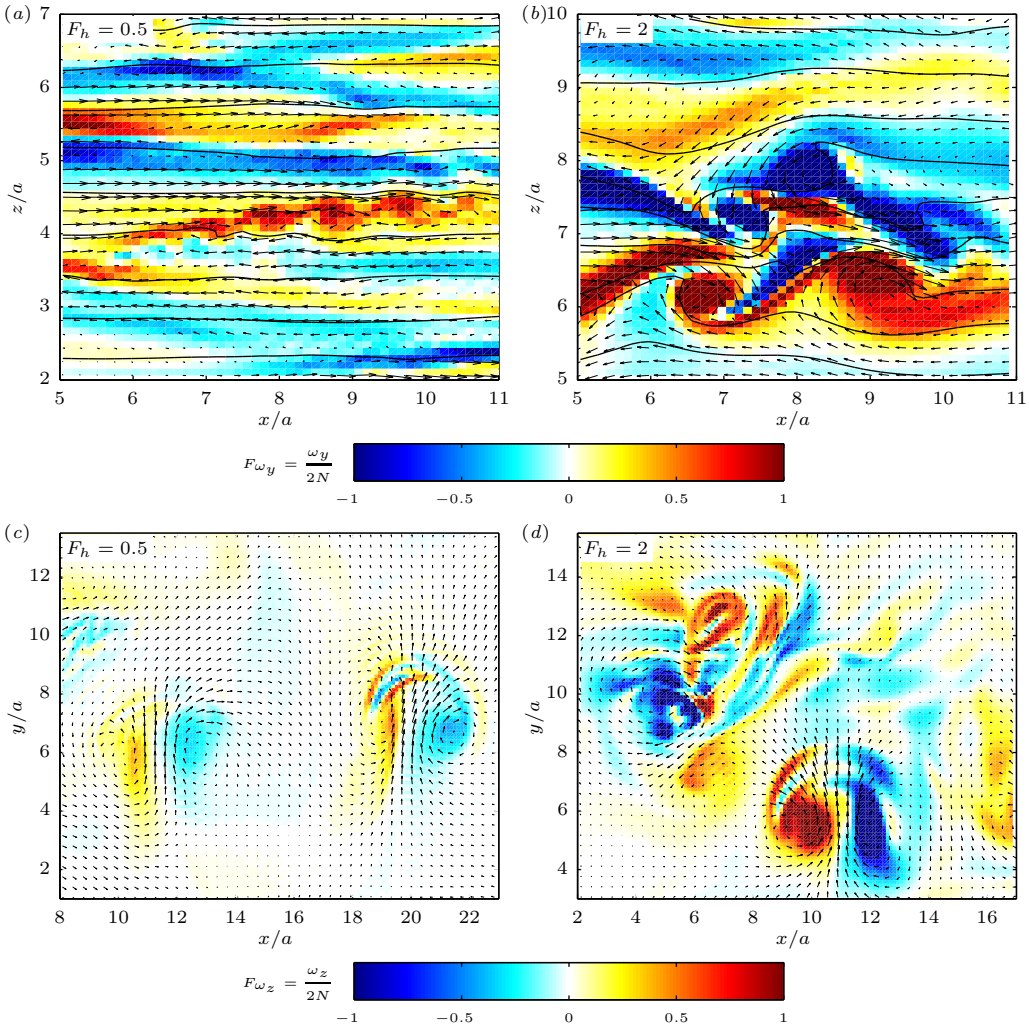

Figure 4.23: Vertical (a,b) and horizontal (c,d) cross-sections for $F_h = 0.5$, $\mathcal{R} = 250$ in (a,c) and for $F_h = 2$, $\mathcal{R} = 1640$ in (b,d). The representations for vertical and horizontal cross-sections are the same as in figure 4.20 and figure 4.19 respectively.

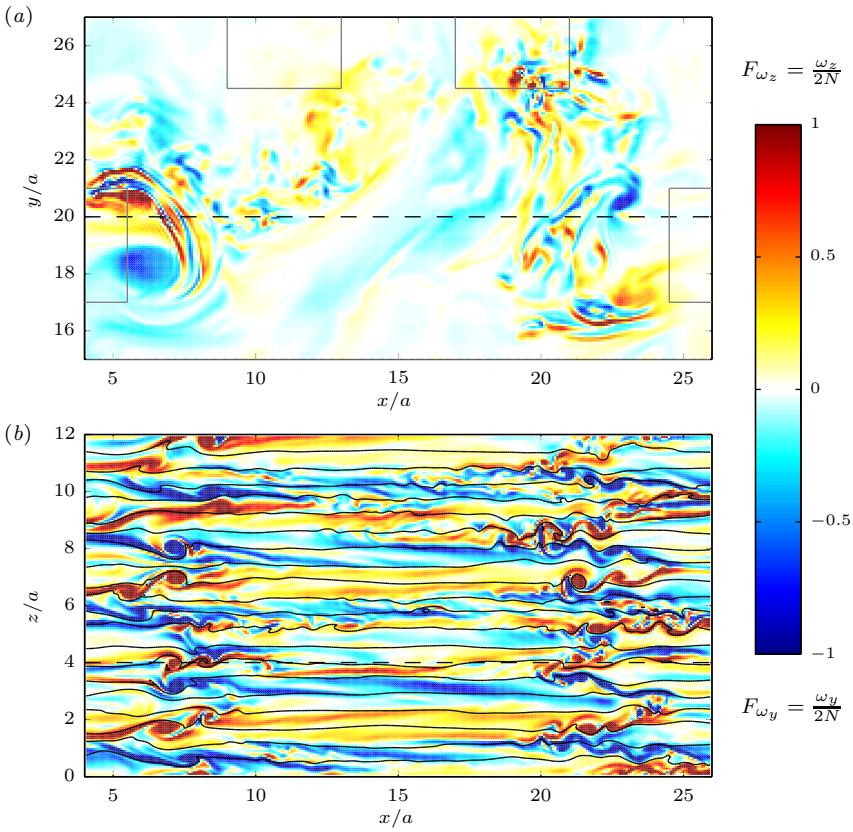

Figure 4.24: Horizontal cross-section of F_{ω_z} (a) and vertical cross-sections of F_{ω_z} (b) for $F_h = 0.85$ and $\mathcal{R} = 1100$. The representation is the same as in figure 4.17.

The horizontal Froude number has been kept constant: $F_h = 0.85$. On the horizontal cross-section (figure 4.24a), we observe much more abundant small scale structures superimposed on the large scale vortices than for $\mathcal{R} = 330$ (figure 4.17a). The vertical cross-section (figure 4.24b) shows that the flow is organized in horizontal layers with a large extent like for $\mathcal{R} = 330$ (figure 4.17b) but with also much finer scale superimposed and more billows in the vicinity of the dipole generators.

Figure 4.25(a) displays the compensated structure functions and figure 4.25(b) the horizontal and vertical compensated kinetic energy spectra $E_K(k_h)\varepsilon_K^{-2/3}{k_h}^{5/3}$ and $E_K(k_z)\varepsilon_K^{-2/3}{k_z}^{5/3}$ respectively, for four buoyancy Reynolds numbers in the range $90 \leqslant \mathcal{R} \leqslant 2200$ for $F_h = 0.85$. The trends already described in figure 4.21 for lower $\mathcal{R}$ are continued and amplified when the buoyancy is increased. There is more energy at small scales, especially for the longitudinal structure function. This leads to a strong increase at small scales of the effective dimension d_{eff} which rises up to 5 for

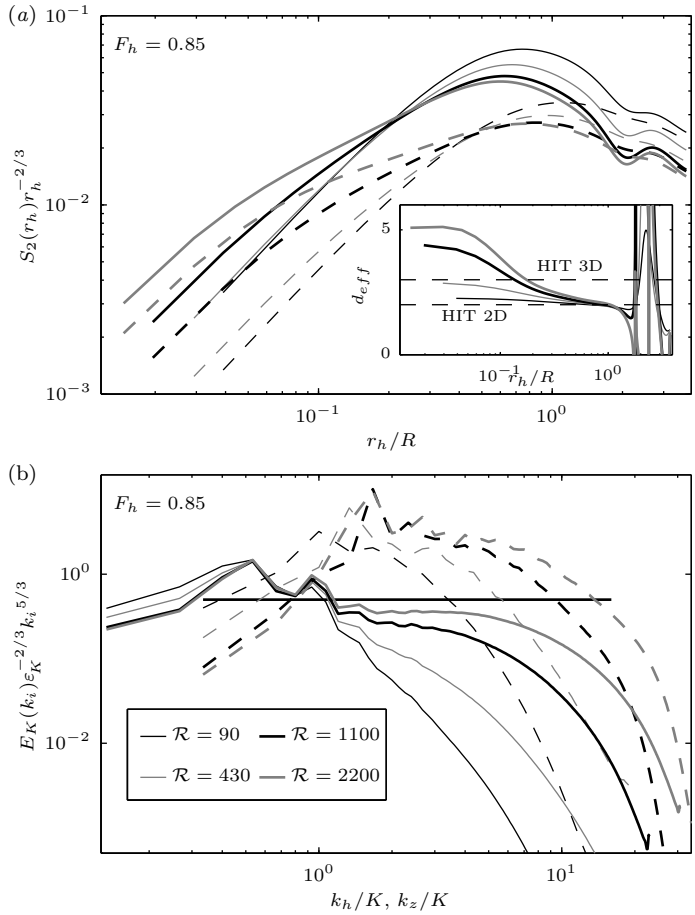

Figure 4.25: Compensated structure functions (a) and horizontal and vertical compensated kinetic energy spectra (b) for large $\mathcal{R}$ and $F_h = 0.85$. The representation is the same as in figure 4.21. In (b), the horizontal thick line corresponds to the $C_1 \varepsilon_K^{2/3} {k_i}^{-5/3}$ law, with $C_1 = 0.5$.

$\mathcal{R} = 2200$. However, we do not see flat compensated structure functions as expected if there were an inertial range. Yet, the compensated horizontal spectrum for the highest $\mathcal{R}$ (figure 4.25*b*) exhibits a $k_h^{-5/3}$ power law at wavenumbers slightly larger than K. The horizontal thick line indicates the $C_1{\varepsilon_K}^{2/3}{k_h}^{-5/3}$ law, with $C_1 = 0.5$, which corresponds to the spectra of forced strongly stratified turbulence (Lindborg, 2006; Brethouwer *et al.*, 2007). We see that the kinetic energy spectrum for $\mathcal{R} = 2200$ is close to this line suggesting that the flow approaches the strongly stratified turbulent regime. However, the associated turbulent buoyancy Reynolds number is only equal to $\mathcal{R}_t = 1.7$ while Brethouwer *et al.* (2007) showed that values larger than approximatively 5 are necessary to really reach this regime. The compensated vertical spectrum (dashed lines in figure 4.25*b*) strongly varies when $\mathcal{R}$ is increased with more and more energy at small vertical scales. This confirms that for the smallest values of $\mathcal{R}$, vertical scales are controled by dissipative effects. However, for $\mathcal{R} = 1100$ and $\mathcal{R} = 2200$, a peak in the compensated vertical spectra can be seen at approximatively $k_z = 1.5K$. For both simulations, this wavenumber is not in the dissipative range in contrast to the simulations for the smaller values of $\mathcal{R}$ where no peak is observed. The appearance of the ${k_h}^{-5/3}$ power law in the horizontal spectra coincides with the appearance of this peak.

Figure 4.26 shows the horizontal and vertical compensated kinetic energy spectra with the same representation and for approximatively the same buoyancy Reynolds numbers but for a lower Froude number $F_h = 0.5$, i.e. a stronger stratification. The horizontal spectra are very similar to those in figure 4.25 but with a wider inertial range because the corresponding Reynolds number is larger. Consistently, the vertical spectrum are translated toward higher vertical wavenumbers. In particular, a peak is also present but for the vertical wavenumber $k_z = 3K$, i.e. approximatively twice larger than for $F_h = 0.85$.

In order to quantify the vertical structure of the flow, we have computed the so-called vertical micro-scale $l_v = \left(2{U_x}^2/\langle[\partial_z u_x]^2\rangle\right)^{1/2}$ and horizontal micro-scale $l_h = \left(2{U_x}^2/\langle[\partial_x u_x]^2\rangle\right)^{1/2}$, where u_x is the velocity component over the x-direction and ${U_x}^2 = \langle {u_x}^2\rangle$. The evolution of the aspect ratio l_v/l_h when $\mathcal{R}$ is varied as shown in figure 4.27. Following Brethouwer *et al.* (2007), two different scaling are tested: a viscous scaling in Fig. 4.27(*a*) and an inviscid scaling in Fig. 4.27(*b*). The viscous scaling is obtained by balancing the dissipation due to vertical gradients and the horizontal advection $l_v \sim \sqrt{\nu l_h/U} \sim l_h/\sqrt{Re}$ (Godoy-Diana *et al.*, 2004). The invicid scaling is obtained by balancing the buoyancy term to the horizontal advection so that $l_v \sim U/N \sim l_h F_h$ (Billant & Chomaz, 2001). We see that the viscous scaling works at low $\mathcal{R} \lesssim 250$ whereas the invicid scaling is better at large $\mathcal{R}$ provided that $F_h \leqslant 1$. It is consistent with the interpretation of a transition around $\mathcal{R} \approx 250$ from a viscous regime for which the vertical length scale is fixed by viscous effects (Godoy-Diana *et al.*, 2004) to a non-linear stratified regime for which the vertical length scale is fixed by an invariance of the hydrostatic Euler equations valid for strong stratification (Billant & Chomaz, 2001). We can also notice that the results for $F_h = 2$ departs slightly from the latter scaling confirming that this value of F_h is outside the strongly stratified regime and corresponds to a moderate stratification.

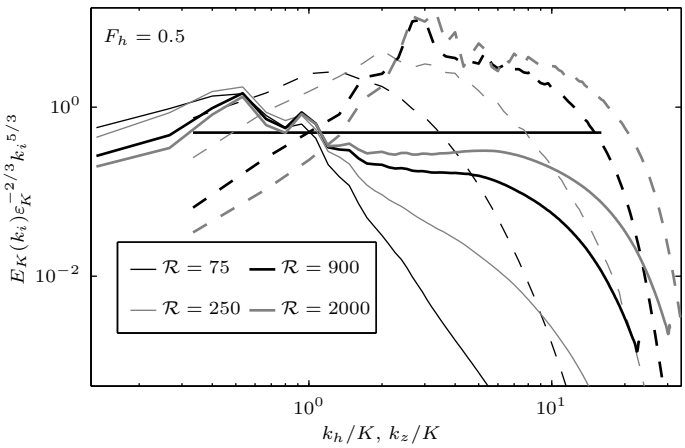

Figure 4.26: Horizontal (solid lines) and vertical (dashed lines) compensated kinetic energy spectra for $\mathcal{R} = 75$, 250, 900 and 2000 and $F_h = 0.5$.

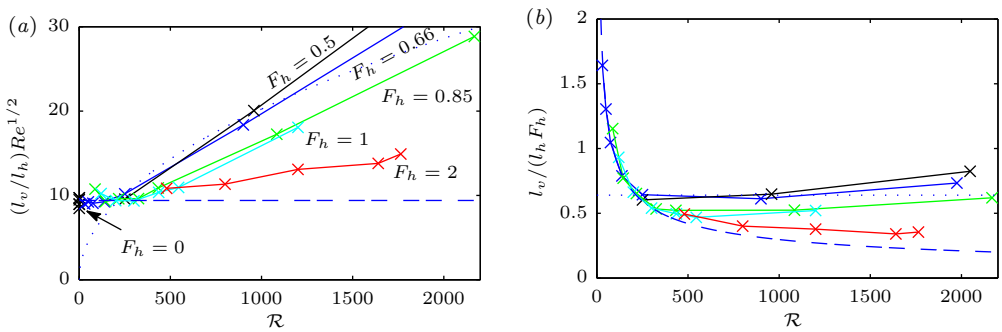

Figure 4.27: Scaled aspect ratio (*a*) $(l_v/l_h)Re^{1/2}$ and (*b*) $l_v/(l_h F_h)$ as a function of $\mathcal{R}$ for different F_h. The theoretical scaling laws $l_v/l_h \simeq 9.4Re^{-1/2}$ and $l_v/l_h \simeq 0.65F_h$, where the constant are empiric, are plotted respectively with a dashed line and a dotted line.

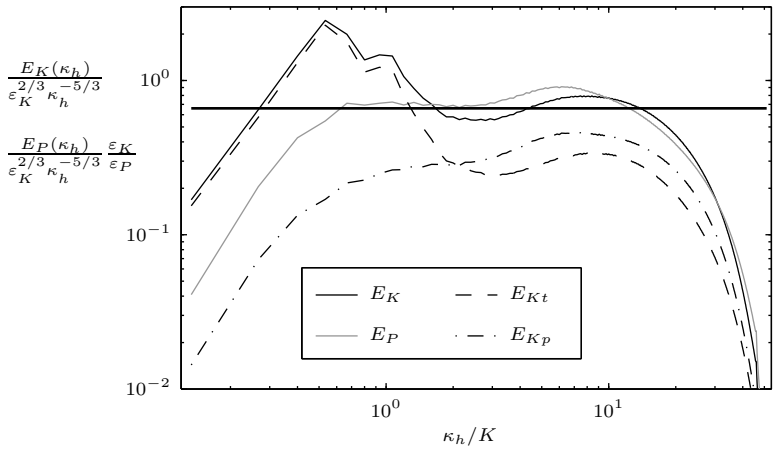

Figure 4.28: Compensated horizontal two-dimensional spectra (kinetic, potential, poloidal and toroidal) as a function of $\kappa_h = |\mathbf{k}_h|$ for $F_h = 0.66$, $\mathcal{R} = 3500$ corresponding to $\mathcal{R}_t = 2.7$. The black horizontal line shows the $C_{2D}\varepsilon_K^{2/3}{k_h}^{-5/3}$ law, with $C_{2D} = 0.66$ (Lindborg & Brethouwer, 2007).

Figure 4.28 displays the compensated horizontal two-dimensional spectra as a function of κ_h for $F_h = 0.66$ and for $\mathcal{R} = 1980$, i.e. one of the highest buoyancy Reynolds achieved with the forcing considered in this section. The compensated horizontal two-dimensional kinetic spectrum $E_K(\kappa_h)\varepsilon_K^{-2/3}\kappa_h^{5/3}$ presents a $k_h^{-5/3}$ power law at wavenumbers smaller than K. Remarkably, it approximately collapses on the horizontal line which indicates the $C_{2D}\varepsilon_K^{2/3}{k_h}^{-5/3}$ law, with $C_{2D} = 0.66$ corresponding to strongly stratified turbulence (Lindborg & Brethouwer, 2007). The compensated horizontal two-dimensional potential spectrum $E_P(\kappa_h)\varepsilon_K^{-2/3}\kappa_h^{5/3}(\varepsilon_K/\varepsilon_P)$ also collapses on this line in agreement with Lindborg & Brethouwer (2007). However, both kinetic and potential spectra exhibit a bottleneck at small scales as also observed by Brethouwer *et al.* (2007).

The toroidal spectrum E_{Kt}, associated to vortical motions and the poloidal spectrum E_{Kp}, associated to the vertical velocity and to the divergence of the horizontal velocity are also plotted in dashed and dotted dashed lines respectively. At large scales, the toroidal spectrum dominates reflecting the vortical nature of the forcing by dipoles. The toroidal and poloidal spectra are of the same order in the inertial range as reported by Lindborg & Brethouwer (2007). However, we can see that the poloidal spectrum is slightly larger than its toroidal counterpart as also observed by Waite (2011). This could be due to the shear instability since Kelvin-Helmholtz rolls with axis along the horizontal direction consist only in poloidal velocity. In any case, Lindborg & Brethouwer (2007) showed that such high poloidal spectrum does not imply that the flow is dominated by waves. Indeed, a poloidal flow corresponds to linear waves only in the limit $F_v \ll 1$.

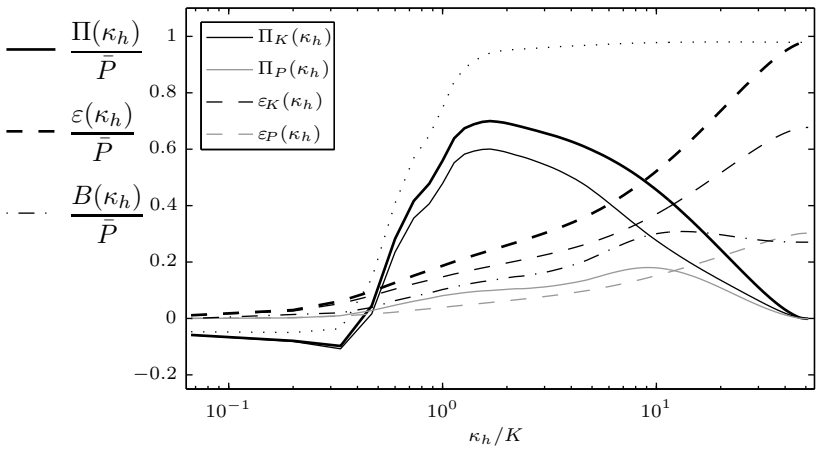

Figure 4.29: Fluxes going out from a vertical cylinder Ω_{κ_h} of radius κ_h in spectral space and dissipation inside this cylinder for $F_h = 0.66$, $\mathcal{R} = 3500$ ($\mathcal{R}_t = 2.7$). The representation is the same as in figure 4.22.

Figure 4.29 presents the energy budget as a function of the horizontal wavenumber κ_h for $F_h = 0.66$ and $\mathcal{R} = 1980$. This figure should be compared to the one for $\mathcal{R} = 330$ (figure 4.22). In contrast to $\mathcal{R} = 330$, positive nonlinear fluxes (continuous lines) dominate the energy dissipation rates (dashed lines) at the typical wavenumber of the forcing $\kappa_h \simeq K$. There is a range of wavenumbers between $\kappa_h \simeq K$ and $\kappa_h \simeq 5K$ for which the flux of total energy (thick continuous line) is of order $0.6\bar{P}$ and slowly varies whereas the dissipation rates remain relatively weak. This range corresponds therefore to an inertial range with a forward energy cascade. For $\kappa_h > 7K$, the total flux rapidly decreases whereas the total dissipation (thick dashed lines) increases, indicating that the dissipative range is separated from the forcing range. Nevertheless, the total dissipation is of order $0.2\bar{P}$ at $\kappa_h = K$ and increases up to approximately $0.4\bar{P}$ in the inertial range. This is consistent with the relatively low value of the turbulent buoyancy Reynolds number $\mathcal{R}_t = 2.7$ compared to the those required to obtain strongly stratified turbulence $\mathcal{R}_t \simeq$ 5-10 (Brethouwer *et al.*, 2007).

The linear local transfer from kinetic to potential energies $B(\kappa_h) = \sum_{|\mathbf{k}_h| \leqslant \kappa_h, k_z} \hat{b}(\mathbf{k})$ (black dotted dashed line) increases slowly in the forcing range and in the inertial range. Remarkably, it decreases in the dissipation range for wavenumber $\kappa_h > 10K$ indicating that there are some transfers from potential to kinetic energies in this range. Even if this transfer occurs in the dissipative range, the underlying mechanism is not necessary a dissipative effect. Indeed, because $\mathcal{R}$ is moderate, the buoyancy scale L_b is of the order of the vertical characteristic dissipative length scale $L_\nu = \sqrt{\nu a/U_h}$ and the Ozmidov length scale l_o is of the order of the Kolmogorov length scale η meaning that many processes act at similar length scales even if these characteristic length scales would be well separated in the limits $F_h \ll 1$ and $\mathcal{R} \gg 1$.

F_h	Re	$\mathcal{R}$	${\mathcal{L}_h}^2 \times \mathcal{L}_z$	${N_h}^2 \times N_z$	F_h^t ($\times 100$)	Re^t	$\mathcal{R}^t$	ν_4 ($\times 10^{-17}$)	$\varepsilon_{\nu_4}/\varepsilon$
0.29	28000	2355	$16^2 \times 2.29$	$1792^2 \times 256$	1.2	36000	5.3	0.017	0.18
0.5	22500	5625	$16^2 \times 4.00$	$1024^2 \times 256$	1.5	45000	10	1.2	0.40
0.66	22500	9800	$16^2 \times 5.33$	$1152^2 \times 384$	2.4	37000	20	0.5	0.37
0.85	20000	14450	$16^2 \times 6.86$	$896^2 \times 384$	2.5	41000	25	2.7	0.42

Table 4.4: Overview of the physical and numerical parameters of the simulations with a randomly located forcing. See table 4.3 for the definitions of each quantity.

Finally, we can notice in figure 4.29 that there is a weak non-linear flux of kinetic energy toward the shear modes that is not balanced by dissipation. As often observed in numerical simulations of strongly stratified turbulence (Smith & Waleffe, 2002; Lindborg, 2006; Brethouwer *et al.*, 2007), the energy of these horizontally invariant modes therefore slowly grows and this simulation has not yet reached an exactly statistically steady state.

We have shown in this section that the numerical simulations with a forcing reproducing the experimental forcing are able to reproduce the experimental results. This validates our numerical methods and the particular forcing with columnar dipoles. However, a drawback of such forcing is that the flow is horizontally inhomogeneous since the dipoles are forced only at the periphery of the numerical box. Moreover, it would be necessary to further increase the buoyancy Reynolds number to have a strongly stratified turbulence with negligible diffusive effects at large scales.

4.2.4 Forcing with a randomly moving dipole generator

Modification of the numerical methods

In order to achieve a larger buoyancy Reynolds number and to generate a turbulence more homogeneous in the horizontal like in strongly stratified turbulence forced in spectral space (Waite & Bartello, 2004; Lindborg, 2006; Brethouwer *et al.*, 2007), we have slightly modified the forcing: instead of being generated at fixed locations, a dipole is forced every 5 time units at a random location all over the computational domain.

The values of the physical and numerical parameters are reported for each run in table 4.4. The horizontal size of the computational domain has been reduced to $\mathcal{L}_h = 16a$. This will allow us to resolve much finer scales for a given resolution and furthermore, such size is sufficient to capture the largest scales produced by the forcing since the characteristic horizontal length scale of the dipoles is of order $R = 4a$. The height is also reduced and set to $\mathcal{L}_v \simeq 8F_h$ since the characteristic vertical length scale of the layers scales like the buoyancy length scale $L_b \propto F_h a$. In this way, a sufficient and approximately constant number of layers is simulated for each simulation. The horizontal Froude number is kept below unity in order to be always in the strongly stratified regime.

The time interval between two successive forcings $T_1 = 5$ is lower than in 4.2.3 but note that dipoles were generated by pair with the experiment-like forcing so that, on average, a dipole was forced every $T_1 = 3.5$. However, the horizontal size of the

computational domain is now smaller so that the frequency of dipole injection by unit of box surface $f_i = 2\pi/(T_1\mathcal{L}_h^2)$ is $f_i = 0.005$ for the present random forcing instead of $f_i = 0.002$ for the experiment-like forcing. Due to this difference of forcing intensity, the ratio $\mathcal{R}/\mathcal{R}_t = \Omega^3 a^2/\varepsilon_K$ between the buoyancy Reynolds number based on the forced vortices $\mathcal{R}$ and the turbulent one $\mathcal{R}_t$ is larger for the experiment-like forcing ($\mathcal{R}/\mathcal{R}_t \simeq 1200$) than for the present random forcing ($\mathcal{R}/\mathcal{R}_t \simeq 500$). In other words, the turbulent buoyancy Reynolds number $\mathcal{R}_t$ will be more than twice higher with the random forcing for a given value of $\mathcal{R}$.

The Reynolds number for these simulations is in the range $20000 \leqslant Re \leqslant 28000$ so that an isotropic hyperviscosity has been always used even if the resolution is high (table 4.4). The effect of the hyperviscosity can be quantified by the ratio $\varepsilon_{\nu_4}/\varepsilon$, where ε_{ν_4} is the dissipation rate due to hyperviscosity and ε is the total energy dissipation rate. This quantity would tend to 0 if the resolution were sufficiently high to perfectly resolve the Kolmogorov length scale.

Description of the turbulent flow for $F_h = 0.66$, $\mathcal{R} = 9800$

We first describe the statistically steady state obtained for $F_h = 0.66$ and $\mathcal{R} = 9800$, corresponding to a large turbulent buoyancy Reynolds number $\mathcal{R}_t = 20$. Figure 4.30 displays horizontal and vertical cross-section of the local horizontal and vertical Froude numbers $F_{\omega_z} = \omega_z/(2N)$ and $F_{\omega_y} = \omega_y/(2N)$, respectively. Compared to figure 4.24, the flow is fully turbulent with small scales nearly everywhere associated to relatively large local Froude numbers. The vertical velocity scaled u_z enables to better see the large scales of the flow (figure 4.31) In contrast to the simulations presented in the previous section, the forced dipoles strongly interact together. The vertical cross-sections show that the flow is layered with large deformations of the isopycnals and abundant density inversions. We can see that several layers are simulated so that the flow is not confined in the vertical direction.

The energy budget as a function of the horizontal wavenumber κ_h is presented is figure 4.32 for the same simulation. The dissipations (dashed lines) are negligible for wavenumber $\kappa_h \lesssim 10K$. As a result the flux of total energy is nearly constant $\Pi \simeq 0.9\bar{P}$ from $\kappa_h \simeq K$ to $\kappa_h \simeq 10K$. In the forcing range for $\kappa_h \lesssim K$ and in the inertial range, the transfer from kinetic to potential energies $B(\kappa_h)$ (dotted dashed line) increases monotonically. As for lower buoyancy Reynolds number (figure 4.29), $B(\kappa_h)$ decreases slightly in the dissipation range indicating some weak transfers from potential to kinetic energy at the dissipative scales. As a consequence of the local linear transfers from kinetic to potential energies in the inertial range, the flux of potential energy increases and the flux of kinetic energy decreases. Even at such large $\mathcal{R}$, there is a weak flux of kinetic energy in the shear modes. Since it is not balanced by dissipation, it leads to a very slow growth of the energy of the shear modes.

In figure 4.33, we have plotted several instantaneous compensated unidimensional horizontal spectra of kinetic energy $E_K(k_h)\varepsilon_K^{-2/3}{k_h}^{5/3}$ (black continuous curves), potential energy $E_P(k_h)\varepsilon_K^{-2/3}{k_h}^{5/3}(\varepsilon_K/\varepsilon_P)$ (black dashed lines) and vertical spectrum of kinetic energy $E_K(k_z)\varepsilon_K^{-2/3}{k_z}^{5/3}$ (grey curves). Due to the periodicity of the forcing,

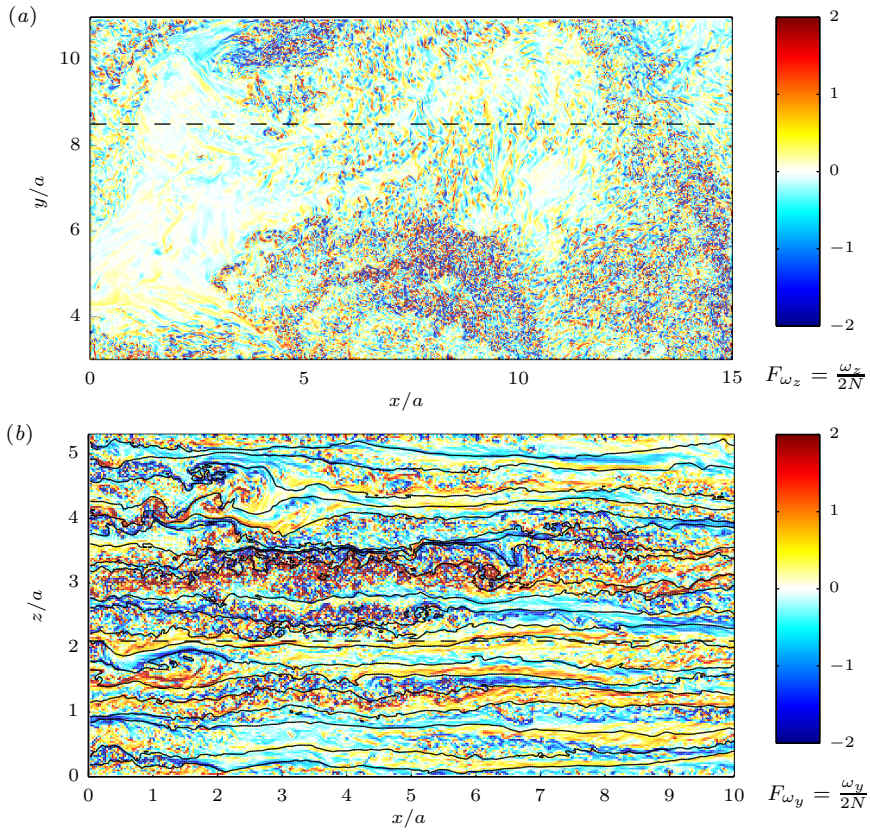

Figure 4.30: Horizontal (a) and vertical (b) cross-sections of the flow for $F_h = 0.66$, $\mathcal{R} = 9800$ ($\mathcal{R}_t = 20$). The representation is the same as in figure 4.17.

the compensated kinetic energy spectrum varies in time between 0.6 and 1 at the lowest wavenumbers $\kappa_h < K$. For larger wavenumbers these spectra are nearly flat and exhibits approximately a $C_1 {\varepsilon_K}^{2/3} k_h^{-5/3}$ power law, with $C_1 = 0.5$ (horizontal thick line), even if there is an energy deficit for $K < \kappa_h < 4K$ and an excess for $4K < \kappa_h < 30K$, which could be due to the shear and convective secondary instabilities (Brethouwer *et al.*, 2007). Such bottleneck could also come from the hyperviscosity, but this is unlikely since the hyperdissipation is relatively weak compared to the normal dissipation $\varepsilon_{\nu_4}/\varepsilon \simeq 0.37$ (table 4.4) and such shapes for the kinetic energy spectra were also observed on the DNS of Brethouwer *et al.* (2007). The compensated horizontal potential energy spectra approximately collapse on the kinetic spectra but is more flat and overtakes the $C_2 \varepsilon_K^{2/3} k_h^{-5/3} (\varepsilon_P/\varepsilon_K)$ law, with $C_2 = 0.5$, found by Lindborg (2006) (horizontal thick line). The vertical kinetic energy spectra (grey lines) follow a ${k_z}^0$ white noise spectrum at small wavenumbers. This means that there is no cor-

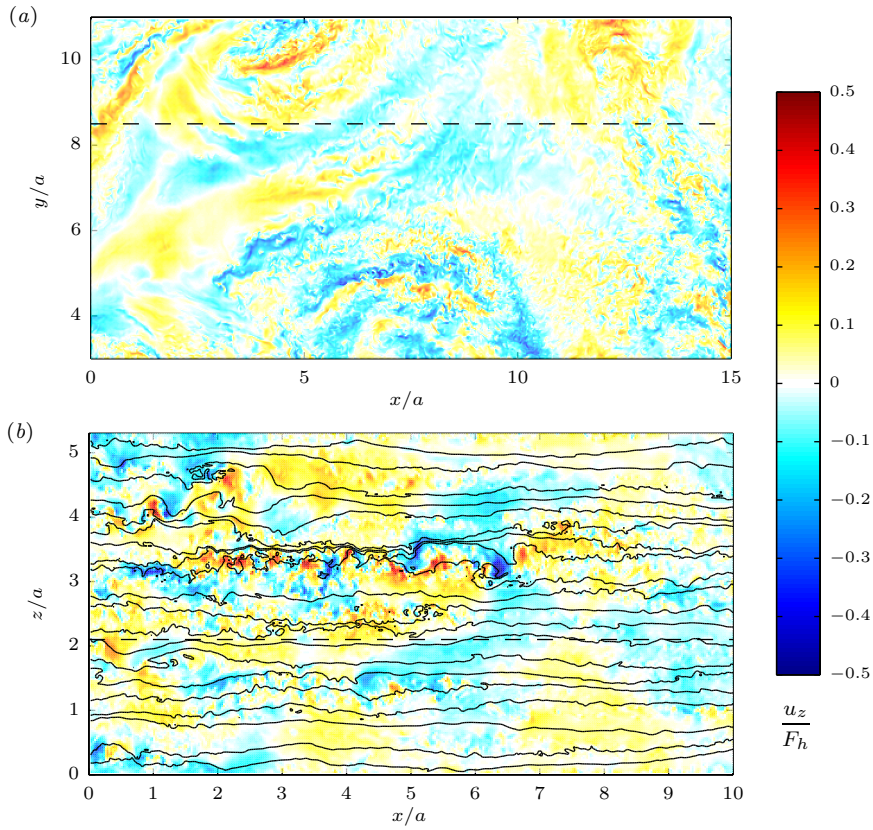

Figure 4.31: Horizontal (a) and vertical (b) cross-sections of the scaled vertical velocity u_z/F_h for $F_h = 0.66$, $\mathcal{R} = 9800$ ($\mathcal{R}_t = 20$). The black lines in (b) are the isopycnals. The dashed horizontal lines indicate the location of the cross-section in the perpendicular direction.

relation between the different velocity fields for these large vertical separations. This proves that the height of the computational domain is sufficiently large compared to the largest characteristic vertical length scale which is L_b. At vertical wavenumbers around $7K$, the vertical spectra are very steep with nearly a k_z^{-3} power law. At larger wavenumbers, the vertical spectra approach the horizontal ones and tend to a $k_z^{-5/3}$ power law. This indicates the beginning of the return to isotropy.

On figure 4.34, toroidal (black), poloidal (light grey) and potential (dark grey) horizontal compensated two-dimensional spectra are presented. As for the 1D spectra, both kinetic and potential spectra seem to be slightly higher than the constant $C_{2D} = 0.66$ (horizontal line) corresponding to the law reported by Lindborg & Brethouwer (2007) for strongly stratified turbulence. The large horizontal scales are dominated by

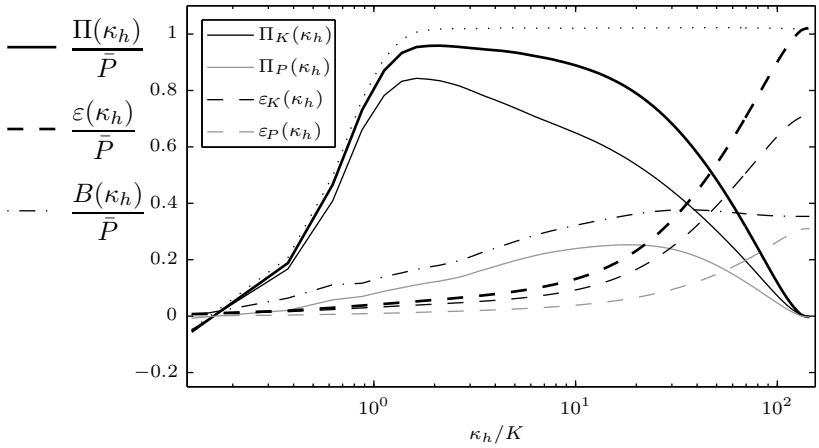

Figure 4.32: Fluxes going out from a vertical cylinder Ω_{κ_h} of radius κ_h in spectral space and dissipation inside this cylinder for $F_h = 0.66$, $\mathcal{R} = 9800$ ($\mathcal{R}_t = 20$). The representation is the same as in figure 4.22.

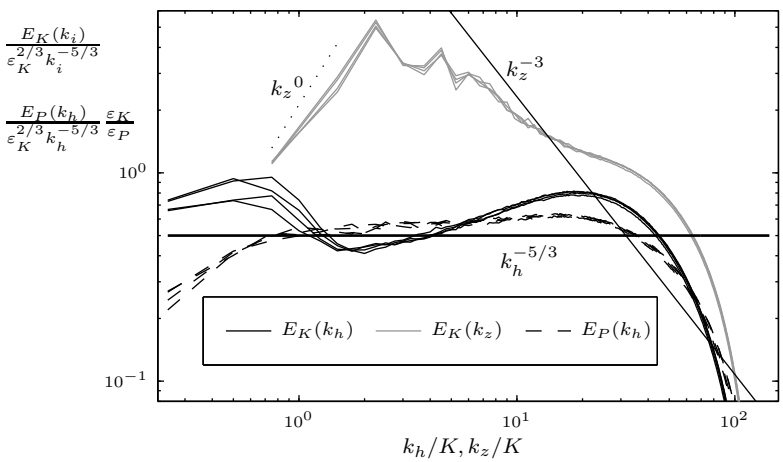

Figure 4.33: Unidimensional horizontal and vertical compensated spectra for $F_h = 0.66$, $\mathcal{R} = 9800$ ($\mathcal{R}_t = 20$) and for 4 different times during the statistically steady state with a time interval of 2 times units. The kinetic energy spectra are plotted in continuous lines and the horizontal potential energy spectrum in dashed line. The thin straight line indicates the k_z^{-3} power law and the horizontal thick line the $C_1 \varepsilon_K^{2/3} k^{-5/3}$ law for the kinetic energy spectra, with $C_1 = 0.5$ and the $C_2 \varepsilon_K^{2/3} k^{-5/3} (\varepsilon_P/\varepsilon_K)$ law for the potential energy spectra, with $C_2 = 0.5$. The dotted line shows a k^0 power law.

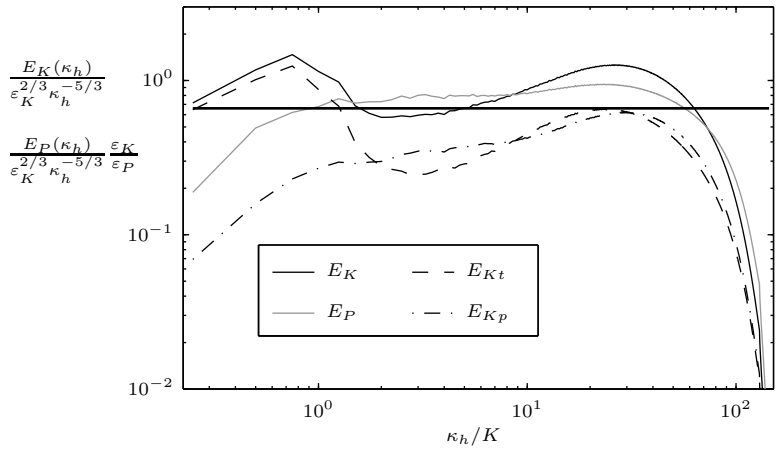

Figure 4.34: Compensated horizontal two-dimensional spectra (kinetic, potential, poloidal and toroidal) as a function of $\kappa_h = |\mathbf{k}_h|$ for $F_h = 0.66$, $\mathcal{R} = 9800$ ($\mathcal{R}_t = 20$). The black horizontal line corresponds to the constant $C_{2D} = 0.66$ (Lindborg & Brethouwer, 2007).

the toroidal component (dashed line) while at smaller horizontal scales, the toroidal and poloidal spectra nearly collapse on each other. At intermediate wavenumbers around $3K$, the poloidal spectrum is slightly higher than the toroidal one.

Effects of the Froude number F_h and of the buoyancy Reynolds number $\mathcal{R}$

We now compare simulations for different Froude numbers $F_h = 0.29$, 0.5, 0.66 and 0.85 keeping a high buoyancy Reynolds number. Figure 4.35 displays the compensated transverse $S_{2T}\varepsilon_K^{-2/3}r_h^{-2/3}$ and transverse $S_{2L}\varepsilon_K^{-2/3}r_h^{-2/3}$ structure functions for these four simulations. In contrast to moderate buoyancy Reynolds number (figure 4.25(a), the compensated structure functions exhibit for all F_h a flat range corresponding to an inertial range. The inset plot shows also the effective dimension d_{eff}. After a peak at intermediate scales, d_{eff} tends to a value slightly larger than 3 for all horizontal Froude number ($d_{eff} = 3$ corresponds to isotropic three-dimensional turbulence).

Figure 4.36 presents horizontal (continuous lines) and vertical (dashed lines) compensated kinetic spectra $E_K(k_h){\varepsilon_K}^{-2/3}{k_h}^{5/3}$ and $E_K(k_z){\varepsilon_K}^{-2/3}{k_z}^{5/3}$, respectively as a function of the wavenumbers scaled by the buoyancy wavenumber $k_b = N/U_h$, where $U_h = \langle(u_x^2 + u_y^2)/2\rangle^{1/2}$ is the square root of the horizontal kinetic energy. All the runs present a relatively flat compensated horizontal spectra corresponding to a $k_h^{-5/3}$ inertial range. Except for $F_h = 0.3$ for which the buoyancy Reynolds number is too low, the horizontal spectra collapse approximately on the horizontal thick line marking the $E_K(k_h) = C_1{\varepsilon_K}^{2/3}k_h^{-5/3}$ spectrum, with $C_1 = 0.5$. As for $F_h = 0.66$ (figure 4.33), there is however a depletion at relatively large horizontal scales and a

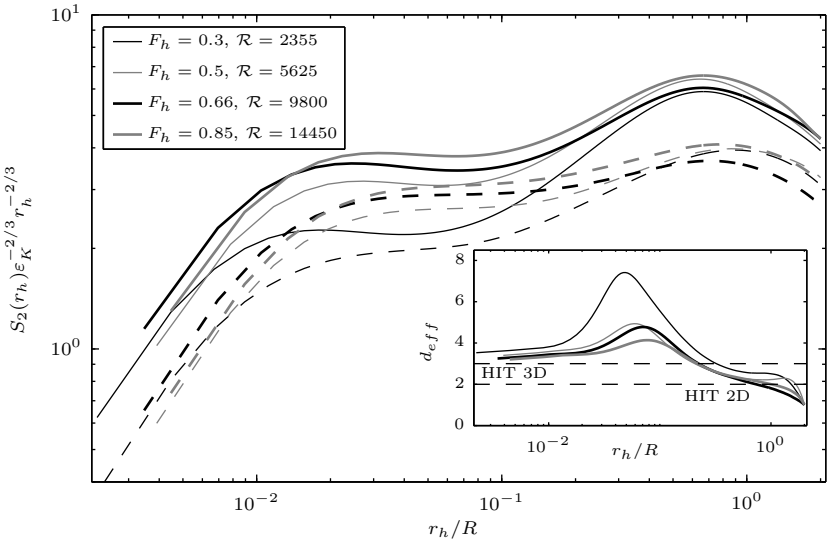

Figure 4.35: Compensated transverse (continuous lines) and longitudinal (dashed lines) horizontal second order structure functions for different values of F_h and $\mathcal{R}$. The inset plot shows the effective dimension $d_{eff}(r_h) = 1 + (r_h \partial_{r_h} S_{2L})/(S_{2T} - S_{2L})$ as a function of the horizontal increment r_h scaled by R. The dotted horizontal lines correspond to $d_{eff} = 2$ and $d_{eff} = 3$ corresponding to homogeneous isotropic turbulence in 2D and in 3D, respectively.

bump at horizontal wavenumbers slightly larger than k_b for each Froude number F_h.

Except for the simulations with the smallest buoyancy Reynolds number $\mathcal{R} = 2355$, the spectra tend to be always slightly higher than the law reported by Lindborg (2006) for strongly stratified turbulence. One may note that the Kolmogorov constant C_K for the unidimensional spectra of kinetic energy in homogeneous isotropic turbulence is approximately equal to unity (Sreenivasan, 1995; Monin & Yaglom, 1975; Gotoh *et al.*, 2002). The departure at large wavenumbers from the Lindborg's power law could be the sign that for $\mathcal{R} \gg 1$ there is a transition from the strongly stratified constant $C_1 \simeq 0.5$ toward the Kolmogorov constant $C_K \simeq 1$. As already observed for $F_h = 0.6$, the vertical spectra are very steep near $k_z = k_b$ and show a tendency to follow a k_z^{-3} slope for all the Froude numbers. However, the transition towards a $k_z^{-5/3}$ power law is observed only for the two highest buoyancy Reynolds number $\mathcal{R} = 9800$ and $\mathcal{R} = 14450$ (thick lines).

The k_z^{-3} dependence of the vertical spectra can be better seen in figure 4.37(a) where the compensated vertical spectra $E_K(k_z)N^{-2}{k_z}^3$ are represented versus k_z/k_b. All the curves collapse to a constant value $C_N \simeq 0.3$ over a narrow range of wavenumbers around k_b. However, the spectra evolves rapidly toward the $k_z^{-5/3}$ power law when k_z increases all the more than $\mathcal{R}$ is large.

In order to describe such mixed type vertical kinetic spectra, Augier *et al.* (2012c)

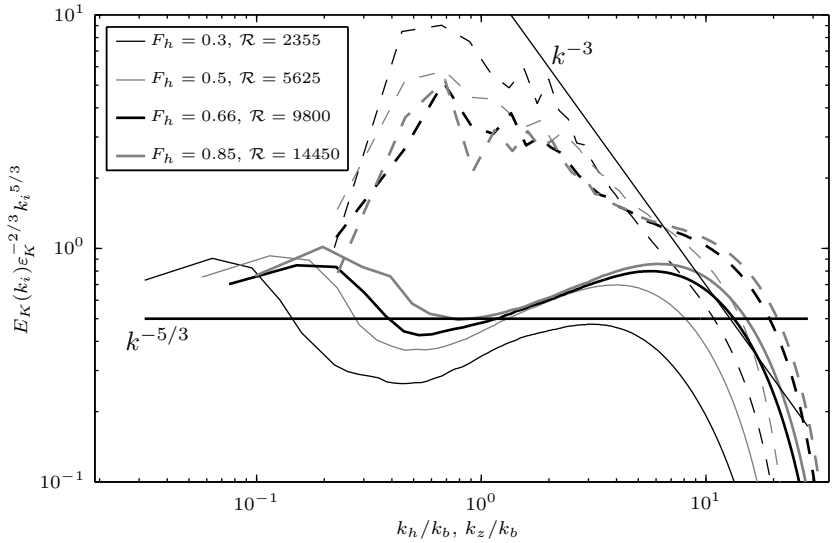

Figure 4.36: Horizontal and vertical compensated unidimensional spectra $E_K(k_i)\varepsilon_K^{-2/3}{k_i}^{5/3}$ as a function of the dimensionless wavenumber k_i/k_b for four different values of the Froude number $F_h = 0.3$, 0.5, 0.66 and 0.85. The thin straight line indicates the k_z^{-3} power law and the horizontal thick line the $C_1{\varepsilon_K}^{2/3}k^{-5/3}$ law, with $C_1 = 0.5$.

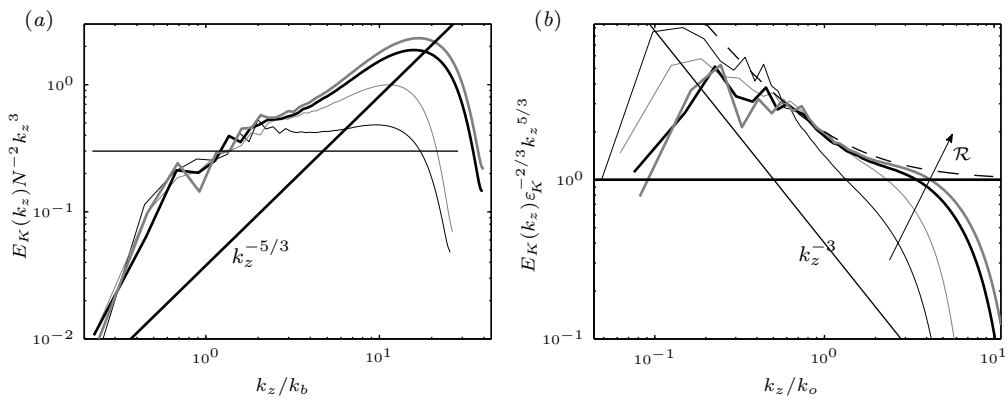

Figure 4.37: Vertical compensated spectra (a) $E_K(k_z)N^{-2}{k_z}^3$ versus k_z/k_b and (b) $E_K(k_z)\varepsilon_K^{-2/3}{k_z}^{5/3}$ versus k_z/k_o. The legend is the same as in figure 4.36. The thick and thin strait lines indicate respectively the $k_z^{-5/3}$ and the k_z^{-3} power laws.

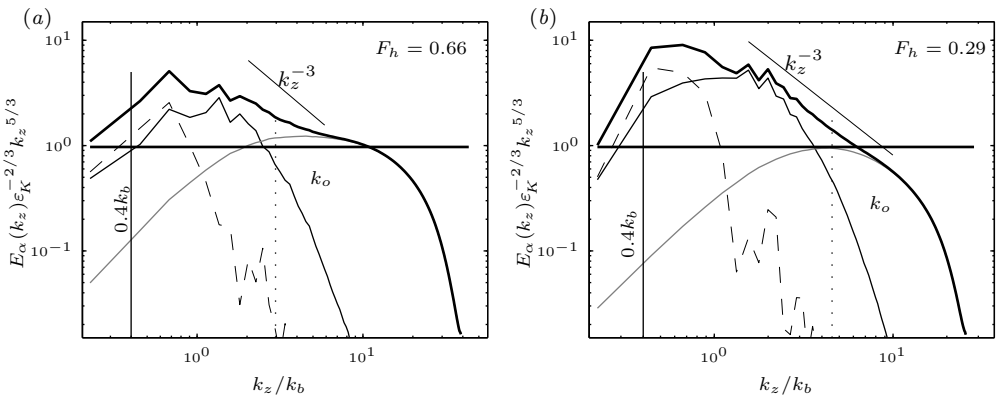

Figure 4.38: Decomposition of the vertical compensated spectra for $F_h = 0.66$ (a) and $F_h = 0.29$ (b). The black thin continuous curves correspond to vertical spectra $E_{[K,0<\kappa_h\leqslant 0.4k_b]}(k_z)$ computed with modes for which $0 < \kappa_h \leqslant 0.4k_b$, the dashed curves to the shear modes vertical spectra $E_{[K,\kappa_h=0]}(k_z)$ and the grey thin curves to spectra $E_{[K,\kappa_h>0.4k_b]}(k_z)$ computed with modes for which $\kappa_h > 0.4k_b$. The continuous vertical lines indicate the conditional wavenumber $0.4k_b$ and the dotted vertical lines the Ozmidov wavenumber k_o. The thick and thin strait lines indicate respectively the $k_z^{-5/3}$ and the k_z^{-3} power laws.

proposed a composite power law of the form:

$$E_K(k_z) = C_N N^2 k_z^{-3} + C_K \varepsilon_K^{2/3} k_z^{-5/3} = ((k_z/k_o)^{-4/3} + 1) C_K \varepsilon_K^{2/3} k_z^{-5/3} \qquad (4.20)$$

where $k_o = 2\pi/l_o$ with $l_o = 2\pi(C_K/C_N)^{3/4}(\varepsilon_K/N^3)^{1/2}$ the Ozmidov length scale. According to (4.20), the transition between the k_z^{-3} and $k_z{}^{-5/3}$ power laws should occur at the Ozmidov length scale. To check this, the compensated vertical spectra $E_K(k_z)\varepsilon_K{}^{-2/3}k_z{}^{5/3}$ are plotted as a function of k_z/k_o in figure 4.37(b). Apart for the Froude number $F_h = 0.3$, all the curves collapse over a large range of vertical wavenumbers including the Ozmidov wavenumber. Furthermore, the spectrum (4.20) with $C_N = 0.3$ (dashed line) describes remarkably well the observed spectra except near the dissipative range. We stress that C_N is the only adjustable parameter because ε_K is measured and $C_K = 1$ is an universal constant. In the sequel, we use the value $C_N = 0.3$ to compute the Ozmidov wavenumber k_o.

Figure 4.38 further presents a decomposition of the vertical kinetic spectra for $F_h = 0.66$ (figure 4.38a) and for $F_h = 0.3$ (figure 4.38b) The black thin curves correspond to conditional vertical spectra $E_{[K,0<\kappa_h\leqslant 0.4k_b]}(k_z)$ computed with modes for which $0 < \kappa_h \leqslant 0.4k_b$, i.e. associated to the large horizontal scales. These conditional vertical spectra are very steep and constitute the major part of the $N^2k_z^{-3}$ spectra. The dashed curves correspond to the conditional vertical spectrum of the shear modes $E_{[K,\kappa_h=0]}(k_z)$. Remarkably, the shear modes spectrum dominates the total vertical spectrum for vertical wavenumbers lower than k_b and decrease abruptly for $k_z > k_b$.

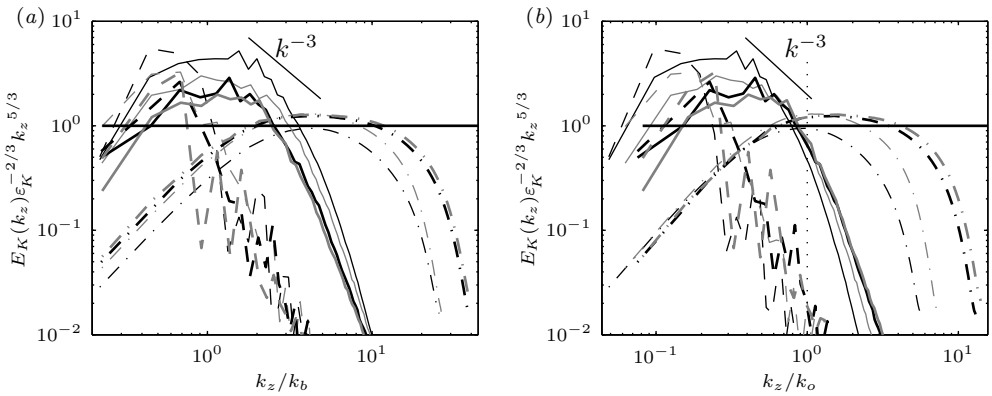

Figure 4.39: Decomposition of the vertical compensated spectra. The continuous curves correspond to vertical spectra $E_{[K,0<\kappa_h\leqslant 0.4k_b]}(k_z)$ computed with modes for which $0 < \kappa_h \leqslant 0.4k_b$, the dashed curves to the shear modes vertical spectra $E_{[K,\kappa_h=0]}(k_z)$ and the dotted dashed curves to spectra $E_{[K,\kappa_h>0.4k_b]}(k_z)$ computed with modes for which $\kappa_h > 0.4k_b$. The dotted vertical lines the Ozmidov wavenumber k_o. The legend is the same as in figure 4.36. The thick and thin strait lines indicate respectively the $k_z^{-5/3}$ and the k_z^{-3} power laws.

The grey thin curves correspond to conditional spectra $E_{[K,\kappa_h>0.4k_b]}(k_z)$ computed with modes for which $\kappa_h > 0.4k_b$, i.e. associated to relatively small horizontal scales. We see that these conditional compensated vertical spectra are negligible for $k_z \lesssim k_b$ and then nearly flat from $k_z \simeq$ 2-3k_b down to the dissipative range, corresponding to a $k_z^{-5/3}$ power law. This indicates that these range of horizontal wavenumbers is dominated by nearly isotropic structures such as Kelvin-Helmholtz billows. In the case of the transition to turbulence of a dipole in a strongly stratified fluid, Augier *et al.* (2012c) have shown that the overturnings due to the shear instability scale as the buoyancy scale, are nearly isotropic and lead to a turbulence with a $k_z^{-5/3}$ kinetic energy spectrum for $k_z > k_b$. This feature is hidden in the non-decomposed vertical kinetic energy spectra at the large vertical scales between the buoyancy length scale and the Ozmidov length scale because of the dominance of the very steep k_z^{-3} spectrum associated to the large horizontal scales.

The compensated conditional vertical spectra for different Froude numbers are plotted in figure 4.39. Two scalings for the horizontal wavenumber κ_h are tested: it is scaled by k_b in (*a*), k_o in (*b*). We see that the conditional spectra $E_{[K,\kappa_h>0.4k_b]}(k_z)$ associated to relatively small horizontal scales perfectly collapse when the horizontal wavenumber is scaled by the Ozmidov wavenumber (figure 4.39*b*).

Finally, figure 4.40 displays the compensated two-dimensional co-spectra $b(\kappa_h){\kappa_h}^{5/3}$, where $b(\kappa_h) = dB(\kappa_h)/d\kappa_h$. This quantity measures the local linear transfer from kinetic to potential energy. The curves are solid when $b(\kappa_h)$ is positive and dashed otherwise. Various scalings for the horizontal wavenumber κ_h are tested: it is scaled

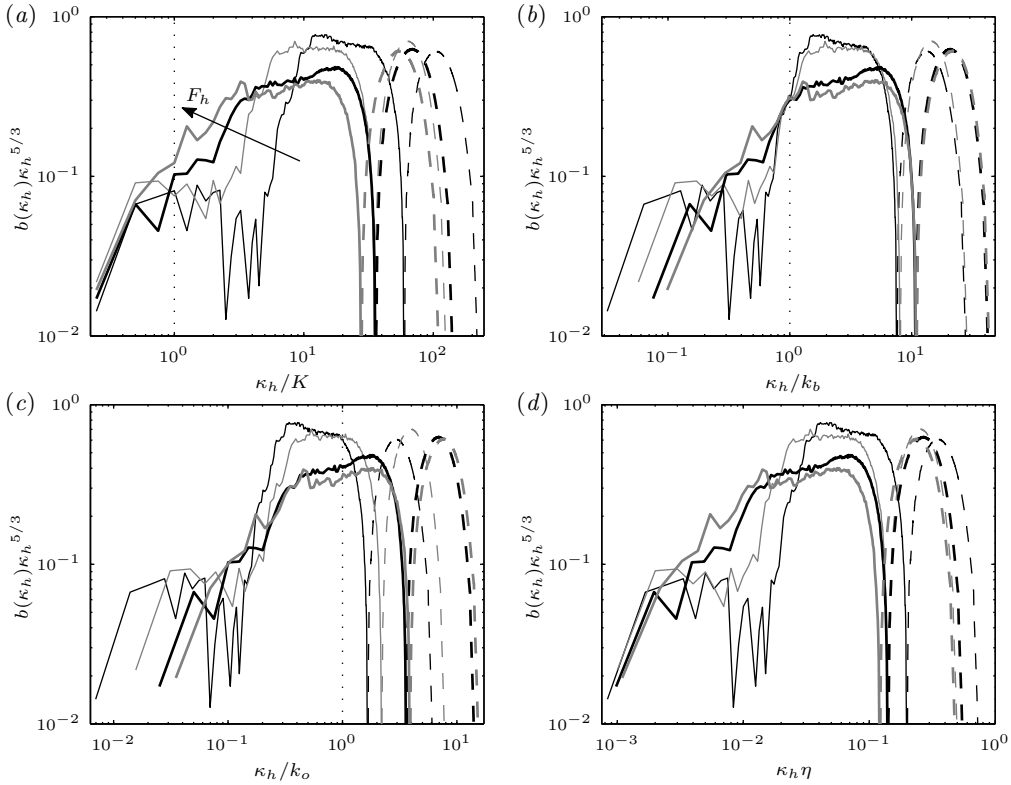

Figure 4.40: Compensated horizontal buoyancy flux spectrum $|b(\kappa_h)\kappa_h{}^{5/3}|$ as a function of the horizontal wavenumber κ_h compensated by K in (a), k_b in (b), k_o in (c) and $1/\eta$ in (d). The lines are solid when $b(\kappa_h)$ is positive and dashed when it is negative. The legend is the same as in figure 4.36.

by K in (a), k_b in (b), k_o in (c) and $1/\eta$ in (d), where $\eta = (\nu^3/\varepsilon_K)^{1/4}$ is the Kolmogorov length scale. At low wavenumber around K (figure 4.40a), $b(\kappa_h)\kappa_h{}^{5/3}$ is lower than 0.1 for all Froude numbers. At a larger wavenumber, $b(\kappa_h)\kappa_h{}^{5/3}$ suddenly increases toward a much larger value of order 0.5. This sharp increase can be due in particular to the shear instability which generates strong overturnings. In a range of wavenumbers, the co-spectra then approximately follow a $\kappa_h^{-5/3}$ power law before again decreasing abruptly. Then, they reach negative values at small-scales (dashed lines) and finally vanish at the largest wavenumbers. Such negative $b(\kappa_h)$ corresponding to transfer from potential to kinetic energies, i.e. to fluid parcels going back to their equilibrium position, has been already reported and described as re-stratification (Holloway, 1988; Staquet & Godeferd, 1998; Brethouwer *et al.*, 2007).

In order to understand the underlying mechanisms driving such features, it is interesting to study at which scales they occur. We see that the first sharp increase

at large scales perfectly collapse when κ_h is scaled by the buoyancy wavenumber k_b (figure 4.40b) whereas no such good collapse is observed for the three other scalings tested. This strongly suggests that, in contrast to the classical interpretation of the Ozmidov length scale (Lesieur, 1997; Riley & Lindborg, 2008), the largest horizontal scale that can overturn is not the Ozmidov length scale but the buoyancy length scale as reported recently by Waite (2011).

This result is not in contradiction with a transition for the vertical spectra at the Ozmidov length scale as explained above and shown in figure 4.38. From figure 4.40, it is difficult to decide at which scale the abrupt decrease of the co-spectrum $b(\kappa_h)$ occurs but it seems to happen for wavenumbers slightly larger than the Ozmidov wavenumber but does not scale with it (figure 4.40c). As seen in figure 4.40(d), the final decrease of $|b(\kappa_h)|$ toward zero collapse relatively well with the the Kolmogorov length scale.

4.2.5 Summary and conclusions

We have presented a numerical study of forced strongly stratified turbulence. The simulations differ from previous simulations of forced stratified turbulence since the forcing consists in vertically invariant columnar vortex pairs generated intermittently, like in the experiments of Augier *et al.* (2012b). A wide range of horizontal Froude number F_h and buoyancy Reynolds number $\mathcal{R} = ReF_h{}^2$ have been investigated, from moderate stratification to strong stratification and from moderate values of $\mathcal{R}$ of the order of those achieved in the experiments to high values that can be reached only by means of high resolution numerical simulations.

For moderate $\mathcal{R}$ and with a forcing very similar to the experimental one consisting of static dipole generators placed at the periphery of the computational domain, the simulations are able to recover the experimental results (Augier *et al.*, 2012b). We observe a rapid three-dimensionalisation of the flows leading to statistically stationary disordered flows exhibiting thin horizontal layers associated to relatively strong vertical gradients. Remarkably, when $\mathcal{R}$ is increased from the lowest value of the buoyancy Reynolds number investigated in the experiments $\mathcal{R} = 90$ (with $F_h = 0.85$) to the largest value $\mathcal{R} = 330$ (with $F_h = 0.85$), there is a transition from quasi-horizontal flows with low local vertical Froude number and smooth large structures strongly affected by viscous effects to turbulent-like flows with local vertical Froude number of order unity, small scale structures superimposed on the large scale horizontal layers and abundant overturning events. When the buoyancy Reynolds number is further increased to $\mathcal{R} \simeq 2000$, this transition is amplified with increasingly small scales and overturnings. This value of the buoyancy Reynolds number is much larger than those achieved in the experiments (Augier *et al.*, 2012b) but is still comparable to what could be obtained in large scale experiments since the buoyancy Reynolds number $\mathcal{R} = ReF_h{}^2 = \Omega^3 a^2/(\nu N^2)$ varies like a^2 if the maximum angular velocity of the vortices Ω and the Brunt-Väisälä frequency N are kept constant. Therefore, it would be sufficient to generate vortices with a radius a only three times larger than in the experiments of Augier *et al.* (2012b). The horizontal second order structure functions only exhibit a strong increase at small scales, but even for $\mathcal{R} = 2000$ no clear $r_h^{2/3}$ dependence is observed as one would expect for an inertial range. Nevertheless, such

inertial range seems to be present since the horizontal kinetic energy spectra exhibit a $k_h^{-5/3}$ power law as soon as $\mathcal{R} \geqslant 1000$. These differences may come from the spatial inhomogeneity of the flow. These results support and extend the experimental study where the first signs of the transition from the viscosity affected stratified regime (Godoy-Diana *et al.*, 2004) to the strongly stratified regime (Brethouwer *et al.*, 2007) were observed (Augier *et al.*, 2012b).

In order to produce a less inhomogeneous turbulence, simulations have been carried out with a slightly different forcing in which a dipole is forced periodically at a random location all over the computational domain. In this way, the forced vortices strongly interact together so that the flow is homogeneous in the statistically stationary regime. By means of high resolution simulations using a weak isotropic hyperviscosity but nearly resolving the Kolmogorov length scale, we have succeeded in achieving high turbulent buoyancy Reynolds numbers $5 \leqslant \mathcal{R}_t \leqslant 25$ (corresponding to $2300 \leqslant \mathcal{R} \leqslant 14000$) for a wide range of horizontal Froude number from $F_h = 0.3$ to $F_h = 0.85$. These values of $\mathcal{R}$ are slightly higher than those of the direct numerical simulations of Brethouwer *et al.* (2007).

For these high buoyancy Reynolds numbers, the second order structure functions exhibit a ${r_h}^{2/3}$ inertial range. The horizontal spectra are in good agreement with previous numerical results (Lindborg, 2006; Brethouwer *et al.*, 2007; Lindborg & Brethouwer, 2007) with horizontal unidimensional spectra of kinetic energy and potential energy scaling like $C_1\varepsilon_K^{2/3}k_h^{-5/3}$ and $C_2\varepsilon_K^{2/3}k_h^{-5/3}(\varepsilon_P/\varepsilon_K)$ respectively, with $C_1 = C_2 \simeq 0.5$ and with horizontal toroidal (vortical) and poloidal spectra nearly collapsing in the inertial range. This equipartition does not mean that half of the flow is composed of waves but only reflects the large value of the vertical Froude number characterizing strongly stratified turbulence.

By forcing columnar dipoles in spatial space in numerical simulations, we have been therefore able to reproduce both the experimental results at moderate $\mathcal{R}$ and the previous numerical results on strongly stratified turbulence at large $\mathcal{R}$ forced in spectral space. This validates the numerical implementation of this new method of forcing.

Like Brethouwer *et al.* (2007), we have observed a depletion in the horizontal kinetic energy spectrum for scales between the integral length scale and the buoyancy length scale and an anomalous energy excess around the buoyancy length scale probably due to direct transfers resulting from the shear and gravitational instabilities. This feature seems to be further amplified when $\mathcal{R}$ increases. For the highest values of $\mathcal{R}$, the kinetic and potential spectra are slightly larger than the two laws proposed by Lindborg (2006) especially at small scales. We can conjecture that this behaviour of the unidimensional kinetic energy spectrum might come from the difference between the Kolmogorov constant $C_K \simeq 1$ for homogeneous isotropic turbulence and the Lindborg constant $C_1 \simeq 0.5$ for strongly stratified turbulence. Some large simulations at larger buoyancy Reynolds numbers would be probably needed to test this conjecture. Such transition could be also present in atmospheric and oceanic 1D-spectra but it does not seem to be observed.

Remarkably, the vertical kinetic energy spectrum exhibit a transition at the Ozmi-

dov length scale from a steep spectrum scaling like $N^2 k_z^{-3}$ at large scales to an inertial $C_K \varepsilon_K^{2/3} k_z^{-5/3}$, with $C_K = 1$ spectrum at scales smaller than the Ozmidov length scale. Following Augier *et al.* (2012c), we have shown that the vertical kinetic energy spectrum is very well modeled by a composite spectrum summing the strongly stratified and inertial spectra. Thanks to conditional spectra, we have further shown that the $N^2 k_z^{-3}$ spectrum corresponds to the large horizontal scales with $0 < \kappa_h \leqslant 0.4 k_b$ whereas the $C_K \varepsilon_K^{2/3} k_z^{-5/3}$ spectrum correspond to the small horizontal scales $\kappa_h > 0.4 k_b$. Strikingly, the $C_K \varepsilon_K^{2/3} k_z^{-5/3}$ spectrum starts at a vertical wavenumber smaller than the Ozmidov wavenumber and which scales like the buoyancy wavenumber.

An abrupt increase of the horizontal buoyancy flux co-spectrum at the buoyancy scale has been interpreted as a signature of the overturnings. This indicates that the size of the largest overturnings does not scale like the Ozmidov length scale in contrast to what has been proposed previously (Lesieur, 1997; Riley & Lindborg, 2008).

From these results, we can envision a new interpretation of the different regimes in strongly stratified turbulence. In the classical representation (see e.g. Lindborg, 2006; Brethouwer *et al.*, 2007; Riley & Lindborg, 2008), the turbulence in strongly stratified fluids is divided in two different regimes with a transition at the Ozmidov length scale. At scales larger than the Ozmidov length scale, the energy cascades via a strongly anisotropic cascade with $l_v \simeq l_b(l_h) \simeq u(l_h)/N$ at each scale l_h. All along this cascade, the horizontal Froude number $F_h(l_h)$ remains low and it is only at the Ozmidov length scale that overturnings can occur since the Froude number is then of order unity $F_h(l_o) \sim 1$.

However, the present results highlight the physical importance of the buoyancy length scale L_b. This has been also recently pointed out for strongly stratified turbulence (Waite, 2011) and for the transition to turbulence of a dipole (Augier *et al.*, 2012c). In order to interpret the results, we need to distinguish three different scale ranges. From the large integral scale to the buoyancy scale L_b, the energy cascades only *via* the strongly stratified hydrostatic cascade with $F_h(l_h) \ll 1$, whereas at scales smaller than the Ozmidov length scale, the turbulence becomes nearly isotropic as described above.

Between the buoyancy length scale L_b and the Ozmidov length scale, the strongly stratified hydrostatic cascade associated to horizontal Froude number

$$F_h(l_h) = u(l_h)/(N l_h) = (l_o/l_h)^{2/3}$$

lower than one seems to coexist with another type of stratified turbulence associated to overturnings with $F_h \sim F_v \sim 1$. These nearly isotropic overturning structures are directly generated from the destabilisation of the large anisotropic scales of the strongly stratified cascade *via* non-local transfers driven by instabilities of the layers such as the shear and the gravitational instabilities. This explains why their velocity can be high enough to be associated to $F_h \sim F_v \sim 1$. Therefore, this intermediate range consists in a mixture of balanced strongly stratified turbulence and unbalanced billows.

4.2.6 Appendix 1: mechanisms of vertical decorrelation and reduced equations

We focus in this appendix on the mechanisms involved in the vertical decorrelation and the vertical length scale selection in the transition from a 2D vertically invariant flow to a 3D layered flow. To address these points, two simulations with the same forcing as in sub-section 4.2.3 have been carried out for a Reynolds number $Re = 50000$. One simulation uses the full Boussinesq Navier-Stokes equations like in the body of the paper with a horizontal Froude number equal to 0.66. In the second simulation, the vertical velocity is set to zero at each time step. Thus, the poloidal component of the velocity is enforced to be zero and only the toroidal component is simulated. The motion is therefore two-dimensional and coupled along the vertical only by viscous effects:

$$(\partial_t + \mathbf{u}_h \cdot \boldsymbol{\nabla})\omega_z = \nu \boldsymbol{\nabla}^2 \omega_z, \tag{4.21}$$

where ω_z is the vertical velocity. This corresponds to the limits $F_h = F_v = 0$ of the Riley and Lilly scaling analysis (Riley *et al.*, 1981; Lilly, 1983; Riley & Lelong, 2000). Godoy-Diana *et al.* (2004) have also obtained these equations but in the limits $F_h \to 0$ and $\mathcal{R} = ReF_h{}^2 \to 0$. In the sequel, we shall call "reduced simulation" the simulation based on (4.21). A white noise with the same amplitude is added at $t = 0$ in the horizontal velocity in both simulations. Since there are only few overturnings during the transition phase and that we need to resolve very small vertical scales, anisotropic mesh and hyperviscosity were used following Lindborg (2006) with $\mathcal{L}_h = 30$, $\mathcal{L}_v = 6$ and $N_h{}^2 \times N_v = 256^2 \times 512$, leading to a ratio of $\delta_h = \mathcal{L}_h/N_h$ over $\delta_v = \mathcal{L}_v/N_v$ equal to 10.

Figure 4.41 presents the temporal evolution of the kinetic energy (figures 4.41*a,b*) and the total dissipation rate (figures 4.41*c,d*) for the full simulation (figures 4.41*a,c*) and the reduced simulation (figures 4.41*b,d*). For the full simulation, the three-dimensional kinetic energy $E_{3D} = E_K - E_{2D}$ (grey curves in figure 4.41*a*), where E_K is the total kinetic energy including the energy associated to the vertical velocity and E_{2D} is the two-dimensional energy, is nearly equal to zero at the beginning of the simulation and increases rapidly after $t \simeq 50$. Remarkably, a similar increase of E_{3D} is also observed for the reduced simulation (figure 4.41*b*) even if the vertical velocity is strictly equal to zero. Another similarity is that the energy growth saturates and that a statistically stationary flow is obtained at late time (not shown) in both simulations.

However, the two flows are very different. The total dissipation rate (black continuous curves in figures 4.41*c,d*) increases more rapidly and less regularly for the full simulation than for the reduced simulation. In the latter case, the dissipation due to vertical gradients (dashed lines) completely dominates the total dissipation whereas it represents only a small portion of the total dissipation for the full simulation. This difference is due to the creation of smaller vertical scales in the reduced simulation and also of smaller horizontal scales in the full simulation. The energy of these structures is dissipated *via* the horizontal hyperviscosity.

Figure 4.42 displays horizontal (figures 4.42*a,b*) and vertical (figures 4.42*c,d*) cross-sections of the vertical vorticity at $t = 40$ for the full simulation (figures 4.42*a,c*) and the reduced simulation (figures 4.42*b,d*). Figure 4.41 shows that at this time the two-

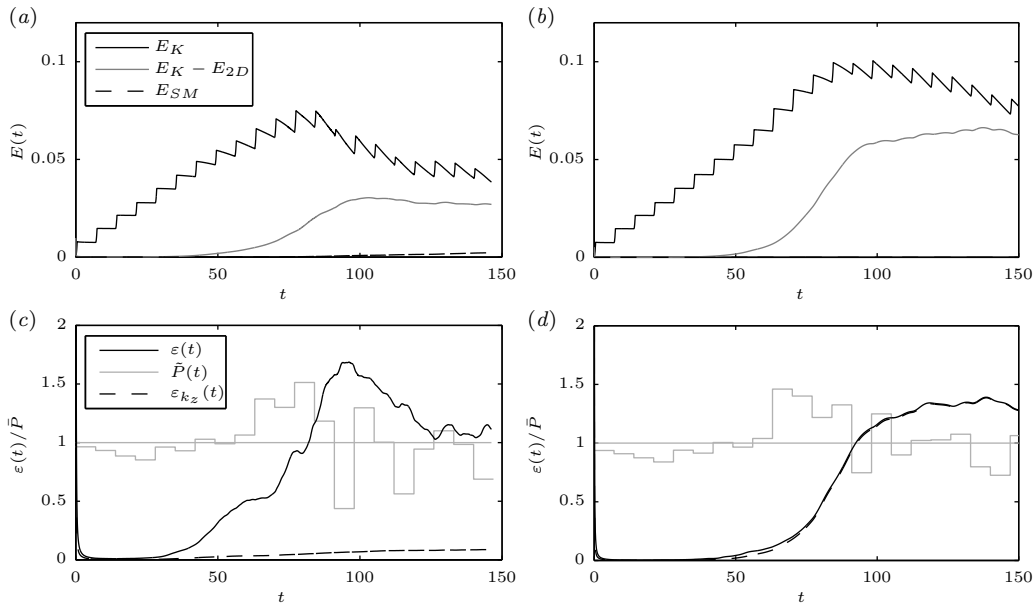

Figure 4.41: Temporal evolution of the kinetic energy (a,b) and the total dissipation rate (c,d) for $Re = 50000$. (a,c) correspond to the simulation of the full Boussinesq Navier-Stokes equations whereas (b,d) correspond to the simulation of the reduced equation (4.21).

dimensional energy still dominates over the three-dimensional energy. Consistently, the vertical cross-sections show that the flows are still roughly columnar even if vertical variations are present in both flows. Remarkably, the columnar vortices located at $x \simeq 11$ and $x \simeq 19$ seem to be slightly less perturbed in the full simulation (figure 4.42c) than in the reduced simulation (figure 4.42d). In contrast, there are many small horizontal and vertical scales around $x = 15$ in the full simulation. These small scales can be also seen in the corresponding horizontal cross-section (figures 4.42a) whereas they are absent in the other simulation (figures 4.42b).

The time evolution of the logarithm of the tridimensional energy $E_{3D} = E_K - E_{2D}$ is plotted in figure 4.43. After an initial decrease, the logarithm of E_{3D} increases approximately linearly for both simulations with nearly the same growth rate $\sigma \simeq 0.053$ (the dashed straight line shows a pure exponential growth at this rate). Around $t = 50$, E_{3D} increases more slowly in the full simulation (black line) whereas it remains approximately exponential until $t \simeq 75$ for the reduced simulation (grey line). This indicates that 3D effects come into play after $t = 50$ and reduce the growth of 3D perturbations. These surprising results suggest that the exponential growth of 3D perturbations is mostly due to a process involving the toroidal velocity. This process can not come from the zigzag instability since this instability needs 3D effects to develop and hence can not occur in the reduced equation (4.21). Such process can not

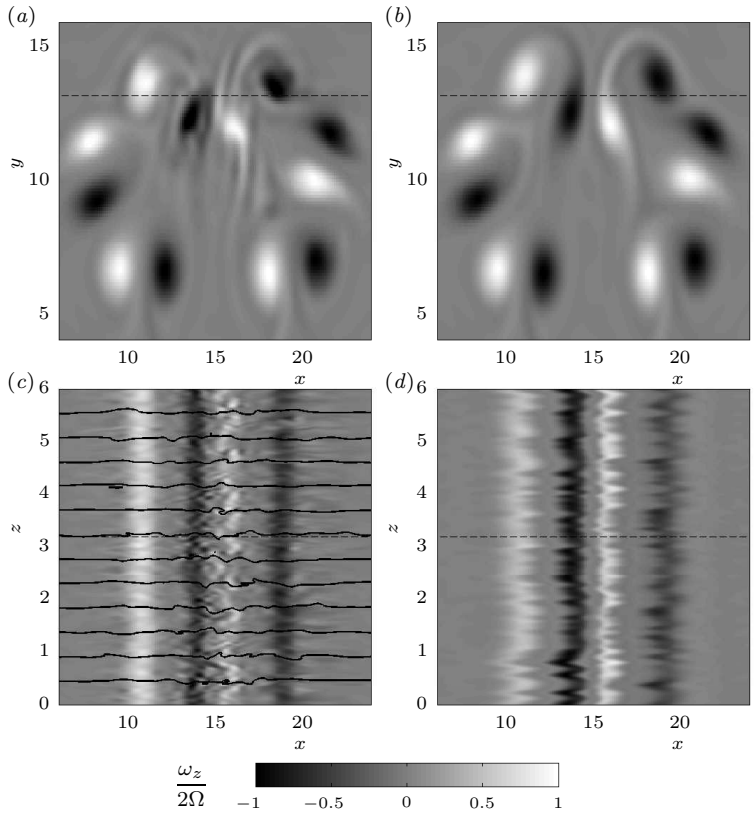

Figure 4.42: Horizontal (a,b) and vertical (c,d) cross-sections of the vertical vorticity for $t = 40$. (a,c) correspond to the full simulation and (b,d) to the reduced simulation. The continuous curves in (c) represent the isopycnals. The dashed horizontal lines indicate the location of the cross-section in the perpendicular direction. In (c,d), the vertical axis has been enlarged by a factor of 3 compared to the horizontal axis.

be due also to the decorrelation mechanism of Lilly (Lilly, 1983) since this mechanism would lead to an algebraic growth of 3D perturbations while here an exponential growth is observed. Therefore, we need to seek a third mechanism in order to explain the exponential growth of 3D perturbations in the reduced simulation. Since the flows at each vertical level in the reduced simulation interact only through viscous effects, vertical gradients can not increase by 3D effects and can only increase if the two-dimensional flows at each vertical level behave differently one from the other.

Figure 4.44 displays horizontal (figures 4.44a,b) and vertical (figures 4.44c,d) cross-sections of the vertical vorticity at $t = 60$ for the full simulation (figures 4.44a,c) and the reduced simulation (figures 4.44b,d). For both flows, there are now much more small vertical length scales than at $t = 40$. However, some coherent vortices remain roughly columnar as seen in the right portion of the figures. We now observe several

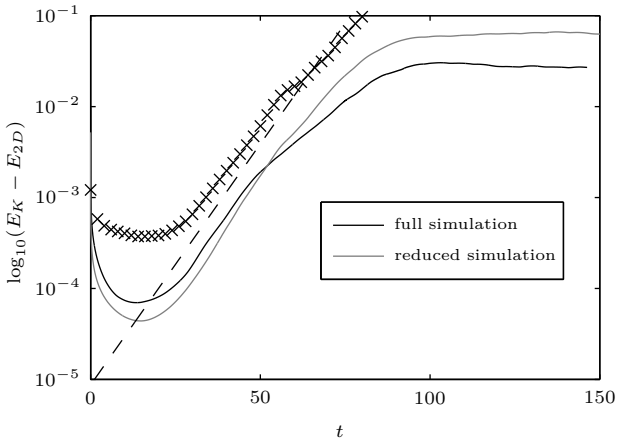

Figure 4.43: Temporal evolution of the logarithm of the tridimensional energy $\log_{10}(E_K - E_{2D})$. The dashed line corresponds to a pure exponential growth with a growth rate equal to $\sigma = 0.053$. The crosses correspond to the logarithm of the energy of the velocity difference between two different two-dimensional simulations.

overturnings in the full simulation (figures 4.44c). There are also much more small horizontal length scales in the full simulation (figures 4.44a) compared to the reduced one. In the vertical cross-section of the full simulation (figure 4.44c) around $x = 21$, some relatively periodic variations can be seen all over the vertical direction. We see in the horizontal cross-section that this structure correspond to a filament produced by the stretching of a vortex. The regularity of the variations along the vertical suggests that they could have been produced by an instability such as the zigzag instability. In contrast, the equivalent structure in figure 4.44(d) exhibits random vertical variations with smaller vertical length scales.

Figure 4.45(a) presents instantaneous vertical kinetic energy spectra (continuous thin lines) for three times $t = 20$, 50 and 80. The vertical spectra are very low of the order of 10^{-6} at $t = 20$ and increase approximately at the same growth rate for the lowest wavenumbers. However, the vertical spectrum for the full simulation at $t = 80$ (black line) decreases at moderate wavenumbers $k_z > 3K$ whereas it decreases only at higher wavenumbers in the dissipative range for the reduced simulation (grey line). This indicates that the vertical length scale selection is due to 3D effects in the full simulation and to viscous effects in the reduced one. This effect is also clearly visible in the vertical kinetic spectra averaged over the statistically stationary regime (thick continuous lines). The two horizontal compensated kinetic energy spectra $E_K(k_h)\varepsilon_K^{-2/3}{k_h}^{5/3}$ averaged over the statistically stationary regime (figure 4.45b) are very different: for the full simulation (black line), the horizontal spectrum follows a $k_h^{-5/3}$ as expected for the strongly stratified inertial range. In contrast, the horizontal spectrum is very steep for the reduced simulation (grey line). It is steeper than the

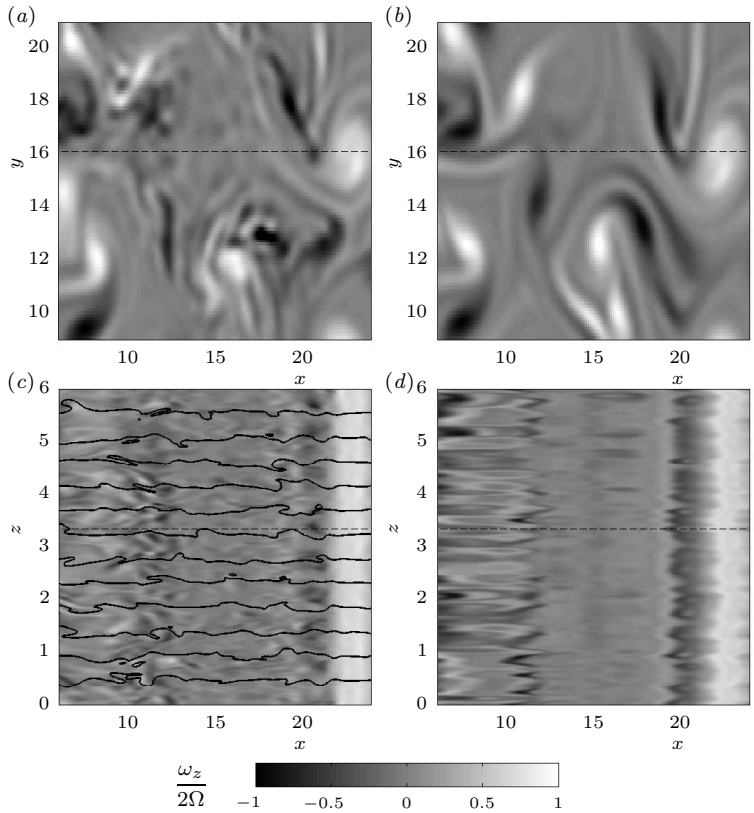

Figure 4.44: Horizontal (*a,b*) and vertical (*c,d*) cross-sections of the vertical vorticity for $t = 60$. (*a,c*) correspond to the full simulation and (*b,d*) to the reduced simulation. The representation is the same as in figure 4.42.

k_h^{-3} spectra observed in 2D-turbulence in the range corresponding to the enstrophy cascade (Kraichnan, 1967) and scales approximately like k_h^{-5} (dashed line) as already reported by Waite & Bartello (2004). This means that there is nearly no energy at small horizontal scales during the statistically stationary regime. In other words, the small structures are directly dissipated due to the strong vertical gradients.

Figure 4.46 displays horizontal (figures 4.46*a,b*) and vertical (figures 4.46*c,d*) cross-sections of the vertical vorticity at $t = 140$ for the full simulation (figures 4.46*a,c*) and the reduced simulation (figures 4.46*b,d*). Both flows present thin horizontal layers (we recall that the vertical coordinate is magnified by a factor of 3). However, in the full simulation the vertical displacements of fluid parcels from their equilibrium levels are approximately as large as the characteristic vertical length scale of the flow whereas in the reduced simulation they are strictly equal to zero (not shown) since this limit is equivalent to have $N = \infty$ so that an infinitely small vertical displacement ζ is able to produce a finite density perturbation. In the full simulation, there are many small

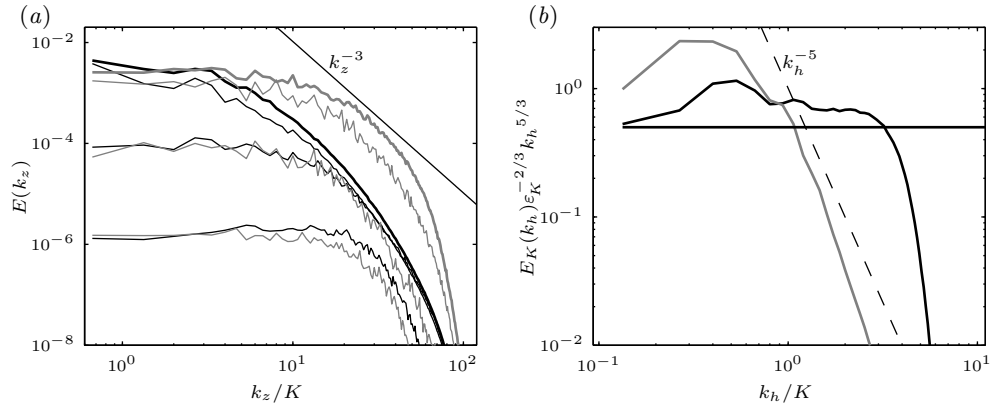

Figure 4.45: (*a*) Unidimensional vertical kinetic spectra for $Re = 50000$ (continuous thin lines) for three times $t = 20$, 50 and 80 (from bottom to up). The black lines correspond to the full simulation and the grey lines to the reduced one. The thick lines correspond to the mean unidimensional vertical spectra averaged over times $130 < t < 150$. The thin straight line corresponds to a k_z^{-3} power law. (*b*) Mean unidimensional compensated horizontal spectra $E_K(k_h)\varepsilon_K^{-2/3}{k_h}^{5/3}$. The thick straight line corresponds to a $k_h^{-5/3}$ power law and the thin dashed line to a k_h^{-5} power law.

horizontal scales whereas in the reduced simulation, large coherent vortices can be seen with very few small scales. It is important to stress that this flow is very different from what would be obtained in a pure 2D-simulation. In the latter case, we would have observed many vorticity filaments stretched by the large scale vortices, whereas, here, such filaments are damped by the strong vertical shear.

In order to understand the origin of the exponential growth of 3D perturbations in the reduced simulation, figure 4.47 presents instantaneous cross-sections of two different two-dimensional simulations for three different time $t = 20$ (figures 4.47*a,d,g,j*), $t = 40$ (figures 4.47*b,e,h,k*) and $t = 60$ (figures 4.47*c,f,i,l*). The simulation presented in figures 4.47(*a,b,c*) has been started from an initial state at rest whereas the initial state of the simulation presented in figures 4.47(*d,e,f*) consisted in a white noise velocity field. Let us denote $\mathbf{u}_{2D}$ and ω_{2D} the velocity and the vertical vorticity of the simulation without initial white noise and $\mathbf{u}_{2D}^{(n)}$ and $\omega_{2D}^{(n)}$ those of the simulation with initial white noise. Since the white noise is weak compared to the forced dipoles, the two flows are very similar at the beginning of the simulations (see figure 4.47*b,e*). However, they rapidly diverge as soon as many vortices are interacting together. The difference of vertical vorticity $\omega' = \omega_{2D}^{(n)} - \omega_{2D}$ is plotted in figures 4.47(*g,h,i*). We clearly see that it increases quickly due to the chaotic nature of these two-dimensional flows.

In figure 4.43, the mean energy associated to the difference of velocity between the two flows $E' = \langle \mathbf{u}'^2/2 \rangle$, where $\mathbf{u}' = \mathbf{u}_{2D}^{(n)} - \mathbf{u}_{2D}$ and the brackets $\langle \cdot \rangle$ denote the space average, are plotted with crosses. We see that this energy first decreases and then

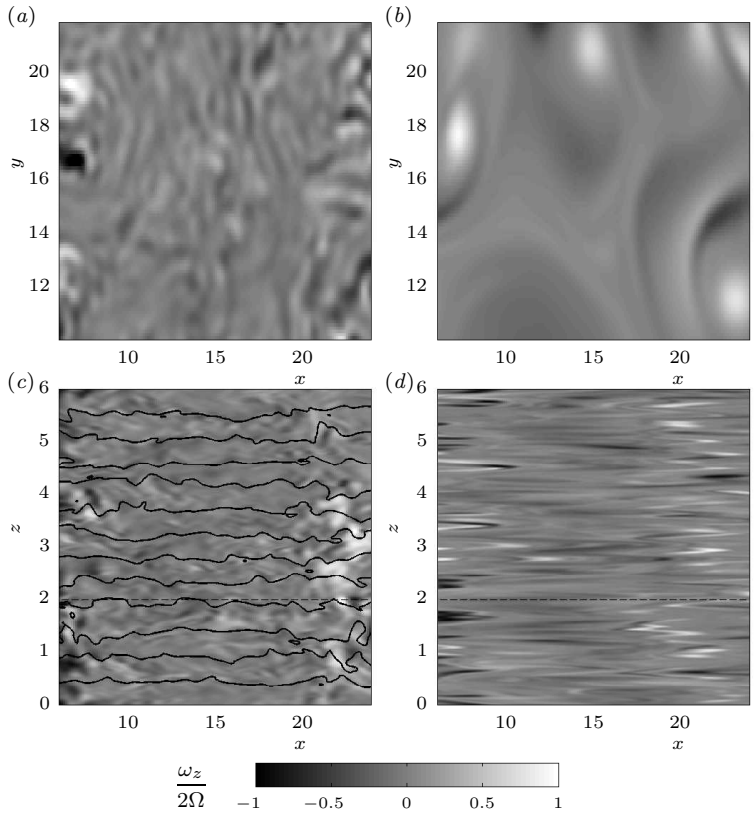

Figure 4.46: Horizontal (a,b) and vertical (c,d) cross-sections of the vertical vorticity for $t = 140$. (a,c) correspond to the full simulation and (b,d) to the reduced simulation. The representation is the same as in figure 4.42.

increases exponentially with a growth rate very close to the growth rate associated to the increase of the three-dimensional energy E_{3D} in the 3D simulations. This confirms that the chaotic divergence of these 2D turbulent flows at each vertical level plays a fundamental role for the vertical decorrelation.

In order to better understand this divergence, let us consider the governing equation for the difference of vertical vorticity ω' in the inviscid limit

$$(\frac{\partial}{\partial t} + \mathbf{u}_{2D}^{(n)} \cdot \boldsymbol{\nabla})\omega' = -\mathbf{u}' \cdot \boldsymbol{\nabla}\omega_{2D}. \tag{4.22}$$

Multiplying (4.22) by ω' and averaging over space gives

$$\frac{d\langle \omega'^2/2 \rangle}{dt} = -\langle \omega' \mathbf{u}' \cdot \boldsymbol{\nabla}\omega_{2D} \rangle. \tag{4.23}$$

The non-averaged forcing term $\omega' \mathbf{u}' \cdot \boldsymbol{\nabla}\omega_{2D}$ scaled by the enstrophy associated to the vorticity difference $Z' = \langle \omega'^2/2 \rangle$ is plotted in figures 4.47(j,k,l). We see that the scaled

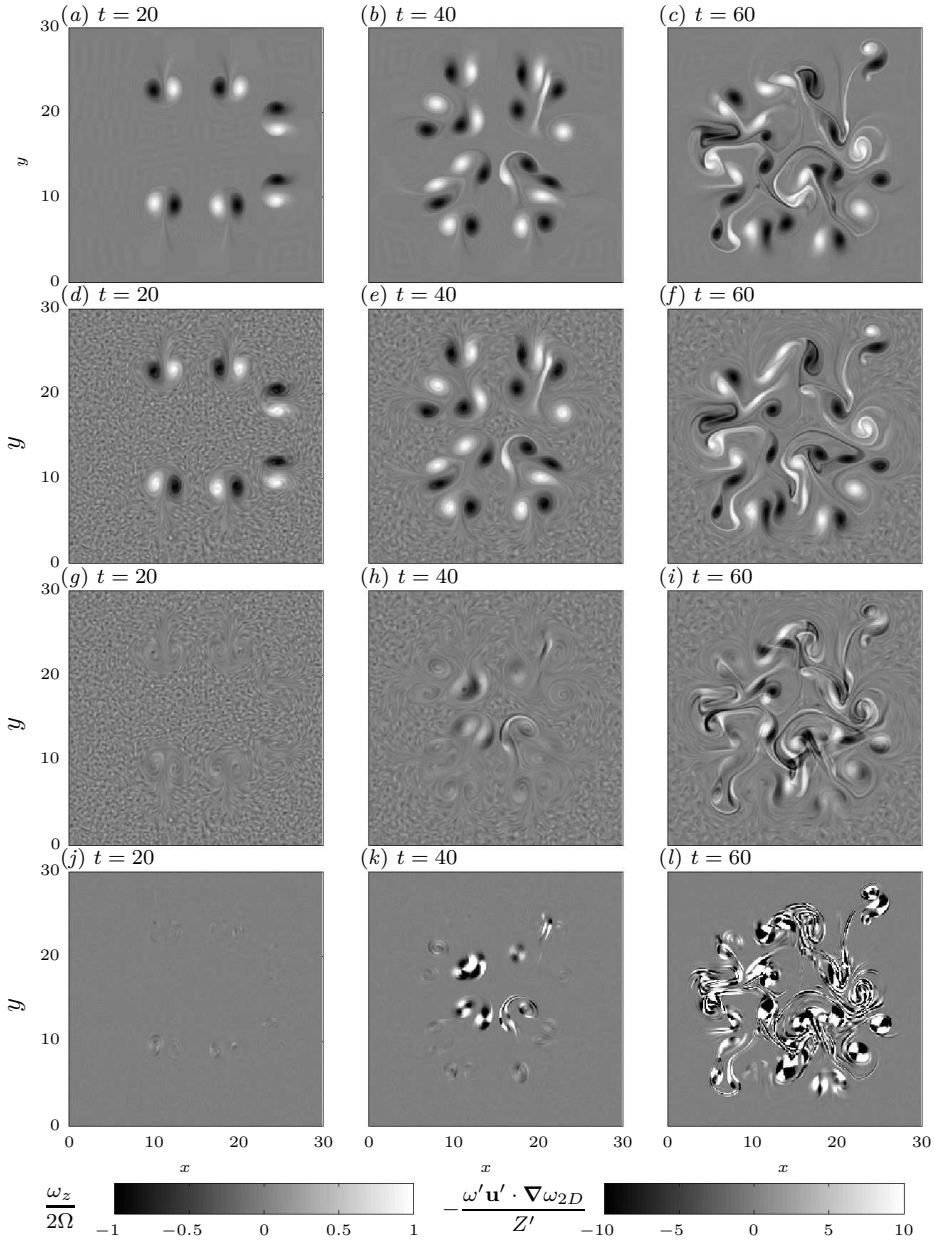

Figure 4.47: Snapshots of the vertical vorticity for three times $t = 20$, 40, 60 and for two 2D simulations differing only by the initial velocity field: a zero velocity field for (*a,b,c*) and a white noise velocity field for (*d,e,f*). (*g,h,i*) represent ω' the difference of vertical velocity between the two flows and (*j,k,l*) the scaled forcing term $\omega'\mathbf{u}' \cdot \boldsymbol{\nabla}\omega_{2D}/Z'$ of (4.23).

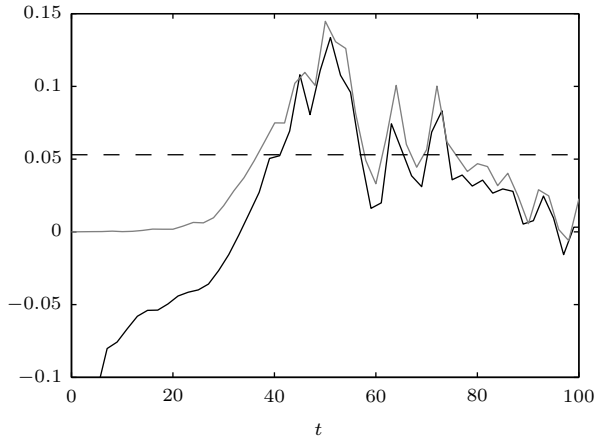

Figure 4.48: Temporal evolution of the instantaneous growth rate $(dZ'/dt)/Z'$ (black line) and of the term $-\langle\omega'\mathbf{u}'\cdot\boldsymbol{\nabla}\omega_{2D}\rangle/\langle{\omega'}^2/2\rangle$ (grey line). The dashed line corresponds to a growth rate equal to $\sigma = 0.053$.

forcing term reaches large values of the order of 10 in the regions where the forced vortices are present.

Figure 4.48 shows the temporal evolution of the instantaneous growth rate $(dZ'/dt)/Z'$ (black line) and of the term $-\langle\omega'\mathbf{u}'\cdot\boldsymbol{\nabla}\omega_{2D}\rangle/Z'$ (grey line). Apart for early times, the two curves nearly collapse. The difference is due to viscous effects which are neglected in (4.23) and also numerical uncertainties in the computation of the time derivative dZ'/dt since this quantity is computed a posteriori from snapshots of the flow separated by two time units. We see that the scaled forcing term is very low before $t = 25$ and then increases to positive values of the order of the measured growth rate for the energy E_{3D}: $\sigma = 0.053$. This strongly suggests that the chaotic divergence of 2D flows is responsible for the initial emergence of vertical variations both in the reduced and in the full simulations.

This chaotic decorrelation mechanism seems to be faster than the zigzag instability and therefore it governs the initial development of 3D perturbations in the full simulation (figure 4.43). However, the strength of this mechanism certainly depends on the characteristics of the forced 2D flows and of the types of initial perturbations since the flow is unsteady. It would be interesting to study its importance compared to the zigzag instability in other types of 2D flows and for various initial perturbations.

We can also note that the importance of the chaotic decorrelation mechanism compared to the zigzag instability should depend on the ratio of the height of the computational domain and the buoyancy length scale L_b. Indeed, the chaotic decorrelation mechanism is expected to occur mainly for vertical scales much larger than L_b, while the zigzag instability and 3D effects operate at vertical scales of the order of the buoyancy length scale. Therefore, if the height of the computational domain

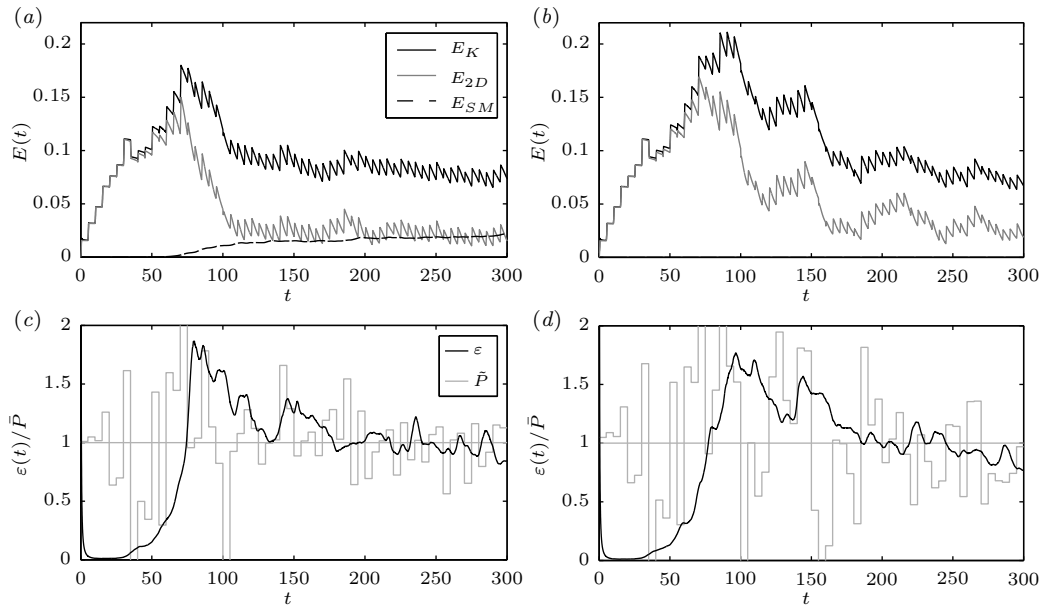

Figure 4.49: Temporal evolution of energy (a,b) and dissipation rate (c,d) for $F_h = 0.66$ and $Re = 10000$. (b,d) correspond to a simulation in which the shear modes have been inhibited and (a,c) to the same simulation but with shear modes.

$\mathcal{L}_z$ is very large compared to L_b, the chaotic decorrelation mechanism will be largely responsible for the emergence of vertical variations. In contrast, when $\mathcal{L}_z$ is of the order of L_b, it is expected to play a less important role whereas 3D effects should appear to be more active.

4.2.7 Appendix 2: shear modes

We now present a simulation in which the shear modes are suppressed numerically and compare it with the same simulation but with shear modes. The forcing and the numerical methods are the same as in subsection 4.2.4. The horizontal Froude number and the Reynolds number are equal to $F_h = 0.66$ and $Re = 10000$, leading to a buoyancy Reynolds number $\mathcal{R} = 5350$ high enough to reach the strongly stratified turbulent regime. Figure 4.49 presents the time evolution of the kinetic energy (figures 4.49a,b) and the total dissipation rate (figures 4.49c,d) for both simulations. The energy of the shear modes (dashed lines) increases after $t \simeq 60$ from zero up to a value of the order of one fourth of the total energy. This ratio is consistent with previous numerical studies of forced strongly stratified turbulence (Smith & Waleffe, 2002; Waite & Bartello, 2004; Lindborg, 2006; Brethouwer *et al.*, 2007). At the same time, the two-dimensional energy E_{2D} decreases rapidly (grey lines in figures 4.49a). Remarkably, this decrease is much slower and less regular in the simulation without

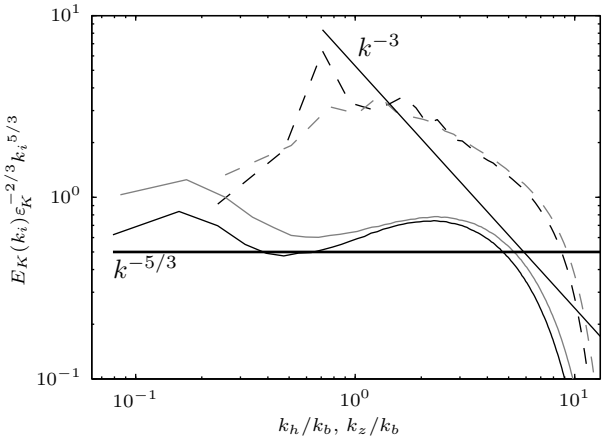

Figure 4.50: Horizontal (continuous lines) and vertical (dashed lines) compensated 1D spectra of kinetic energy $E_K(k_i)\varepsilon_K^{-2/3}{k_i}^{5/3}$ as a function of the scaled wavenumber k_i/k_b, where k_i denotes either the horizontal wavenumber k_h or the vertical wavenumber k_z. Black lines correspond to a simulation with shear modes and grey lines to a simulation without shear mode.

shear modes (figure 4.49*b*). The kinetic energy is also larger around $t = 125$ when the shear modes are absent. However, the levels of kinetic energy reached after $t = 250$ during the statistically stationary regime are approximately equal for both simulations. It seems that there are more larger variations and slightly higher values of the two-dimensional energy in the simulation without shear modes than in the other one. Another difference between the two simulations concerns $\tilde{P}(t)$ the injection rate averaged over one injection period $\Delta t = 5$, which varies much more in the simulation without shear modes than in the other one. This could be due to a difference of structure between the two flows with less layers and more columnar dipoles when the shear modes are absent.

In figure 4.50, the horizontal compensated unidimensional spectra of kinetic energy $E_K(k_h)\varepsilon_K^{-2/3}{k_h}^{5/3}$ are plotted as a function of the horizontal wavenumber k_h scaled by k_b the buoyancy wavenumber for both simulations with (black lines) and without (grey lines) shear modes. The vertical compensated spectra $E_K(k_z)\varepsilon_K^{-2/3}{k_z}^{5/3}$ are also shown with dashed lines. The horizontal spectra are similar but there is more energy at the large horizontal scales in the simulation without shear mode. This lead to a different shape with weaker anomalies at intermediate scales and at the buoyancy scale compared to the simulation with shear modes. However, the compensated spectrum for the simulation without shear modes is slightly higher than 0.5. The vertical compensated spectra differ mainly by the presence of two peaks in the simulation with shear modes: a large one at $k_z \simeq 0.7k_b$ and a much smaller one at $k_z \simeq 1.5k_b$, i.e. at a wavenumber corresponding approximately to the first harmonic of the first peak. The

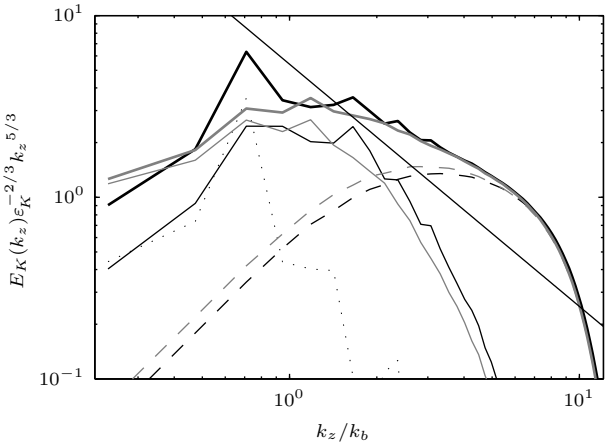

Figure 4.51: Decomposition of the vertical compensated spectra. Black lines correspond to a simulation with shear modes and grey lines to a simulation without shear mode. The continuous thick curves correspond to the total vertical spectra, the continuous thin curves to vertical spectra $E_{[K,0<\kappa_h\leqslant 0.4k_b]}(k_z)$ computed with modes for which $0 < \kappa_h \leqslant 0.4k_b$, the dotted curve to the shear modes vertical spectra $E_{[K,\kappa_h=0]}(k_z)$ and the dashed curves to spectra $E_{[K,\kappa_h>0.4k_b]}(k_z)$ computed with modes for which $\kappa_h > 0.4k_b$. The thin straight line indicates the k_z^{-3} power law.

first large peak should be related to the shear modes. The spectrum for the simulation without shear modes is slightly higher at the lowest vertical wavenumbers.

Figure 4.51 presents a decomposition of the vertical kinetic spectra as done in figure 4.38. As already mentioned, for the simulation with shear modes, the conditional vertical spectra $E_{[K,0<\kappa_h\leqslant 0.4k_b]}(k_z)$ associated to the large horizontal scales: $0 < \kappa_h \leqslant 0.4k_b$ (thin black continuous line), is approximately equal to the conditional vertical spectrum of the shear modes $E_{[K,\kappa_h=0]}(k_z)$ (dotted line). The conditional vertical spectra $E_{[K,0<\kappa_h\leqslant 0.4k_b]}(k_z)$ is higher at wavenumber $k_z < 0.5k_b$ for the simulation without shear modes leading to a total vertical spectra of the same order in both simulations. The second peak at $k_z \simeq 1.5k_b$ in the total vertical spectra appears in the conditional vertical spectra $E_{[K,0<\kappa_h\leqslant 0.4k_b]}(k_z)$ meaning that it corresponds to relatively large horizontal scales. The spectra $E_{[K,\kappa_h>0.4k_b]}(k_z)$ corresponding to small horizontal length scales are almost similar except that it is slightly higher for the simulation without shear modes than for the other.

To conclude, the shear modes represent a non-negligible part of the total energy and seems to play an important role in the dynamics. Further investigations are needed to better understand this issue.

Chapter 5

Kolmogorov laws for stratified turbulence

Kolmogorov laws for stratified turbulence

Pierre Augier[1], Sébastien Galtier[2] and Paul Billant[1]

[1]LadHyX, CNRS, École Polytechnique, 91128 Palaiseau Cedex, France

[2]Institut d'Astrophysique Spatiale, Université Paris-Sud, bâtiment 121, 91405 Orsay, France, Institut universitaire de France, sebastien.galtier@ias.u-psud.fr

Following the Kolmogorov's technique, an exact relation for a vector third-order moment **J** is derived for three-dimensional incompressible stably stratified turbulence under the Boussinesq approximation. In the limit of a small Brunt-Väisälä frequency, isotropy may be assumed which allows us to find a generalized Kolmogorov's four-thirds law. For a strong stratification we make the ansatz that **J** is directed along axisymmetric surfaces parametrized by a scaling law relating horizontal and vertical coordinates. The intensity of anisotropy is then parametrized by a unique real coefficient. The exact relation is integrated under this hypothesis and the assumption of an axisymmetric turbulence with respect to the vertical direction to obtain a generalized Kolmogorov law which applies to any type of anisotropic axisymmetric turbulence; the limits of three-dimensional and two-dimensional isotropic turbulences are indeed recovered. A prediction for stratified turbulence is made based on the relation between horizontal and vertical scales predicted by scaling analysis.

5.1 Introduction

The "four-fifths law" (Kolmogorov, 1941a) is one of the only exact results of the theory of three-dimensional homogeneous isotropic turbulence in the limit of large Reynolds numbers. Its more common expression is $\langle[\delta v_L(\mathbf{r})]^3\rangle = -\frac{4}{5}\varepsilon_K r$, where ε_K is the mean kinetic energy dissipation rate per unit mass, $\delta v_L(\mathbf{r}) = (\mathbf{u}(\mathbf{x}+\mathbf{r})-\mathbf{u}(\mathbf{x}))\cdot\mathbf{r}/r$ the longitudinal velocity increment and $\langle\cdot\rangle$ denotes a mean value. Alternatively, the Kolmogorov law can be expressed as (Antonia *et al.*, 1997)

$$J_L(\mathbf{r}) = -\frac{4}{3}\varepsilon_K r, \tag{5.1}$$

where $\mathbf{J}(\mathbf{r}) = \langle|\delta\mathbf{u}(\mathbf{r})|^2\delta\mathbf{u}(\mathbf{r})\rangle$ is the vector third-order moment of the fluctuations; it is the so-called 4/3s law. The Kolmogorov law is one of the most important result in the theory of homogeneous isotropic turbulence (Frisch, 1995) for both fundamental and practical reasons. It gives the scaling law $\delta u \sim (\varepsilon_K r)^{1/3}$ and the exact coefficient of proportionality. The law expresses the nonlinear fluxes through scales in the inertial range as a function of measurable third-order moment quantities. Extensions of the isotropic Kolmogorov law to other fluids have been made: it concerns for example scalar passively advected such as the temperature or a pollutant in the atmosphere (Yaglom, 1949), quasi-geostrophic flows (Lindborg, 2007b) or magnetized fluids (Politano & Pouquet, 1998; Galtier, 2008a,b; Meyrand & Galtier, 2010).

The Kolmogorov 4/5s law comes from the theory of homogeneous isotropic turbulence where tensorial calculations are developed. Even if symmetries are used to

simplify the analysis, it is somehow difficult to follow the main steps of the derivation and the physical meaning can be hidden by technical difficulties. Hopefully, an easier alternative derivation exists (Monin & Yaglom, 1975; Podesta, 2008) in which isotropy may be introduced only after an intermediate more general result, which is

$$\boldsymbol{\nabla} \cdot \mathbf{J} = -4\,\varepsilon_K. \tag{5.2}$$

It is important to emphasize that the assumption of isotropy must be dropped out in many realistic situations like in geophysical turbulence, and more generally when rotation, stratification or an imposed magnetic field act on the flow. These physical ingredients drastically change the flow dynamics (with different invariants and instabilities) and break the isotropy. From a theoretical point of view, the lack of isotropy renders the derivation of the counterpart of the 4/3s law much more difficult. However, recent progress have been made in that direction for rotating or magnetized flows (Galtier, 2009a,b,c). Relaxing the isotropy assumption for the less restrictive case of axisymmetry, and adopting the critical balance view point in which one makes the assumption of a scale-by-scale balance between the two timescales of the system (*i.e.* between the eddy turnover time and the wave time), the correlation space was assumed to become foliated in the sense that the vector third-order moments have a specific distribution. This new geometrical interpretation of the correlation space allows us to integrate equation (5.2) and find the counterpart of the 4/3s law for the studied axisymmetric turbulences.

In the present paper we are mainly interested with purely stratified (non magnetized, non rotating) flows. It is well known that geophysical turbulence in the Earth's fluid envelopes is strongly influenced by density stratification and rotation. Because the Brunt-Väisälä frequency N characterizing the stratification is usually much larger than the local rotation frequency f, there are intermediate ranges of scales (1 m-100 km in the atmosphere and 1 m-1 km in the oceans) where the Earth's rotation effect is negligible but where the stratification is strong.

The distinguishing attribute of these strongly stratified flows is a small horizontal Froude number $F_h = U/(NL_h)$, where U is a characteristic velocity scale, L_h an horizontal scale and N the Brunt-Väisälä frequency. Although the dynamics of strongly stratified turbulence has been a matter of debate for a long time, its understanding has significantly improved over the last decade and it is now well established that it is fully three-dimensional and strongly anisotropic. The characteristic vertical scales of a given structure is much smaller than its typical horizontal length scale and is of the order of the buoyancy length scale $L_b = U/N$ (Billant & Chomaz, 2001; Lindborg, 2006). Despite this strong anisotropy, Lindborg (2006) has shown that there is an inertial range with a direct energy cascade from larges to small horizontal scales as in isotropic homogeneous turbulence. Such inertial range exists however only if the buoyancy Reynolds number, $\mathcal{R} = Re{F_h}^2$, where Re is the Reynolds number, is large (Brethouwer *et al.*, 2007). This condition requires very large Reynolds number since $F_h \ll 1$. This is largely fulfilled in geophysical flows but is much more difficult to achieve in direct numerical simulations or experiments. Nevertheless, such strongly stratified inertial range has been observed in many numerical simulations and also in situ (Riley & Lindborg, 2008). Brethouwer *et al.* (2007) have shown that the strongly

stratified inertial range should be followed at small scales by a nearly isotropic range since stratification effects weaken as the scale decreases down to the dissipative scale.

The purpose of the paper is to derive a third-order structure function relation taking into account the anisotropy of strongly stratified turbulence in the stratified inertial range. Such relation should be of interest for interpreting in-situ measurements or numerical simulations. For example, Lindborg (1999), Cho & Lindborg (2001) and Lindborg & Cho (2001) performed statistical studies on air-plane measurements to compute the nonlinear fluxes using a 4/3s law derived for stratified rotating turbulence and for horizontal velocity increments. A vectorial anisotropic law applying especially to strongly stratified turbulence should allow one to gain further information from these data.

The paper is organized as follows. In §2 we derive an exact relation in terms of vector third-order moments; it is the first main part of the paper. In particular, we discuss the case of weak stratification for which an universal 4/5s law may be proposed. Strong stratification is considered in §3 which is the second main part of the paper. We introduce the idea that the directional characteristics of the vector third-order moments of the increments is constrained by stratification to follow a particular power law. Under this hypothesis, the intensity of anisotropy is parametrized by a single coefficient and we can derive a generalised Kolmogorov law potentially describing all types of axisymmetric turbulence. The Kolmogorov vectorial law that should be valid for strongly stratified turbulence is derived based on scaling analyses of strongly stratified flows. Finally, the main results of the paper are summarized in §5.

5.2 Derivation of an exact relation for the vectorial third-order structure function

5.2.1 Governing equations

The equations for an incompressible, nondiffusive and inviscid stably stratified fluid in the Boussinesq approximation read

$$\partial_t \mathbf{u} + \mathbf{u}\cdot\boldsymbol{\nabla}\mathbf{u} = -\boldsymbol{\nabla} p + N^2\zeta \boldsymbol{e_z}, \tag{5.3}$$

$$\partial_t \zeta + \mathbf{u}\cdot\boldsymbol{\nabla}\zeta = u_z, \tag{5.4}$$

$$\boldsymbol{\nabla}\cdot\mathbf{u} = 0, \tag{5.5}$$

where $\mathbf{u}$ is the velocity, u_z its vertical component, p the rescaled pressure (energy per unit mass), $N=\sqrt{-(g/\rho_0)(d\bar{\rho}/dz)}$ the Brunt-Väisälä frequency, $\boldsymbol{e_z}$ the vertical unit vector and $\zeta=\rho' g/(\rho_0 N^2)$, with g the gravity, ρ_0 a reference density, $\bar{\rho}(z)$ the mean density and $\rho'(\mathbf{r})$ the density perturbation. The quantity ζ can be interpreted as the vertical displacements of isopycnals (iso-density surfaces) from their unperturbed position when the stratification is linear. Note that with the Boussinesq approximation, it is assumed that $\rho_0 \gg \bar{\rho}, \rho'$.

Equations (5.3-5.4) have two invariants: the total energy and the potential enstro-

phy which are respectively (see *e.g.* Kurien *et al.*, 2006)

$$E = \frac{1}{2}\langle \mathbf{u}^2 \rangle + \frac{1}{2}\langle N^2 \zeta^2 \rangle, \tag{5.6}$$

$$Q = \frac{1}{2}\langle q^2 \rangle, \tag{5.7}$$

where $q = (g/\rho_0)\boldsymbol{\omega} \cdot \boldsymbol{\nabla}\rho = N^2 \boldsymbol{\omega} \cdot \boldsymbol{\nabla}\zeta - N^2 \omega_z$ is the potential vorticity, with ρ the total density and $\boldsymbol{\omega} = \boldsymbol{\nabla} \times \mathbf{u}$ the vorticity. Note that the potential vorticity is non linear. The conservation of potential enstrophy does not imply an inverse cascade of energy like in two-dimensional turbulence or quasi-geostrophic turbulence. Indeed, Lindborg (2006) has shown that the energy cascade is direct (Lindborg, 2006; Brethouwer *et al.*, 2007). In the sequel, we shall focus on the first invariant, i.e. the energy.

5.2.2 Stationary developed turbulence

The following assumptions specific to fully developed turbulence will be assumed (Kolmogorov, 1941a; Frisch, 1995). First, we suppose the presence of a large-scale forcing $\mathcal{F}$ and a small-scale dissipation $\mathcal{D}$. Second, we take the long time limit for which a stationary state is reached with a finite mean total energy dissipation rate per unit mass. Third, we consider the infinite Reynolds number limit for which the mean total energy dissipation rate per unit mass tends to a finite limit, ε.

It is simpler to consider the concept of fully developed stationary turbulence in spectral space in which the forcing and the dissipative terms are well localised. We use the definition of the Fourier transform adapted to a periodic three-dimensional box of side $\mathcal{L}$:

$$\hat{\mathbf{u}}(\mathbf{k}) \equiv \int_{\mathcal{L}^3} \mathbf{u}(\mathbf{x}) e^{-i\mathbf{k}\cdot\mathbf{x}} \frac{d^3\mathbf{x}}{\mathcal{L}^3}. \tag{5.8}$$

The equation of evolution of the energy of a mode $\mathbf{k}$ in Fourier space $\hat{E}(\mathbf{k}) = \frac{1}{2}|\hat{\mathbf{u}}|^2 + \frac{1}{2}N^2\hat{\zeta}^2$ can be written as

$$\partial_t \hat{E} = \hat{T} + \hat{\mathcal{F}} - \hat{\mathcal{D}}, \tag{5.9}$$

where $\hat{T}$ is the conservative nonlinear transfer. The sums over all spectral modes of $\hat{\mathcal{F}}$ and $\hat{\mathcal{D}}$ are respectively the energy injection P and the total dissipation ε, whereas the sum of $\hat{T}$ over all the spectral modes is null. For stationary turbulence, time derivative is null and $P = \varepsilon$. Fully developed turbulence is characterized by a strong separation of scales between large-scale forcing and small-scale dissipation when the Reynolds number is very large. In between, an inertial range of scales exists where all the terms of equation (5.9) are null in the stationary regime; in this case a divergenceless energy flux $\hat{\mathbf{\Pi}}$ is expected, with by definition $\hat{T} \equiv -\partial\hat{\Pi}_i/\partial k_i$. Although the nonlinear transfers consist in spectral space in triadic interactions and do not naturally express as the divergence of a flux vector, we will explain in subsection 5.2.4 how to compute the flux $\hat{\mathbf{\Pi}}$. We now turn to the equivalent of equation (5.9) in the correlation space. Because the inverse Fourier transform of $|\hat{\mathbf{u}}|^2$ leads to the two-point correlation function of velocity we shall derive the equation of evolution of the latter quantity.

5.2.3 von Kármán-Howarth equation

In this subsection, we derive the evolution equation of two-point correlation functions. Because we aim at describing the inertial range we will neglect hereafter the forcing and dissipative terms. First, we start with the velocity correlation using the notation

$$\langle u_i u'_j \rangle = \langle u_i(\mathbf{x}) u_j(\mathbf{x}') \rangle, \tag{5.10}$$

where $\mathbf{x}' = \mathbf{x} + \mathbf{r}$, where $\mathbf{r}$ is the separation vector, we have for the second-order correlation tensor

$$\begin{aligned} \partial_t \langle u_i u'_j \rangle(\mathbf{r}) &= \langle u_i \partial_t u'_j \rangle + \langle u'_j \partial_t u_i \rangle \\ &= -\langle u_i u'_\ell \partial'_\ell u'_j \rangle - \langle u_i \partial'_j p' \rangle - \langle u_i N^2 \zeta' \delta_{jz} \rangle \\ &\quad -\langle u'_j u_\ell \partial_\ell u_i \rangle - \langle u'_j \partial_i p \rangle - \langle u'_j N^2 \zeta \delta_{iz} \rangle. \end{aligned} \tag{5.11}$$

Using the homogeneity assumption and the divergence free condition we get

$$\begin{aligned} \partial_t \langle u_i u'_j \rangle &= \partial_{r_\ell} [\langle u'_j u_\ell u_i \rangle - \langle u_i u'_\ell u'_j \rangle] - \langle u_i N^2 \zeta' \delta_{jz} \rangle - \langle u'_j N^2 \zeta \delta_{iz} \rangle \\ &\quad + \partial_{r_i} \langle p u'_j \rangle - \partial_{r_j} \langle p' u_i \rangle. \end{aligned} \tag{5.12}$$

The velocity-pressure correlation terms is non-zero since up to now isotropy is not assumed. When the diagonal part of the energy tensor is only retained their contributions disappear (Batchelor, 1953) leading to (with the Einstein's notation)

$$\partial_t \langle u_i u'_i \rangle = 2 \boldsymbol{\nabla} \cdot \langle (u_i u'_i) \mathbf{u} \rangle - N^2 [\langle u_z \zeta' \rangle + \langle u'_z \zeta \rangle]. \tag{5.13}$$

Secondly, we have for the scalar correlation

$$\begin{aligned} \partial_t \langle \zeta \zeta' \rangle(\mathbf{r}) &= \langle \zeta \partial_t \zeta' \rangle + \langle \zeta' \partial_t \zeta \rangle \\ &= -\langle \zeta u'_\ell \partial'_\ell \zeta' \rangle + \langle \zeta u'_z \rangle - \langle \zeta' u_\ell \partial_\ell \zeta \rangle + \langle \zeta' u_z \rangle. \end{aligned} \tag{5.14}$$

The homogeneity hypothesis and the divergence free condition give

$$\partial_t \langle \zeta \zeta' \rangle = 2 \boldsymbol{\nabla} \cdot \langle \zeta \zeta' \mathbf{u} \rangle + \langle \zeta u'_z \rangle + \langle \zeta' u_z \rangle. \tag{5.15}$$

The combination of relations (5.13) and (5.15) gives eventually

$$\partial_t E(\mathbf{r}) = \boldsymbol{\nabla} \cdot \langle [u_i u'_i + N^2 \zeta \zeta'] \mathbf{u} \rangle. \tag{5.16}$$

where $E(\mathbf{r}) = (1/2)[\langle u_i u'_i \rangle + N^2 \langle \zeta \zeta' \rangle]$.

Equation (5.16) is nothing else than the inverse Fourier transform of (5.9) where the forcing and dissipative terms have been neglected; it can be written as

$$\partial_t E(\mathbf{r}) = T(\mathbf{r}) + \mathcal{F}(\mathbf{r}) - \mathcal{D}(\mathbf{r}). \tag{5.17}$$

By identification, we see that

$$T(\mathbf{r}) = \boldsymbol{\nabla} \cdot \langle [u_i u'_i + N^2 \zeta \zeta'] \mathbf{u} \rangle = \boldsymbol{\nabla} \cdot \mathbf{M}, \tag{5.18}$$

which means that, in physical space, the non-linear transfers naturally express as a local flux of correlation given by $\mathbf{M}$. This is the first intermediate result of this paper. It has to be pointed out that $E(\mathbf{r}) = TF^{-1}[\hat{E}]$ is a correlation function which should not be confused with the energy in physical space.

5.2.4 Relation between $T(\mathbf{r})$ and the energy flux

It is a classical result of homogeneous, isotropic, stationary developed turbulence that $T(\mathbf{r})$ is equal in the inertial range to the opposite of Π, the energy flux from small to large wave-numbers, *i.e.* $T(\mathbf{r}) = \mathcal{D}(\mathbf{r}) - \mathcal{F}(\mathbf{r}) = -\Pi$. However, this result is not obvious. Following Lindborg & Cho (2001), we present, hereafter, a simple justification of this relation. Let us apply to equation (5.9) the operator sum over a volume Ω of the spectral space; we obtain

$$\frac{\partial E_\Omega}{\partial t} = -\Pi_\Omega + P_\Omega - \varepsilon_\Omega, \tag{5.19}$$

where $\Pi_\Omega = -\sum_{\mathbf{k}\in\Omega} \hat{T}(\mathbf{k})$ is the energy flux going out of the volume Ω, $P_\Omega = \sum_{\mathbf{k}\in\Omega} \hat{\mathcal{F}}$ and $\varepsilon_\Omega = \sum_{\mathbf{k}\in\Omega} \hat{\mathcal{D}}$. Let us define some particular inertial subspaces noted Ω_i containing all the forcing modes, i.e. $P_{\Omega_i} = P$, and for which the dissipation is negligible: $\varepsilon_{\Omega_i} \simeq 0$. Then, the flux cascading out of the inertial subspace is equal to the forcing P and is linked to $T(\mathbf{r})$ by the following relation

$$P = \Pi_{\Omega_i} = -\sum_{\mathbf{k}\in\Omega_i} \hat{T}(\mathbf{k}) = -\sum_{\mathbf{k}\in\Omega_i} \int_{\mathcal{L}^3} T(\mathbf{r}) e^{-i\mathbf{k}\cdot\mathbf{r}} \frac{d^3\mathbf{r}}{\mathcal{L}^3}. \tag{5.20}$$

It is straightforward to show that $T(\mathbf{r})$ monotonically goes to zero as $\mathbf{r} \to 0$. Thus the integral in space is dominated by the extended inertial range where $T(\mathbf{r})$ is equal to a constant T_0. With this assumption, we have

$$\Pi_{\Omega_f} \simeq -\sum_{\mathbf{k}\in\Omega_f} T_0 \int_{\mathcal{L}^3} e^{-i\mathbf{k}\cdot\mathbf{r}} \frac{d^3\mathbf{r}}{\mathcal{L}^3} = -T_0. \tag{5.21}$$

All together, we have a broad justification that in the inertial range $T(\mathbf{r}) = -\mathcal{F}(\mathbf{r}) = -P = -\varepsilon$. A more rigorous derivation of this relation has been proposed by Frisch (1995), Lindborg (1999) and Podesta (2008). Note that the general relation $T(\mathbf{r}) = -\varepsilon$ is also valid for a system without external forcing (Landau & Lifchitz, 1989). In this case, one has to deal with the decay problem for which the time derivative of the total energy is equal (up to a sign) to the mean energy dissipation rate per unit mass ε. However, this leads to the same relation.

5.2.5 Exact result for homogeneous stratified turbulence

The intermediate result $T(\mathbf{r}) = -\varepsilon$ leads eventually to a general relation valid both in decaying and forced turbulence

$$\boldsymbol{\nabla} \cdot \langle \mathbf{u}(u_i u_i') + N^2 \mathbf{u}\zeta\zeta' \rangle = -\varepsilon. \tag{5.22}$$

Since data analyses use generally structure functions, it is convenient to rewrite (5.22) by introducing the vector third-order moment of increments:

$$\boldsymbol{\nabla} \cdot \mathbf{J} = \boldsymbol{\nabla} \cdot \langle [(\delta\mathbf{u})^2 + N^2(\delta\zeta)^2]\delta\mathbf{u} \rangle = -4\varepsilon. \tag{5.23}$$

Equation (5.23) is the first main result of the paper. It describes homogeneous stratified turbulence. This relation remains valid even when the turbulence is anisotropic. Note that the flux $\mathbf{J}$ can be divided into a kinetic flux and a potential flux which may be calculated independently. In practice, it is also interesting to quantify the term of exchange from kinetic to potential energies which is

$$B(\mathbf{r}) = \frac{N^2}{2}(2\langle u_z\zeta\rangle - \langle \delta u_z \delta\zeta\rangle). \tag{5.24}$$

5.2.6 Weak stratification limit

When N is small, the stratification effects may be seen as a correction to the dynamics of a non-stratified fluid. Then, we may expect that the assumption of isotropy still holds at first order. In this case, we can integrate expression (5.23) over a full sphere of radius r; after the application of the divergence theorem we obtain the universal law

$$\langle[(\delta\mathbf{u})^2 + N^2(\delta\zeta)^2]\delta u_L\rangle = -\frac{4}{3}\varepsilon r. \tag{5.25}$$

where L means the longitudinal component of the vector, *i.e.* the one along the $\mathbf{r}$–direction. The stratification term appears as a correction to the 4/3s law derived under this form by Antonia *et al.* (1997). This law not only provides a linear scaling for third-order structure functions within the inertial range of length scales, but it also fixes the value of the numerical factor appearing in front of the scaling relation. Note finally that a simple dimensional analysis performed on the universal law (5.25) leads to the isotropic spectral relation $E^\zeta(k) \sim k^{-5/3}$ as for passive scalar (Obukhov, 1949; Corrsin, 1951).

5.3 Kolmogorov law for anisotropic axisymmetric turbulence

We now derive the counterpart of the Komogorov law for anisotropic axisymmetric turbulence starting from the general expression (5.23) which is exact for homogeneous turbulence. An application to strongly stratified turbulence will be next presented.

5.3.1 Assumption on the direction of the flux J

The case of a strong stratification is more difficult to analyze since turbulence becomes anisotropic. However, we may assume that stratified turbulence remains axisymmetric, i.e. statistically invariant under rotation around the vertical axis. This implies that the flux $\mathbf{J}$ has a null azimuthal component and does not depend on the azimuthal coordinate, i.e. $\mathbf{J} = J_v(r_h, r_v)\boldsymbol{e_v} + J_h(r_h, r_v)\boldsymbol{e_h}$, where r_v is the vertical coordinate, $r_h = \sqrt{{r_x}^2 + {r_y}^2}$ the radial coordinate and $\boldsymbol{e_v}$ and $\boldsymbol{e_h}$ the associated unit vectors. However, this result alone is insufficient to integrate (5.23). Indeed, the axisymmetry does not fully determine the type of flow. For example, 2D and 3D isotropic turbulences are both axisymmetric but lead to different Kolmogorov laws.

Hence, we have to specify the degree of anisotropy. Following Galtier (2009c, 2011), we assume that the flux $\mathbf{J}$ is directed along axisymmetric surfaces parametrized by

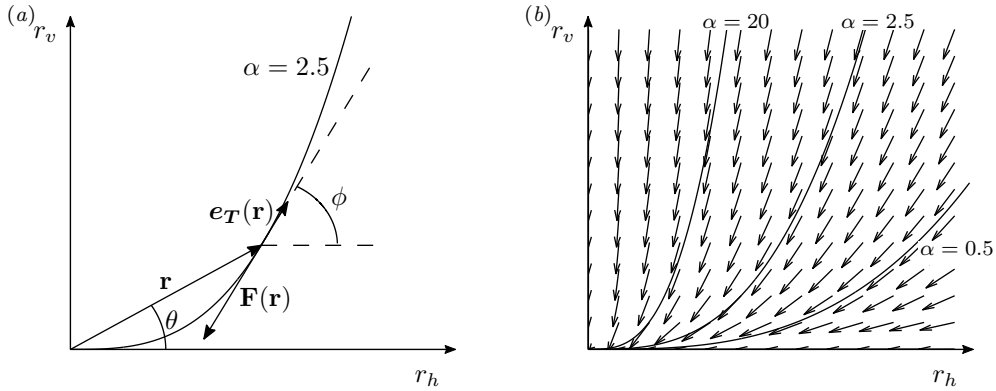

Figure 5.1: Graphical representation of the assumption on the direction of the flux $\mathbf{J}$. (a) illustrates the unit vector $\boldsymbol{e_T}$ tangent to $\mathbf{J}$ for a particular point. In (b), the direction of $\mathbf{J}$ (i.e. $-\boldsymbol{e_T}$) is plotted for $n > 1$.

the power law

$$r_v = f_n(r_h) = \alpha {r_h}^n, \tag{5.26}$$

where α and n are two real parameters. Because power laws are ubiquitous in turbulence this hypothesis seems natural and will be justified later for strongly stratified turbulence. The variation of the coefficient α defines a continuous set of surfaces allowing to describe the direction of $\mathbf{J}$ in the entire correlation space. The exponent n parametrizes the degree of anisotropy. For example the 2D isotropic case is obtained for $n = 0$ with a horizontal flux $\mathbf{J} = J_h \boldsymbol{e_h}$. The 3D isotropic case is obtained for $n = 1$ with a radial flux $\mathbf{J} = (\mathbf{r} \cdot \mathbf{J})\mathbf{r}/|\mathbf{r}|^2$.

In the general case, we assume that the flux $\mathbf{J}$ is directed along along the curves (5.26), i.e. $\mathbf{J}(r_h, r_v) = J_T(r_h, r_v)\boldsymbol{e_T}(r_h, r_v)$, where $\boldsymbol{e_T}(\mathbf{r})$ is the unit vector tangent to the curves (5.26) given by

$$\boldsymbol{e_T}(r_h, r_v) = \frac{\boldsymbol{e_h} + f_n'(r_h)\boldsymbol{e_v}}{\sqrt{1 + f_n'(r_h)^2}} = \frac{\boldsymbol{e_h} + n \tan\psi \boldsymbol{e_v}}{\sqrt{1 + n^2 \tan^2 \psi}}, \tag{5.27}$$

with ψ the angle between $\mathbf{r}$ and the horizontal plane (see figure 5.1a). The angle ϕ between $\mathbf{J}$ and the horizontal direction is therefore given by

$$\tan\phi = \frac{J_v}{J_h} = n \tan\psi. \tag{5.28}$$

Figure 5.1(b) shows an example of the vector field $-\boldsymbol{e_T}$ for $n = 3$. The space (r_h, r_v) is covered by varying the parameter α as illustrated by the curves shown for three different values of α.

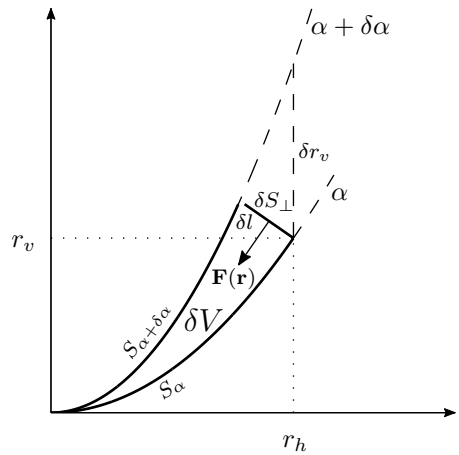

Figure 5.2: Infinitesimal volume δV used for the integration. The infinitesimal surface closing the infinitesimal volume at the radius r_h is given by $\delta S_\perp = 2\pi r_h \delta l$.

5.3.2 Integration of (5.23)

Having specified the direction of the flux $\mathbf{J}$, we can now integrate (5.23), i.e. the relation $\boldsymbol{\nabla} \cdot \mathbf{J} = -4\varepsilon$. We adopt a global method as it is classically done in the isotropic case with an integration over a sphere in 3D and over a disk in 2D (Lindborg, 1999). However, we show in the Appendix that the same result can be obtained through a local method. In the anisotropic axisymmetric case we have to consider an infinitesimal volume δV drawn in figure 5.2 enclosed between two infinitesimally close surfaces S_α and $S_{\alpha+\delta\alpha}$ defined by (5.26). The volume is closed at the radius r_h by an infinitesimal axisymmetric surface $\delta S_\perp = 2\pi\delta l$ perpendicular to the vector $\mathbf{J}$.

Because the flux is assumed to flow along (and not through) the surfaces S_α and $S_{\alpha+\delta\alpha}$, the divergence theorem applied over the infinitesimal volume δV yields

$$\int_{\delta V} \boldsymbol{\nabla} \cdot \mathbf{J} \, d^3\mathbf{r} = \int_{S_\alpha,\, S_{\alpha+\delta\alpha},\, S_\perp} \mathbf{J} \cdot d\boldsymbol{S} = \delta S_\perp J_T(r_h, r_v) \,. \tag{5.29}$$

Integrating the expression (5.23) over the infinitesimal volume δV leads to

$$J_T(r_h, r_v) = -4\varepsilon \frac{\delta V(r_h, r_v, \delta\alpha)}{\delta S_\perp(r_h, r_v, \delta\alpha)}. \tag{5.30}$$

In the limit $\delta\alpha \to 0$, the infinitesimal surface simply expresses as $\delta S_T(r_h, r_v, \delta\alpha) = 2\pi r_h \cos\phi \delta r_v$ and the infinitesimal volume δV can be computed as

$$\delta V(r_h, r_v, \delta\alpha) = \int_0^{r_h} dr'_h 2\pi r'_h \delta r'_v = 2\pi\delta\alpha \int_0^{r_h} dr'_h {r'_h}^{n+1} = 2\pi\delta r_v \frac{{r_h}^2}{n+2}. \tag{5.31}$$

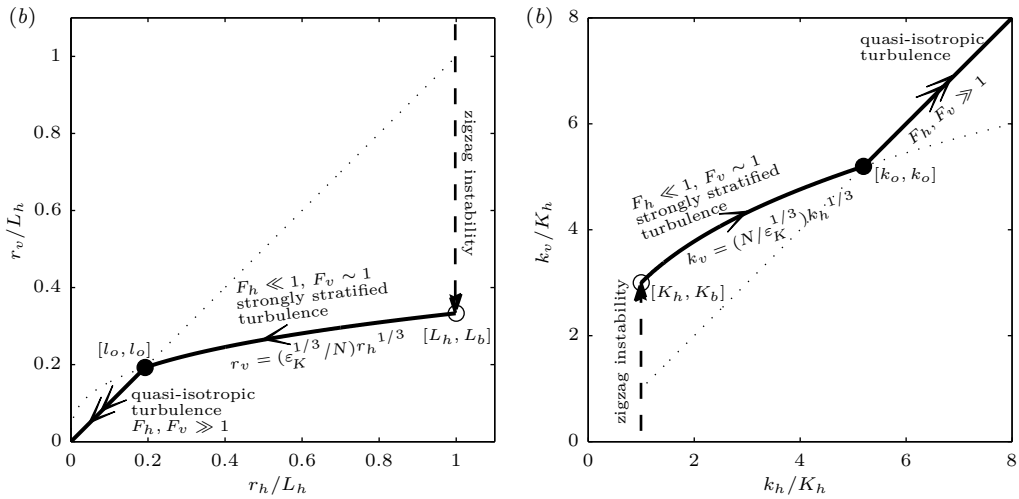

Figure 5.3: Schematic representation of the scaling laws relating vertical and horizontal characteristic length scales l_v and l_h in strongly stratified turbulence in real space (a) and in spectral space (b). Arrows symbolize energy fluxes through different flow regimes. The empty circles correspond to the large anisotropic structures.

The combination of the different expressions gives the following law $J_T = -4/(n+2)\varepsilon r_h/\cos\phi$ which can be rewritten as

$$J_T(r_h, r_v) = -\frac{4}{n+2}\varepsilon r \cos\psi \sqrt{1 + n^2 \tan^2\psi}, \tag{5.32}$$

$$= -\frac{4}{n+2}\varepsilon \sqrt{{r_h}^2 + n^2 {r_v}^2}\,. \tag{5.33}$$

The flux is therefore given by

$$\mathbf{J}(r_h, r_v) = -\frac{4\varepsilon}{n+2}(r_h \boldsymbol{e_h} + n r_v \boldsymbol{e_v}). \tag{5.34}$$

It is the second main result of the paper. We see that the vectorial law (5.33) for anisotropic axisymmetric turbulence has a form close to the isotropic case with, dimensionally, a linear dependence in r; however, anisotropy may be taken into account simply through the parameter n. Expression (5.33) is quite general and allows one to potentially describe different types of axisymmetric turbulence. In particular, the well-known three-dimensional isotropic law $J(r) = -(4/3)\varepsilon r$ is recovered for $n = 1$ and the two-dimensional law $J(r_h) = 2\varepsilon r_h$ is also recovered for $n = 0$ (the sign depends on the type of cascade and it is fixed by hand).

5.3.3 Anisotropy in strongly stratified turbulence

We now discuss the main results known on the anisotropy of strongly stratified turbulent flows in order to justify the assumption (5.26) and to find the appropriate

value of the exponent n. As discussed in the introduction, it is now well established that strongly stratified turbulence is strongly anisotropic and fully three-dimensional. Billant & Chomaz (2001) have shown that the Boussinesq Euler equations have an invariance in the limit of strong stratification (i.e. $F_h \ll 1$) that sets the characteristic vertical length scale L_v to the buoyancy length scale $L_b = U/N$, where U is a characteristic horizontal velocity. This scaling law is supported by simulations of stratified homogeneous turbulence (Waite & Bartello, 2004; Godeferd & Staquet, 2003; Lindborg, 2006; Brethouwer *et al.*, 2007), three-dimensional stability analyses of various flows (Billant & Chomaz, 2000b; Leblanc, 2003; Otheguy *et al.*, 2006b) and experiments (Park *et al.*, 1994; Holford & Linden, 1999) provided that $\mathcal{R} = ReF_h^2 \gg 1$, a condition ensuring negligible viscous effects.

Lindborg (2006) further assumed that this scaling law holds at each horizontal scale l_h in strongly stratified turbulence, i.e.

$$l_v \sim \delta u_h / N, \tag{5.35}$$

where δu_h is the characteristic horizontal velocity associated to l_h. This is equivalent to the so-called critical balance which states a scale-by-scale balance between the wave and the nonlinear time scales (Nazarenko & Schekochihin, 2011) and which is widely used for magnetized fluids (see *e.g.* Goldreich & Sridhar, 1995; Galtier *et al.*, 2005; Bigot *et al.*, 2008) Using this scaling law, Lindborg (2006) presented a theory and numerical evidence for a direct cascade of energy from large to small horizontal scales in strongly stratified turbulence. Through this cascade, the characteristic horizontal velocity δu_h is given by

$$\delta u_h(l_h) \sim {\varepsilon_K}^{1/3} {l_h}^{1/3} \tag{5.36}$$

as in homogeneous isotropic turbulence. As shown by many authors (Lindborg, 2006; Brethouwer *et al.*, 2007; Riley & Lindborg, 2008; Nazarenko & Schekochihin, 2011), the combination of (5.35) and (5.36) yields

$$l_v = l_o (l_h/l_o)^{1/3}. \tag{5.37}$$

where $l_o = (\varepsilon_K/N^3)^{1/2}$ is the Ozmidov length scale. This relation between horizontal and vertical characteristic length scales shows that structures have a pancake shape with $l_v \ll l_h$ when $l_h \gg l_o$. However, the isotropy is recovered when l_h is of the order of the Ozmidov length scale l_o. For scales l_h smaller than l_o, the horizontal Froude number $F_h(l_h) = u_h(l_h)/(Nl_h) = (l_o/l_h)^{2/3}$ is larger than unity so that they are only weakly affected by the stratification. This led Brethouwer *et al.* (2007) to argue that the strongly stratified inertial range exists only up to the Ozmidov length scale and that there is a transition to quasi-isotropic homogeneous turbulence for scales smaller than the Ozmidov length scale and down to the Kolmogorov length scale. These two regimes are sketched in figure 5.3(a) in the space (l_h, l_v). The turbulence is assumed to be forced at the large horizontal scales L_h (representated by an empty circle) as in the numerical simulations of Waite & Bartello (2004); Lindborg (2006); Brethouwer *et al.* (2007). The corresponding vertical scale is L_b but this scale is not forced in these simulations but small vertical scales arise spontaneously through decorrelation

processes such as the zigzag instability (Billant & Chomaz, 2000b), internal wave resonances (Leblanc, 2003), weakly nonlinear wave turbulence (Caillol & Zeitlin, 2000) and Lilly decorrelation process (Lilly, 1983). The equivalent picture in spectral space (k_h, k_v), where $k_h = 2\pi/l_h$ and $k_v = 2\pi/l_v$, is also shown in figure 5.3(b). In spectral space, (5.37) becomes $k_v = k_o(k_h/k_o)^{1/3}$, where $k_o = 2\pi/lo$.

5.3.4 Discussion on the appropriate value of n for strongly stratified turbulence

Although the scaling law (5.37) has the same form as (5.26), their physical meanings are completely different. The relation (5.37) relates the horizontal and vertical characteristic length scales of structures whereas (5.26) specifies the direction of the flux $\mathbf{J}$ in the correlation space (r_h, r_v). Thus, even if this is tempting at first sight, one can not simply set $n = 1/3$. The determination of the parameter n turns out to be more subtle.

The relation (5.37) means that the typical correlation length in the vertical direction l_v is smaller than the one in the horizontal direction l_h. Therefore, if we assume that the iso-lines of correlation are ellipsoidal, they should be given by

$$\left(\frac{r_h}{l_h}\right)^2 + \left(\frac{r_v}{l_v}\right)^2 = 1, \tag{5.38}$$

In other words, the iso-correlation lines are flattened in the vertical direction. By using (5.37), (5.38) can be rewritten as

$$r_h{}^2 + \left(\frac{l_h}{l_o}\right)^{4/3} r_v{}^2 = l_h{}^2. \tag{5.39}$$

The aspect ratio of the elliptic contours of constant correlation $p = l_h/l_v = (l_h/l_o)^{2/3}$ is therefore not constant but varies with l_h. It decreases from values larger than unity for the strongly stratified turbulent cascade ($l_h \gg l_o$) down to unity at the Ozmidov length scale where the isotropy is recovered. We can notice that the iso-lines of the flux modulus $|\mathbf{J}|$ are also ellipsoidal according to (5.33) and such as $r_h{}^2 + n^2 r_v{}^2 = const.$ However, the iso-correlation lines and the iso-flux lines have not necessary the same shape so that it seems not possible to deduce n from these considerations.

In order to obtain n, it is interesting to go back to the divergence equation (5.23). A general way to solve this equation is to write the flux in the form $\mathbf{J} = \boldsymbol{\nabla} G + \boldsymbol{\nabla} \times H$. H remains undetermined whereas the potential G satisfies a Poisson equation

$$\nabla^2 G = -4\varepsilon. \tag{5.40}$$

The solution is uniquely determined if we assume that G is not singular at $r_h = r_v = 0$ and is constant on the outer elliptic contour corresponding to the large integral scales L_h and L_v in the correlation space, i.e. $r_h{}^2 + (L_h/L_v)^2 r_v{}^2 = L_h{}^2$. It is simply given by

$$G = -\frac{2\varepsilon}{2 + P_G{}^2}(r_h{}^2 + P_G{}^2 r_v{}^2). \tag{5.41}$$

where $P_G = L_h/L_v$. This parameter is constant and related to the Froude number F_h: $P_G \simeq 1/(C_{F_h} F_h)$, where C_{F_h} is a constant of order unity depending of the precise definition of the Froude number F_h.

Therefore, we see that the isolines of potential G are elliptical with all the same aspect ratio P_G. Assuming that $H = 0$, it is straightforward to compute the flux

$$\mathbf{J} = -\frac{4\varepsilon}{2 + {P_G}^2}(r_h \boldsymbol{e_h} + {P_G}^2 r_v \boldsymbol{e_v}) \tag{5.42}$$

Remarkably, the flux is completely determined by the anisotropy of the large scales. Furthermore, (5.42) has exactly the same form as (5.34) and implies directly that the flux is directed along lines defined as in the power law (5.26) with $n = {P_G}^2 = const$ (see figure 5.1*b*). Therefore, we find

$$n \simeq 1/(C_{F_h} F_h)^2. \tag{5.43}$$

The above reasoning could be refined by solving (5.40) between a sphere at the Ozmidov scale in order to recover isotropy and an oblate at the integral scale.

5.4 Conclusion

In this paper a new exact relation for homogeneous, incompressible, stably stratified turbulence has been derived. This relation shows the modifications brought by the stratification to the Kolmogorov vectorial relation. When the Brunt-Väisälä frequency is small, isotropy is still expected at first order; in such a limit we have derived the corresponding universal 4/3s law.

For a strong stratification anisotropy cannot be neglected anymore. We have made the ansatz that the development of anisotropy implies that the flux of correlation follows a simple power law. The intensity of anisotropy is then parametrized by a single real coefficient n. The exact relation has been integrated under this hypothesis to obtain a generalized Kolmogorov law potentially valid for any type of axisymmetric turbulence. The Kolmogorov laws for both three-dimensional and two-dimensional isotropic turbulences are also recovered. The scaling law for the vertical scale $L_v \sim U/N$ in strongly stratified turbulence has been used to obtain an explicit prediction for the flux $\mathbf{J}$.

It would be interesting to check these predictions, in particular the assumption on the direction of the flux in the correlation space. In that context, it is interesting to note that Lamriben, Cortet, & Moisy (2011) have recently measured anisotropic energy transfers in an experiment on rotating turbulence.

5.5 Appendix: alternative integration methods

In this Appendix, the relation (5.33) is rederived by two alternative methods. First, a classical local integration is performed. Then, we focus on the previous results obtained by Galtier (2009c,a,b) with an integration of equations of the form (5.2) over

a surface. Remarkably, these results differ from our result (5.33) whereas the same assumptions are made. In order to understand this discrepancy, we investigate the method to integrate (5.2) over a curved surface. Finally, our result (5.33) is once again recovered by this alternative method.

5.5.1 Local integration

In cylindrical coordinates, the divergence operator (using axisymmetry) reads $\boldsymbol{\nabla}\cdot\mathbf{J} = (1/r_h)\partial_{r_h}(r_h J_h)+\partial_{r_v}J_v$. Since $J_v = n\alpha {r_h}^{n-1} J_h$ and $r_v = f_n(r_h) = \alpha {r_h}^n$, the equation (5.23) yields

$$\frac{1}{r_h}\frac{\partial}{\partial r_h}\left(r_h J_h\right) + \frac{1}{{r_h}^{n-1}}\frac{\partial}{\partial r_h}\left({r_h}^{n-1} J_h\right) = -4\varepsilon, \tag{5.44}$$

which can be rewritten

$$\frac{\partial}{\partial r_h}({r_h}^{n/2} J_h) = -2\varepsilon {r_h}^{n/2}. \tag{5.45}$$

Integrating (5.45) leads eventually to

$$J_h = -\frac{4}{n+2}\varepsilon r_h. \tag{5.46}$$

Since $J_T = \sqrt{1+f_n'(r_h)^2}J_h$, (5.46) is identical to (5.33). We can remark that the coefficient α does not appear in (5.46) meaning that J_h is independent of r_v.

Considering the three-dimensional isotropic case, one can note that this method of integration is different to the classical method for which one considers that the vector only depends on ${r_v}^2+{r_h}^2$ and is radial. Herein, we integrate along a particular radius such as $r_v = \alpha r_h$ considering only that the vector is radial, i.e. that $J_v = \alpha J_h$. The isotropic assumption is then implicitly used once again when the result is considered to be independent of the angular coordinates.

5.5.2 Global integration on a surface

We now focus on the method used by Galtier (2009a,b,c) to integrate an equation of the form (5.2) with the two-dimensional divergence theorem (Green's flux theorem):

$$\int_{S_\alpha} \mathrm{div}_S\,\mathbf{J} dS = \oint_{\partial S_\alpha} J_T dl, \tag{5.47}$$

where $\mathrm{div}_S\,\mathbf{J}$ is the surface divergence operator. Remarkably, the obtained result differs from our simple expression (5.33). The fundamental reason is that the correlation space was supposed to be foliated in the previous paper. This assumption is not made in the present paper where $\mathbf{J}$ is a three-dimensional vector field. If $\mathbf{J}$ is tangent to the surface S_α as in our problem there is no curvature term and the surface divergence is simply given by

$$\mathrm{div}_S\,\mathbf{J} = \boldsymbol{\nabla}\cdot\mathbf{J} - \boldsymbol{e_S}\cdot\boldsymbol{\nabla}(\boldsymbol{e_S}\cdot\mathbf{J}), \tag{5.48}$$

where $\boldsymbol{e_S}$ is the unit vector locally perpendicular to the surface. Since the second term of the right-hand side in not null and $\mathrm{div}_S\,\mathbf{J}$ is not constant even if $\boldsymbol{\nabla}\cdot\mathbf{J} = -4\varepsilon$, the two-dimensional divergence theorem must be used carefully.

We can overcome this difficulty by using appropriate generalized orthogonal curvilinear coordinates: $q_1 = s$, the coordinate along the curves defined by the functions $r_v = f_n = \alpha {r_h}^n$, q_2 the azimuthal coordinate θ and $q_3 = \alpha$. In this local frame, J_2 and J_3 are null and the divergence operator expresses as (Batchelor, 1967)

$$\boldsymbol{\nabla}\cdot\mathbf{J} = \frac{1}{h_1 h_2 h_3}\frac{\partial}{\partial s}\left(h_2 h_3 J_T\right), \tag{5.49}$$

where $h_1 = 1$, $h_2 = r_h$ and $h_3 = \cos\phi {r_h}^n$ are the metric coefficients of the set of coordinates. The integration of (5.49) over a surface S_α yields

$$\begin{aligned}\int_{S_\alpha}\boldsymbol{\nabla}\cdot\mathbf{J}dS &= \int\frac{1}{h_1 h_2 h_3}\frac{\partial h_2 h_3 J_T}{\partial s}h_1 ds h_2 d\theta &(5.50)\\ &= 2\pi\int\frac{1}{h_3}\frac{\partial h_2 h_3 J_T}{\partial s}ds. &(5.51)\end{aligned}$$

Since h_3 is not constant, the last term can not be directly integrated. Nevertheless, multiplying equation (5.49) by h_3 before integrating over the surface leads to

$$\begin{aligned}\int_{S_\alpha}h_3\boldsymbol{\nabla}\cdot\mathbf{J}dS &= \int h_3\frac{1}{h_1 h_2 h_3}\frac{\partial h_2 h_3 J_T}{\partial s}h_1 ds h_2 d\theta &(5.52)\\ &= 2\pi\int\frac{\partial h_2 h_3 J_T}{\partial s}ds = 2\pi h_2 h_3 J_T. &(5.53)\end{aligned}$$

It has to be pointed out that this relation is not strictly speaking a two-dimensional divergence theorem. However, applied to our problem (5.2), it allows to recover our result (5.33):

$$\begin{aligned}J_T &= \frac{\int_{S_\alpha}\cos\phi {r_h}^n(-4\varepsilon)dS}{2\pi\cos\phi {r_h}^{(n+1)}} &(5.54)\\ &= -4\varepsilon\frac{\int_{S_\alpha}\cos\phi {r_h}^{(n+1)}ds}{\cos\phi {r_h}^{(n+1)}} = -\frac{4\varepsilon}{n+2}\frac{r_h}{\cos\phi}, &(5.55)\end{aligned}$$

where we have used that $\cos\phi ds = dr_h$. To conclude, we have presented three different methods to obtain our result (5.33) from the integration of equation (5.2) under the assumption of axisymmetry.

Chapter 6

Conclusions and Perspectives

6.1 Conclusions

During this thesis, we have investigated the dynamics of turbulent flows strongly influenced by a stable density stratification by means of experimental, numerical and theoretical methods. Two different and complementary approaches have been adopted. First, we have studied the transition to turbulence of a simple flow in order to better understand the basic physical mechanisms involved in stratified turbulence. Second, we have characterized the statistics and dynamics of disordered and fully turbulent stratified flows.

In chapter 3, we have investigated by means of numerical simulations the dynamics at high Reynolds number of two counter-rotating vortices in a stratified fluid. We have first focused on the onset of the secondary instabilities on the zigzag instability on a Lamb-Chaplygin dipole. We have shown that the secondary instabilities produce a transition to turbulence when $(Re - Re_0){F_h}^2 \geqslant \mathcal{R}_c$, where $Re_0 \simeq 400$ and $\mathcal{R}_c \simeq 4$. We have demonstrated that two types of secondary instabilities develop simultaneously but in different regions of the dipole: a shear instability develops in the most bent region of the vortex cores whereas a gravitational instability develops in the middle between the two vortices.

We have further investigated by a spectral analysis this transition to turbulence of the Lamb-Chaplygin dipole. We have shown that the transition to turbulence has a two steps dynamics. First, a shear instability feeds quasi-isotropic and fast Kelvin-Helmholtz billows with a vertical Froude number of order unity $F_{vKH} \sim 1$ and a typical scale of the order of the buoyancy scale, i.e. larger that the Ozmidov length scale. Second, the destabilization of these billows and the gravitational instability generate a turbulence from the buoyancy scale down to the dissipative scales. The spectra have been shown to be strongly anisotropic. The horizontal kinetic spectra exhibit a $k_h^{-5/3}$ inertial range. There is a deficit of energy between the large scales associated to the dipole and the buoyancy length scale associated to the secondaries instabilities and an excess at the buoyancy length scale. Remarkably, at smaller scales and down to

the dissipative scales, the kinetic and potential energy spectra approximately collapse respectively on the ${C_1{\varepsilon_K}^{2/3}k_h^{-5/3}}$ and ${C_2{\varepsilon_K}^{2/3}k_h^{-5/3}\varepsilon_P/\varepsilon_K}$ laws, with $C_1 \simeq C_2 \simeq 0.5$ as measured in numerical simulations of forced stratified turbulence. The vertical kinetic spectrum follows at large vertical scales a $C_N N^2 k_z^{-3}$ law, with $C_N \simeq 0.1$. For the largest values of the buoyancy Reynolds number $\mathcal{R}$, it exhibits a transition at the Ozmidov length scale l_o toward the ${C_1{\varepsilon_K}^{2/3}k^{-5/3}}$ spectrum. We have shown that the steep portion of the vertical kinetic spectrum is mainly due to the large horizontal scales of the dipole strongly deformed by the zigzag instability. In contrast, the vertical kinetic spectrum computed with spectral modes with horizontal wavenumbers larger than the buoyancy wavenumber k_b does not present any k_z^{-3} power law but exhibits a $k_z^{-5/3}$ power law from a vertical wavenumber slightly larger than k_b down to the dissipative range.

If the shear and the gravitational instabilities are active in the simple case of the zigzag instability of a dipole, it is likely that they also occur in more complicated turbulent flows. Thus, similar statistical results should be observed in stratified turbulence.

In chapters 4 and 5, we have focused on disordered and fully turbulent stratified flows. We have set-up a novel experiment of continuously forced, stratified disordered flows with maximum turbulent buoyancy Reynolds number of order one and small horizontal Froude number $F_h < 1$. This set-up differs from previous experiments of stratified turbulence since the forcing consists in vertically invariant columnar vortex pairs generated intermittently. After an initial spontaneous three-dimensionalisation of the flow, a statistically stationary disordered state is reached.

It exhibits thin horizontal layers associated with relatively strong vertical gradients. When the frequency of dipole generation and circulation of the vortices are increased, both buoyancy Reynolds number $\mathcal{R}$ and horizontal Froude number increase and we observe a transition between two very different flow regimes. For very low $\mathcal{R}$ (and F_h), the horizontal flows corresponding to different layers are quasi two-dimensional and the structures are smooth suggesting that these experiments are in the viscosity affected stratified regime (Godoy-Diana *et al.*, 2004; Brethouwer *et al.*, 2007). In contrast, for the largest $\mathcal{R}$ achieved, we observe small scale structures superimposed on the large scale horizontal layers, indicating that these experiments approach the strongly stratified turbulent regime (Brethouwer *et al.*, 2007). Consistently, the local vertical Froude number $F_{\omega_x} \equiv \omega_x/(2N)$ reaches extrema of order unity. Vertical cross-sections show that overturnings are common features of the flow. We interpret such events as the result of some instabilities similar to those occurring in the case of the stratified dipole. We call this flow "stratified turbulence-like" because the maximum turbulent buoyancy Reynolds number is still quite small $\mathcal{R}_t \simeq 0.4$ compared to the values achieved in the direct numerical simulations of Brethouwer *et al.* (2007) where an inertial range has been observed. Consistently, the compensated horizontal second order structure functions do not exhibit any clear $r_h^{2/3}$ slope but only a flattening. However, because of the limited size of the experimental set-up, it has not be possible to increase the buoyancy Reynolds further keeping a low horizontal Froude number.

Therefore, these experimental results have been supported and extended by numerical simulations. The flow is forced similarly like in the experiments with coherent columnar dipoles. The numerical results obtained for the same parameters as in the experiments agree with the experimental results. For the experimental parameters, numerical and experimental results are in good agreements. In particular, we observe when $\mathcal{R}$ is increased a similar transition between a viscously affected regime and a strongly stratified nearly turbulent regime with overturning at small scales. When the buoyancy Reynolds number is further increased, strongly stratified turbulence is obtained as in Brethouwer *et al.* (2007). Very large simulations have been carried out with large buoyancy Reynolds number and quite low Froude number. Remarkably, the statistical quantities present similarities with those obtained for the stratified dipole. In particular, we have shown that overturnings occur at the buoyancy scale drive a small-scale turbulence starting from this scale. However, the depletion of the spectra between the large integral scale and the buoyancy scale is much less pronounced than for the dipole, indicating that energy is locally transferred *via* a hydrostatic strongly stratified cascade as in Lindborg (2006) and Lindborg & Brethouwer (2007).

Finally, a new exact relation for third order structure function for homogeneous, incompressible, stably stratified turbulence has been derived. This relation shows the modifications brought by the stratification to the Kolmogorov vectorial relation. For a strong stratification, we have made the ansatz that the development of anisotropy implies that the flux of correlation follows a simple scaling law. The intensity of anisotropy is then parametrized by a single coefficient n. The exact relation has been integrated under this hypothesis to obtain a generalized Kolmogorov law potentially able to describe any types of axisymmetric turbulence. The Kolmogorov laws for both three-dimensional and two-dimensional isotropic turbulences are also recovered. A prediction for stratified turbulence is made based on the relation between horizontal and vertical scales predicted by scaling analysis.

6.2 Suggestions for future work

This work opens perspectives in several experimental, numerical, theoretical and observational directions.

6.2.1 Large scale experiments

In the experimental paper, we have concluded on the possibility to set-up a large scale experiment in order to produce strongly stratified turbulence in a laboratory. This is indeed possible in a large experimental facility as for example the large rotating table in Grenoble when it will be rebuild (see e.g. Sommeria, 2008) or in the large-stratified channel of Meteo-France. Let's list some of the optimal conditions that would be important to obtain. We have to use the strongest stratification possible but with the lowest possible variation of the refractive index. This may imply the use of gradients of salt and alcohol in water. Advanced measurement and data assimilation techniques should be used such as high-resolution 3D particle imaging velocimetry (Praud *et al.*, 2005). This implies to use particles with a precise size uniformly distributed in the

fluid, i.e. with the adapted density distribution. A modular forcing, able to force large columnar vortices and/or gravitational waves varying the characteristic vertical length scale would be convenient. Let us recall that Lindborg & Brethouwer (2007) have shown that, if $F_v \sim 1$, the dynamics is the same when turbulence is forced with waves or with columnar vortices. It could be interesting to force with a set of wave generators (Gostiaux *et al.*, 2007) focusing the energy in a central region and varying the vertical Froude number. Alternatively, we also could imagine to force with an oscillating pseudo-random topography (or a rescaled Atlantic ridge) forcing a set of non-linear upward waves. A non-linear density profile could be used to focus the wave beams in a strongly stratified region. In such an experiment, the anisotropic non-linear energy transfers could be computed following Lamriben *et al.* (2011).

6.2.2 Numerical and theoretical work

We have seen in section 4.2 that the Ozmidov and Kolmogorov length scales are of the same order of magnitude even in the largest simulations achieved for which the turbulent Reynolds number is of the order of 20. In order to have a finite inertial range between these two length scales, forced strongly stratified turbulence at even larger turbulent buoyancy Reynolds number would be necessary. Such values of $\mathcal{R}_t$ requires very high resolution simulations which would necessitate to highly parallelize the code NS3D. Indeed, the more recent super-computers have now hundreds of thousands of cores. To run a simulation in such computers, it is necessary to obtain good speed-up up to thousands of cores. A first solution could be to share data over the two horizontal directions. It is likely that the code NS3D modified in this way would have good numerical performances for very large simulations with resolutions of order $N_h^2 \times N_z = 4096^2 \times 1024$. It would be also possible to share the modes in the three directions as explained for example by Vallgren (2010). In order to visualize the field from such very high resolution simulations, the visualization tools based on homemade Matlab fonctions have to be replaced by a powerful visualization software such as for example VAPOR (Clyne & Rast, 2005). This will require to adapt the outputs of ns3d.

Since the code has been adapted to save the anisotropic non-linear energy transfers in spatial space, it should be interesting to test the theoretical predictions of chapter 5 on the Kolmogorov laws for stratified turbulence.

In section 4.2, we have presented a new method of forcing for which some coherent structures are forced in spatial space. This method has been used to achieve a very simple forcing with Lamb-Oseen dipoles of constant ratio separation distance between the 2 vortices b on radius of a vortex a equal to $b/a = 2$. In fact, this method is very general and could be used to force any 2D flows with any temporal dependence (and it should be also straightforward to adapt the method to force in spatial space 3D flows). For instance, the effect of the ratio b/a could be easily studied. This issue is interesting because it is difficult to produce in the laboratory vortices with very large core. In contrast, it is possible to produce large dipoles by increasing the separation distance between the 2 vortices. More generally, many new experimental designs of stratified turbulence could be tested with this method.

This method of forcing could be also used for the post-processing of experimental data from PIV. For strongly turbulent flows, it could be difficult with such measurement techniques to resolve the finest flow scales. It could be possible to force a flow to stay close to large scale PIV velocity fields as it is done in the meteorological context. One could gain many informations from these simulations stick to experimental data in terms of spatial and temporal resolutions, of measured quantities and for the statistical analysis of the flows.

In this thesis, we have related the results for a simple particular flow and those for turbulent flows obtained with different methods and on different aspects: scaling laws, detailed mechanisms, instabilities and statistical analyses. This opens many perspectives on the application of this general method and the tools developed during this thesis for other flows. Two examples are briefly presented :

- The dynamics of a co-rotating vortex pair in stratified fluids has been studied at LadHyX in particular during the PhD thesis of Otheguy (2005). However, we do not know if the scenario for the non-linear evolution for large Re is similar to the one for two counter-rotating vortices. We have already performed some preliminary simulations and it seems that surprisingly it is not the case. The shear and gravitational instabilities do not occur during the vortex merging. However, we have observed the development of some small scales, resembling waves. It would be interesting to test if these structures are indeed waves by using for example the wave detection method used by Lindborg & Brethouwer (2007). This method has been already implemented in the code and we have reproduced some of the results of Lindborg & Brethouwer (2007). Moreover, the Pointing vector (energy fluxes in real space) could also be directly measured.

- It would be very interesting to apply our methods to study the transition to turbulence from the parallel vertical shear layer. This simple flow has been already widely studied but the statistical characterization of the produced turbulence could give interesting results. This flow is interesting because it is an important elementary mechanism for stratified turbulence and because it is a convenient model flow to quantify the influence of the stratification on the small-scale turbulence.

We have developed during this thesis a small code performing a statistical decomposition of the non-linear terms into triads for stratified flows. This method could be powerful to investigate some issues such as the non-local transfers and the effect of the shear modes. However, this code have to be fully tested and need to be parallelized in order to analyse the results of large simulations.

Finally, it should be interesting to carry out simulations of the hydrostatic primitive equations for strongly stratified turbulence. Comparing such simulations with similar simulations of the Navier-Stokes equations should allow one to better understand the effects of overturnings and small-scale non-hydrostatic turbulence in stratified turbulence.

6.2.3 Application to the study of geophysical fluids

The natural applications of the present results concern geophysical issues. Collaborations with applied oceanographers, meteorologists and climatologists would therefore be very fruitful. It would be interesting to seek in observational data evidences for the mechanisms characterised in this thesis. Another application could be to develop mixing schemes based on the results and knowledge gained from this thesis.

Eventually, statistical data analysis could bring new knowledge on turbulent processes in geophysical contexts. It is easier to perform such studies with numerical data of simulations of the atmosphere and of the ocean at very high resolution General Circulation Model (GCM) and regional models. The tools of the statistical analysis could be used to seek the presence of internal waves and to compute the nonlinear transfers and the buoyancy flux. This research project, applied on the issue of the atmospheric dynamics, will be soon made a reality during a post-doctoral position at KTH in Stockholm.

Appendix A

Statistical and numerical methods

This appendix presents our statistical and numerical methods. In a first section, we define some statistical quantities and explain how they are computed. Then, a second section presents the numerical code used to simulate the dynamics of stratified incompressible fluids.

A.1 Statistical description of stratified flows

A.1.1 Analyzing and projecting a turbulent flow state

As already said, describing entirely the state of a turbulent flow for a high Reynolds number requires a huge quantity of data. In order to save some data with a correct temporal resolution, it is interesting to project the flow state and to consider statistical quantities that give interesting informations on the flow. This can be done in a clever way in order to highlight the main kinematic and dynamical features.

A first step in this direction is to drop the phase between the different Fourier modes, i.e. to consider the kinetic energy per Fourier modes $\hat{E}_K(\mathbf{k}) = |\hat{\mathbf{u}}|^2/2$ and the potential energy per Fourier modes $\hat{E}_P(\mathbf{k}) = N^2|\hat{\zeta}|^2/2$. However, these quantities are still function of a three-dimensional vector and so their saving is still very costly.

In order to compress the data, a classical method consists in using some symmetries of the system. For example, it is usual to consider for homogeneous isotropic turbulence the quantities averaged over a sphere which depends only of a radial coordinate. In the case of stratified flows, we can use the intrinsic symmetry of the equations, which are axisymmetric (invariant by a rotation over the vertical axis) and to consider azimuthally averaged quantities.

A.1.2 Energy distribution (order 2 quantities)

Global means and decomposition

In chapter 1, we have already defined the mean potential and kinetic energies E_K and E_P. These quantities express as the sum of the energy per of all Fourier modes

$$E_\alpha = \sum_{\mathbf{k}} \hat{E}_\alpha(\mathbf{k}) \tag{A.1}$$

where the subscript α denotes either the subscript P or K. Similarly, the enstrophy Z (simply related to the kinetic energy dissipation $\varepsilon_K = 2\nu Z$) expresses as the sum of the enstrophy of each Fourier mode $\hat{Z} = |\mathbf{k}|^2 \hat{E}_K$. In order to characterize the flow structure, these mean quantities can be decomposed considering only some particular components of the vectors and some particular Fourier modes. For example, we can consider the part of the enstrophy linked to the vertical gradient of horizontal velocity $Z_{\{\mathbf{u}_h, k_z\}} = \sum {k_z}^2 |\hat{\mathbf{u}}_h|$ or the energy contained in the shear modes $E_{SM} = \sum_{\{\mathbf{k} \text{ such as } \kappa_h = 0\}} \hat{E}(\mathbf{k})$, where $\kappa_h = |\mathbf{k}_h|$.

Directional length scales

The energy distribution between the Fourier modes can also be characterized by various length scales. In isotropic turbulence, it is usual to define integral scale and Taylor micro-scale. For an anisotropic flow, one must generalize the classical isotropic quantities and consider directional length scales (Godeferd & Staquet, 2003). A general expression of such length scales is

$$L_{\beta m \alpha} \propto \left(\frac{\sum_{\mathbf{k}} \hat{E}_\alpha}{\sum_{\mathbf{k}} {k_\beta}^m \hat{E}_\alpha} \right)^{1/m} \tag{A.2}$$

where k_β denotes a particular component of the wavenumber (Brethouwer *et al.*, 2007). In this thesis, we consider only length scales characterizing the structure of kinetic energy and no potential energy, so $\alpha = K$. Different scaling factors can be introduced in (A.2) to obtain the classical isotropic quantities. However, in this thesis, we have used these quantities to verify some scaling laws so that these factors are unimportant.

The choice $m = -1$ gives integral length scales, i.e. scales characterizing the large structures. The choice $m = 2$ defines the classical Taylor microscale used for example by Riley & de Bruyn Kops (2003). Brethouwer *et al.* (2007) argued that too much weight is put on the small scales with the value $m = 2$ and choose $m = 1$. The anisotropic characteristic length scales corresponding to these three values of m and to $k_\beta = \kappa = |\mathbf{k}|$, $k_\beta = \kappa_h$ and $k_\beta = k_z$ are regularly saved during the numerical simulations.

Unidimensional spectra

The simplest way to represent the energy distribution between scales is to plot unidimensional spectra. These spectra can be obtained in particular with a classical

experimental setup in which a probe (often a hot-wire) is fixed in a turbulent flow with a high mean velocity (typically in a grid turbulence). The probe measures a temporal signal of one velocity component (either parallel or perpendicular to the mean flow). If the mean flow is large enough, the situation is equivalent to a probe moving through a quasi-steady flow (as in the case of a probe fixed on a fast enough plane flying through the atmosphere). In this way, the experimentalists can obtain a velocity signal as a function of a space component r_1 (it is the Taylor estimation). The longitudinal and transverse unidimensional spectra are obtained from the signal respectively parallel $u_1(r_1)$ and perpendicular $u_2(r_1)$ to the mean flow *via* a Fourier transform.

More precisely, the energy 1D spectra are defined by the relation

$$E_\alpha = \sum_{k_h \geqslant 0} E_\alpha(k_h)\delta k_h, \tag{A.3}$$

where $\delta k_h = 2\pi/\mathcal{L}_h$. Besides, the mean energy expresses as a function of the energy per Fourier modes $\hat{E}_\alpha(\mathbf{k})$ as the sum

$$E_\alpha = \sum_{k_h \geqslant 0} \sum_{\{|k_x|=k_h, k_y, k_z\}} \hat{E}_\alpha, \tag{A.4}$$

and we get by identification and using axisymmetry (horizontal directions are considered equivalent)

$$E_\alpha(k_h) = \frac{1}{2\delta k_h} \left[\sum_{\{|k_x|=k_h, k_y, k_z\}} \hat{E}_\alpha + \sum_{\{|k_y|=k_h, k_x, k_z\}} \hat{E}_\alpha \right]. \tag{A.5}$$

Due to the vectorial nature of the velocity, many different unidimensional spectra can be considered. All longitudinal and transverse 1D spectra are regularly saved during the numerical simulations. Moreover we also save the co-spectrum of vertical velocity and ζ which is linked to the buoyancy flux (the dynamical point of view is dealt with in a following section).

Tridimensional spectra

Another classical spectral quantity is the tridimensional spectra function of the wavevector modulus $\kappa = |\mathbf{k}|$. In particular, it is widely used is numerical studies of isotropic turbulence. Since its definition is

$$E_\alpha = \sum_{\kappa} E_\alpha(\kappa)\delta\kappa, \tag{A.6}$$

where $\delta\kappa$ is the thickness of the shells in Fourier space, it is given as a function of the energy per Fourier mode $\hat{E}(\mathbf{k})$ by

$$E_\alpha(\kappa) = \frac{1}{\delta\kappa} \sum_{\{\kappa<|\mathbf{k}|<\kappa+\delta\kappa\}} \hat{E}_\alpha(\mathbf{k}). \tag{A.7}$$

Azimuthally average spectra and two-dimensional spectra

Since the unidimensional spectra are functions of a single variable, they lack many informations. Using the axisymmetry of the equations, we can average the energy per mode over the azimuthal direction. We define the azimuthally average spectra by the relation

$$E_\alpha = \sum_{\kappa_h, k_z} E_\alpha(\kappa_h, k_z)\delta\kappa_h\delta k_z. \tag{A.8}$$

These spectra offer two advantages: first, it is straightforward to compute horizontal 2D spectra $E_\alpha(\kappa_h)$ from them *via* a sum over the vertical wavenumber. Second, they are fully adapted for the analysis with the poloidal-toroidal decomposition. Thus, the set of toroidal, poloidal and potential azimuthally summed spectra is an informative and not too expensive (for numerical memory) representation of a flow. Since these spectra are only functions of two variables, it is possible to save them with a high temporal resolution.

Values of the corresponding Kolmogorov constants for isotropic turbulence

In three-dimensional isotropic turbulence, the Kolmogorov's prediction of a power law dependence with a form $E(k) = C\varepsilon^{2/3}k^{-5/3}$ holds for all defined spectra. However, the associated Kolmogorov constants have different values which can be related assuming isotropy.

Once precisely defined the different spectra, we can give numerical values of the different Kolmogorov constants. The more classical Kolmogorov constants are those associated to the unidimensional spectrum of the longitudinal velocity component C_{11}, to the spectrum of a transverse velocity component C_{12} and to the three-dimensional energy spectrum C_{3D}. It can be shown under the assumption of isotropy that $C_{12} = (4/3)C_{11}$ and that $C_{3D} = (55/18)C_{11}$. The measured values are approximately $C_{11} \simeq 0.53$ and $C_{3D} \simeq 1.6$ (Sreenivasan, 1995; Monin & Yaglom, 1975; Gotoh *et al.*, 2002).

In this thesis, we consider unidimensional spectrum of kinetic energy whose associated Kolmogorov constant is $C_{1D} = (C_{11}+2C_{12})/2 \simeq 0.97$ (the factor 2 comes from the difference between a kinetic energy spectrum and the spectra of velocity components). We also plot two-dimensional spectra of kinetic energy with an associated Kolmogorov constant $C_{2D} = 1.40C_{1D} = 1.36$ (Lindborg, 1999; Lindborg & Brethouwer, 2007).

Unidimensional correlations and structure functions

As already said, similar statistical analysis can be done equivalently in real space with correlation functions $C_{ii}(r_j) = \langle u_i(\mathbf{x})u_i(\mathbf{x} + r_j\boldsymbol{e_j})\rangle$, where the brackets denote average over $\mathbf{x}$, or the structure functions of order two $S_{ii}(r_j) = \langle|\delta u_i(r_j\boldsymbol{e_j})|^2\rangle = 2(\langle {u_i}^2\rangle - C_{ii}(r_j))$, where $\delta u_i(r_j\boldsymbol{e_j}) = u_i(\mathbf{x}+r_j\boldsymbol{e_j}) - u_i(\mathbf{x})$ are the velocity increments (for these definitions the repeated subscripts are not summed). Experimentally, the structure functions are computed from Particles Image Velocimetry (PIV) data with "PIVMat", a PIV post-processing and data analysis toolbox for Matlab developed by

F. Moisy[1]. Numerically, we obtain the correlation functions from the unidimensional spectra. For example the longitudinal correlation function $C_{xx}(y)$ is computed as $C_{xx}(y) = \langle u_x(\mathbf{x}) u_x(\mathbf{x} + y\boldsymbol{e_y})\rangle = TF_{1D}^{-1}[2E_{u_x}(k_y)]$.

Azimuthally averaged correlation functions

Is real space, the equivalent of the azimuthally summed spectra are the azimuthally averaged correlation functions computed as $C_K(r_h, z) = \langle C_K(\mathbf{r})\rangle_\theta$, where $C_K(\mathbf{r}) = TF^{-1}[|\hat{\mathbf{u}}|^2]$ and the brackets $\langle\cdot\rangle_\theta$ denote the average over the azimuthal direction.

Frequency spectra

Finally, it is also useful to consider frequency spectra (Lindborg & Brethouwer, 2007) defined by the relation

$$\hat{E}(\mathbf{k}) = \int d\omega \hat{F}(\omega, \mathbf{k}), \tag{A.9}$$

where ω is the frequency. Gravity waves appear through two equal peaks in the poloidal and potential frequency spectra at a frequency close to the frequency predicted by the linear dispersion law.

A.1.3 Phase-dependent quantities and stability

For many purposes, the phase-coherence is very important because it determines the precise shape of flow structures. During the numerical simulations, temporal signals of maximums of the velocity components and of probes localized in real space are saved. The phase-coherence is also important for local quantities involved in stability conditions. Probability density functions of the local Richardson number $Ri(\mathbf{x})$, of local vertical Froude number $F_{\omega_h} = |\boldsymbol{\omega}_h|/(2N)$ and of $\partial_z \rho_{tot}$ are also saved.

A.1.4 Dynamical analysis: non-linear transfers, dissipation and buoyancy flux

The dynamics of turbulence can be studied with the governing equations for the second order quantities, energy per mode in spectral space and correlation functions in real space. For isotropic turbulence, these equations correspond respectively to the Lin and Kármán-Howarth equations.

[1] See http://www.fast.u-psud.fr/pivmat/

Global fluxes in spectral space

The evolution equations of the kinetic and potential energies $\hat{E}_K(\mathbf{k})$ and $\hat{E}_P(\mathbf{k})$ of a wavenumber $\mathbf{k}$ can be expressed as

$$\frac{d\hat{E}_K(\mathbf{k})}{dt} = \hat{T}_K - \hat{b} - \hat{D}_K, \tag{A.10}$$

$$\frac{d\hat{E}_P(\mathbf{k})}{dt} = \hat{T}_P + \hat{b} - \hat{D}_P, \tag{A.11}$$

where $\hat{T}_K = -\Re[\hat{\mathbf{u}}^*(\mathbf{k})\cdot\widehat{(\mathbf{u}\cdot\boldsymbol{\nabla}\mathbf{u})}(\mathbf{k})]$ and $\hat{T}_P = -N^2\Re[\hat{\zeta}^*(\mathbf{k})\widehat{(\mathbf{u}\cdot\boldsymbol{\nabla}\zeta)}(\mathbf{k})]$ are the kinetic and potential nonlinear transfers, $\hat{D}_K(\mathbf{k}) = \nu|\mathbf{k}|^2|\hat{\mathbf{u}}|^2$ and $\hat{D}_P(\mathbf{k}) = \kappa N^2|\mathbf{k}|^2|\hat{\zeta}|^2$ are the kinetic and potential mean energy dissipation and $\hat{b}(\mathbf{k}) = N^2\Re[\hat{\zeta}^*(\mathbf{k})\hat{w}(\mathbf{k})]$ is the buoyancy flux from kinetic to potential energy. $\Re$ denotes the real part and the star the complex conjugate. When (A.10) and (A.11) are summed over the wavenumbers inside a vertical cylinder Ω_{κ_h} of radius κ_h in spectral space, we obtain,

$$\frac{dE_K(\kappa_h)}{dt} = -\Pi_K(\kappa_h) - B(\kappa_h) - \varepsilon_K(\kappa_h), \tag{A.12}$$

$$\frac{dE_P(\kappa_h)}{dt} = -\Pi_P(\kappa_h) + B(\kappa_h) - \varepsilon_P(\kappa_h). \tag{A.13}$$

$E_K(\kappa_h) = \sum_{|\mathbf{k}_h|\leqslant\kappa_h,k_z}$, $\Pi_K(\kappa_h)$ the kinetic flux going outside of Ω_{κ_h}, $B(\kappa_h)$ the flux of energy going from kinetic to potential energies inside Ω_{κ_h} and $\varepsilon_K(\kappa_h)$ the kinetic dissipation inside Ω_{κ_h}. The quantities with the subscript P are the same but for the potential energy.

The azimuthally summed non-linear transfers and buoyancy flux are regularly saved during the numerical simulations. With this data, it is easy to numerically compute all the quantities defined here.

Global fluxes in real space

We now turn to the equivalent of equations (A.10) and (A.11) in the correlation space. The stratified Kármán-Howarth equations write

$$\frac{1}{2}\frac{\partial C_K}{\partial t} = T_K - b - D_K, \tag{A.14}$$

$$\frac{1}{2}\frac{\partial C_P}{\partial t} = T_P + b - D_P, \tag{A.15}$$

where $C_K = \langle\mathbf{u}\cdot\mathbf{u}'\rangle$ and $C_P = N^2\langle\zeta\zeta'\rangle$. These equations govern the two-point correlation functions because $TF^{-1}[|\hat{\mathbf{u}}|^2] = \langle\mathbf{u}\cdot\mathbf{u}'\rangle$

In the article of chapter 5, we give expressions of the different implied functions. In particular, we prove the stratified counterpart of a very classical result linked to the 4/5s law. In real space, the nonlinear fluxes express as the divergence of a vectorial flux of correlation: $T(\mathbf{r}) = \boldsymbol{\nabla}\cdot\mathbf{M}$, where

$$\mathbf{M} = \langle[u_i u_i' + N^2\zeta\zeta']\mathbf{u}\rangle. \tag{A.16}$$

Because we only care about the divergent part of $\mathbf{M}$, we define a potential of correlation flux Φ such as $\mathbf{M} = -\boldsymbol{\nabla}\Phi$. Numerically, it is easy to compute $\hat{T}$ and finally the potential of correlation flux by the formula $\Phi = -TF^{-1}[\hat{T}/|\mathbf{k}|^2]$. During numerical simulations, poloidal, toroidal and potential azimuthally averaged potential of correlation flux Φ_α are regularly saved.

Triadic decomposition of the non-linear transfers

One can go further into the analysis of the non-linear transfers by their decomposition into triads (Alexakis *et al.*, 2005; Mininni *et al.*, 2006; Koudella & Staquet, 2006). Indeed, the kinetic transfer expresses as

$$\hat{T}_K(\mathbf{k}) = -\Re\{\hat{u}_i^*(\mathbf{k})\widehat{u_j\partial_j u_i}(\mathbf{k})\}. \tag{A.17}$$

Since the Fourier transform of a product is equal to the convolution of the Fourier transforms, it gives

$$\widehat{u_j\partial_j u_i}(\mathbf{k}) = \sum_{\mathbf{p}} \hat{u}_j(\mathbf{k}-\mathbf{p}) i p_j \hat{u}_i(\mathbf{p}), \tag{A.18}$$

and we obtain

$$\hat{T}_K(\mathbf{k}) = \Im\{\hat{u}_i^*(\mathbf{k}) \sum_{\mathbf{p}} \hat{u}_j(\mathbf{k}-\mathbf{p}) p_j \hat{u}_i(\mathbf{p})\}. \tag{A.19}$$

We define $\hat{T}(\mathbf{k},\mathbf{p})$ the energy transfer between two wavevector $\mathbf{k}$ and $\mathbf{p}$ (through the interaction with wavevector $\mathbf{q} = \mathbf{k} - \mathbf{p}$)

$$\hat{T}(\mathbf{k},\mathbf{p}) = \Im\{\hat{u}_i^*(\mathbf{k})\hat{u}_j(\mathbf{k}-\mathbf{p}) p_j \hat{u}_i(\mathbf{p})\}, \tag{A.20}$$

such as $\hat{T}(\mathbf{k}) = \sum_{\mathbf{p}} \hat{T}(\mathbf{k},\mathbf{p})$. It is straightforward to show that $\hat{T}(\mathbf{k},\mathbf{p}) = \hat{T}(\mathbf{p},\mathbf{k})$ which express the energy conservation. Finally, we sum over the azimuthal direction to obtain the triadic interaction function $T(\kappa_h, k_z, p_h, p_z)$. In practice, we compute and save this quantity for only some couples $[\kappa_h, k_z]$. Let's note that the different triads can be further characterized by their locality, the resonance condition and the kind of transfer (for example from poloidal to toroidal *via* toroidal, see e.g. Waite & Bartello, 2006a).

A.2 Evolutions of the numerical code NS3D

In this section, we present the numerical code used to simulate stratified flows. We focus in particular on the improvements of the code performed during this thesis which have lead to a new version oriented toward Direct Numerical Simulation (DNS) of turbulent flows.

A.2.1 NS3D: a parallel Navier-Stokes solver

During this thesis, we have used a efficient parallel NS solver called NS3D. The Navier-Stokes equations under the Boussinesq approximation (1.8-1.9) are solved in a three

dimensional space. The code is based on a pseudo-spectral scheme in Cartesian coordinates with periodic boundary conditions. The time integration of the nonlinear terms is carried out using a fourth-order Runge-Kutta scheme and the viscous terms are exactly integrated. NS3D was first written for a homogeneous fluid by Vincent & Meneguzzi (1991) and later adapted to stratified fluids by Billant & Chomaz (2000c) and Otheguy *et al.* (2006a).

Recently, its parallelization has been implemented by Deloncle (2007). This improvement is significant and for technical aspects, the reader can refer to Axel Deloncle's manuscript thesis. The principle is to use many processors to share the calculations. Both shared memory parallelism (achieved with the OpenMP multi-threading paradigm) and distributed memory parallelism (achieved through the use of Message Passing Interface, MPI) have been implemented. We have prefered the second solution which is much more efficient when several processors are used. The data structure is split up and resided as "slices" in the local memory of each task (generally one processor corresponds to one task). All the tasks work concurrently and exchange data through communications by sending and receiving "messages".

Most of the calculation time is spent for the forward and backward Fourier transforms (it is the sole nonlocal operation). Thus, the performance of the code relies on the efficiency of the FFT library. During this thesis we have used mainly the library FFTW 3.2. Since a task needs all the numerical points in a direction to perform a FFT transform in this direction, implementing the FFT algorithm in three dimensions in parallel with distributed memory is not obvious. Some operations of transposition and of communications have to be done. The data is stored in large tables and distributed over the different processors along one particular direction and in a particular way. Let's note that the data is not stored in the same way in real and spectral space as represented by the symbolic expression

$$(x, y, z^*) \rightleftarrows (k_z, k_x, k_y^*), \tag{A.21}$$

where the starts indicate the splitting directions. Finally, MPI parallelism allows to run large simulations with a large number of processors and with a good speedup.

NS3D is a powerful code fully adapted for instability studies. For example, it is able to simulate the linear or non-linear evolution of a perturbation around a base state. However, the code as it was at the beginning of the thesis was not fully adapted for DNS of turbulent flows. The time control was oriented toward numerical aspects with the choices of the numerical time-step dt and of the number of time-steps let to the user. There was nearly no output of statistical quantities and only a classical Navier-Stokes dissipation. No forcing method was implemented.

A.2.2 Time stepping and human interface

The human interface has been improved and oriented toward hydrodynamics aspects in order to make easier the launching and the control of runs. The user can choose either the time-step dt and the number of numerical time-step or the final hydrodynamical time. In this case, the code uses an adaptable time step procedure maximizing the

time step over a Courant-Friedrichs-Lewy condition (Lundbladh *et al.*, 1999)

$$dt\left(\frac{|u_x|}{dx}+\frac{|u_y|}{dy}+\frac{|u_z|}{dz}\right)<1.2, \tag{A.22}$$

taking into account the group velocity of internal waves. Beside, the control of the output times is now based on the real time and not on the number of numerical time-steps. The interface also facilitates the stop and the restart of a run with increase of the resolution.

A.2.3 Outputs

Many quantities defined in the previous section are regularly saved during the simulation. The user sets the periods for the different outputs with these lines in the launching script:

```
*** Output ***
*** time-step and numerics **   (# time-steps)
output1_period_______________   1
*** restart global fields ***   (hydrodynamic time)
output2_period_______________   2.
*** fast outputs ************   (hydrodynamic time)
output_turb_period___________   0.01
output_probes_period_________   0.01
output_maxv_period___________   0.01
*** other outputs ***********   (hydrodynamic time)
output_spectres1D_period_____   0.5
output_axisym_period_________   0.5
output_correlations_period___   0.5
output_pdf_period____________   0.5
output_transfert_period______   0.5
output_forcing2D_period______   0.5
```

A.2.4 Isotropic hyperviscosity

In order to increase the stability of runs at high Re and to simulate flows less influenced at large scales by diffusive effects, we have implemented a hyperdissipation. The classical viscous force per mass unit in Fourier space is replaced by

$$\hat{f}_d=(\nu|\mathbf{k}|^2+\nu_4|\mathbf{k}|^8)\hat{\mathbf{u}}, \tag{A.23}$$

where ν_4 is the hyperviscosity coefficient. The same diffusive operator is used for ζ. We use this sum of a classical dissipation plus a hyperdissipation in order to perform "quasi-DNS". For a particular flow, we first perform a set of real DNS in order to evaluate the required viscosity ν_{OK} as a function of the resolution $\delta=2\pi/k_{max}$, where $k_{\max}$ is the maximum wavenumber (with the de-aliasing taken into account).

The results are fitted with a function of a sole parameter ϵ having the dimensions of an energy dissipation rate

$$\nu_{OK}(\delta) = \epsilon^{1/3}\delta^{4/3}. \tag{A.24}$$

Then, the value of the parameter ϵ is written in the launching script and the adapted viscosity can be evaluated during the run for all resolutions. If we use an inferior viscosity, we have to add hyperdissipation. The hyperviscosity coefficient is determined at the beginning of each run by the equality

$$\nu(\alpha_{\nu_4} k_{\max})^2 + \nu_4(\alpha_{\nu_4} k_{\max})^8 = \nu_{OK}(\delta)(\alpha_{\nu_4} k_{\max})^2, \tag{A.25}$$

where α_{ν_4} a parameter approximatively equal to 0.85 that the user can modify in the launching script. The lack of resolution can be quantified by the temporal maxima of the ratio $\varepsilon_{\nu_4}(t)/\varepsilon(t)$, where $\varepsilon_{\nu_4}(t)$ is the hyperdissipation rate. This ratio would tend to 0 if the resolution were increased enough to perfectly resolve the Kolmogorov length scale.

A classical anisotropic hyperdissipation such as hyperdissipation used for example by Lindborg (2005) has also been implemented (see subsection 4.2.6).

It has to be noted that the use of hyperviscosity presents some disadvantages: the velocity maximum can increase by dissipative effects and an anomalous bottleneck can develop (Frisch *et al.*, 2008).

A.2.5 Modified projectors

The pseudo-spectral codes are based on a projection operator. For incompressible flows, only the dynamics of the solenoidal velocity field (perpendicular to the wavevector) is computed. At each time-step, all terms of the equations are projected on the solenoidal variety.

Thus, it is numerically very simple to modify the projector in order to simulate modified NS equations. In this thesis, we have implemented two new projectors. A first projector only slightly modify the dynamics by inhibiting the shear modes. A second unusual projector cancels the poloidal part of the flow. When this projector is used, only the toroidal dynamics is simulated.

A.2.6 Forcing with coherent structures

Two forcing methods have been implemented. The forcing method used in chapter 4.2 is quite unusual. Columnar coherent hydrodynamical structures are periodically forced. The 2D forcing fields are created before the simulation by a matlab function and saved in a file which is read by the program NS3D during the simulation. Many different forcings can be implemented with this numerical method (see chapter 4.2).

Another very simple method has been used only as a reference in order to force an isotropic turbulence and test some output procedures. The largest modes of the flow are frozen and only the dynamics of the other modes is computed. In 3D, a statistically stationary direct cascade is then obtained with a mean injection rate depending on the initial velocity field.

Annexe B

Tourbillons et dipôles colonnaires en milieu stratifié

Dans cette thèse, on étudie la dynamique d'écoulements dans lesquels interagissent des tourbillons colonnaires. Cette annexe rappelle quelques résultats simples sur ces tourbillons. La dernière section regroupe quelques résultats utiles sur l'instabilité zigzag de deux tourbillons contra-rotatifs.

Tourbillons bidimensionnels et nombres sans dimension

On considère le cas simple d'un tourbillon bidimensionnel et axisymétrique dans un fluide incompressible. Un tel tourbillon est complètement caractérisé par une distribution de vorticité $\omega_z(r)$ ou par la distribution de vitesse associée $\mathbf{u}(r)$, où r est la distance au centre du tourbillon. On associe à un tourbillon isolé une circulation $\Gamma \equiv \oint d\mathbf{l} \cdot \mathbf{u}(r) = \int dS\omega_z(r)$, quantité conservée aux effets visqueux près. On définit le rayon caractéristique du tourbillon

$$a \equiv \frac{2}{\sqrt{\pi}} \frac{\int dSr\omega_z}{\int dS\omega_z}. \tag{B.1}$$

Le coefficient $2/\sqrt{\pi}$ simplifie les expressions dans le cas du tourbillon gaussien. La définition de ce rayon caractéristique est arbitraire et correspond pour le tourbillon gaussien à environ 1.25 fois la largeur à mi-hauteur.

On se limite dans cette présentation à des tourbillons axisymétriques (invariant par rotation autour de leur centre) et tel que $\omega_z(0) = \omega_{max}$ et $\partial_r\omega_z(0) = 0$, où $r = 0$ correspond au centre du tourbillon et $\omega_{max} = \max(\omega_z)$. A proximité du centre, là où $\omega_z(r) \simeq \omega_{max}$, on a une rotation de type solide avec une vitesse azimutale variant linéairement avec la distance au centre $u_\theta(r) = \omega_{\max} r/2$. La vitesse angulaire au centre[1] du tourbillon est ainsi égale à $\Omega = \omega_{\max}/2$.

[1] Contrairement à ce que laisse penser la dénomination de vitesse angulaire, Ω est bien la pulsation caractéristique du tourbillon.

Les deux grandeurs Ω et rayon a caractérisent de façon simple et très générale un tourbillon. On définit ainsi des nombres sans dimension en fonction de Ω et a : le nombre de Reynolds, le nombre de Froude horizontal et le nombre de Reynolds de flottabilité comme respectivement

$$Re = \frac{\Omega a^2}{\nu}, \qquad F_h = \frac{\Omega}{N}, \qquad \text{et} \qquad \mathcal{R} = ReF_h^2 = \frac{\Omega^3 a^2}{\nu N^2}. \tag{B.2}$$

Tourbillon de Lamb-Oseen

Un tourbillon de Lamb-Oseen est caractérisé par définition par une distribution gaussienne de vorticité

$$\omega(r) = 2\Omega e^{-(\frac{r}{a})^2}, \tag{B.3}$$

où a est la taille caractéristique définie dans la section précédente. Dans ce cas, on a simplement $\Gamma = 2\pi\Omega a^2$ et les nombres sans dimension définis plus haut se réécrivent

$$Re = \frac{\Gamma}{2\pi\nu}, \qquad F_h = \frac{\Gamma}{2\pi a^2 N}, \qquad \text{et} \qquad \mathcal{R} = \left(\frac{\Gamma}{2\pi a}\right)^3 \frac{a^2}{\nu N^2}. \tag{B.4}$$

Notons que la vitesse angulaire est donnée par $u_\theta(r) = (\Omega a^2/r)[1 - exp(-(r/a)^2)]$ et que l'on peut utiliser comme unités naturelles de temps, de longueur et de vitesse, les grandeurs $T^{LO} = \Omega^{-1}$, ${L_h}^{LO} = a$ et $V^{LO} = a\Omega$.

Dipôle de tourbillons contrarotatifs

On appelle dipôle un couple de tourbillons contrarotatifs séparés d'une distance b tel que la circulation totale est nulle. Dans la limite $b \gg a$, chaque tourbillon évolue dans le champ de vitesse lointain de son voisin. A l'ordre 0 en a/b, les tourbillons sont advectés à une vitesse $\Omega a^2/b = \Gamma/(2\pi b)$ ce qui entraîne une translation globale du dipôle. L'effet d'ordre supérieur en a/b est l'étirement des tourbillons par leur voisin, égal à $\Gamma/(2\pi b^2)$. Cet étirement provoque une modification de la forme des tourbillons et joue un rôle important pour les instabilités du dipôle (par exemple pour l'instabilité elliptique en milieu homogène, Kerswell, 2002).

Dipôle de Lamb-Chaplygin

Le dipôle de Lamb-Chaplygin est une solution exacte des équations d'Euler qui est constituée de deux tourbillons contrarotatifs très rapprochés $b/a \lesssim 2$. La fonction de courant bidimensionnelle S_0 s'écrit avec les coordonnées cylindriques centrées entre les deux tourbillons :

$$S_0(r,\theta) \equiv \begin{cases} \dfrac{-2UR}{\mu_1 J_0(\mu_1)} J_1(\mu_1 r/R)\cos(\theta) & \text{if } r < R, \\ \\ Ur\left(1 - \dfrac{R^2}{r^2}\right)\cos(\theta) & \text{if } r = R, \end{cases} \tag{B.5}$$

où U est la vitesse de propagation du dipôle, R son rayon, J_0 et J_1 sont les fonctions de Bessel d'ordre 0 et 1 et $\mu_1 \simeq 3.8317$ est la première racine de J_1. On peut calculer la circulation $\Gamma \simeq 6.83UR$, la vitesse maximum dans le référentiel du laboratoire $U_{max} = 3.5U$ et le rayon des tourbillons $a \simeq 0.42R$. Il est naturel d'utiliser les grandeurs caractéristiques U et R pour définir les nombres sans dimension de la façon suivante :

$$Re^{LC} = \frac{UR}{\nu}, \qquad F_h^{LC} = \frac{U}{RN}, \quad \text{et} \quad \mathcal{R}^{LC} = \frac{U^3}{R\nu N^2}. \tag{B.6}$$

On peut relier ces nombres sans dimension classiquement utilisés pour le dipôle de Lamb-Chaplygin aux nombres sans dimension définis plus haut. Pour $r < R$, i.e. là où sont les tourbillons, la distribution de vorticité est donnée par

$$\omega(r,\theta) = -\frac{2U\mu_1}{J_0(\mu_1)R} J_1(\mu_1 r/R)\cos(\theta).$$

La vitesse angulaire au centre de chaque tourbillon est donc $\Omega \simeq 5.54U/R$ et on obtient à partir des définitions (B.2)

$$Re \simeq 0.98\ Re^{LC}, \qquad F_h \simeq 5.5\ F_h^{LC}, \quad \text{et} \quad \mathcal{R} \simeq 30.7\ \mathcal{R}^{LC}. \tag{B.7}$$

Les unités naturelles de temps, de longueur et de vitesse $T^{LC} = R/U$, ${L_h}^{LC} = R$ et $V^{LC} = U$ sont reliées aux unités naturelles associées à un tourbillon de Lamb-Oseen par $T^{LC} \simeq 5.5T^{LO}$, ${L_h}^{LC} \simeq 2.4{L_h}^{LO}$ et $V^{LC} \simeq 0.44V^{LO}$.

Instabilité zigzag sur 2 tourbillons colonnaires contra-rotatifs

On donne quelques résultats utiles pour la suite sur l'instabilité zigzag sur un dipôle en milieu stratifié non-tournant. Dans le cas fortement stratifié $F_h < 1$ et pour les grandes séparations entre les tourbillons $b/a \gg 1$, l'instabilité zigzag courbe le dipôle avec un taux de croissance égal à l'étirement $\sigma = \Gamma/(2\pi b^2)$. La longueur d'onde verticale du mode dominant de l'instabilité est $\lambda_z \simeq 1.9bF_h$ (Billant, 2010; Billant *et al.*, 2010). Au dessus du seuil $F_h = 1$, l'instabilité zigzag devient amortie par une couche critique et le taux de croissance diminue très fortement.

Pour le cas des dipôles avec des tourbillons rapprochés (similaire au dipôle de LC), il n'existe pas de résultats analytiques généraux pour toutes stratifications et longueurs d'onde. Billant & Chomaz (2000b) ont dérivé dans le cas du dipôle de LC des résultats valables dans les limites de fortes stratifications et de grandes longueurs d'onde. La génération par une étude numérique a montré que pour le mode dominant de l'instabilité zigzag $\sigma \simeq 0.7U/R$ et $\lambda_z \simeq 10F_hR$ (Billant & Chomaz, 2000c). Notons que pour le dipôle de LC, on observe une transition entre l'instabilité elliptique (instabilité caractéristiques des milieux non stratifiés) et l'instabilité zigzag pour $F_h^{LC} \gtrsim 0.2$ ($F_h \gtrsim 1$). L'invariance du mode dominant de l'instabilité zigzag selon F_h, caractéristique des écoulements très fortement influencés par la stratification, est obtenue pour $F_h^{LC} \lesssim 0.1$ ($F_h \lesssim 0.5$). Notons enfin que pour un dipôle de Lamb-Oseen avec $b = 2.5a$, le mode dominant de l'instabilité zigzag est caractérisé par $\lambda_z \simeq 1.73bF_h$ (Deloncle *et al.*, 2008).

Bibliography

Alexakis, A., Mininni, P. D. & Pouquet, A. 2005. Shell-to-shell energy transfer in magnetohydrodynamics. I. Steady state turbulence. *Phys Rev. E*, 72(046301).

Alvedius, K. 1999. Random forcing of three-dimensional homogeneous turbulence. *Phys. Fluids*, 11:1880–1889.

Antonia, R. A., Ould-Rouis, M., Anselmet, F. & Zhu, Y. 1997. Analogy between predictions of Kolmogorov and Yaglom. *J. Fluid Mech.*, 332:395–409.

Arobone, E. & Sarkar, S. 2010. The statistical evolution of a stratified mixing layer with horizontal shear invoking feature extraction. *Phys. Fluids*, 22(115108).

Augier, P. & Billant, P. 2011. Onset of secondary instabilities on the zigzag instability in stratified fluids. *J. Fluid Mech.*, 662:120–131.

Augier, P., Billant, P. & Chomaz, J.-M. 2012a. Stratified turbulence forced with columnar dipoles. Part 2. Numerical study. *in preparation for submission to J. Fluid Mech.*

Augier, P., Billant, P., Negretti, M. E. & Chomaz, J.-M. 2012b. Stratified turbulence forced with columnar dipoles. Part 1. Experimental study, on the edge of the strongly stratified turbulent regime. *in preparation for submission to J. Fluid Mech.*

Augier, P., Chomaz, J.-M. & Billant, P. 2012c. Spectral analysis of the transition to turbulence from a dipole in stratified fluids. *submitted to J. Fluid Mech.*

Augier, P., Galtier, S. & Billant, P. 2012d. Kolmogorov laws for stratified turbulence. *in preparation.*

Bartello, P. 1995. Geostrophic adjustment and inverse cascades in rotating stratified turbulence. *J. Atmos. Sci.*, 52(24):4410–4428.

Basak, S. & Sarkar, S. 2006. Dynamics of a stratified shear layer with horizontal shear. *J. Fluid Mech.*, 568:19–54.

Batchelor, G.K. 1967. *An introduction to fluid dynamics.* Cambridge Univ. Press, Cambridge.

Batchelor, G. K. 1953. *The theory of homogeneous turbulence.* Cambridge Univ. Press, Cambridge.

Bigot, B., Galtier, S. & Politano, H. 2008. Energy decay laws in strongly anisotropic MHD turbulence. *Phys. Rev. Lett.*, 100:074502–4.

Billant, P. 2010. Zigzag instability of vortex pairs in stratified and rotating fluids. Part 1. General stability equations. *J. Fluid Mech.*, 660:354–395.

Billant, P. & Chomaz, J.-M. 2000a. Experimental evidence for a new instability of a vertical columnar vortex pair in a strongly stratified fluid. *J. Fluid Mech.*, 418:167–188.

Billant, P. & Chomaz, J.-M. 2000b. Theoretical analysis of the zigzag instability of a vertical columnar vortex pair in a strongly stratified fluid. *J. Fluid Mech.*, 419:29–63.

Billant, P. & Chomaz, J.-M. 2000c. Three-dimensional stability of a vertical columnar vortex pair in a stratified fluid. *J. Fluid Mech.*, 419:65–91.

Billant, P. & Chomaz, J.-M. 2001. Self-similarity of strongly stratified inviscid flows. *Phys. Fluids*, 13:1645–1651.

Billant, P., Deloncle, A., Chomaz, J.-M. & Otheguy, P. 2010. Zigzag instability of vortex pairs in stratified and rotating fluids. Part 2. Analytical and numerical analyses. *J. Fluid Mech.*, 660:396–429.

Boffetta, G. 2007. Energy and enstrophy fluxes in the double cascade of two-dimensional turbulence. *J. Fluid Mech.*, 589:253–260.

Brethouwer, G. & Lindborg, E. 2008. Passive scalars in stratified turbulence. *Geophys. Res. Lett.*, 35:–.

Brethouwer, G. & Lindborg, E. 2009. Numerical study of vertical dispersion by stratified turbulence. *J. Fluid Mech.*, 631:149–163.

Brethouwer, G., Billant, P., Lindborg, E. & Chomaz, J.-M. 2007. Scaling analysis and simulation of strongly stratified turbulent flows. *J. Fluid Mech.*, 585:343–368.

Brucker, K. A. & Sarkar, S. 2007. Evolution of an initially turbulent stratified shear layer. *Phys. Fluids*, 19(10).

Bryan, F. 1987. Parameter sensitivity of primitive equation ocean general-circulation models. *J. Phys. Oceanogr.*, 17(7):970–985.

Caillol, P. & Zeitlin, V. 2000. Kinetic equations and stationary energy spectra of weakly nonlinear internal gravity waves. *Dyn. Atm. Oceans*, 32:81–112.

Cambon, C. 2001. Turbulence and vortex structures in rotating and stratified flows. *Eur. J. Mech. B - Fluids*, 20:489–510.

Cardoso, O., Marteau, D. & Tabeling, P. 1994. Quantitative experimental study of the free decay of quasi-two-dimensional turbulence. *Phys. Rev. E*, 49(1):454–461.

Carnevale, G. F., Briscolini, M. & Orlandi, P. 2001. Buoyancy- to inertial-range transition in forced stratified turbulence. *J. Fluid Mech.*, 427:205–239.

Charney, J. G. 1971. Geostrophic turbulence. *J. Atmos. Sci.*, 28(6):1087–&.

Chevillard, L., Castaing, B., Lévêque, E. & Arneodo, A. 2006. Unified multifractal description of velocity increments statistics in turbulence: Intermittency and skewness. *Physica D: Nonlinear Phenomena*, 218(1):77–82.

Cho, J. Y. N. & Lindborg, E. 2001. Horizontal velocity structure functions in the upper troposphere and lower stratosphere 1. Observations. *J. Geoph. Res.-Atmos.*, 106(D10): 10223–10232.

Cho, J. Y. N., Newell, R. E. & Barrick, J. D. 1999. Horizontal wavenumber spectra of

winds, temperature, and trace gases during the Pacific Exploratory Missions: 2. Gravity waves, quasi-two-dimensional turbulence, and vortical modes. *J. Geoph. Res.*, 104(D13): 16297–16308.

Clyne, J. & Rast, M. 2005. A prototype discovery environment for analyzing and visualizing terascale turbulent fluid flow simulations. In Erbacher, RF and Roberts, JC and Grohn, MT and Borner, K, editor, *Visualization and Data Analysis 2005*, volume 5669, pages 284–294. SPIE; Soc Imaging Sci & Technol.

Corrsin, S. 1951. On the spectrum of isotropic temperature fluctuations in an isotropic turbulence. *J. Appl. Phys.*, 22(4):469–473.

Craya, A. D. 1958. Contribution à l'analyse de la turbulence associée à des vitesses moyennes. *Ministère de l'air, France*, PST 345.

Cushman-Roisin, B. 1994. *Introduction to geophysical fluid dynamics*. Prentice Hall.

Deloncle, A. 2007. *Three dimensional instabilities in stratified fluids*. PhD thesis, LadHyX, Polytechnique.

Deloncle, A., Billant, P. & Chomaz, J.-M. 2008. Nonlinear evolution of the zigzag instability in stratified fluids: a shortcut on the route to dissipation. *J. Fluid Mech.*, 599:229–238.

Deloncle, A., Billant, P. & Chomaz, J.-M. 2011. Three-dimensional stability of vortex arrays in a stratified and rotating fluid: theoretical analysis. *J. Fluid Mech.*, 678:482–510.

Deloncle, A., Chomaz, J.-M. & Billant, P. 2007. Three-dimensional stability of a horizontally sheared flow in a stably stratified fluid. *J. Fluid Mech.*, 570:297–305.

Dewan, E. 1997. Saturated-cascade similitude theory of gravity wave spectra. *J. Geophys. Res.-Atmos.*, 102(D25):29799–29817.

Dewan, E. M. & Good, R. E. 1986. Saturation and the universal spectrum for vertical profiles of horizontal scalar winds in the atmosphere. *J. Geophys. Res.-Atmos.*, 91(D2):2742–2748.

Diamessis, P. J., Spedding, G. R. & Domaradzki, J. A. 2011. Similarity scaling and vorticity structure in high-Reynolds-number stably stratified turbulent wakes. *J. Fluid Mech.*, 671: 52–95.

Falkovich, G. & Sreenivasan, K. R. 2006. Lessons from hydrodynamic turbulence. *Phys. Today*, 59(4):43–49.

Fincham, A. M., Maxworthy, T. & Spedding, G. R. 1996. Energy dissipation and vortex structure in freely decaying, stratified grid turbulence. *Dynamics of Atmospheres and Oceans*, 23(1-4):155 – 169.

Fjortoft, R. 1953. On the changes in the spectral distribution of kinetic energy for twodimensional, nondivergent flow. *Tellus*, 5(3):225–230.

Fofonoff, N. P. 1969. Spectral characteristics of internal waves in the ocean. *Deep.Sea Res.*, 16(Suppl. S):58–71.

Frisch, U. 1995. *Turbulence: the legacy of A.N. Kolmogorov*. Cambridge Univ. Press, Cambridge.

Frisch, U., Kurien, S., Pandit, R., Pauls, W., Ray, S. S., Wirth, A. & Zhu, J.-Z. 2008. Hyperviscosity, galerkin truncation, and bottlenecks in turbulence. *Phys. Rev. Lett.*, 101

(144501).

Fritts, D. C. 1984. Gravity-wave saturation in the middle atmosphere - a review of theory and observations. *Rev. Geophys.*, 22(3):275–308.

Fritts, D. C. & Alexander, M. J. 2003. Gravity wave dynamics and effects in the middle atmosphere. *Rev. Geophys.*, 41(1).

Gage, K. S. 1979. Evidence for a $k^{-5/3}$ law inertial range in mesoscale 2-dimensional turbulence. *J. Atmos. Sci.*, 36(10):1950–1954.

Gage, K. S. & Nastrom, G. D. 1986. Theoretical interpretation of atmospheric wave-number spectra of wind and temperature observed by commercial aircraft during GASP. *J. Atmos. Sci.*, 43(7):729–740.

Galtier, S. 2008a. Exact scaling laws for 3D electron MHD turbulence. *J. Geophys. Res.*, 113:A01102–4.

Galtier, S. 2008b. von Karman-Howarth equations for hall magnetohydrodynamic flows. *Phys. Rev. E*, 77:015302(R)–4.

Galtier, S. 2009a. Consequence of space correlation foliation for electron magnetohydrodynamic turbulence. *Phys. Plasmas*, 16:112310–6.

Galtier, S. 2009b. Exact vectorial law for axisymmetric MHD turbulence. *Astrophys. J.*, 704: 1371–1384.

Galtier, S. 2009c. Exact vectorial law for homogeneous rotating turbulence. *Phys. Rev. E*, 80:046301–9.

Galtier, S. 2011. Third-order elsässer moments in axisymmetric MHD turbulence. *C.R. Physique*, 12:151–159.

Galtier, S., Pouquet, A. & Mangeney, A. 2005. On the spectral scaling laws for incompressible anisotropic MHD turbulence. *Phys. Plasmas*, 12:092310–5.

Gargett, A. E., Hendricks, P. J., Sanford, T. B., Osborn, T. R. & Williams, A. J. 1981. A composite spectrum of vertical shear in the upper ocean. *J. Phys. Oceanogr.*, 11(9): 1258–1271.

Garrett, C. & Munk, W. 1979. Internal waves in the ocean. *Annu. Rev. Fluid Mech.*, 11: 339–369.

Gerin, R., Poulain, P.-M., Taupier-Letage, I., Millot, C., Ismail, S. Ben & Sammari, C. 2009. Surface circulation in the Eastern Mediterranean using drifters (2005-2007). *Ocean Sci.*, 5 (4):559–574.

Godeferd, F. S. & Cambon, C. 1994. Detailed investigation of energy transfers in homogeneous stratified turbulence. *Phys. Fluids*, 6(6):2084–2100.

Godeferd, F. S. & Staquet, C. 2003. Statistical modelling and direct numerical simulations of decaying stably stratified turbulence. Part 2. Large-scale and small-scale anisotropy. *J. Fluid Mech.*, 486:115–159.

Godoy-Diana, R., Chomaz, J.-M. & Billant, P. 2004. Vertical length scale selection for pancake vortices in strongly stratified viscous fluids. *J. Fluid Mech.*, 504:229–238.

Goldreich, P. & Sridhar, S. 1995. Towards a theory of interstellar turbulence II. Strong alfvénic turbulence. *Astrophys. J.*, 438:763–775.

Goosse, H., Deleersnijder, E., Fichefet, T. & England, M. H. 1999. Sensitivity of a global coupled ocean-sea ice model to the parameterization of vertical mixing. *J. Geophys. Res.-Oceans*, 104(C6):13681–13695.

Gostiaux, L. & Dauxois, T. 2004. Propagation et réflexion d'ondes internes dans l'océan : le mystère de l'angle critique. *BUP*, 868.

Gostiaux, L., Didelle, H., Mercier, S. & Dauxois, T. 2007. A novel internal waves generator. *Experiments in Fluids*, 42:123–130.

Gotoh, T., Fukayama, D. & Nakano, T. 2002. Velocity field statistics in homogeneous steady turbulence obtained using a high-resolution direct numerical simulation. *Phys. Fluids*, 14 (3):1065–1081.

Gregg, M. C. 1987. Diapycnal mixing in the thermocline - a review. *J. Geophys. Res.-Oceans*, 92(C5):5249–5286.

Hamilton, K., Takahashi, Y. O. & Ohfuchi, W. 2008. Mesoscale spectrum of atmospheric motions investigated in a very fine resolution global general circulation model. *J. Geophys. Res.-Atmos.*, 113(D18).

Hazel, P. 1972. Numerical studies of the stability of inviscid stratified shear flows. *J. Fluid Mech.*, 51:39–61.

Hebert, D. A. & de Bruyn Kops, S. M. 2006a. Predicting turbulence in flows with strong stable stratification. *Phys. Fluids*, 18.

Hebert, D. A. & de Bruyn Kops, S. M. 2006b. Relationship between vertical shear rate and kinetic energy dissipation rate in stable stratified flows. *Geophys. Res. Lett.*, 33.

Herring, J. R. 1974. Approach of axisymmetric turbulence to isotropy. *Phys. Fluids*, 17: 859–872.

Herring, J. R. & Metais, O. 1989. Numerical experiments in forced stably stratified turbulence. *J. Fluid Mech.*, 202:97–115.

Hines, C. O. 1991. The saturation of gravity-waves in the middle atmosphere. 1. Critique of linear-instability theory. *J. Atmos. Sci.*, 48(11):1348–1359.

Holford, J. M. & Linden, P. F. 1999. Turbulent mixing in a stratified fluid. *Dyn. Atmos. Oceans*, 30(2-4):173–198.

Holloway, G. 1980. Oceanic internal waves are not weak waves. *J. Phys. Oceanogr.*, 10(6): 906–914.

Holloway, G. 1983. A conjecture relating oceanic internal waves and small-scale processes. *Atm. Ocean*, 21(1):107 – 122.

Holloway, G. 1988. The buoyancy flux from internal gravity wave breaking. *Dyn. Atmos. Oceans*, 12:107 – 125.

Howard, L. N. 1961. Note on a paper of John W. Miles. *J. Fluid Mech.*, 10:509–512.

Itsweire, E. C., Helland, K.N. & Vanatta, C. W. 1986. The evolution of grid-generated

turbulence in a stably stratified fluid. *J. Fluid Mech.*, 162:299–338.

Ivey, G. N., Winters, K. B. & Koseff, J. R. 2008. Density stratification, turbulence, but how much mixing? *Annu. Rev. Fluid Mech.*, 40(1):169–184.

Jacobitz, F. G., Rogers, M. M. & Ferziger, J. H. 2005. Waves in stably stratified turbulent flow. *J. Turbul.*, 6(32).

Kerswell, R. R. 2002. Elliptical instability. *Annu. Rev. Fluid Mech.*, 34.

Kitamura, Y. & Matsuda, Y. 2010. Energy cascade processes in rotating stratified turbulence with application to the atmospheric mesoscale. *J. Geophys. Res.-Atmos.*, 115.

Klein, P., Hua, B. L., Lapeyer, G., Capet, X., Gentil, S. Le & Sasaki, H. 2008. Upper ocean turbulence from high-resolution 3D simulations. *J. Phys. Oceanogr.*, 28:1748–1763.

Kolmogorov, A. N. 1941a. Dissipation of energy in the locally isotropic turbulence. *Dokl. Akad. Nauk SSSR*, 32:16–18.

Kolmogorov, A. N. 1941b. The local structure of turbulence in incomressible viscous fluids for very large reynolds numbers. *Compt. Rend. Acad. Sci. (USSR)*, 30:301–305.

Kolmogorov, A. N. 1962. A refinement of previous hypotheses concerning the local structure of turbulence in a viscous incompressible fluid at high reynolds number. *Journal of Fluid Mechanics*, 13(01):82–85.

Koshyk, J. N. & Hamilton, K. 2001. The horizontal kinetic energy spectrum and spectral budget simulated by a high-resolution troposphere-stratosphere-mesosphere GCM. *J. Atmos. Sci.*, 58(4):329–348.

Koudella, C. R. & Staquet, C. 2006. Instability mechanisms of a two-dimensional progressive internal gravity wave. *J. Fluid Mech.*, 548:165–196.

Kraichnan, R. H. 1967. Inertial-range in 2-dimensional turbulence. *Phys. Fluids*, 10(7): 1417–&.

Kraichnan, R. H. 1971. Inertial-range transfer in 2-dimensional ans 3-dimensional turbulence. *J. Fluid Mech.*, 47(JUN14):525–&.

Kurien, S., Smith, L. & Wingate, B. 2006. On the two-point correlation of potential vorticity in rotating and stratified turbulence. *J. Fluid Mech.*, 555:131–140.

Lamriben, C., Cortet, P.-P. & Moisy, F. 2011. Direct measurements of anisotropic energy transfers in a rotating turbulence experiment. *Phys. Rev. Lett.*, 107(2):024503.

Landau, L. & Lifchitz, E. 1989. *Mécanique des fluides*. Éd. Mir (2nd ed.), Sov. Union.

Lapeyre, G. 2010. A propos de processus nonlinéaires associés à la sous-mésoéchelle dans l'océan et à l'échelle synoptique dans l'atmosphère.

Laval, J. P., McWilliams, J. C. & Dubrulle, B. 2003. Forced stratified turbulence: Successive transitions with Reynolds number. *Phys. Rev. E*, 68(3, Part 2).

Leblanc, S. 2003. Internal wave resonances in strain flows. *J. Fluid Mech.*, 477:259 – 283.

Lelong, M. P. & Dunkerton, T. J. 1998a. Inertia-gravity wave breaking in three dimensions. Part I Convectively stable waves. *J. Atmos. Sci.*, 55(15):2473–2488.

Lelong, M. P. & Dunkerton, T. J. 1998b. Inertia-gravity wave breaking in three dimensions. Part II: Convectively unstable waves. *J. Atmos. Sci.*, 55(15):2489–2501.

Lelong, M. P. & Riley, J. J. 1991. Internal wave vortical mode interactions in strongly stratified flows. *J. Fluid Mech.*, 232:1–19.

Lesieur, M. 1997. *Turbulence in Fluids.* 3rd ed. Kluwer Academic.

Leweke, T. & Williamson, C. H. T. 1998. Cooperative elliptic instability of a vortex pair. *J. Fluid Mech.*, 360:85–119.

Lienhard, J. H. & Van Atta, C. W. 1990. The decay of turbulence in thermally stratified flow. *J. Fluid Mech.*, 210:57–112.

Lilly, D. K. 1983. Stratified turbulence and the mesoscale variability of the atmosphere. *J. Atmos. Sci.*, 40:749–761.

Lilly, D. K., Bassett, G., Droegemeier, K. & Bartello, P. 1998. Stratified turbulence in the atmospheric mesoscales. *Theo. Comp. Fluid Dyn.*, 11(3-4):139–153.

Lin, J. T. & Pao, Y. H. 1979. Wakes in Stratified Fluids. *Annu. Rev. Fluid Mech.*, 11: 317–338.

Lindborg, E. 1999. Can the atmospheric kinetic energy spectrum be explained by two-dimensional turbulence? *J. Fluid Mech.*, 388:259–288.

Lindborg, E. 2002. Strongly stratified turbulence: a special type of motion. In *Advances in Turbulence IX, Proceedings of the Ninth European Turbulence Conference*, Southampton.

Lindborg, E. 2005. The effect of rotation on the mesoscale energy cascade in the free atmosphere. *Geophys. Res. Lett.*, 32(1).

Lindborg, E. 2006. The energy cascade in a strongly stratified fluid. *J. Fluid Mech.*, 550: 207–242.

Lindborg, E. 2007a. Horizontal wavenumber spectra of vertical vorticity and horizontal divergence in the upper troposphere and lower stratosphere. *J. Atmos. Sci.*, 64(3):1017–1025.

Lindborg, E. 2007b. Third-order structure function relations for quasi-geostrophic turbulence. *J. Fluid Mech.*, 572:255–260.

Lindborg, E. & Brethouwer, G. 2007. Stratified turbulence forced in rotational and divergent modes. *J. Fluid Mech.*, 586:83–108.

Lindborg, E. & Brethouwer, G. 2008. Vertical dispersion by stratified turbulence. *J. Fluid Mech.*, 614:303–314.

Lindborg, E. & Cho, J. Y. N. 2001. Horizontal velocity structure functions in the upper troposphere and lower stratosphere 2. Theoretical considerations. *J. Geoph. Res.-Atmos.*, 106(D10):10233–10241.

Lindborg, E. & Fedina, E. 2009. Vertical turbulent diffusion in stably stratified flows. *Geophys. Res. Lett.*, 36.

Lindborg, E. & Riley, J. J. 2007. A condition on the average Richardson number for weak non-linearity of internal gravity waves. *Tellus Ser. A-Dyn. Meteorol. Oceanol.*, 59(5):781–

784.

Lumley, J. L. 1964. The spectrum of nearly inertial turbulence in a stably stratified fluid. *J. Atmos. Sci.*, 21(1):99–102.

Lundbladh, A., Berlin, S., Skote, M., Hildings, C., Choi, J., Kim, J. & Henningson, D. S. 1999. An efficient spectral method for simulation of incompressible flow over a flat plate. *Trita-mek. Tech. Rep.*, 11.

Lvov, Y. V. & Tabak, E. G. 2001. Hamiltonian formalism and the garrett-munk spectrum of internal waves in the ocean. *Phys. Rev. Lett.*, 87(16):168501.

Metais, O. & Herring, J. R. 1989. Numerical simulations of freely evolving turbulence in stably stratified fluids. *J. Fluid Mech.*, 202:117–148.

Metais, O., Bartello, P., Garnier, E., Riley, J. J. & Lesieur, M. 1996. Inverse cascade in stably stratified rotating turbulence. *Dyn. Atmos. Oceans*, 23(1-4):193–203.

Meyrand, R. & Galtier, S. 2010. A universal law for solar-wind turbulence at electron scales. *Astrophys. J.*, 721:1421–1424.

Miles, J. W. 1961. On the stability of heterogeneous shear flows. *J. Fluid Mech.*, 10:496–508.

Mininni, P. D., Alexakis, A. & Pouquet, A. 2006. Large-scale flow effects, energy transfer, and self-similarity on turbulence. *Phys Rev. E*, 74(016303).

Moisy, F., Agostini, L. & Tan, G. 2009. Third order structure function and energy transfers in forced and decaying rotating turbulence. unpublished.

Monin, A.S. & Yaglom, A.M. 1975. *Statistical Fluid Mechanics, vol. 2.* Cambridge MA, MIT Press.

Morize, C. 2006. *De la turbulence 3D en déclin à la turbulence anisotrope dominée par la rotation.* PhD thesis, Paris 7 - Denis Diderot.

Munk, W. 1981. *Evolution of Physical Oceanography*, chapter Internal waves and small-scale processes, pages 264–291. ed. B. A. Warren & C. Wunsch, MIT Press.

Nastrom, G. D. & Gage, K. S. 1985. A climatology of atmospheric wavenumber spectra of wind and temperature observed by commercial aircraft. *J. Atmos. Sci.*, 42(9):950–960.

Nastrom, G. D., Gage, K. S. & Jasperson, W. H. 1984. Kinetic-energy spectrum of largescale and mesoscale atmospheric processes. *Nature*, 310(5972):36–38.

Nazarenko, S.V. & Schekochihin, A.A. 2011. Critical balance in MHD, rotating and stratified turbulence: towards a universal scaling conjecture. *J. Fluid Mech.*, 677:134–153.

Oboukhov, A. M. 1962. Some specific features of atmospheric tubulence. *Journal of Fluid Mechanics*, 13(01):77–81.

Obukhov, A. M. 1949. Structure of the temperature field in turbulent flows. *Izv. Akad. Nauk. SSSR, Ser. Geogr. and Geophys.*, 13(58).

Osborn, T.R. & Cox, C. S. 1972. Oceanic fine structure. *Geophys. Fluid Dyn.*, 3:321–345.

Otheguy, P. 2005. *Dynamique de l'appariement tourbillonnaire en milieu stratifié et stratifié tournant.* PhD thesis, LadHyX, Polytechnique.

Otheguy, P., Billant, P. & Chomaz, J.-M. 2006a. The effect of planetary rotation on the zigzag instability of co-rotating vortices in a stratified fluid. *J. Fluid Mech.*, 553:273–281.

Otheguy, P., Billant, P. & Chomaz, J.-M. 2007. Theoretical analysis of the zigzag instability of a vertical co-rotating vortex pair in a strongly stratified fluid. *J. Fluid Mech.*, 584: 103–123.

Otheguy, P., Chomaz, J.-M. & Billant, P. 2006b. Elliptic and zigzag instabilities on co-rotating vertical vortices in a stratified fluid. *J. Fluid Mech.*, 553:253–272.

Ozmidov, R. V. 1965. On the turbulent exchange in a stably stratified ocean. *Izv. Acad. Sci. USSR, Atmos. Oceanic Phys.*, 1:493–497.

P. Y. Le Traon, P. Klein, Hua, B. L. & Dibarboure, G. 2008. Do altimeter wavenumber spectra agree with the interior or surface quasigeostrophic theory? *J. Phys. Oceanogr.*, 38:1137–1142.

Park, Y. G., Whitehead, J. A. & Gnanadeskian, A. 1994. Turbulent mixing in stratified fluids - layer formation and energetics. *J. Fluid Mech.*, 279:279–311.

Pedlosky, J. 1987. *Geophysical fluid dynamics*. Springer.

Peltier, W. R. & Caulfield, C. P. 2003. Mixing efficiency in stratified shear flows. *Annu. Rev. Fluid Mech.*, 35(1):135–167.

Podesta, J. J. 2008. Laws for third-order moments in homogeneous anisotropic incompressible magnetohydrodynamic turbulence. *J. Fluid Mech.*, 609:171–194.

Politano, H. & Pouquet, A. 1998. von Karman-Howarth equation for MHD and its consequences on third-order longitudinal structure and correlation functions. *Phys. Rev. E*, 57: R21–R24.

Praud, O., Fincham, A. M. & Sommeria, J. 2005. Decaying grid turbulence in a strongly stratified fluid. *J. Fluid Mech.*, 522:1–33.

Praud, O., Sommeria, J. & Fincham, A. M. 2006. Decaying grid turbulence in a rotating stratified fluid. *J. Fluid Mech.*, 547:389–412.

Rieutord, M. 1997. *Une introduction à la dynamique des fluides*. Masson.

Riley, J. J. & Lelong, M.-P. 2000. Fluid motions in the presence of strong stable stratification. *An. Rev. Fluid Mech.*, 32:613–657.

Riley, J. J. & Lindborg, E. 2008. Stratified turbulence: A possible interpretation of some geophysical turbulence measurements. *J. Atmos. Sci.*, 65:2416–2424.

Riley, J. J. & de Bruyn Kops, S. M. 2003. Dynamics of turbulence strongly influenced by buoyancy. *Phys. Fluids*, 15(7):2047–2059.

Riley, J. J., Metcalfe, R. W. & Weissman, M. A. 1981. Direct numerical simulations of homogeneous turbulence in density-stratified fluids. *Proc. AIP Conf.*, 76:79–112.

Saddoughi, S. G. & Veeravalli, S. V. 1994. Local isotropy in turbulent boundary layers at high Reynolds number. *J. Fluid Mech.*, 268(333-372).

Sagaut, P. & Cambon, C. 2008. *Homogeneous turbulence dynamics*. Cambridge University Press.

Skamarock, W. C. 2004. Evaluating mesoscale NWP models using kinetic energy spectra. *Mon. Weather Rev.*, 132(12):3019–3032.

Smith, L. M. & Waleffe, F. 2002. Generation of slow large scales in forced rotating stratified turbulence. *J. Fluid Mech.*, 451:145–168.

Smith, S. A., Fritts, D. C. & Vanzandt, T. E . 1987. Evidence for a saturated spectrum of atmospheric gravity-waves. *J. Atmos. Sci.*, 44(10):1404–1410.

Smyth, W. D. & Moum, J. N. 2000a. Anisotropy of turbulence in stably stratified mixing layers. *Phys. Fluids*, 12(6):1343–1362.

Smyth, W. D. & Moum, J. N. 2000b. Length scales of turbulence in stably stratified mixing layers. *Phys. Fluids*, 12(6):1327–1342.

Smyth, W. D., Moum, J. N. & Caldwell, D. R. 2001. The efficiency of mixing in turbulent patches: inferences from direct simulations and microstructure observations. *J. Phys. Oceanogr.*, 31(8):1969–1992.

Sommeria, J. 2008. On the role of physical modelling in atmospheric and oceanic forecast. *Environ. Fluid Mech.*, 8(5-6, SI):485–493.

Sreenivasan, K. R. 1995. On the universality of the Kolmogorov constant. *Phys. Fluids*, 7 (11):2778–2784.

Staquet, C. 1998. Internal gravity waves in geophysical fluids. *CSIM Course on Environmental Stratified Flows*, 479:75–131.

Staquet, C. & Godeferd, F. S. 1998. Statistical modelling and direct numerical simulations of decaying stably stratified turbulence. Part 1. Flow energetics. *J. Fluid Mech.*, 360:295–340.

Staquet, C. & Riley, J. J. 1989. On the velocity field associated with potential vorticity. *Dynamics of Atmospheres and Oceans*, 14:93–123.

Staquet, C. & Sommeria, J. 2002. Internal gravity waves: from instabilities to turbulence. *Annu. Rev. Fluid Mech.*, 34(1):559–593.

Taylor, G. I. 1935. Statistical theory of turbulence part i-ii. *Proc. R. Soc. Lond.*, A 151: 421–64.

Vallgren, A. 2010. *Dynamic properties of two-dimensional and quasi-geostrophic turbulence.* PhD thesis, KTH Engineering Sciences.

Vallgren, A., Deusebio, E. & Lindborg. 2012. A possible explanation of the atmospheric kinetic and potential energy spectra. *accepted in Phys. Rev. Lett.*

Vallis, G. K. 2006. *Atmospheric and Oceanic Fluid Dynamics.* Cambridge University Press.

Vallis, G. K., Shutts, G. J. & Gray, M. E. B. 1997. Balanced mesoscale motion and stratified turbulence forced by convection. *Q. J. R. Meteorol. Soc.*, 123(542, Part B):1621–1652.

Vincent, A. & Meneguzzi, M. 1991. The spatial structure and statistical properties of homogeneous turbulence. *J. Fluid Mech.*, 225:1–20.

Waite, M. L. 2011. Stratified turbulence at the buoyancy scale. *Physics of Fluids*, 23(6): 066602.

Waite, M. L. & Bartello, P. 2004. Stratified turbulence dominated by vortical motion. *J.*

Fluid Mech., 517:281–308.

Waite, M. L. & Bartello, P. 2006a. Stratified turbulence generated by internal gravity waves. *J. Fluid Mech.*, 546:313–339.

Waite, M. L. & Bartello, P. 2006b. The transition from geostrophic to stratified turbulence. *J. Fluid Mech.*, 568:89–108.

Waite, M. L. & Smolarkiewicz, P. K. 2008. Instability and breakdown of a vertical vortex pair in a strongly stratified fluid. *J. Fluid Mech.*, 606.

Waite, M. L. & Snyder, C. 2009. The Mesoscale Kinetic Energy Spectrum of a Baroclinic Life Cycle. *J. Atmos. Sci.*, 66(4):883–901.

Wunsch, C. & Ferrari, R. 2004. Vertical mixing, energy and the general circulation of the oceans. *Annu. Rev. Fluid Mech.*, 36:281–314.

Yaglom, A. M. 1949. On the local structure of a temperature field in a turbulent flow. *Dokl. Akad. Nauk SSSR*, 69:743–746.

Yoon, K. H. & Warhaft, Z. 1990. The evolution of grid-generated turbulence under conditions of stable thermal stratification. *J. Fluid Mech.*, 215:601–638.